Thèse n° 9932

Ultrafast X-ray Spectroscopy of Heme Proteins

Présentée le 20 janvier 2020

à la Faculté des sciences de base
Laboratoire de spectroscopie ultrarapide
Programme doctoral en chimie et génie chimique

pour l'obtention du grade de Docteur ès Sciences

par

Dominik KINSCHEL

Acceptée sur proposition du jury

Prof. U. A. Hagfeldt, président du jury
Prof. M. Chergui, directeur de thèse
Dr T. Penfold, rapporteur
Dr M. Négrerie, rapporteur
Dr C. Milne, rapporteur

École
polytechnique
fédérale
de Lausanne

2020

Dedication

Etiquette would suggest dedicating my thesis
to a relative or a former teacher.
However, this thesis was started and accomplished
with the sole purpose of contributing to the field of basic science.
I have learnt a lot from previous scientists' contributions
and I hope this present work will be of help to other researchers.
Therefore, I dedicate my doctoral thesis:

To whoever may find it interesting and stimulating.

Acknowledgements

First, I want to highlight, that this thesis represents a team effort and not the work of a single person, many people contributed with their ideas, their support during the numerous beamtimes and many fruitful discussions.

A big thank you goes to Majed, for offering me this project, supporting all the travels for beamtimes and providing the materials which were needed to carry out the experiments, providing excellent scientific collaborators, many fruitful scientific discussions and many more things. Thank you.

Special thanks also go to all the jury members, for their time to read and review my thesis, the fruitful discussions and a big thank you for those who had to travel a long way.

I would like to thank all the past and present members of the X-ray team, which is a sub-team of LSU, focusing on all X-ray related experiments. Fabio, Lars, Thomas, Giacomo, Mario, Jakob, James, Giulia, Camila, Oliviero, Boris, Jeremy and Lijie. Thank you all for over 32 crazy beamtimes. A special thanks goes to Oliviero, Camila and Boris, who helped me with the XFEL beamtimes in Hamburg and Japan, working crazy hours and all the support to make both experiments a success and the great time we had in Japan together. It would have not worked out so well without you!

Following this, also thank you to our Japanese collaborators for the experiment at SACLA, especially Tetsuo. I want to thank Prof. Misawa, Prof. Suzuki and Makina Yabashi for supporting us with women and men power for the beamtime and Junichi for his help with Japanese chemical and chemical waste regulations and support during the beamtime. Thanks to Obara for the excellent support during the beamtime and everyone for making it a success and thank you for the unique chance of experiencing Japanese working culture.

Thank you, Fred, for your support and help with the preparation of the XFEL experiments and sharing all your wisdom about myoglobins and sample handling with me. Also, I want to thank the team of FXE at European XFEL, Christian, Fred, Wojciech, Dmitry, Peter and Sebastian.

The SwissFEL team, namely Chris, Gregor and Claudio together with collaborators Anna and Jakub deserve a big thank you for giving me the chance to complement my project, supporting me during the beamtime and all the help. Thanks Anna for doing crazy shifts.

I want to thank the whole team of LSU, Frank, Jeremy, Lars, Malte, Luca, Ben, Serhii, Natalia, Rebecca, Olivierio, Camila, Giulia, Livia, Hugo, Tania, Lijie, Fabio, both Thomas, Chris, José, Jakob, Gloria, Janina and Andre for all the support, fruitful discussions, funny times inside and outside of EPFL, the great skiing retreats, their support and for treating me still like a part of the team in the last two years which I spent far away at PSI. A special thanks goes also to my office mate Luca, this PhD would have not been possible without you! Thanks for always having an open ear to talk about anything and supporting each other. And Serhii who joined our office later, thank you for all the interesting questions and discussions.

The former and current secretaries of LSU, Monique, Anissa and Annick, thank you for all the hard work behind the scenes! And also thank you Anne Lene, secretary from the doctoral school, for all the support.

Thanks also to my project student Tomislav, you did a great job and I wish you all the best for your future.

Thank you, Alberto, for always cheering me up and motivating me to keep going in difficult times. Ghil, Riccardo and Ivan for the trips to the mountains and being there for no matter which reason I needed help with. Gloria, for the introduction to the group, the numerous dinners and parties! Lars, thank you for the patience and teaching me a lot about ultrafast spectroscopy. Vero, thanks for all the coffee breaks and inspiring discussions, and not to forget the fun skiing trips.

Andre and Kirsten, my office mates at PSI, thank you for giving me the chance to see what it is like to build a beamline from scratch, and for hosting me in their office. Thank you, Chris M., for always supporting us during beamtimes when the situation seemed hopeless, for your patience and sharing your wisdom and passion about X-ray spectroscopy. Claudio, thank you for introducing me to X-ray beamtimes, my first beamtime at Elletra in Trieste with you and later for numerous collaborations, fruitful discussion and hosting me in your office together with Chris for the last months of my PhD.

I want to acknowledge the numerous people behind the scenes at all the X-ray free electron laser facilities, accelerator physicists, engineers, controls people, laser scientists, machine people, IT people, technicians, cleaning personal and so on, such large-scale facilities only work thanks to a collaboration of hundreds of people and it is important to me to highlight also their contribution.

My girlfriend for supporting me over all this time and understanding the difficulties of beamtime life. And a big thank you to my parents and family, sorry for missing many events and get togethers during this time, thank you for all your support and understanding!

Abstract

With the advent of X-ray free-electron lasers (XFELs) time-resolved X-ray spectroscopic techniques have advanced to the femtosecond regime. These are element selective techniques which offer unique insight into the electronic and chemical environment and dynamics of a sample. Specifically, X-ray emission spectroscopy probes the occupied density of states and is sensitive to the spin and local structure of the element of interest, whereas X-ray absorption spectroscopy is a tool for probing the unoccupied density of electronic states which makes it sensitive to the oxidation state, ligation and local structure around a specific atom. The tunable photon energy of the X-ray from XFELs allows to selectively probe the element of interest in the sample and additionally, the high intensity (10^{11} to 10^{12} photons per pulse) makes it possible to study dilute biological samples in physiological conditions. The sample studied in this work is myoglobin with nitric oxide as ligand, which has long been used as a model system to gain deeper understanding of the class of heme proteins. These proteins all have an iron porphyrin (heme) as an active center and play a crucial role in oxygen storage and transport in all mammals for example, amongst many other functions.

In heme proteins, the change of the low-spin (LS) hexacoordinated heme (ground state) to the high spin (HS) pentacoordinated domed form (excited state) is promoted by a reversible ligand detachment, which can be induced by light, representing the “transition state” that ultimately drives the respiratory function. Here we investigate Myoglobin-NO (MbNO) by employing femtosecond Fe K_α and K_β non-resonant X-ray emission spectroscopy (XES) at an XFEL upon photolysis of the Fe-NO bond. We find that the photoinduced change from the LS ($S = 1/2$) MbNO to the HS ($S = 2$) deoxy-myoglobin (deoxyMb) heme occurs in ~800 fs, and it proceeds via an intermediate ($S = 1$) spin state. The XES results also show that upon NO recombination to deoxyMb, the return to the planar MbNO ground state is an electronic relaxation from HS to LS taking place in ~30 ps. Thus, the entire ligand dissociation-recombination cycle in MbNO is a spin cross-over followed by a reverse spin cross-over process. Femtosecond X-ray absorption near edge spectroscopy (XANES) experiments show that NO dissociates in <75 fs and the intermediate ($S = 1$) spin state which has antibonding character is populated in ~110 fs. The XANES spectrum at short time delays (t=1 ps) shows a similarity to the steady state difference spectrum (deoxyMb minus MbNO) suggesting that at 1 ps the present species is very similar to deoxyMb in terms of electronic and local geometric structure. XAS time-traces at the pre- and rising-edge (7112, 7122.5 and 7127 eV) reveal the shortest pathway of geminate recombination which takes ~30 ps.

Keywords

Proteins, Myoglobin, Time-resolved, X-ray Emission Spectroscopy, X-ray Absorption Spectroscopy X-ray Free electron laser, femtosecond, Spin Dynamics, Heme proteins

Zusammenfassung

Die Entwicklung von Röntgenstrahl Freie-Elektronen-Lasern (XFEL) eröffneten die Möglichkeit zeitaufgelöste Röntgenspektroskopie im Femtosekundenbereich durchzuführen. Diese Elementspezifischen Techniken gewähren einzigartige Einsichten in die chemische und elektronische Umgebung und Dynamik einer Probe. Röntgenemissionsspektroskopie untersucht insbesondere die besetzte Zustandsdichte und erlaubt die Auflösung von Spin und lokaler Struktur des spezifischen Elements. Wohingegen die Röntgenabsorptionspektroskopie die Dichte, der nicht besetzten elektronischen Zustände erlaubt und Rückschlüsse auf den Oxidationszustand, die Ligation und lokale Struktur gibt. Die Möglichkeit die Photonenenergie in einer XFEL Messung zu variieren erlaubt es, selektiv Elemente einer Probe zu untersuchen und durch die hohe Intensität (10^{11} bis 10^{12} Photonen pro Puls) des Röntgenstrahls, ist es möglich auch verdünnte biologische Proben in physiologischen Bedingungen zu untersuchen.

Die in dieser Arbeit untersuchte Probe ist Myoglobin mit einem Stickstoffoxid als Liganden, was lange als Modellsystem diente um ein tieferes Verständnis für die Klasse der Hämproteine zu gewinnen. Das aktive Zentrum dieser Proteinklasse ist ein Eisenporphyrin (Häm), welchem unter anderem eine entscheidende Rolle bei der Speicherung und dem Transport von Sauerstoff bei Säugetieren zukommt.

In Hämproteinen wird durch eine reversible, licht-induzierte Liganden Ablösung eine strukturelle Veränderung von einem Low-Spin (LS) hexakoordiniertem Häm (Grundzustand) zur pentakoordinierten High-Spin (HS) Form (angeregter Zustand) erzielt. Die pentakoordinierten High-Spin (HS) Form repräsentiert den Übergangszustand welcher letztlich für die Atmungsfunktion verantwortlich. In dieser Arbeit untersuchen wir Nitrosyl-myoglobin (MbNO), mittels Femtosekunden Fe K_α and K_β nicht-resonanter Röntgen Emissions Spektroskopie (XES) an einem XFEL nach der Photolyse der Fe-NO Bindung. Wir fanden, dass die photoinduzierten Veränderungen vom LS ($S = 1/2$) zum HS ($S = 2$) deoxy-Myoglobin (deoxyMb) heme in ~800 fs stattfindet, und via einen Übergangszustand ($S = 1$) erfolgt. Die XES Ergebnisse zeigen ebenfalls, dass nach der Rekombination von NO zu deoxyMb, der Übergang zum planaren MbNO Grundzustand eine elektronische Relaxation vom HS zum LS Zustand in ~30 ps stattfindet. Daher ist der ganze Liganden Dissoziations- und Rekombinationszyklus in MbNO ein Spin Übergang gefolgt von einem umgekehrten Spin Übergang. Femtosekunden Röntgen-Nahkanten-Absorptions-Spektroskopie (XANES) Experimente wurden ebenfalls an XFELs durchgeführt und zeigen, dass NO in <75 fs dissoziiert und der Übergangszustand ($S = 1$), welcher antibindenden Charakter hat in ~110 fs populiert wird. Das XANES Spektrum bei kurzen Verzögerungszeiten zwischen Anregungs- und Probe-puls ($t = 1$ ps) zeigt eine Ähnlichkeit zu dem statischen Differenz-Spektrum (deoxyMb minus MbNO). Dies weißt darauf hin, dass die bei 1 ps vorgefunden Spezies sehr ähnlich in Bezug auf elektronische und geometrische Struktur zu deoxyMb ist. XAS Zeitspuren bei der Vorkante und steigenden Kante (7112, 7122.5 and 7127 eV) zeigen den kürzesten Weg für Rekombination von NO zu Mb* in ~30 ps.

Schlüsselwörter

Proteine, Myoglobin, Zeit-aufgelöste Spektroskopie, X-ray Emissions Spektroskopie, X-ray Freier Elektronen Laser, Femtosekunde, Spin Dynamik,

Abbreviations

Symbol	**Description**
CVD	Chemical Vapor Deposition
DFT	Density Functional Theory
DNA	Deoxyribonucleic acid
EXFEL	European X-ray Free Electron Laser
Far	Farnesene (a chemical compound)
fs	femtosecond
FWHM	Full width half maximum
GR	Geminate Recombination
Hb	Hemoglobin
HOMO	Highest Occupied Molecular Orbital
HS	High Spin
IR	Infrared
IRF	Instrument Response Function
JASRI	Japan Synchrotron Radiation Research Institute
LS	Low Spin
LUMO	Lowest Unoccupied Molecular Orbital
MXAN	Method for extracting structural information from XANES spectra
NIR	Near Infrared
ps	picosecond
rms	Root mean square
SACLA	Spring-8 Angstrom Compact free electron Laser
SASE	Self-Amplified Spontaneous Emission
SCO	Spin-Cross-Over
SLS	Swiss Light Source
S/N	Signal-to-noise
TA	Transient Absorption
TDDFT	Time-Dependent Density Functional Theory
TFY	Total Fluorescence Yield
TR	Time-resolved
TR-NXES	Time-resolved Non-resonant X-ray Emission Spectroscopy
TR-XAS	Time-resolved X-ray Absorption Spectroscopy
UV	Ultraviolet
VIS	Visible
VR	Vibrational Relaxation
XANES	X-ray Absorption Near Edge Structure
XAS	X-ray Absorption Spectroscopy

XDS	X-ray Diffuse Scattering
XES	X-rays Emission Spectroscopy
XFEL	X-ray free electron laser

Table of Contents

Acknowledgements .... **vii**

Abstract .... **ix**

Keywords .... **x**

Zusammenfassung .... **xi**

Schlüsselwörter .... **xii**

Abbreviations .... **xiii**

Table of Contents .... **xv**

Chapter 1 Introduction **19**

Chapter 2 Heme Proteins **21**

2.1 Protein Structure 22

2.2 Conjugated Proteins 25

2.3 Heme Proteins 26

2.4 Myoglobin 27

2.4.1 Iron as the Active-Center 30

2.4.2 Myoglobin-NO 31

2.5 Time Scales of Important Processes in Proteins 32

2.6 Previous Studies on Myoglobin-NO 34

Chapter 3 Ultrafast X-ray Spectroscopic Techniques **41**

3.1 Observing Molecular Motion 41

3.2 X-ray Interaction with Matter 43

3.3 X-ray Absorption Spectroscopy 43

3.4 X-ray Emission Spectroscopy 46

3.5 X-ray Free Electron Lasers 49

Chapter 4 Experimental Setups **52**

4.1.1 JASRI – SACLA, BL3 52

4.1.2 European XFEL 55
4.1.3 SwissFEL 56
4.2 Sample Delivery Systems 57
4.3 Sample Preparation and Handling 59
4.3.1 UV-VIS and Sample Monitoring 60
Chapter 5 Femtosecond X-ray Emission Spectroscopy of Myoglobin 61
5.1 Introduction 61
5.2 Experimental Details 63
5.2.1 Methods Summary 63
5.2.2 Time-resolved X-ray Emission Spectroscopy (SACLA) 63
5.2.3 Determination of the Instrument Response Function 63
5.2.4 Fit of the Kinetic Traces 63
5.2.5 Steady-state X-ray Emission Spectroscopy (EXFEL) 65
5.2.6 Theoretical Modelling (DFT) 65
5.2.7 Estimation of the Photodissociation Quantum Yield 67
5.2.8 Derivation of the K_α and K_β Difference Spectra 68
5.2.9 Error Analysis 68
5.3 Results and Discussion 69
5.4 Conclusion & Outlook 86
Chapter 6 Femtosecond X-ray Absorption Spectroscopy of Myoglobin 87
6.1 Introduction 87
6.2 Static Reference Spectra 88
6.3 Static Difference Spectra 93
6.4 Fluence Dependence 94
6.5 Potential Fluence Effects 96
6.6 Time-resolved X-ray Absorption Spectra (SACLA) 99
6.7 X-ray Absorption Time-Traces (SACLA) 101
6.7.1 Overview of All XAS Time-Traces 102
6.7.2 XAS Rise-Times 104

6.7.3 Kinetic Time-Traces at the Iron K-edge of MbNO 105

6.8 Discussion 109

6.8.1 Assignments of Transitions for each Spectral Region 109

6.8.1 Possible Fluence Effects 110

6.8.1 Overall Model 110

6.9 Conclusion & Outlook 114

Chapter 7 Conclusion & Outlook 117

7.1 Future developments 121

Chapter 8 Appendix 123

8.1 Fluence calculations (SACLA) 123

8.1.1 Calculations for the XAS measurements (SACLA) 123

8.1.2 Calculations for the XES measurements (SACLA) 124

8.2 Data Processing and Treatment 124

8.2.1 XES Raw Data Processing 124

8.2.2 Energy Calibration XES 126

8.2.3 Smoothing 126

8.2.4 XAS Raw Data Processing 126

8.2.5 Fitting of the Time-Traces 127

8.3 Additional Information -XES 128

8.3.1 Kinetic Model 128

8.3.2 Further insight into the XES K_α DFT simulations 129

8.3.3 Additional Plots 132

8.4 Additional XAS Plots (SACLA) 133

8.4.1 Comparison of Static XAS (SACLA) to Literature 133

8.4.2 GVM Calculation for Different Jet Thicknesses 133

8.4.1 Absorbance at Different Jet Thicknesses 134

8.4.2 IRF of Different Jet Thicknesses 134

8.5 DFT Simulations 135

8.5.1 Experimental Details (DFT) 135

8.5.2 DFT Spectra ... 136

Table of Figures ... 136

References ... 149

Curriculum Vitae ... 163

Chapter 1 Introduction

Biological systems, specifically proteins are the molecular “tools” in humans and all living organisms which can serve very diverse functions depending on their structure, for example, the movements of cells, ion pumps, catalysts of chemical reactions, signaling and many more. The focus of this work lies on myoglobin, which was the first protein to have its three-dimensional structure resolved by X-ray crystallography , approximately 60 years ago.[1] After only another 2 years of hard work its crystal structure was obtained with 2 Å resolution.[2] For comparison, a C-C bond length is around 1.2-1.5 Å.[3] It served since then as an important model system for understanding hemeproteins and protein dynamics and function in general. Up to today many questions remain open and this thesis aims to contribute with more insight about the interesting and remarkable chemical versatility of myoglobin and its interaction with nitric oxide (NO·). For a long time, only information about the reactant and the product was available, with few cases were an intermediate state was captured by freezing or isolating intermediate states.[4,5] Only the advent of time-resolved spectroscopy (in the early times called flash photolysis)[6] enabled to look at transition states of chemical reactions with time. The rapid developments of lasers allowed for shorter and shorter time resolution down to the femtosecond[7] and attosecond[8] regime. This allows to study important ultrafast processes which enable a deeper understanding of matter and its transformation processes. Details of those ultrafast processes are outlined in Chapter 2. The approach used was to take advantage of the potential of time-resolved X-ray spectroscopic techniques in investigating local structural and electronic changes with femtosecond time-resolution in physiological conditions, such that it more closely relates to the biological protein function in its native environment.

An introduction to heme proteins, their characteristics, structure and diverse functions followed by a review over the previous studies on myoglobins and similar systems is given in Chapter 2. Chapter 3 introduces the pump-probe scheme which was applied to X-ray absorption (XAS) and X-ray emission (XES) spectroscopy, as well as the basics of the interaction of X-rays with matter. Thanks to the advent of X-ray free electron lasers, such as SACLA[9,10], European XFEL[11,12], SwissFEL[13], which deliver high-intensity pulses (10^{11} to 10^{12} photons per pulse[13]) with a few femtoseconds (fs) pulse duration new fs-time resolved techniques are now available. Time-resolved XAS and XES offer insight on the temporal evolution of the electronic and geometric structure of in this case iron in myoglobin in dilute physiological conditions. The fourth chapter gives an overview over the XFEL facilities used for this work as well as newly developed sample delivery systems and the sample preparation. Chapter 5 focuses on fs time-resolved XES used to study the photodissociation process, which mimics ligand dissociation of NO from myoglobin-NO and the consequent evolution of spin and iron motion. This is complemented in Chapter 6 with fs time-resolved XAS studies of the X-ray absorption near edge (XANES) region of iron in MbNO. A summary and outline of the obtained results and future perspectives of this work is given in Chapter 7.

Chapter 2 Heme Proteins

Proteins are large biomolecules which consist of hundreds or even thousands of amino acids. Their abundance and diversity are the key elements in all aspects of cell function and structure. The pattern, by which each protein is created to perfectly fit its function, is encoded in a specific sequence of nucleotide bases in DNA. A segment of DNA, which has encoded information about the synthesis of a specific protein is called a gene. This, so called, expression of the gene is the “cooking recipe” for the protein and equips it with its unique functions.[14,15]

Proteins can be divided into three basic classes (Figure 2-1) according to their shape and solubility. The first class are globular proteins which are roughly spherical in shape and have the hydrophilic sidechains on the outside and are therefore usually water soluble. Myoglobin is shown in Figure 2-1a as an example of a globular protein. The second class of proteins are called membrane proteins. These proteins have their hydrophobic amino acid chains pointing outwards which makes them insoluble in aqueous solutions. The potassium channel protein (Figure 2-1b) is a representative of the membrane proteins class. The function of the potassium channel is to transports potassium ions (purple) through the cell membranes. The third class are fibrous proteins, whose role is often to provide the structure for the cells. For example, keratin (Figure 2-1c) makes up the structure of hair and skin. The structure of fibrous proteins is typically relatively simple and linear. In addition, the majority of these proteins are water insoluble.[14,15]

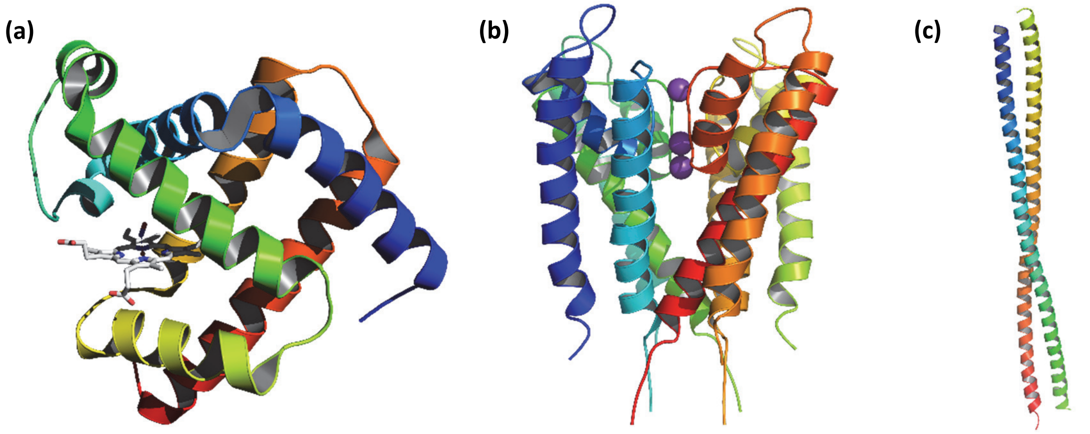

Figure 2-1: (a) Myoglobin with the heme as active center as stick structure, a globular protein (PDB: 2FRJ); (b) Potassium channel with potassium ions (purple) moving through the pore in the center, a membrane protein (PDB: 1BL8); (c) Keratin, a fibrous structural protein (PDB: 3TNU).

2.1 Protein Structure

The complex architecture of proteins can be resolved by defining different levels of structural organization. The simplest “chemical building block” of a protein is an amino acid. All proteinogenic (protein-creating) amino acids are α-amino acids. Figure 2-2a shows the general structure of the α-amino acids. It consists of a central carbon atom (α carbon) connected to amino (-NH_2) and carboxylic (-COOH) functional groups, a hydrogen atom, and a side chain (-R). The polarity and charge of the amino acid are dictated by the side chain. For example, histidine (Figure 2-2b) has a polar imidazole group as a side chain and hence is a neutral and able to form weak hydrogen bonds[16]. The side chains play a crucial role in determining the structure and function of the proteins.

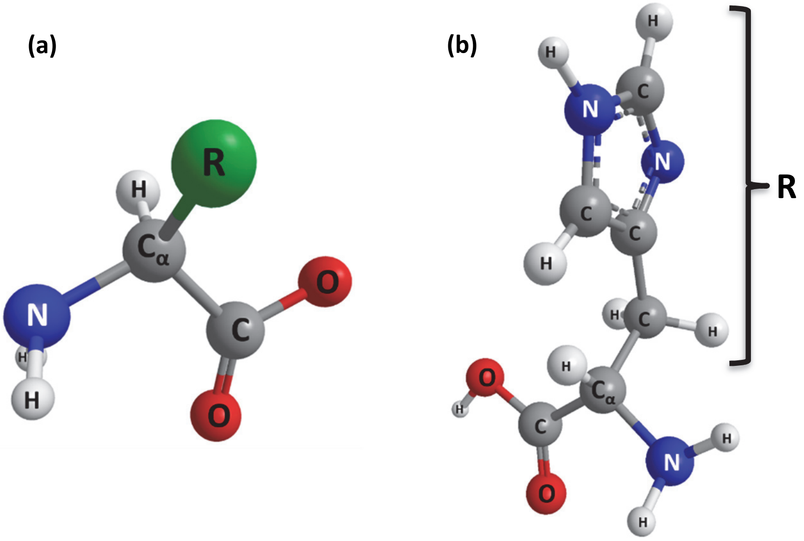

Figure 2-2: (a) General structure of an α-amino acid. The atoms are labelled, and R stands for side chain. (b) Histidine structure with its imidazole side chain.

The primary structure of the protein is the sequence of amino acids that are linked to each other by peptide (amide) bond. Each amino acid is assigned one or three letter code. Figure 2-3a shows the polypeptide chain made up of the first ten amino acids of myoglobin and Figure 2-3b presents the corresponding one letter code.[14]

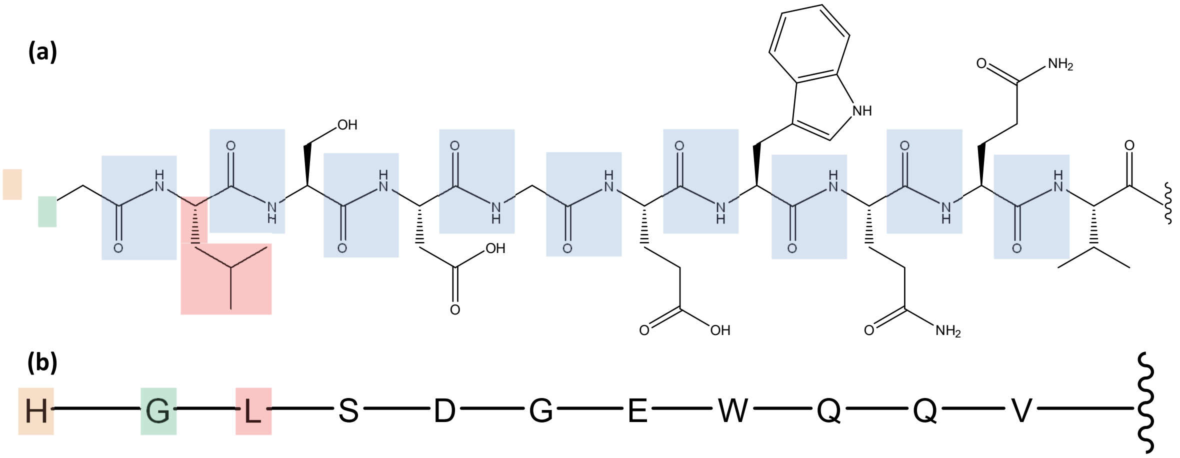

Figure 2-3: (a) Full chemical structure of the first ten amino acids of myoglobin connected by peptide bond (highlighted in blue) (b) One letter code corresponding to each of the ten amino acids (H indicates the beginning of the chain)

The polypeptide chain can arrange itself into three dimensional structures, such as α-helices and β-sheets, which are helical and pleated segments respectively. These are the two most common motifs of the proteins secondary structure. The model of an α-helix is shown in Figure 2-4a, and its detailed molecular structure is presented in Figure 2-4b as a stick model. The α-helix is stabilized via hydrogen bonding between the NH and CO groups of the same polypeptide chain backbone. Whereas β-sheets are formed by hydrogen bonding between the NH and CO groups of the adjacent β-strands (short polypeptide chains). Figure 2-4c and Figure 2-4d show the model and a molecular structure respectively of β-strands. Essentially, secondary structure is the local three-dimensional protein shape and can be thought of as "structural bricks" of the proteins. While the primary structure (amino acids) are the "chemical building blocks".[14,15]

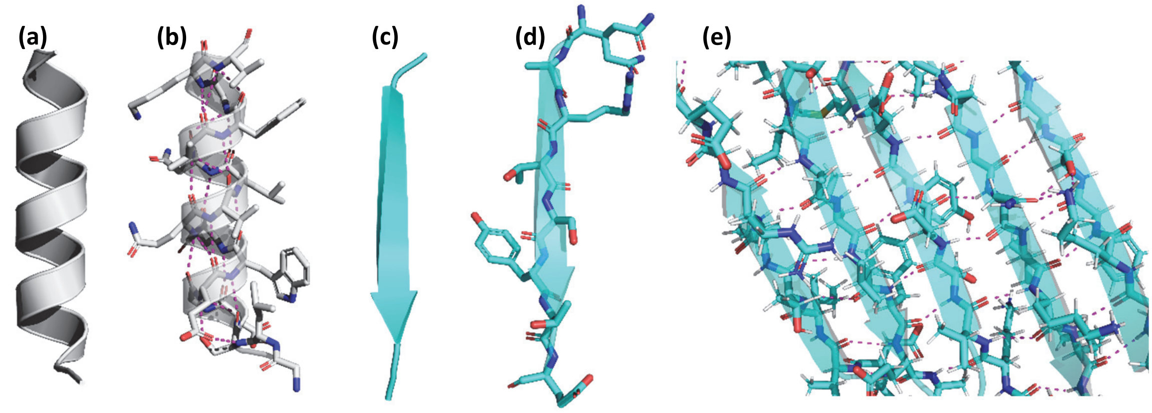

Figure 2-4: (a) "Shorthand" α-Helix; (b) α-Helix with the structure of the amino acids shown as sticks, C (grey), N (blue), O (red), Hydrogen bonds (magenta). Shown are the first 16 amino acids of Myoglobin (PDB: 2FRJ); (c) "Shorthand" β-Strand; (d) β-Strand with the structure of the amino acids shown as sticks, C (cyan), N (blue), O (red). β-Strand is taken from Inward-rectifier potassium channel (PDB: 1N9P) and represents an eight amino acid sequence (Q_{310}-E_{317}). (e) β-Sheet consisting of 5 β-Strands from human C (cyan), N (blue), O (red), H (white), Hydrogen bonds (magenta). PCNA (PDB: 1AXC).

The tertiary structure is the global or overall three-dimensional shape of the protein. It is largely determined by the interactions of the amino acids side chains (-R). For example, in an aqueous environment, the tertiary structure is a result of hydrophobic interactions and the tendency of the side chains to be “hidden” from water in the interior of the protein. Other interactions involved are: hydrophilic interactions, hydrogen bonding, disulphide bridges and ionic bonds. Depending on the protein function different shapes exhibit different benefits. A globular shape, for example, yields the lowest surface-to-volume ratio, reducing the interaction of the protein interior with its environment.[14] Figure 2-5 shows different representations of the tertiary structure: (a) represents the folding of the carbon chain in dark blue with the heme as stick structure, (b) shows the three-dimensional arrangement of α-Helices and β-Strands in Trypsine, (c) is a surface representation of Myoglobin-NO which illustrates the open pocket containing the heme as stick model with an Fe-atom as its active center and in (d) the space filling model of Myoglobin-NO is shown with the different α-Helices marked in colors as in Figure 2-1a..

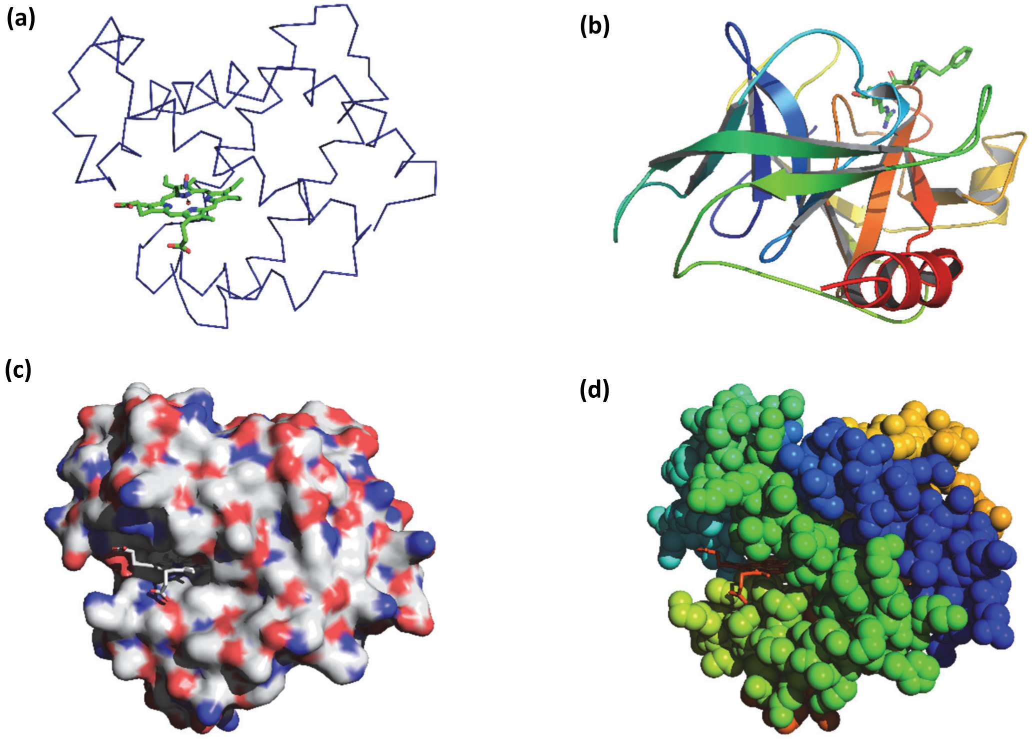

Figure 2-5: (a) Myoglobin-NO tertiary structure (dark blue), heme is highlighted as stick structure, C (green), N (blue), O (red), PDB: 2FRJ; (b) Trypsin ribbon showing the three-dimensional arrangement of α-Helices and β-Strands, PDB: 1FXY; (c) Myoglobin-NO surface representation, with its open pocket containing the heme; (d) Myoglobin-NO space filling model, the different colors mark the different α-Helices (Figure 2-1a). PDB: 2FRJ.

So far only single polypeptide chain proteins were considered, but many proteins consist of multiple polypeptide chains. Each polypeptide chain is called a subunit of the protein. The organization and interactions between those subunits is called quaternary structure.[14,15] In Figure 2-6 the ribbon structure of Hemoglobin (PDB: 1GZX) illustrates the organization of polypeptide chains to a quaternary structure. The four subunits are arranged in a roughly tetrahedral shape. The α-Helices are connected in a globin fold arrangement, which is the same in other hemes/globins such as myoglobin. In addition, a pocket which strongly binds the heme is formed.

To summarize, the primary structure of a protein is defined by the order of amino acids which are bound covalently. Secondary structure elements are α-Helices and β-Strands. The overall shape of a single polypeptide chain is the tertiary structure and the arrangement of multiple subunits is called quaternary structure. While only covalent bonds are involved in the formation of the primary structure, other noncovalent forces such as hydrogen bonds, ionic forces, van der Waals and hydrophobic interactions are important for establishing secondary and higher structures.

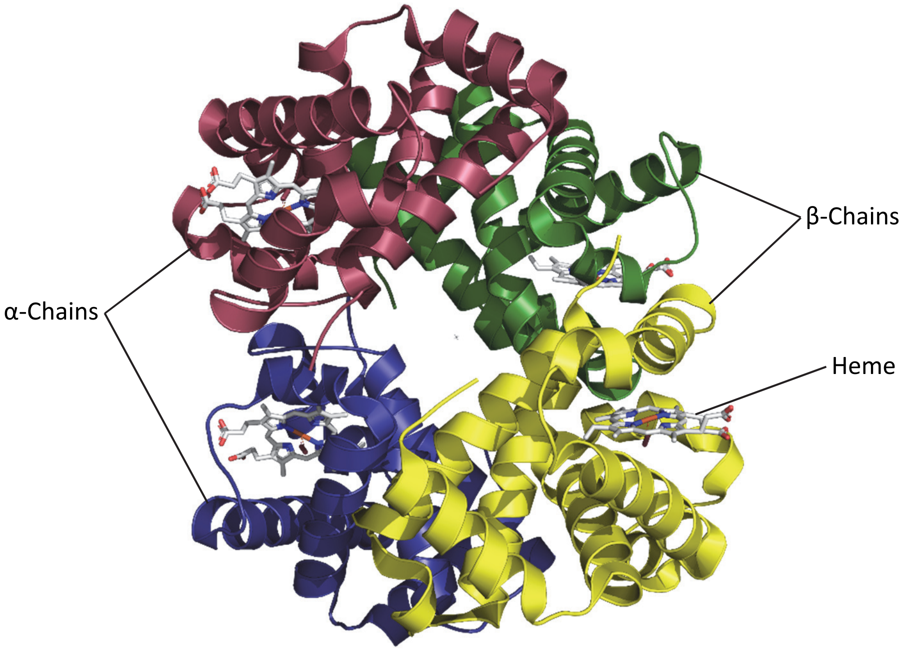

Figure 2-6: Ribbon structure of Hemoglobin, which is a tetramer of four polypeptide chains (two so called α chains and two β chains). The hemes are presented as stick structures. PDB: 1GZX

2.2 Conjugated Proteins

After classifying a protein into one of the three categories explained in chapter 2.1, namely, globular, membrane or fibrous protein, one can go one step further and differentiate between simple proteins and conjugated proteins. The former consists of only amino acids, whereas the latter contain also other chemical compounds or metals. These modifications are in general introduced after the protein is synthesized and can be bound covalently or noncovalently. This is of importance as it allows to prepare a protein in an inactive state and only activate it when needed via the introduction of a chemical group or metal. The focus of this work is on myoglobins (heme proteins), which belong to the class of conjugated proteins and are explained in more detail in the next subchapter.[14,15]

2.3 Heme Proteins

The uniqueness of heme proteins is the so-called heme group, which is a non-protein part and can be bound covalently or noncovalently to the protein. It consists of a porphyrin ring acting as a tetradentate ligand for an iron atom in the center. In addition, the iron atom can bind up to two axial ligands (see Figure 2-7). Examples of this class of proteins are cytochromes, heme peroxidase, catalases, myoglobin and others. In Figure 2-7 the heme is shown from the side, so its planar structure is visible. In the proximal side the porphyrin ring the iron ion is coordinated by the nitrogen of a histidine (proximal His) which is part of the peptide chain. In the distal side, small ligand molecules can bind to the iron ion, in Figure 2-7c the heme of MbNO is shown, where nitric oxide (NO) is bound. These small ligands can be either stabilized or destabilized by the a histidine group (distal His), which in the case of NO is stabilizing via hydrogen bonding (Figure 2-9a). Important to highlight is that not for all heme proteins is the heme planar as shown in Figure 2-7c, but can take other shapes (e.g. domed, ruffled, etc.). These differences allow the proteins to fine tune the electronic properties of the heme.[17]

Looking closer at the heme, four major types of hemes can be differentiated (see Table 2-1), heme A, B, C and O. The difference among them are different functional groups in the positions C_3, C_8, C_{18} (see Figure 2-7a).

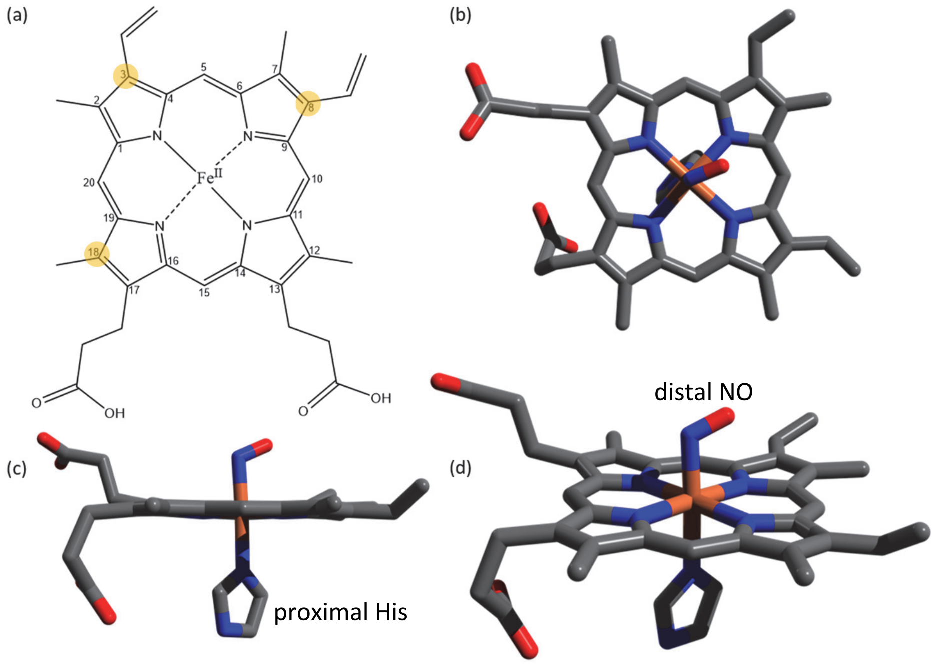

Figure 2-7: (a) Shorthand line structure of heme B with atomic numbering for the ring carbon atoms. Important are the functional groups in positions 3, 8 and 18. (b), (c), (d) Different views on the heme stick structure in Myoglobin-NO, carbon (grey), nitrogen (blue), oxygen (red), iron (orange). PDB: 1HJT. In (c) the plane of the porphyrin ring is clearly visible as well as the distal histidine residue under the iron and the nitric oxide (NO) in the proximal position.

Heme B is the most common type and as seen in Figure 2-7, it is also present in myoglobins and hemoglobins. Heme C is also important and represented in cytochrome c for example, where the “c” indicates the type of heme.

Table 2-1: Overview over the main biologically important types of hemes and their functional groups in position C_3, C_8, C_{18}. Far = farnesene.

Functional group	*Heme A*	*Heme B*	*Heme C*	*Heme O*
at C_3	$-CH(OH)CH_2Far$	$-CH{=}CH_2$	-CH(cysteine-S-yl)CH_3	$-CH(OH)CH_2Far$
at C_8	$-CH{=}CH_2$	$-CH{=}CH_2$	-CH(cysteine-S-yl)CH_3	$-CH{=}CH_2$
at C_{18}	$-CH{=}O$	$-CH_3$	$-CH_3$	$-CH_3$

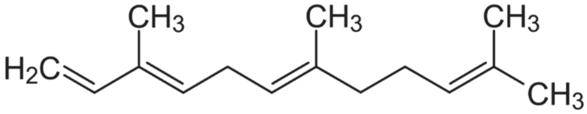

Figure 2-8: Chemical structure of α-farnesene

According to their main biological function heme proteins can be classified in five different groups:

a) Oxygen transport and storage: hemoglobin, myoglobin, neuroglobin, cytoglobin, leghemoglobin.[18]

b) Enzymes which often activate O_2 for hydroxylation or oxidation: cytochrome c[19] oxidase[20], cytochrome P450s[21], peroxidase[22], ligninases[23], catalase[18].

c) Electron transfer: cytochrome a,b,c[19,24,25]

d) Sensory functions: FixL (oxygen sensor)[26], CooA (carbon monoxide sensor)[27].

e) Receptor: soluble guanylyl cyclase (nitric oxide receptor)[28]

2.4 Myoglobin

Myoglobin (Mb) is a compact heme protein, made of a single polypeptide chain (153 amino acids) and a heme b, forming its active center (Figure 2-9). It is found in muscle tissue of vertebrates and almost all mammals. When muscles are put into action, a large amount of energy in the form of oxygen are required rapidly. For this purpose, Mbs are used in muscle cells to store oxygen and to accelerate oxygen diffusion.[29] The active site is made of a porphyrin ring (protoporhyrin IX) complexing an iron ion (Fe^{2+}, Fe^{3+}) .[30] The heme b is itself anchored to the F helix of the protein via a proximal histidine bound to the iron atom(Figure 2-9). The similarity of Mb and hemoglobin (Hb), which is the oxygen transport protein in red blood cells, is illustrated by showing an α- and β-chain of horse methemoglobin and human myoglobin as well as an overlap of all of them in Figure 2-10. The α-chain of Hb and Mb have 38 amino acid sequence identities and the strong homology is also reflected in the tertiary structure shown in the bottom right of Figure 2-10.

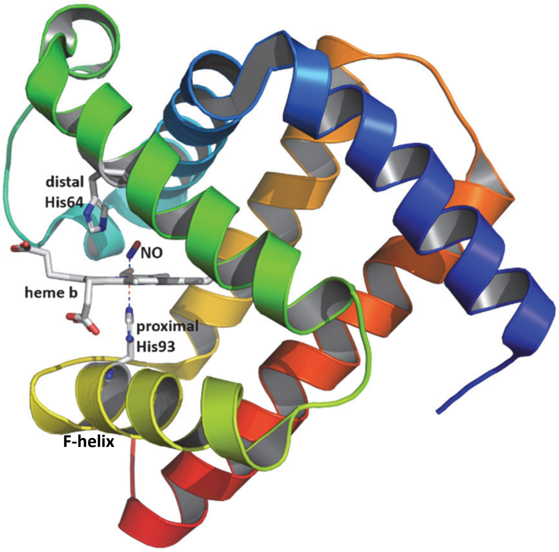

Figure 2-9: Structure of Myoglobin-NO, the heme b, the proximal His93, the distal His64 and the NO ligand are highlighted as stick structure. PDB: 2FRJ

Various small ligand molecules, such as O_2, NO, CO, CO_2, H_2O, CN, N_3 and others bind to the iron atom in heme, thereby inducing changes to the protein shape and activating heme proteins (Figure 2-11). In Figure 2-9 the proximal histidine (His93) and distal histidine (His64) are shown which play an important role in stabilizing the ligands via hydrogen bonds, ionic forces and van der Waals interactions or destabilizing via the lack thereof. Among the small ligands, NO has been highlighted as a key biological messenger[31] whose concentration controls various physiological responses, such as NO-synthases and message transduction (soluble guanylyl cyclases)[32,33]. Further, NO transport and oxidation is carried out by hemoglobin, myoglobin and nitrophorin[34–36] and neuroglobin regulates the NO/O_2 balance.[37,38] It has also been found that Mb is involved in controlling the flux of NO in the heart under physiological conditions.[39] Consequently, there is great interest in understanding in depth the nature of NO binding to heme proteins and its biochemical role.

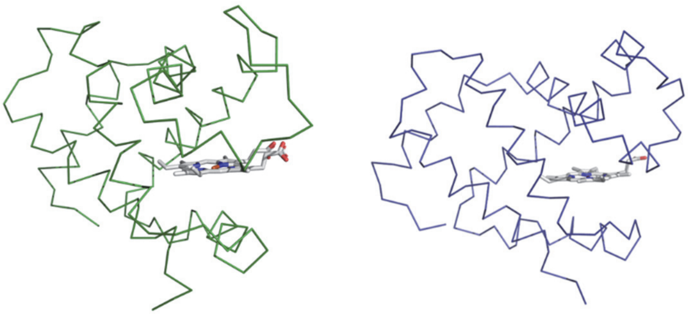

α-chain of horse methemoglobin

β-chain of horse methemoglobin

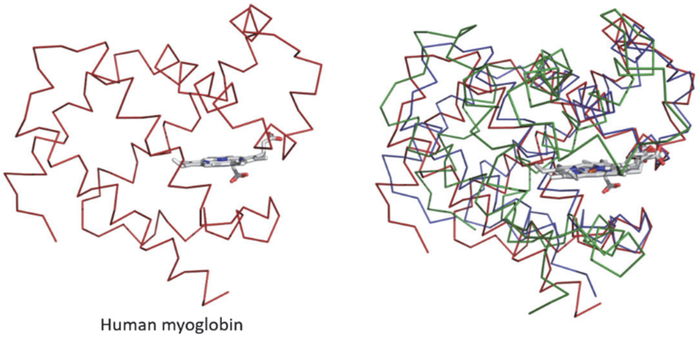

Human myoglobin

Figure 2-10: Ribbon structures of the α- and β-chain of horse methemoglobin (PDB: 1NS9) and Human myoglobin (PDB: 3RGK) and in the bottom right the overlap of all of them. The α- and β-chain of horse methemoglobin share 64 residues of their approximately 140 amino acids. Myoglobin and the α-chain of hemoglobin have 38 amino acid sequence identities. This strong degree of homology is also reflected in the tertiary structure which is shown in the bottom right.

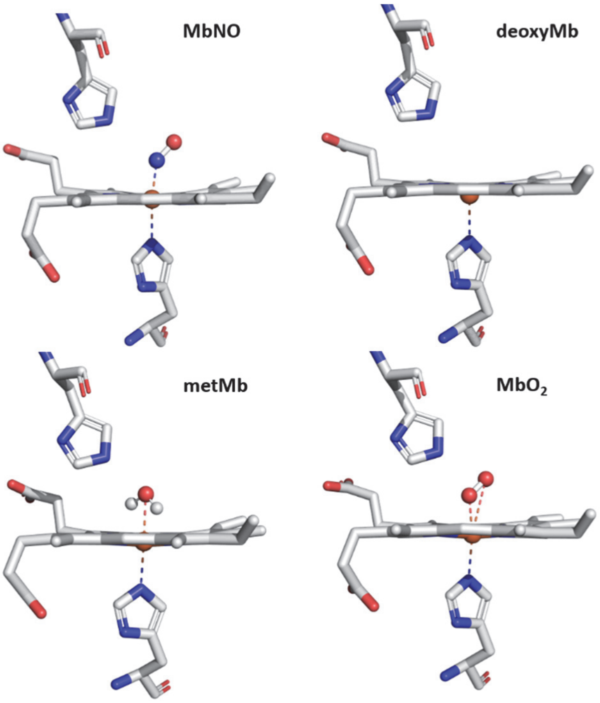

Figure 2-11: Overview over the heme structure in different forms of myoglobin: MbNO (PDB: 2FRJ), deoxyMb (PDB: 2V1K), metMb (PDB: 2MBW), MbO$_2$ (PDB: 1MNO). Shown is the heme plane from the side with the His64 and His93 side chains. Grey (C), blue (N), red (O), orange (Fe).

The unique capability of myoglobin, and heme proteins in general to perform such a variety of tasks lies in the ability of heme to conduct coordination spin, and electronic changes from the iron to the protein structure.[17] One way to introduce such changes are the binding of different ligands, which form different bond geometries, and interact in diverse ways with close-by amino acid residues via weak forces like hydrogen bonding or Van der Waals forces.[40]

Consequently, there is great interest in understanding the nature of NO binding to heme proteins and its biochemical role in depth.

2.4.1 Iron as the Active-Center

The element iron exerts an extraordinary number of functions in nature. In organisms it is present in the form of iron-proteins, which transport and store small gas molecules (especially oxygen) and take care of electron transfer reactions. Iron proteins can be classified into two main groups, 1) heme proteins and 2) nonheme proteins. Nonheme proteins contain iron-sulfur clusters or iron-protein complexes whereas heme proteins contain iron-porphyrine complexes. Myoglobin, a representative of the class of heme proteins, is the focus of this work. The versatility in functions of iron in proteins origins in the ability of both iron oxidation state , spin and iron coordination changes. An overview of possible variations in terms of spin and oxidation state for the case of myoglobin is shown in Figure 2-12a and the structural changes of iron going from unligated (top) to ligated (bottom) are illustrated in Figure 2-12b.[17,41] MbNO is missing in Figure 2-12 because it is a special case and will be discussed in the next subchapter.

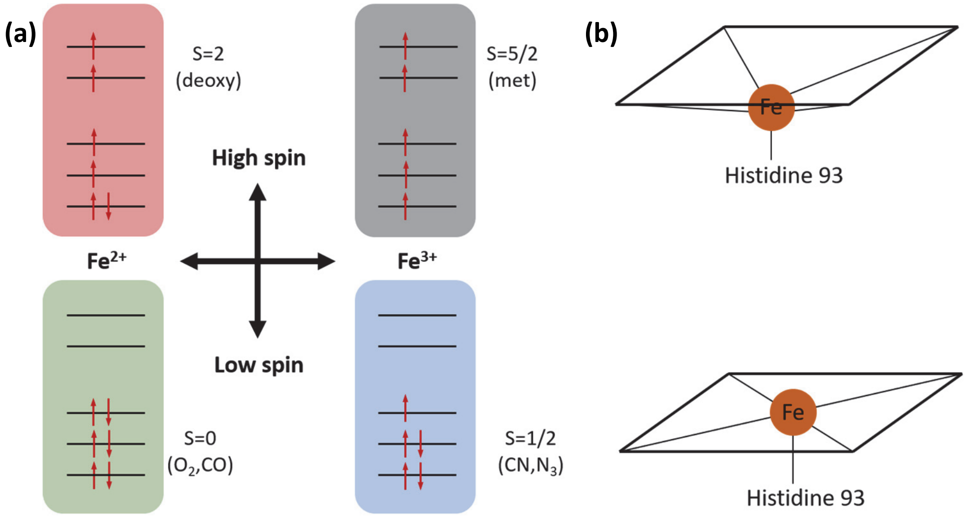

Figure 2-12: Schematic diagram of the electron configuration of the d-orbitals of Iron (Fe) in different forms of Myoglobin, their multiplicity (S) and in brackets the ligands (deoxyMb[42], metMb[43], MbO_2[44], MbCO[45], MbCN[46], MbN_3[47]). On the right side the schematic structure is shown of the domed deoxyMb (top) and the planar Mb geometry (bottom).

2.4.2 Myoglobin-NO

Nitric oxide (NO·) is in its role as a ligand molecule unique due to its electronic and functional properties and many of which are still being discovered. Some examples of physiological function of NO· include as neurotransmitter, signal transductor and as endothelial relaxing factor (relaxes the walls of blood vessels). It has a partially filled π* orbital which pushes it into a bent geometry when bound to the heme-Fe^{2+} (Figure 2-11).[15] In the ligated form, the hexacoordinated Fe^{2+} ion of the heme is in a low-spin (LS) planar doublet state. Upon ligand detachment, it turns to a high-spin (HS) quintet state with the pentacoordinated Fe in an out-of-plane, so-called domed, deoxyMb configuration (Figure 2-11). The LS planar to HS domed spin cross-over (SCO) defines the "transition state" of the respiratory function in which the forces initially localized on the Fe-ligand bond act normal to the heme plane and displace the F helix, ultimately leading to the transition from the tense to the relaxed state of hemoglobin at later times.[48]

The structure of MbNO with a zoom into the active center (heme) is shown in Figure 2-13, with the His93 highlighted, which connects the iron via a covalent bond to the F helix of the amino acid chain. As mentioned previously MbNO forms a special case in terms of spin and oxidation state. The molecular orbital diagram of the valence orbitals of MbNO is shown in Figure 2-14[49]. We can see that it has a spin state of S=1/2 due to one unpaired electron in the $d_{yz} - \pi_y$ orbital and is a ferrous system (Fe^{2+}). NO· in the heme bound state exerts a repulsive *trans* effect on the histidine 93 (His93) to iron bond, which results in a weakening.[50] This is caused by delocalization of electron density from the NO· to the d_{z^2} orbital towards the proximal ligand. MbNO is only stable in the absence of O_2, when O_2 is present, NO· is oxidized to NO_3^- and the iron in heme is oxidized from Fe^{2+} to Fe^{3+} forming metMb.

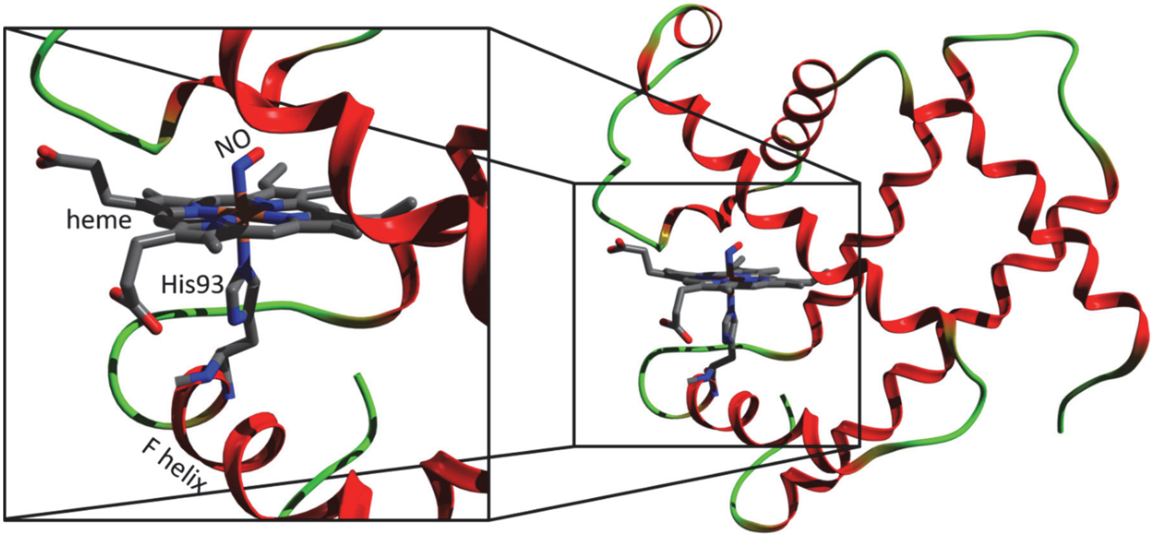

Figure 2-13: Crystal structure of the Nitrosyl-Myoglobin (MbNO). The heme is highlighted as sticks (Fe [orange], C [grey], N [blue], O [red]). PDB: 1HJT. The zoom (left) shows the distal NO ligand and proximal histidine 93 (His93), which links the Fe atom of the heme porphyrin to the F helix.

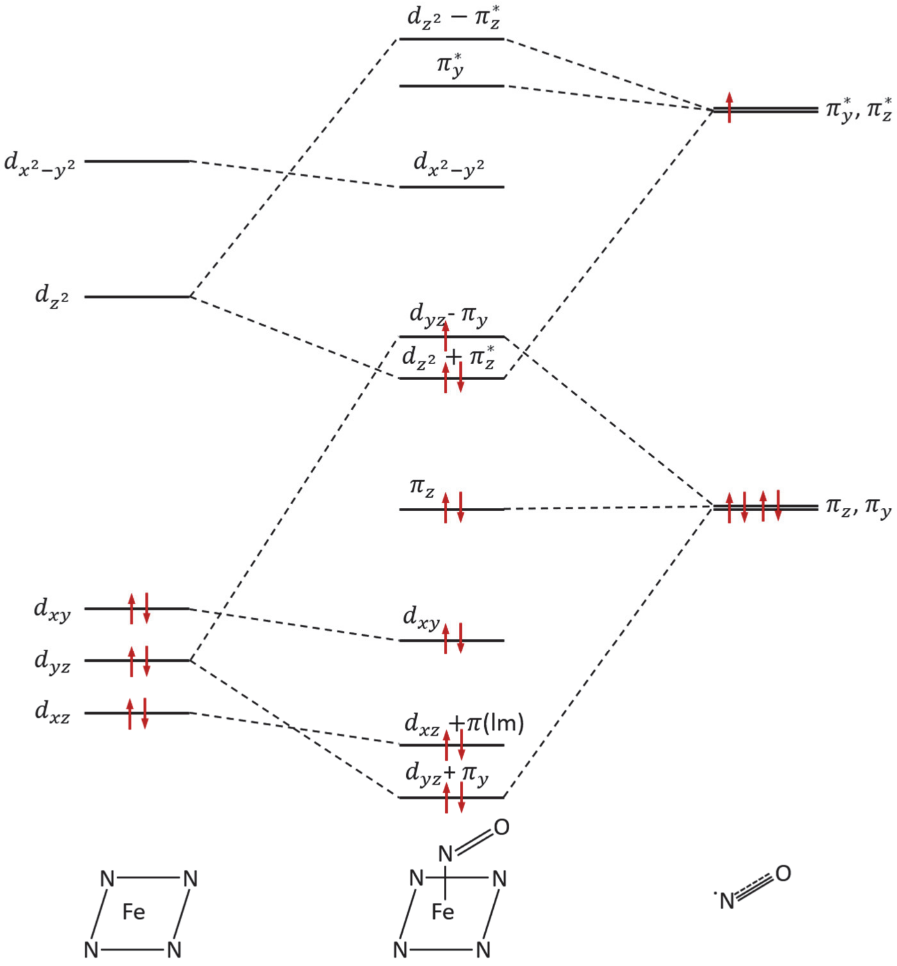
$d_{z^2} - \pi_z^*$
π_y^*
π_y^*, π_z^*
$d_{x^2-y^2}$
$d_{x^2-y^2}$
d_{z^2}
$d_{yz} - \pi_y$
$d_{z^2} + \pi_z^*$
π_z
π_z, π_y
d_{xy}
d_{yz}
d_{xz}
d_{xy}
$d_{xz} + \pi(\mathrm{Im})$
$d_{yz} + \pi_y$
Fe
Fe
N
O

Figure 2-14: Molecular Orbital diagram of MbNO. Adapted from Morse R. H. et al.[49]

2.5 Time Scales of Important Processes in Proteins

The size of proteins spans from about sub nm (11 amino acids)[51] up to ~ 1 µm (34k amino acids)[52]. Myoglobin is a rather small protein with a diameter of 3.5 nm. This gives rise to a diverse range of time scales for processes important in proteins. An overview is given in Table 2-2 and shows that the most important processes observed in the timescales investigated in this work (fs to ps) are electron transfer prosses, lifetimes of transition states as well as small motions (e.g. heme doming).

Table 2-2: Overview over fast timescales in proteins.[15,53]

Time (sec)	*Process*	*Examples*
10^{-15}	Electron transfer	Light reactions in photosynthesis, Redox reactions at hemes, iron-sulfur clusters, copper centers, flavins, reducible disulfides and quinones.

10^{-15} to 10^{-11}	Lifetime of transition states	In chemical reactions e.g. at the active center of a protein, lifetimes are inverse to the frequency of bond vibrations
10^{-11}	H-bond lifetimes	H bonds are exchanged due to the rotation of water molecules
10^{-12} to 10^{3}	Motion in proteins	Fast: Methyl rotations, Tyrosine ring flips Slow: Bending motions between protein domains
10^{-6} to 10^{0}	Enzyme catalysis	The catalytic cycle of cytochrome c oxidase has time scales ranging from 40 µs for electron equilibration to 0.1 s for interprotein electron transfer

Table 2-3 contains a compilation of fs to ns time-scales reported for different ferrous (MbNO, MbCO, MbO_2, cyt c, HbO_2, deoxyMb) and ferric (metMb) heme proteins. They also differ in their ligation, deoxyMb is pentacoordinated whereas the rest are hexacoordinated and in their spin state (see Figure 2-12).

Table 2-3: Compilation (not exhaustive) of the time scales reported for different ferrous and ferric (metMb) ligated heme proteins as well as deoxmyoglobin. XES= X-ray emission spectroscopy, TA=transient absorption, XAS= X-ray absorption spectroscopy. Cyt c = Cytochrome c.

Species	**Method**	τ_1	τ_2	τ_3	τ_4
MbNO (this work)	XES	< 100 fs	800±150 fs	30±9 ps	ns
MbNO[54]	Resonance Raman	< 100 fs		30±10 ps	
MbNO[55]	Optical TA	< 100 fs	400-1000 fs	3-5, 19 ps	126 ps
MbCO[56]	Monochromatic XAS	< 70 fs	300-400 fs		
MbCO[57]	Optical TA				180 ns
MbO_2[58]	Optical TA	<100 fs	490 fs	2.9 ps	55 ns
metMb (ferric)[43]	UV-VIS TA	~60 fs	~500 fs	1.1 ps	4.7 ps
Ferrous Cyt c[59,60]	Optical TA and fluorescence	<100 fs	600±70 fs	1.8±0.5 ps	5.9±0.1 ps
HbO_2[61]	Optical TA	45±5 fs	680±80 fs		>2 ps
DeoxyMb[62]	Optical TA	< 50 fs	200-600 fs	2-4.5 ps	15-25 ps

2.6 Previous Studies on Myoglobin-NO

The UV-VIS spectra of MbNO and other Mb forms in Figure 2-15 illustrate the two main features present in the UV-VIS region. First, around 400 to 450 nm, the so called Soret (or B) band which arises mainly due to π-π* transitions (HOMO/HOMO-1 to LUMO+1) located on the porphyrine ring .[63–65] And second, in the region of ~500 to 650 nm we can see the Q-band, which is also due to π-π* transitions (HOMO/HOMO-1 to LUMO) located on the porphyrine ring, but can be split into more than one peak (Q-bands) due to vibrational excitations and symmetry breaking.[64,65] It was found by Aldane and Smith that ligand detachment from the iron (ferrous) in heme can be induced by visible-ultraviolet excitation of either of the two bands (Q or Soret-bands) of the iron-porphyrine (heme).[66] The dissociation and rebinding kinetics of NO in myoglobin have been studied by a variety of time-resolved spectroscopic techniques, upon excitation of the Soret (~400 to 450 nm) or the Q-bands (~500 to 650 nm, see Figure 2-15), while the probing was done by transient absorption (TA) in the UV-Visible,[54,55,67–74] the near infrared (IR),[75–77] the mid-IR[77–79] or by resonance Raman spectroscopy[54]. The latter is sensitive to bond stretching and for the case of MbNO[54] and MbCO[80] the Fe-His bond has been studied as a marker for doming after photodissociation of the ligand. Mid-IR looks at bond vibrations, which was used to study the NO recombination kinetics in solvents with different viscosity by looking at the NO bond vibrations.[77] Another possibility of mid-IR is to look at the amide vibrational band, which allows to track the protein confirmation.[77] The UV-VIS consists of the Soret band and the Q bands which are located on the porphyrine, whereas in the UV amino-acids of the protein absorb, so probing in these regions allows to track geminate recombination[54,55,67–74] These studies concluded that photodissociation of the diatomic ligands and doming are prompt, typically <50-100 femtoseconds (fs), and simultaneous events. The actual formation of the ground state HS deoxyMb form has been interpreted in two main ways: a) a vibrationally excited ground-state is formed promptly after excitation, and vibrational cooling ensues;[81] b) the process is a cascade through intermediate electronic excited states.[82,83] An overview of timescales and their assignments is presented in Table 2-4. All these studies report multi-exponential recombination kinetics with time constants spanning from sub-picosecond (ps) to several hundreds of ps or even longer. Upon photoexcitation 50 ± 5% of the MbNO molecules dissociate the Fe-NO bond.[84] The remaining ~45% that do not dissociate NO follow a pathway of direct energy relaxation via heating of the residual six-coordinate heme, and subsequent cooling.[85–87] Theoretical[85] and experimental[86] studies obtained time constants of ~6 ps for monophasic cooling and another molecular dynamics simulation study[87] found 1-4 ps and 20-40 ps for a biphasic cooling. As energy dissipation mechanisms a pathway via the heme side chains to water molecules and the energy transfer to the protein are suggested[85,87].

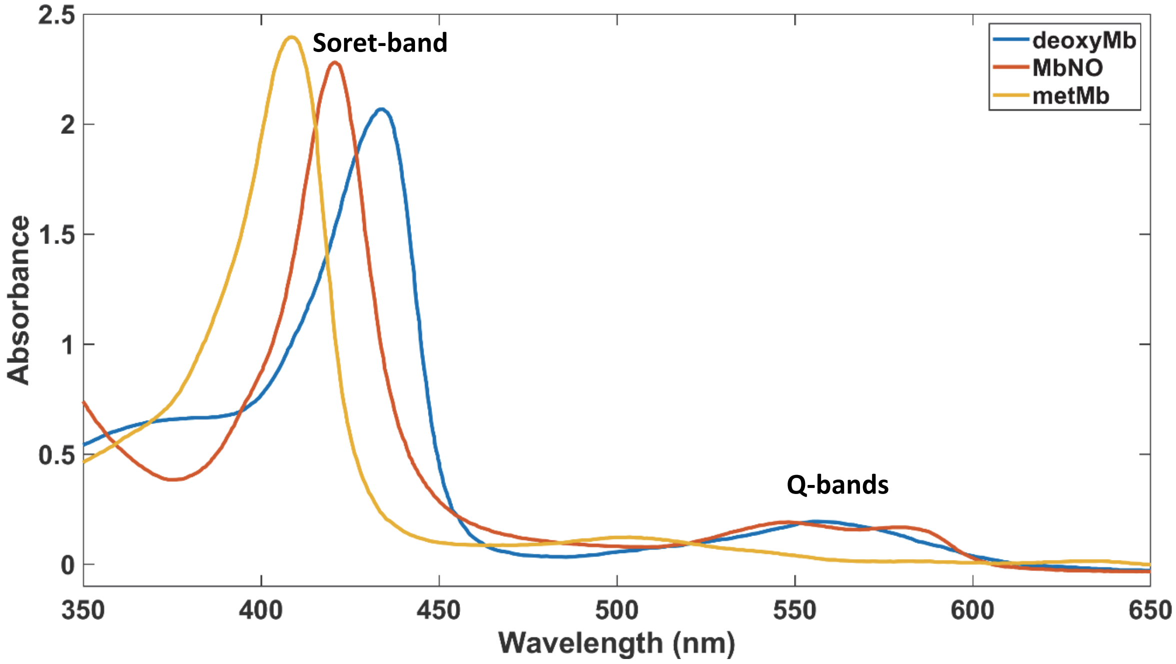

Figure 2-15: UV-VIS spectra of solutions of deoxyMb, metMb and MbNO measured in a quartz cuvette. The region of 500-650 nm contains the Q-bands and the region of 3700-460 nm the soret-band.

Table 2-4: Overview of the timescales which have been previously assigned to vibrational relaxation (VR) and geminate recombination (GR) of NO to the iron in myoglobin. Various time-resolved experimental techniques are listed as well as the pump-wavelengths were MbNO was excited. Q bands in MbNO correspond to 500-650 nm and the Soret Band to 350-500 nm. ∞ for τ_3 means an offset was obtained. The two main timescales for GR in MbNO are found to be in the range of 8-40 ps and 150-300 ps.

Method & Reference	**Exc. WL (nm)**	**Probe WL (nm)**	**τ_{vr} (ps)**	**τ_1 (ps)**	**τ_2 (ps)**	**τ_3 (ps)**
UV-VIS TA[84]	400	White light	1.8 (42%) VR	13.8 (24%) GR	200 (34%) GR	
UV-VIS TA[73]	400	420 nm 438 nm		13 (41%) GR	195 (59%) GR	
UV-VIS TA[70]	570	White light		9 GR	200 GR	
UV-VIS TA[68]	574	438		28 (52%) GR	279 (48%) GR	
UV-VIS TA[84]	580	White light	1.1 (50%) VR	8 (30%) GR	170 (20%) GR	
UV-VIS TA[73]	580	420 nm 438 nm		8 (60%) GR	170 (40%) GR	
VIS TA[75]	564	650-800 nm	4 VR	17 GR	800 GR	

VIS TA[75]	564	Soret Band (SVD)		13 (40%)	148 (50%)	∞ (10%)
VIS TA[75]	564	Q band		14 (45%)	204 (37%)	∞ (18%)
Mid-IR TA[78]	400	Mid-IR	1 and 4 (35%) GR	42 (29%) GR	238 (36%) GR	
Mid-IR TA[79]	580	Mid-IR		5.3 (54%) GR	133 (46%) GR	
Resonance Raman[54]	560-70	435		30 hc domed to planar		
XAS[88]	532	X-rays (~7 keV)			192 (75%) GR	>1.3 (25%)

Following the pathway of the Mbs which dissociate NO, the shortest time scales (1-4 ps) were attributed to vibrational relaxation (VR) in the unligated heme, while the longer ones have been attributed to geminate recombination (GR), which is the recombination of two transient species produced from a common precursor before separation by diffusion occurs. GR in MbNO can be classified into two main groups: 10-30 ps and 170-250 ps.[54,55,68,69,72,73,75,77,78]. The 10-30 ps time scale was attributed to rebinding of NO from the center of the distal pocket, very close to the iron,[73] while the 170-250 ps component was assigned to recombination of NO ligands from an outside heme pocket (Figure 2-16).[89] Both recombination processes are hypothesized to be caused by NO binding to an out-of-plane iron in the domed high spin (HS) state of the heme (Figure 2-16). Resonance Raman studies[54,75,90] revealed an additional ~30 ps component, which was attributed to the return from the hexacoordinated HS domed species to the planar form in the low spin (LS) ground state. Thus, the transition from domed to planar is not a prompt one (contrary to the reverse process which is reported to be sub 100 fs[54,55,71–74,91]) and its time scale was attributed to the constraints that the protein exerts on the heme,[72,73,77,79] while DFT studies have attributed it to a relaxation from high to low spin states.[92,93]

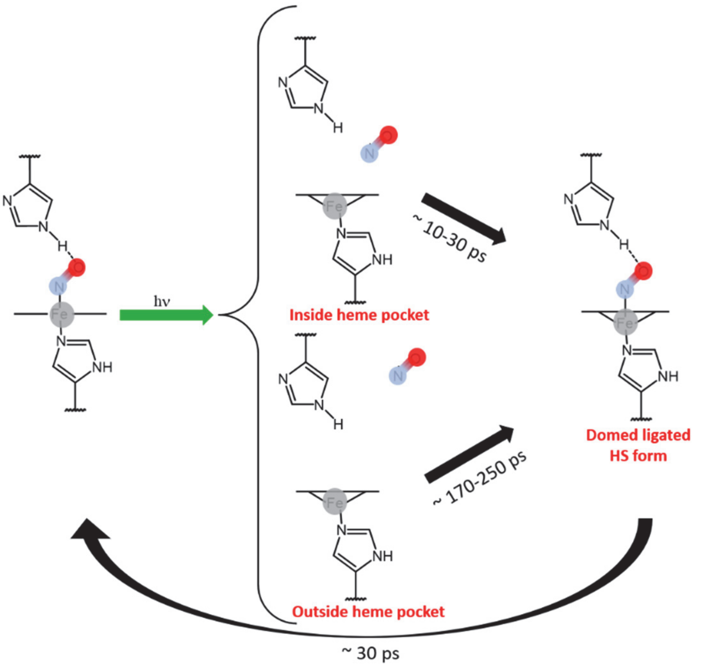

Figure 2-16: Overview of photocycle for the dissociation and recombination of MbNO suggested by previous experiments.

In summary, the optical domain time-resolved studies conclude: a) that the recombination of NO to the deoxy-Myoglobin (unligated myoglobin) leads to a hexacoordinated domed species; b) this recombination occurs over two time scales, typically 10-30 ps and ~170-250 ps, which are respectively due to NO in close proximity to the iron atom (probably in the Xe1 site) and to NO farther away, in the Xe4 pocket; c) the relaxation of the domed to planar hexacoordinated species occurs in ~30 ps, which may be due to constraints exerted by the protein and/or relaxation among spin states of the iron (Figure 2-16). It is important to stress that none of the optical techniques probe the active center of the reaction, i.e. the iron atom and therefore none is directly sensitive to the local electronic structure of the iron.

To understand the sensitivity of different energy regions in the XAS spectrum of different forms of myoglobin Lima et al.[94] carried out a detailed static XAS study combined with MXAN simulations. MXAN is a method for extracting structural information from XANES spectra, it is based on a comparison between many theoretical, calculated spectra which are obtained by varying structural parameters and the experimental spectra.[95,96] Several prominent spectral features close to the absorption edge (7100 – 7350 eV) were identified and assigned. Ionisation resonances above the edge were assigned to multiple (7160 – 7220 eV range) and single (above 7240 eV) scattering resonances. It was found that the pre-edge feature (7114 eV) appears due to the low symmetry of the heme environment.[94] The pre-edge transition corresponds to the dipole forbidden 1s → 3d transition. However, the low symmetry allows metal 4p and 3d orbitals mixing, resulting in some electric dipole allowed 1s → 4p transition.[97] In addition, the feature at ca. 7119 eV just below the absorption edge (7119 to 7131 eV) can be assigned to the 1s → 4p transition, which is dipole allowed and therefore more intense than the pre-edge feature.

Silatani et al. recently carried out time-resolved X-ray absorption spectroscopy (TR-XAS) measurements with 70 ps time resolution at the Swiss Light Source to follow the recombination kinetics of NO to deoxyMb.[88] It was found that indeed an intermediate is formed that decays on the time scale of ~200 ps and bears many characteristics of the deoxy form (high spin, domed structure, etc.). It was concluded that this intermediate is the domed hexacoordinated iron that is populated by the return of distant NO molecules and relaxes in ~30 ps according to the TR Raman studies[54]. While this experiment established for the first time the feasibility of time-resolved X-ray absorption spectroscopy (XAS) in the picosecond regime on heme proteins, the first ever was Mills et al. who performed time-resolved XAS on MbCO with a 300 ms time-resolution.[98] The time resolution of neither of the two experiments was sufficient to probe the information-rich first tens of picoseconds. In addition, the low signal-to-noise ratio were such that further analysis to retrieve the structural parameters of the hexacoordinated domed heme was not possible. Indeed, the only known differences between deoxyMb and the domed ligated MbNO form are due to the presence of NO. This shows up as a small difference in the region of 7131 to 7145 eV between the deoxyMb-MbNO and the transient spectrum at 70 ps time-delay (see Figure 2-17). NO is a weak scatterer of the photoelectron and therefore does not contribute much to the XANES spectrum.

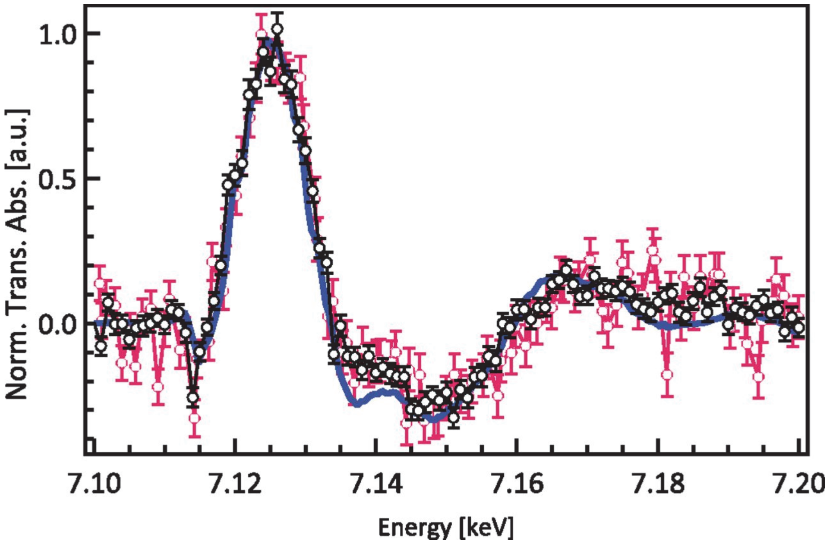

Figure 2-17: XAS transient spectra of MbNO at 70 ps time-delay. Presented are two series of measurements (series I: red, series II: black) and the static difference spectrum in blue (deoxyMb minus MbNO). Norm. Trans. Abs., normalized transient absorption. From Silatani et al.[88]

Table 2-5 summarizes time-scales reported for different ferrous ligated heme proteins as well as deoxyMb from XAS, resonance raman and optical experiments. Whereas the biological function, protein structure and electronic configuration are very different among different forms of ligated and unligated heme proteins, the time-scales which are not dependent on the ligand (which differs among them) are expected to be similar, and indeed τ_1 and τ_2 (see Table 2-5) confirm this. The ligand dissociation is immediate, after which the Q-state to excited state decay (τ_1) and its consecutive decay (τ_2) are thought to be ligand independent.

Table 2-5: Compilation (not exhaustive) of the time-scales reported for different ferrous ligated heme proteins as well as deoxmyoglobin. We do not preclude of the assignments proposed in the different reports. TA=transient absorption, XAS= X-ray absorption spectroscopy.

Species	Method	τ_1	τ_2	τ_3	τ_4
MbNO[54]	Resonance Raman	< 100 fs		30±10 ps	
MbNO[55]	Optical TA	< 100 fs	400 - 1000 fs	3 - 5, 19 ps	126 ps
MbCO[56]	Monochromatic XAS	< 70 fs	300 - 400 fs		
MbO_2[58]	Optical TA	< 100 fs	490 fs	2.9 ps	55 ns
Ferrous Cyt c[59,60]	Optical TA and fluorescence	< 100 fs	600 ± 70 fs	1.8 ± 0.5 ps	5.9 ± 0.1 ps
HbO_2[61]	Optical TA	45 ± 5 fs	680 ± 80 fs		> 2 ps
DeoxyMb[62]	Optical TA	< 50 fs	200 - 600 fs	2 - 4.5 ps	15 - 25 ps

To clarify the open questions: a) What is the timescale of NO dissociation? b) What is the structure of the transition state which has so far only been concluded by TR Raman studies[54]? c) Are there other unknown sub-100 ps timescales? d) What are the spin dynamics of the iron in Myoglobin-NO and how do they affect the structure? we carried out a time-resolved XAS study at the iron K-edge of MbNO in physiological solution (pH = 7).

In order to address these questions TR-XAS and TR-XES are ideal techniques. The structural information about the transition states can be obtained from TR-XAS, the local electronic structure from the iron XAS pre-edge[97,99] as well as the femtosecond to picosecond dynamics electronic and structural changes in MbNO from XAS time scans at different energies. Whereas the spin dynamics of the iron in MbNO and their relation to structural changes can be obtained from TR-XES.

Chapter 3 Ultrafast X-ray Spectroscopic Techniques

This chapter introduces the time-resolved spectroscopic techniques used for this work and gives an insight about the technical details of different X-ray Free electron lasers (XFELs). Furthermore, the challenge of sample delivery for air-sensitive and biological samples is discussed and developed sample delivery techniques are presented.

3.1 Observing Molecular Motion

For a long time, the knowledge about chemical reactions was based on the observation of the initial state and the final state structure. In rare cases it was possible to freeze intermediate states, called transition states, to learn more about how chemical reactions work (Figure 3-1b). In 1949 flash photolysis was developed[6] and opened up the possibility to follow chemical reactions and observe light-induced changes on a microsecond timescale. With the advances of pulsed lasers, the time resolution of the so called "pump-probe spectroscopy" continuously improved down to the femtosecond[60,100–106] and recently even attosecond[8,107–109] regime. The system is excited by a short laser pulse (usually 5-300 fs), the so-called pump pulse, and after a variable known time delay analyzed by a second, typically weaker probe pulse (Figure 3-1a). This allows one to record "molecular movies", which probe evolution and relaxation of a system as a series of snapshots. The cross-correlation of the intensity profiles of both pulses determines the time resolution.

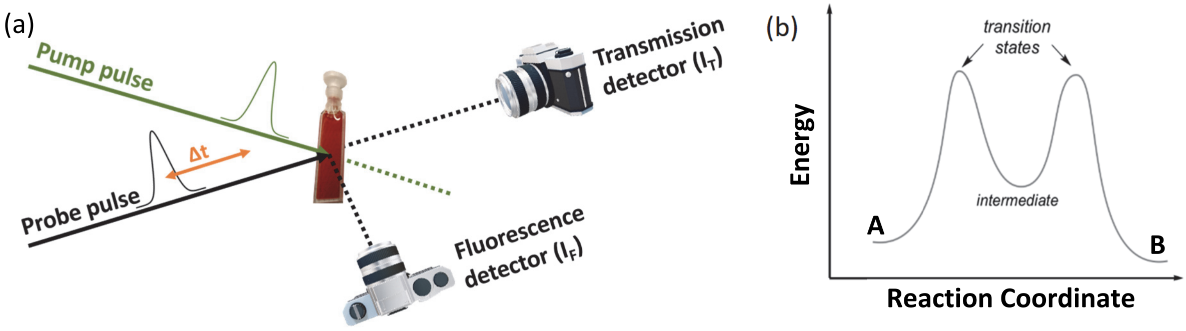

Figure 3-1: (a) Scheme of pump-probe spectroscopy showing the pump pulse (green) and the probe pulse (black) and the time delay (Δt) between the two. After interaction at the sample cell (cuvette) the probe pulse can be detected in transmission (I_F) or fluorescence from the sample (I_F). (b) Reaction coordinate diagram showing a reaction starting from the reactant (A), which reacts via two transition states and one intermediate state to the product (B) along the reaction coordinate.

Phenomena like molecular motion, molecular vibration, bond cleavage and formation take place on a femto- to picosecond timescale (see Figure 3-2 for more details). Therefore, the use of ultrafast pump-probe techniques allows to follow these phenomena on their characteristic timescales. This is beneficial for a deeper understanding of light induced changes in molecules, to follow chemical reactions and to determine transition states.

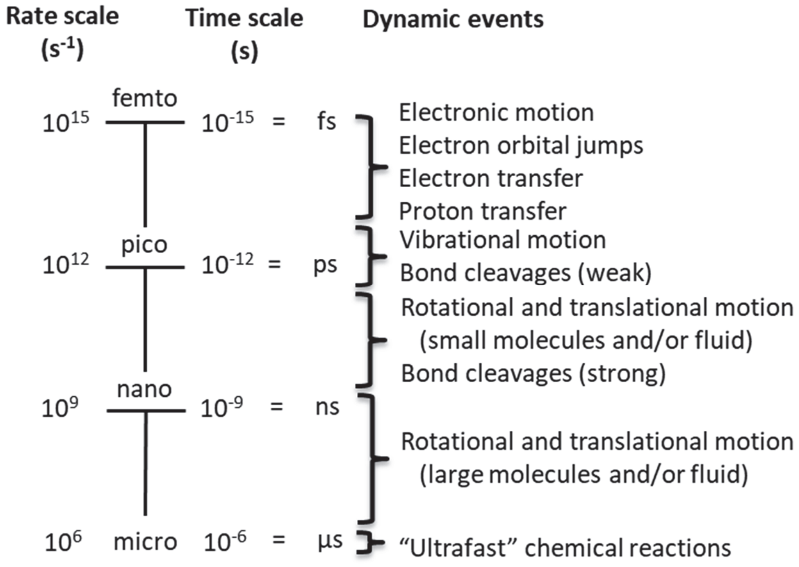
Rate scale (s-1)
Time scale (s)
Dynamic events
10^15 femto 10^-15 = fs
Electronic motion
Electron orbital jumps
Electron transfer
Proton transfer
10^12 pico 10^-12 = ps
Vibrational motion
Bond cleavages (weak)
Rotational and translational motion (small molecules and/or fluid)
Bond cleavages (strong)
10^9 nano 10^-9 = ns
Rotational and translational motion (large molecules and/or fluid)
10^6 micro 10^-6 = µs
"Ultrafast" chemical reactions

Figure 3-2: Overview of dynamic events happening at femto to micro second time-scales. An electron orbital jump refers to an electron absorbing energy and "jumping" to a higher orbital. Information from Turro et al.[110]

The specific properties one can investigate with pump-probe spectroscopy depend mainly on the characteristics of the probe pulse. Using common tabletop laser sources both the pump and the probe pulse typically lie within the UV to NIR region, so the involved transitions occur within the valence orbitals. In addition, sub Angström spatial resolution can be accomplished by molecular coherence, which allows localization of the nuclei in the initial step of excitation.[111–114] Champion et al.[114] utilized femtosecond coherent probe laser pulses to investigate low-frequency nuclear motion in the heme group of MbNO after photolysis.[114] They found distinct oscillations with two different periods (430 fs and 150 fs) and attributed the 430 fs to heme doming and the 150 fs to the iron-histidine motion after photolysis.[114] Another option to obtain structural information is the combination with time-dependent density functional theory (TDDFT) simulations. This allows, if in good agreement with the experimental results, an insight into structural changes and assignment of all possible transitions. Such simulations are vital especially in the case of complex molecules.[115–117]

A further complication arises for liquid samples, where additional intermolecular (e.g. solute-solvent) interactions can play an important role for the dynamics of the system. In certain cases, the solvent can also contribute or overlap with the signal of interest which further complicates the analysis.

One possible way to overcome some of the difficulties of obtaining good structural information and avoid the influence of solvent interactions is to use high-energy radiation, which enables a high spatial resolution due to its short wavelength.[118,119] Methods of choice for this work are time-resolved X-ray Absorption Spectroscopy (TR-XAS) and non-resonant X-ray Emission Spectroscopy (TR-NXES). In both cases the sample is excited by an ultrashort optical laser pulse ~20-100 fs in the UV-VIS region (Q-band or Soret-bands) and then probed with an X-ray pulse, which usually determines the time resolution, depending on its pulse width. This is only true, if the sample (jet) thickness is thin enough that group velocity mismatch (GVM), which is the temporal separation of pulses in a medium (e.g. liquid jet) due to different group velocities, does not play a role. Third generation synchrotrons deliver X-ray pulses with a typical pulse length of 10-100 ps, which limits its use to samples with sufficiently long-lived reaction intermediates and/or long enough excited state lifetimes. An X-ray free electron laser is capable of producing X-ray pulses as short as a few femtoseconds[120] and is explained in more detail in the next section.

3.2 X-ray Interaction with Matter

Since its discovery by Roentgen in 1895[121], X-rays, which is electromagnetic radiation of the range of 100 eV to 200 keV (0.03 to 3 nm), plays a crucial role in studying the structure of matter. Nowadays X-rays play a crucial role in many industrial applications such as medical diagnostics, material characterization, quality control, etc. and even more scientific applications, e.g. X-ray spectroscopy, X-ray scattering, X-ray ptychography, X-ray imaging, material characterization, and many more.[122] X-rays can be treated both, as a wave or as a particle, like other electromagnetic radiation as well.[123] When an X-ray photon hits an atom it can interact in two ways, first it can be scattered, or second it can be absorbed.[124] In the former case X-rays are deflected from their original propagation pathway and two cases can be differentiated: 1) elastic scattering (Rayleigh scattering) for which the kinetic energy is conserved or 2) inelastic scattering in which the kinetic energy of the photon is not conserved (Compton scattering). For the way of the X-ray photon being absorbed by an atom, its energy is transferred to an electron from the inner shells, which is then either excited to free valence orbitals or ionized.[124]

3.3 X-ray Absorption Spectroscopy

A sharp increase in the absorption of X-rays encountering a sample is observed when the energy of the incoming X-rays is high enough to excite a core electron of an atom to the unoccupied states or to the continuum. This sharp increase in the absorption is called an absorption edge, which is characteristic for each element. Figure 3-3 shows the possible core electron transitions. The absorption edges are named based on the electronic level the core electron originates from. For example, the transition of the 1s electron to the unoccupied states or to the continuum is called K-edge. Transitions from the second (2s or 2p) or higher shells to vacant levels are named L- and M-edges respectively.[118,124–126] This most intense absorption at the edge is often referred to as “white line”, which dates back to the days when X-ray absorption spectra were recorded on photographic film and the intense absorption at the edge appeared as a heavily exposed white line on the developed film. The energy needed to excite a core electron to vacant levels is unique to each element, which makes XAS an excellent element-specific analytical technique.

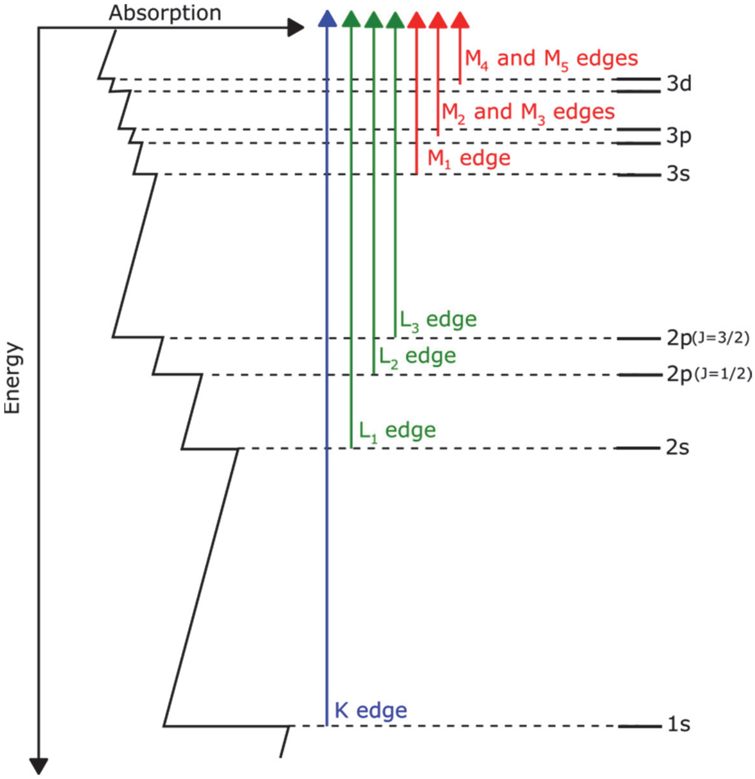

Figure 3-3: Transitions contributing to XAS absorption edges. (By Atenderholt at English Wikipedia, CC BY-SA 3.0, https://commons.wikimedia.org/w/index.php?curid=38941860).

Figure 3-4 shows the iron K-edge X-ray absorption spectrum of MbNO in solution, containing iron with the oxidation state of +2.[94] Typically, a XAS spectrum is divided into two main regions: absorption near edge structure (XANES) and extended X-ray absorption fine structure (EXAFS). The former region encompasses the pre-edge, rising edge and and up to ~50 eV above the rising edge and the latter region extends from ~50 eV up to 1000 eV above the rising edge (Figure 3-4). [118,119,125,126] EXAFS corresponds to the single-scattering regime which allows to extract structural information like bond lengths and angles.[124]

For XANES region the transitions start from core initial states with well-defined symmetries and therefore the quantum mechanical selection rules explain the symmetry of the possible final states The absorption in the iron pre-edge region corresponds to the dipole-forbidden and quadrupole-allowed 1s → 3d transitions (Δl = ±2).[97] As a general rule, the pre-edge intensity is quite low because quadrupole-allowed transitions are weak.[127,128] However, the mixing of iron 3d and 4p orbitals is possible for non-centrosymmetric molecules (e.g. tetrahedral). When the 3d and 4p orbital mixing takes places, the 3d orbitals gain a certain amount of 4p character. Since 1s → 4p transition is dipole-allowed (Δl = ±1) and very prominent, the intensity of the pre-edge feature increases as a molecule deviates from the centrosymmetry.[129] The pre-edge feature position, splitting and intensity spread also reflect the oxidation[130] and spin state[97] of the iron.

The rising edge spectral feature represent the dipole-allowed 1s → 4p transition and is very intense. The position of the rising edge reflects the local charge density and hence the oxidation state. This happens because the increase in the formal oxidation state induces the reduced shielding of the nuclear charge. As a result, the binding energy of the core electrons (e.g. 1s) increases and the edge position shifts to higher energies. However, various other parameters such as bond distances and angles, coordination and the type of ligands can affect the absorption edge position and shape.[131] In addition, the multiple scattering of the ejected photoelectron (vide infra) is contributing to the XANES region.[132] Multiple scattering refers to the process when the excited electrons bounce two or more times between neighboring atoms before coming back to the absorbing atom.[133]

At a certain incoming X-ray energy, the core electron will be ejected from an atom. The electron wave is backscattered from the neighboring atoms and interferes with the outgoing photoelectron wave. The resulting interference can be either constructive or destructive. The former will increase while the latter will decrease the absorption coefficient (Figure 3-4). EXAFS is great tool for probing the local geometric structure, revealing the information about the coordination, bond distance and the neighboring atoms.[134]

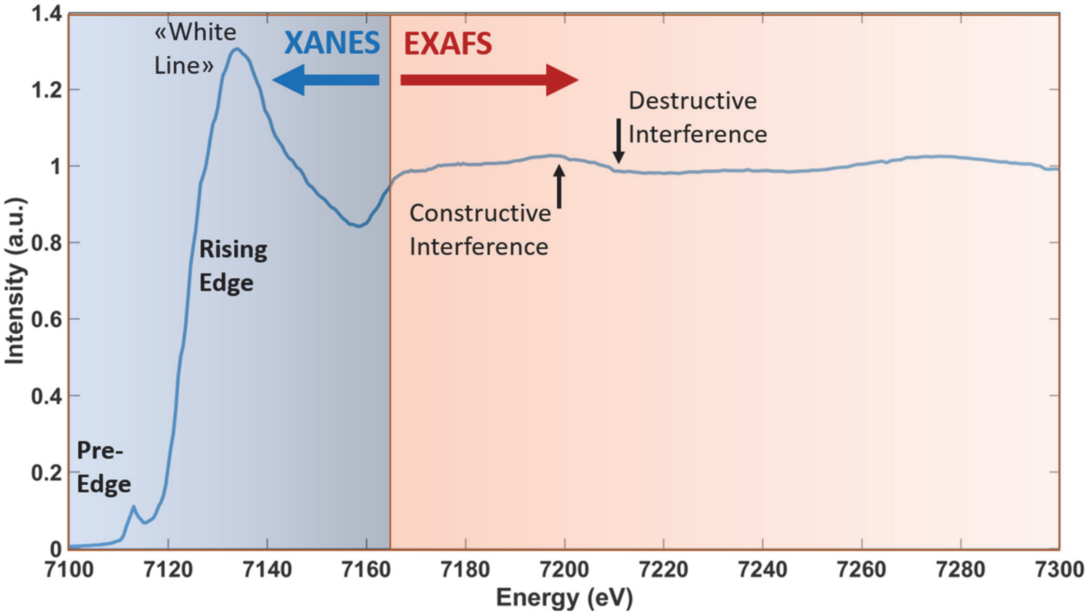

Figure 3-4: : XAS spectrum of the K-edge of Fe(II) in MbNO in solution illustrating the two regions: the low-energy XANES region up to ~50 eV above the ionization potential and the high-energy EXAFS region >7170 eV.

Summarizing XAS probes the unoccupied states (valence d and p shells in the case of iron) and is sensitive to different properties like spin, oxidation state, ligation, etc. in different regions of the X-ray absorption spectrum. Applying the pump-probe scheme, one obtains all above mentioned information with a ps-fs time resolution which makes it a powerful tool to follow chemical reactions and excited state dynamics.[118,119,125,126]

3.4 X-ray Emission Spectroscopy

Similar to XAS, X-ray emission spectroscopy (XES) is element specific, but the main difference is that in emission the *occupied* density of electronic states of a material is probed (Figure 3-5).[135] On the right of Figure 3-5 an example XAS and XES spectrum of MbNO is shown and we can see that X-ray emission energies are lower than the corresponding X-ray absorption. Two forms of XES can be differentiated: resonant X-ray emission spectroscopy (RXES) or non-resonant X-ray emission spectroscopy (NXES). For both, a core level electron is excited by an X-ray photon, but for RXES the core electron is promoted to a bound state and for NXES it is promoted to the continuum.[124] Hence, for RXES the incoming X-ray energy affects the spectrum, while for NXES it has no effect. In this work, an NXES study was performed with the incoming energy well above the edge. After an electron is excited to the continuum, a core hole is left behind which is filled by an electron from the outer shells. The excess in energy is either emitted in the form of a photon or a so-called Auger electron is ejected from one of the outer shells. If an electron from the 2p orbitals fills the core hole the resulting line is named K_α and 3p -> 1s is called a K_β line (Figure 3-6). The $K_{\alpha1}$ and $K_{\alpha2}$ lines originate from the splitting of the 2p orbital ($2p_{1/2}$ and $2p_{3/2}$), whereas for K_β these lines, originating from the 3p orbital are degenerate, resulting in the line labelled $K_{\beta1,3}$ in Figure 3-6. The valence-to-core transition is responsible for the $K_{\beta2,5}$ line (see Figure 3-6).

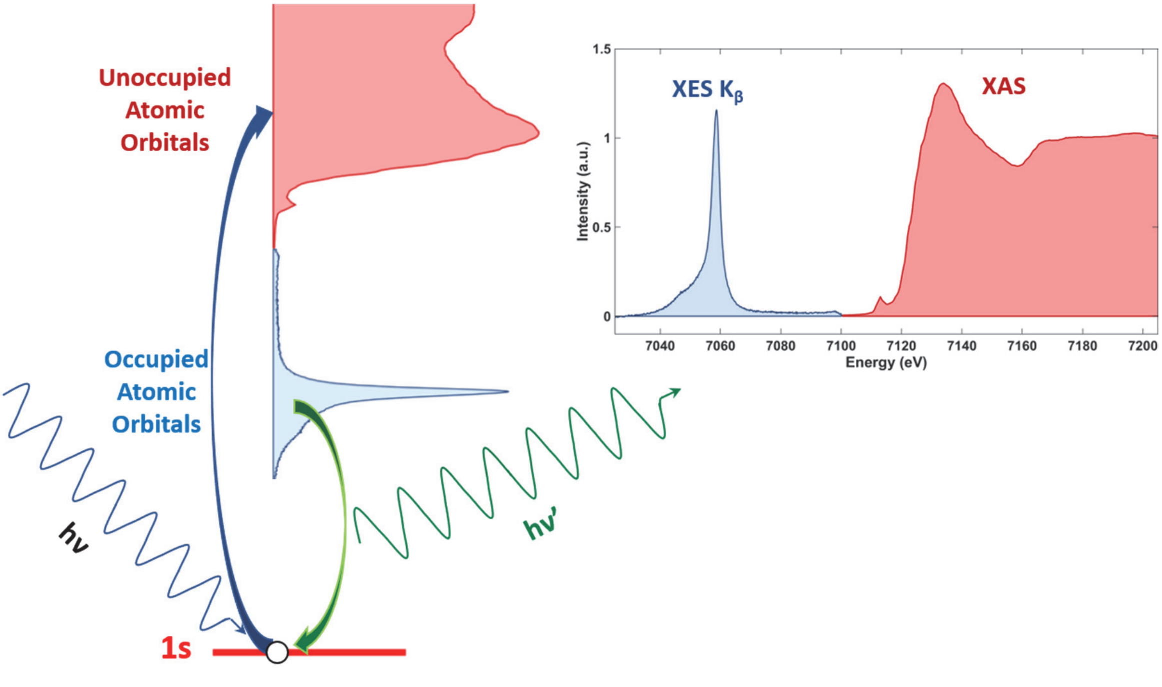

Figure 3-5: Simplified representation of XAS and XES. Static spectra in the top right are MbNO in physiological solution measured at SACLA.

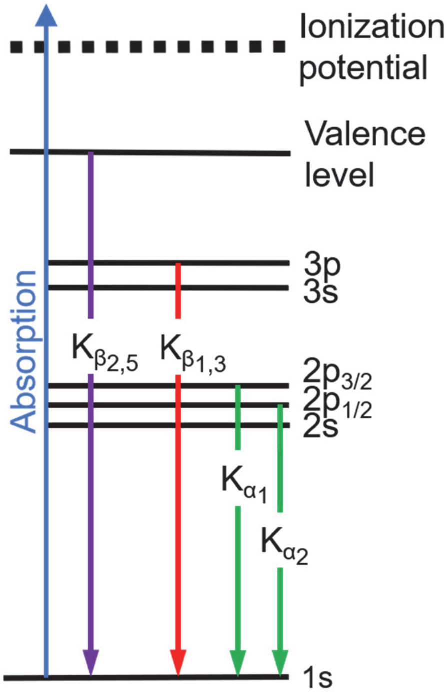
Ionization potential
Valence level
3p
3s
Absorption
$K_{\beta 2,5}$
$K_{\beta 1,3}$
$2p_{3/2}$
$2p_{1/2}$
2s
$K_{\alpha 1}$
$K_{\alpha 2}$
1s

Figure 3-6: Energy level diagram showing the origin of the K_{α} and K_{β} fluorescence after creation of a hole in the 1s (K) shell. The $K_{\alpha 1}$ and $K_{\alpha 2}$ lines (green) originate from the splitting of the 2p orbital ($2p_{1/2}$ and $2p_{3/2}$), whereas for K_{β} these lines are degenerate, resulting in the line labelled $K_{\beta 1,3}$ (red). The valence-to-core transition is responsible for the $K_{\beta 2,5}$ line (purple). The resulting spectra for all these transitions for the case of MbNO are shown in Figure 3-7.

In Figure 3-7 an illustration of the emission lines, which were introduced in the paragraph above. Namely, $K_{\alpha 1}$, $K_{\alpha 2}$, $K_{\beta'}$, $K_{\beta 1,3}$, $K_{\beta''}$ and $K_{\beta 2,5}$ of MbNO measured at SACLA. Shown are their shape, emission energy and relative intensities to each other, the colours correspond to the transitions shown in Figure 3-6.

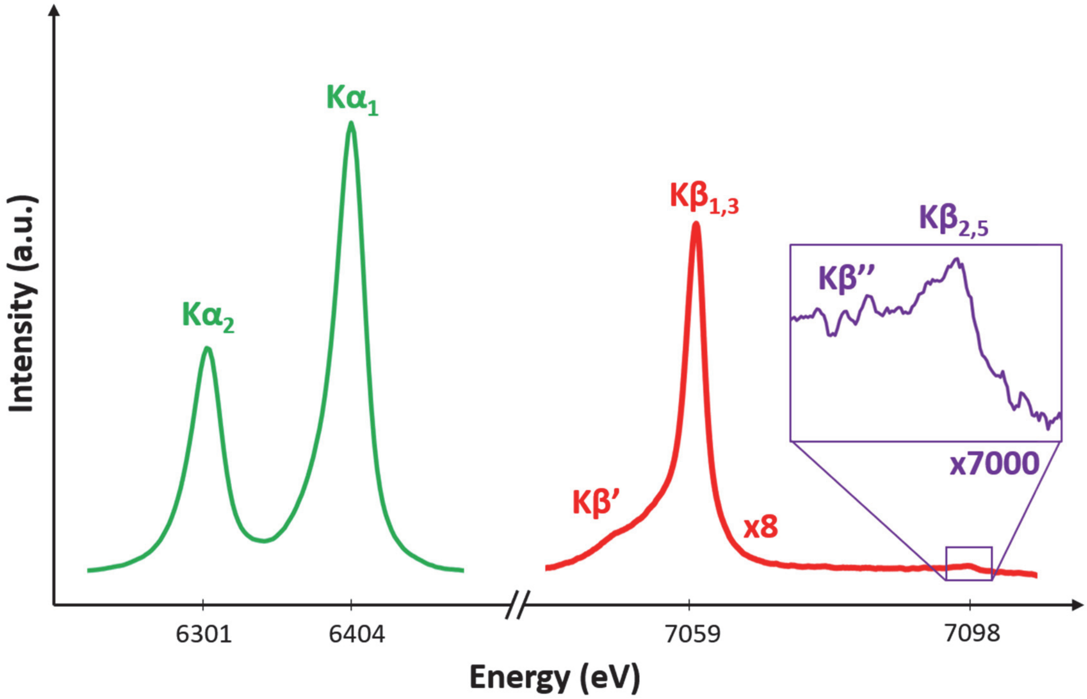

Figure 3-7: Static XES spectra of iron in MbNO in physiological medium to illustrate the different emission lines and their intensities. The corresponding transitions are shown in the energy level diagram in Figure 3-6 and are colour coded.

All emission lines presented above are probing occupied orbitals and are therefore sensitive to the electronic configuration of the element of interest. With the help of model compound reference spectra XES K_α and K_β are ideal markers for the spin state due to 2*p*-3*d* and 3*p*-3*d* exchange interactions, respectively.[124,131] In addition K_α is sensitive to the oxidation state and commonly used in heterogenous catalysis to determine in-situ speciation of relevant elements.[136,137] Recently, the feasibility of valence-to-core pump-probe spectroscopy was shown by March et al.[138], highlighting it as a powerful addition to the current X-ray toolbox for a deeper understanding of the local geometrical and electronic structure of intermediates.[138,139]

To measure X-ray emission spectra experimentally two different types of spectrometers are differentiated: a) wavelength dispersive spectrometers, b) energy dispersive spectrometers. The latter ones discriminate the energy of the emitted photons with solid state detectors achieving an energy resolution of 150 eV or worse.[140] The most common wavelength dispersive spectrometer types are Johann[141], Johansson[142] and von Hamos[143]. They all use bent crystals in different geometries. For this work a von Hamos spectrometer was used, which is shown schematically in Figure 3-8a, with the two cylindrically bent crystals, one for collecting K_α emission and one for K_β emission and the sample and MPCCD detector in the same plane. The crystals are bent in one direction for focusing of the X-rays and flat in the other to disperse the energy as shown in Figure 3-8b. The source (sample) and the detector are placed in the axis of the cylinder of the bent crystal (see Figure 3-8c). This allows the acquisition of the full XES spectrum in a single shot.[140,144] By increasing the bending radius of the crystal a higher energy resolution can be achieved, but this causes a lower collection efficiency due to the decrease of solid angle. Figure 3-8c illustrates the solid angle as grey area and the blue dotted line can be either one bent crystal or a several crystals in a segmented geometry, the latter allows easy implementation for any scattering geometry.[144]

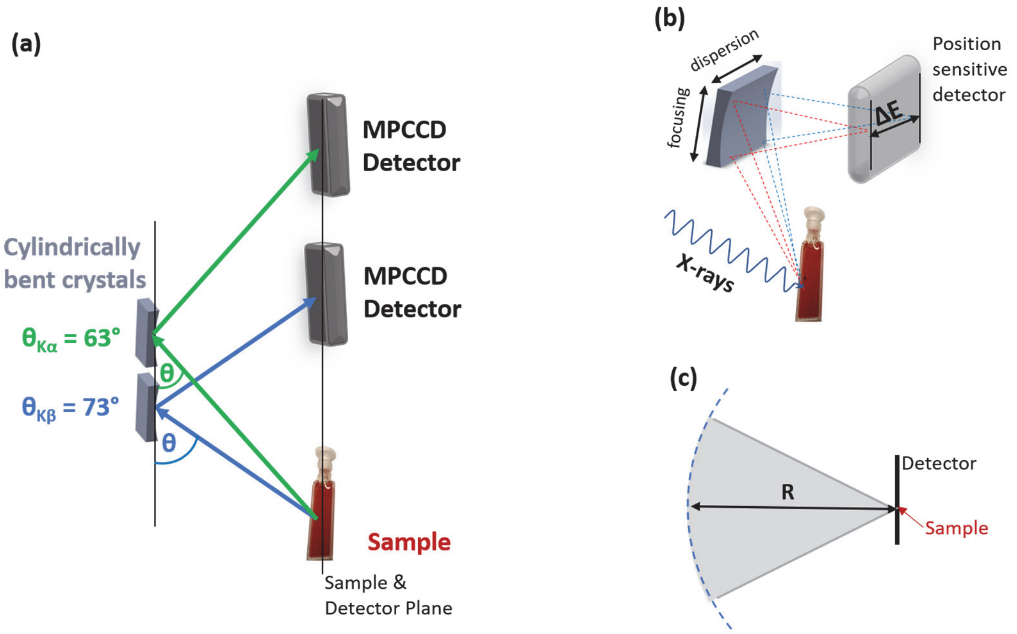

Figure 3-8: (a) von Hamos geometry (top view, along the dispersive plane) for iron Kα and Kβ emission measurements. Θ is the Bragg angle. (b) Schematic of the von Hamos geometry (side view), illustrating the dispersion and focusing directions of the crystal and the energy range (ΔE) covered by the crystal. (c) Projection along the focusing plane, R is the radius of the curvature. The grey area illustrates the solid angle which defines the collection efficiency. Figure adapted from ref.[144]

3.5 X-ray Free Electron Lasers

An X-ray free electron laser (XFEL) uses electrons to produce light.[145–147] After acceleration of the electron bunches to relativistic energies (> GeV) in linear accelerators, the electrons are forced to wiggle in an undulator (periodic structure of dipole magnets, ~100-200m) which creates X-rays of tunable frequency, high intensity and short pulse width (as to fs).[148] After the undulator section the electron bunches are discarded into the electron dump. An illustration of an XFEL from the accelerator to the electron dump and beam delivery is shown in Figure 3-9. When an electron bunch enters the undulator section a process called self-amplification of spontaneous emission (SASE) starts, which results from the interaction of the electrons with the X-ray radiation they emit. This first spontaneous emission of radiation in the pointing direction of the undulator axis is caused by wiggling (Figure 3-9). The electric field in the undulator section has a small component in the (zigzag course) direction of the electron movement. [145–147] If now some electrons are before (first half cycle) the maximum, they get accelerated, and if they are ahead (first half cycle after the maximum) they get decelerated. [145–147] This leads to the formation of so called microbunches (see Figure 3-10). In the bottom left and middle part of Figure 3-10, the micro-bunching (longitudinal density modulation) of the electron bunch is shown. During their formation the power increases exponentially and upon saturation all electrons radiate coherently. [145–147] It is important to note that in reality the number of micro-bunches is much larger (>10^5). [145–147] Another important effect present in the undulators is that the electrons slip (slippage) by one radiation wavelength with respect to the (faster) electromagnetic field. This is an important prerequisite for the SASE process.

A big challenge for XFELs is the lack of temporal coherence, which is caused by the noisy startup process of emitting radiation in the undulators (bottom left in Figure 3-10). This can nowadays easily be overcome using arrival time diagnostics which determine the arrival time of each X-ray pulse and allows for post-process correction of the temporal jitter. Two common timing tools are spectral and spatial encoding. At SACLA the spectra encoding technique is used. After branching a small portion of the XFEL pulse and focusing it in one dimension onto a GaAs wafer it induces a transient reflectivity change which can then be measured by an optical laser.

The recent construction of two new XFELs in Europe, namely SwissFEL[13] at the Paul Scherrer Institute in Villigen, Switzerland and European-XFEL[11,149,150] in Hamburg, Germany enable the investigation of transition and excited states with very short lifetimes in the femtosecond (fs) to picosecond (ps) regime. Both started operation in 2017 and deliver intense <50 fs (SwissFEL)[13] and <100 fs (European XFEL)[12] X-ray pulses. In addition the intense photon flux of about 10^{12} photons per pulse[13,151] allows to study systems which exhibit only small signals. Other hard X-ray XFELs are

1) SACLA[9,10] at the Japan Synchrotron Radiation Research Institute in Hyogo, Japan,
2) Linac Coherent Light Source (LCLS)[152], at the Stanford Linear Accelerator Center (SLAC) at Stanford, USA,
3) PAL-XFEL[153] at the Pohang Accelerator Laboratory in South Korea.

The three instruments, SACLA; EXFEL and SwissFEL at which the experiments for this thesis were carried out are explained in more detail in the following chapter.

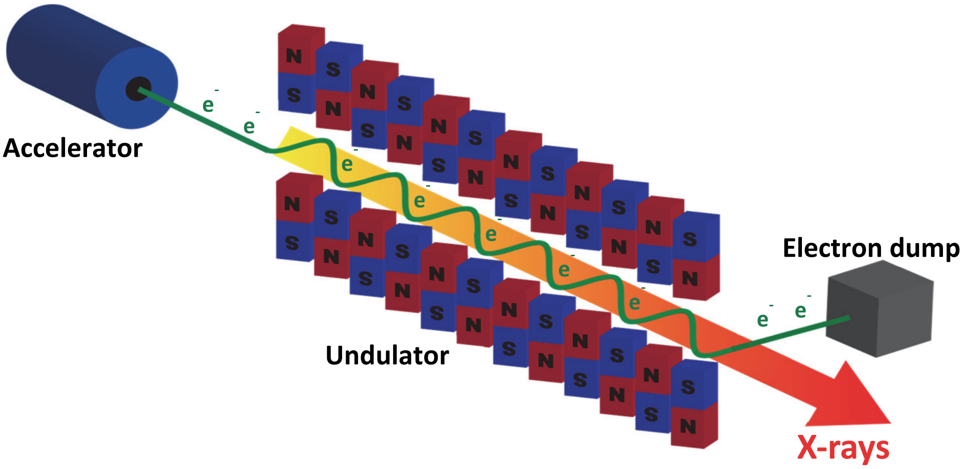

Figure 3-9: Scheme of an X-ray Free Electron Laser (XFEL). After acceleration of an electron bunch to relativistic velocities, it travels through the undulator section, where it is forced to wiggle by electromagnetic fields and emits X-ray radiation. After the undulator section the electrons are dumped into an electron dump and the tunable X-rays can be used for experiments.

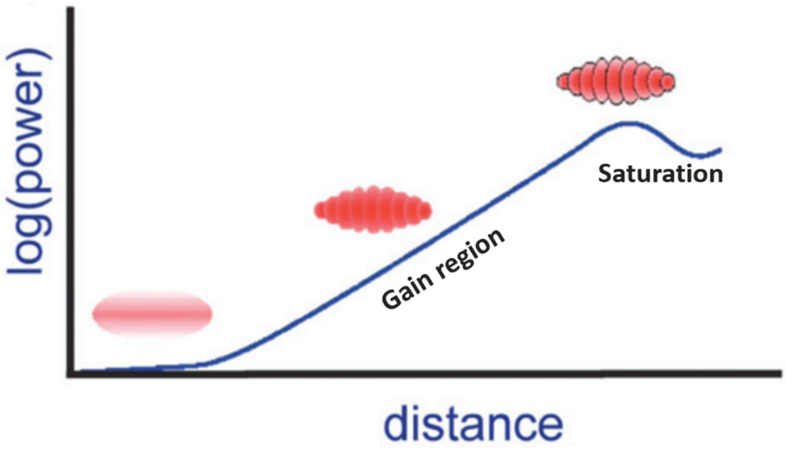

Figure 3-10: Illustration of self-amplification of spontaneous emission (SASE) in an undulator. SASE results from the interaction of the electrons with the X-ray radiation they emit. In the bottom left and middle part of the figure, the micro-bunching (longitudinal density modulation) of the electron bunch is shown. Micro-bunching results in an exponential growth of the X-ray radiation power during the travel through the undulators. It is important to note that in reality the number of micro-bunches is much larger (>10^5). From ref.[13]

Chapter 4 Experimental Setups

This chapter summarizes the experimental details of the three different XFEL facilities at which the experiments for this work were carried out. Furthermore, the challenge of sample delivery for air-sensitive and biological samples is discussed and developed sample delivery systems are presented.

4.1.1 JASRI – SACLA, BL3

The time-resolved XAS and XES experiments were performed at BL3[9] of SACLA[154] using total fluorescence yield detection method to obtain the XAS spectra. Figure 4-1a illustrates the experimental scheme used, and Figure 4-1b shows the inside of the experimental chamber used with the jet, catcher and XAS (TFY) diode and a depiction of the optical pump laser path and the X-ray probe beam path. The intrinsically broad X-ray photon energy distribution due to SASE was centered near 7.1-7.2 keV at the Fe K-edge by adjusting the electron beam energy of SACLA, and monochromatized with a Si (111) X-ray monochromator[10] to scan the photon energy. The energy calibration was done several months before using a Ni foil, therefore an offset in energy can occur due to long term drifts of monochromator. An offset in energy of -1 eV was found and therefore the data is energy calibrated (shifted by +1 eV) using spectra from Lima A. F. et al.[94] (see Appendix 8.4.1).The beam was focused to 8 µm by Beryllium compound refractive lenses.[10] The different sample solutions were flowed through a liquid jet with an inner diameter of 100 and 200 µm in a closed circulating system. The XES data presented in Chapter 5 were recorded using the 200 µm jet and the XAS data in Chapter 6 were recorded mainly with the 100 µm jet and some scans were repeated with the 200 µm jet. The calculation of the corresponding group-velocity mismatch (GVM) is presented in Chapter 8.4.2. The sample bottle was kept under constant N_2 overpressure and the experimental chamber was filled with He (> 98 %) to avoid air scattering and sample oxidation (Figure 4-1b).

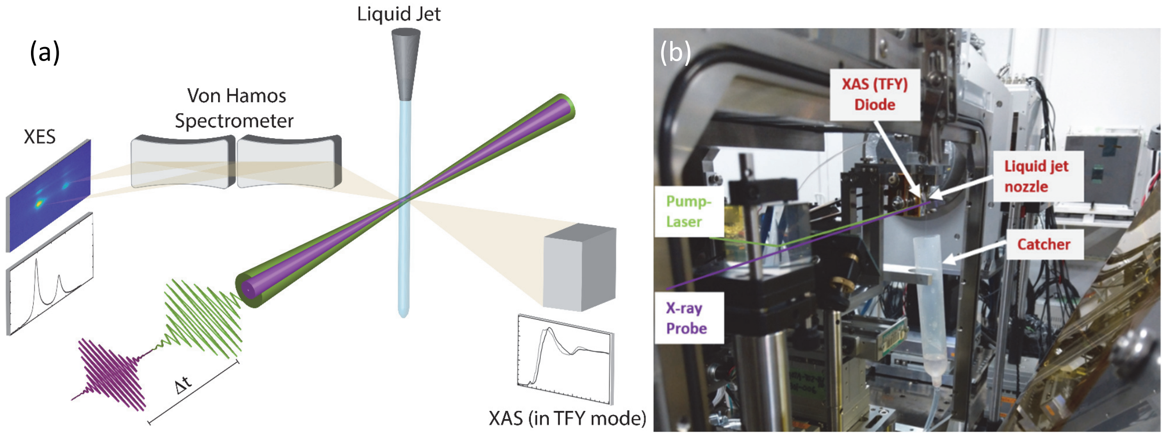

Figure 4-1: (a) Experimental Setup at BL3, SACLA, Japan. XAS was recorded in total fluorescence yield (TFY). XES Kα and Kβ were recorded with two crystals each in Von Hamos geometry and the laser pump and X-ray probe beam were close to colinear. (b) Photograph of the inside of the experimental chamber illustrating the beam path of X-rays and pump-laser, the liquid jet, catcher and the XAS (TFY) diode. The XES crystals were placed outside of the chamber and are not visible in the photograph.

The fluence of optical laser pulses was set at 195 mJ/cm^2 which was in the linear regime of the transient signal at the main XAS edge at 7122.5 eV. The timing between optical laser and X-ray pulses was recorded with the diagnostics based on the X-ray beam splitting scheme.[155,156] For the jitter correction, a 30 fs and 60 fs interval bin width was applied. The instrument response function was evaluated to be ~70 ± 30 fs by a fit of the risetime of the transient XAS signal at 7127 eV, which is the main edge feature,[88] using the 100 µm thick jet, where the fastest rise was observed (Figure 6-22). For the thicker jet (200 µm) an instrument response function of 150 ± 40 fs was obtained from the fit (Figure 4-2) under the same conditions. The rise of the XAS signal at this energy does not show any data points on the rise with 30 fs binning and is therefore assumed to be IRF limited. It was fitted using the function described in § 5.2.4 (Equation 5-1). The obtained IRF for the 200 µm jet was then used to fit the XES kinetic traces.

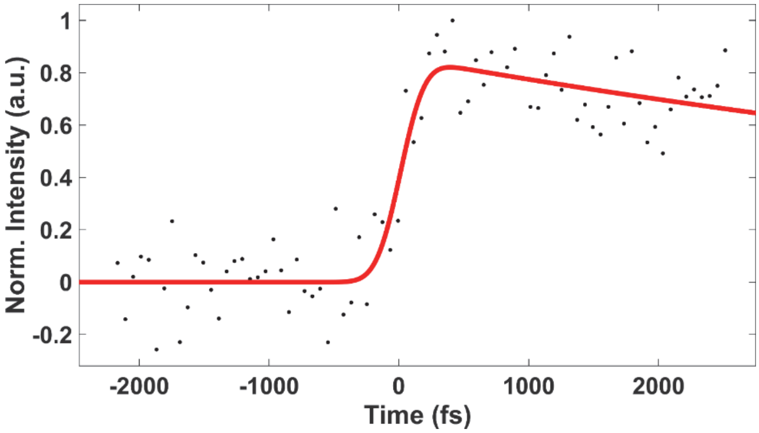

Figure 4-2: Rise time of the X-ray absorption transient signal of MbNO at 7127 eV (dots). The red trace is a fit to obtain the IRF of the experiment (see § S6), which is σ = 150 fs.

The inherent fluctuations in intensity and spectral shape of the X-ray pulses due to the self-amplified stimulated emission (SASE) process of SACLA were normalized with the X-ray pulse intensity (I_0). An overview over all the experimental parameters used for the time-resolved XAS and XES measurements at BL3, SACLA is given in Table 4-1.

Table 4-1: Overview of the experimental parameters at BL3, SACLA, Japan.

Description	**Parameters**
Sample	4 mM MbNO, metMb, deoxyMb in physiological medium
Sample delivery	100 & 200 μm jet in chamber (He atmosphere)
XFEL	
X-ray photon energy	7.1-7.15 keV (8.168 keV for XES)
X-ray pulse energy	~500 μJ
Pulse duration	~10 fs (estimated)
Beam size at focus position	~8 μm
Repetition rate	30 Hz
Optical Laser (Ti:Sapph +OPA)	
Pump wavelength (Width)	533 nm (15 nm FWHM)
Pulse duration	~45 fs FWHM at 533 nm (estimated) ~24 fs at 800 nm (measured)
Beam size at focus position	153 x 193 μm
Pulse energy (Fluence) at sample position	~45 μJ (195 mJ/cm^2)
Repetition rate	15 Hz
Von Hamos Spectrometer (VHS)	
Crystals and geometry for K_α	2x Ge(333): $\theta_B=63^\circ$
Crystals and geometry for K_β	2x Si(531): $\theta_B=73^\circ$
Detector	MPCCD (30 Hz)

For the XES measurements, the intrinsically broad X-ray photon energy distribution ($\Delta E/E \simeq 5*10^{-3}$) was tuned above the Fe K-edge to 8.168 keV by adjusting the conditions of the accelerator and undulators of SACLA. Non-resonant X-ray emission spectra were recorded in the von Hamos geometry using two Ge(333) crystals at a Bragg angle of $\theta_B=63^\circ$ for Fe K_α, two Si(531) crystals at $\theta_B=73^\circ$ for Fe K_β and a multiport charge-coupled device (MPCCD, 30 Hz) for detection. The MPCCD has a pixel size of $50 \times 50\ \mu m^2$, an imaging area of $25.6 \times 51.2\ mm^2$ and a quantum efficiency of ~ 0.6 at 7 keV. The probe X-ray (pink beam) was focused on the sample solution by beryllium compound refraction lenses to a focal beam diameter of 8 μm. A small fraction of the X-ray pulse was sampled using a Kapton film to monitor its intensity. The sample-jet was placed in a chamber filled with Helium gas (>98%) to prevent sample oxidation and to reduce X-ray light attenuation in air. The crystals and the MPCCD were placed outside the chamber. The energy resolution, after overlapping contributions from all crystals, was evaluated to be ~0.5 eV for Fe K_β and ~0.6 eV for Fe K_α. As we are detecting shifts of a single peak, the energy resolution is not the limiting factor. This is illustrated in Figure 5-9, Figure 5-10, Figure 5-15 and Figure 5-16, which show the XES K_β and K_α lines of laser-on (pumped) spectra for different early times, where one can clearly measure shifts below the energy resolution of the experiment.

The sample was excited by a 533 nm pulse (14.5 nm spectral width), into the Q-bands of MbNO (Figure 4-6). The pump pulse was generated using an amplified Ti:Sapphire laser system equipped with an optical parametric amplifier (HE-TOPAS, Coherent). The pulse duration of 533 nm light was estimated to be ~45 fs. Figure 5-1b shows a scheme of the experimental setup for ultrafast XES. The pump-laser light was reduced to 15 Hz using a chopper wheel and focused onto the liquid jet. The XES transients were recorded at a laser pulse energy of about 45 μJ, comparable to previous experiments on myoglobins[56,88,157], and corresponding to 2-3 photons per molecule. The spatial profile of the laser-beam at the sample position was found to be Gaussian with an effective spot diameter of 153x192 μm^2 (horizontal x vertical, FWHM) using a beam profiler. The laser pointing fluctuations were characterized to be 2.77% horizontally and 3.65% vertically.

4.1.2 European XFEL

Steady-state XES K_α and K_β reference spectra of $[Fe(bpy)_3]^{2+}$, deoxyMb and MbNO were recorded at the Eu-XFEL (see Figure 5-3, Figure 5-8 and Figure 5-14), using the high-intensity X-ray pulses (pulse energy ~500 µJ) from the European XFEL. The pulses have an estimated duration of ~100 fs and a repetition rate of 30 pulses per train (at 10 Hz) and 1.1 MHz intra-bunch train repetition rate.(*4-6*) The intrinsically broad X-ray photon energy distribution ($\Delta E/E \simeq 10^{-3}$) was centred above the Fe K-edge to 9.3 keV. Non-resonant static X-ray emission spectra were recorded in the von Hamos geometry using seven Ge(220) crystals at a Bragg angle of θ_B=75.45° for Fe K_α, eight Si(531) crystals at θ_B=73.09° for Fe K_β and a GreatEyes CCD (10 Hz) for detection. Due to the limited repetition rate (10 Hz) of the GreatEyes detector, the XES signal was detected cumulative and could not be resolved on a shot-to-shot basis. The X-ray (pink beam) was focused on the sample solution to a focal beam diameter of 40-50 μm by beryllium refraction lenses. The sample-jet was placed in a small chamber filled with Nitrogen gas to prevent oxidation and a Helium bag was placed between the sample chamber, the crystals and the detector to reduce X-ray light attenuation in air. An overview over all the experimental parameters used for the static and time-resolved XES measurements at FXE, European XFEL is given inTable 4-2.

Table 4-2: Overview of the experimental parameters at FXE, European XFEL, Germany.

Description	**Parameters**
Sample	4 mM MbNO, metMb, deoxyMb in physiological medium
Sample delivery	200 µm jet in chamber (N_2 atmosphere)
XFEL	
X-ray photon energy	~9.3 keV
X-ray pulse energy	>500 µJ

Pulse duration	~100 fs (estimated)
Beam size at focus position	~40-50 µm
Repetition rate	300 Hz (10 Hz bursts with 30 pulses/burst and an intra burst repetition rate of 1.1 MHz)
Optical Laser (Ti:Sapph +OPA)	
Pump wavelength	515 nm
Pulse length	~24 fs at 800 nm
Beam size at focus position	80-100 µm
Pulse energy (Fluence) at sample position	~4-5 µJ (~100 mJ/cm^2)
Repetition rate	1.1 MHz
Von Hamos Spectrometer (VHS)	
Crystals and geometry for K_α	7x Ge(220): n=2, θ_B=75.45°
Crystals and geometry for K_β	8x Si(531): n=1, θ_B=73.09°
Detector	GreatEyes CCD: 10Hz

4.1.3 SwissFEL

The measurements were carried out at the Alvra end-station of the Swiss Free Electron Laser (SwissFEL) at the Paul-Scherrer-Institute (Villigen).[13] The sample was delivered to the interaction region by a cylindrical liquid jet of 100 µm diameter, running in a closed loop (in He and N_2 atmosphere). The jet (inside a He chamber) was pumped by an HPLC pump and the catcher by a peristaltic one. On the way from the catcher back to the sample reservoir, a UV-VIS spectrometer was placed to provide on-line monitoring of the sample integrity. No sample damage was observed during the measurements. The pump pulse was generated by an 800 nm Ti:Sapphire amplified laser system coupled to an optical parametric amplifier, running at 25 Hz (half the repetition rate of the X-ray pulses), yielding 530 nm laser pulses to excite the sample. The jet speed was such that the sample was completely refreshed between consecutive pairs of laser pump/X-ray probe pulses.

The laser and X-ray beams were nearly collinear. The X-ray beam was focused into an 8x8 µm (FWHM) spot by a pair of Kirkpatrick-Baez mirrors. The laser focus was in the order of 110x110 µm (FWHM). Tunable monochromatic X-rays in the 7.1-7.2 keV range were used for the Fe K-edge absorption measurements, that were generated by scanning the undulator and the Si(111) monochromator central energies. The energy calibration of the monochromator was performed using an iron foil right before the XAS measurements were performed.

The XAS signal was recorded with a Be shielded Si diode in total fluorescence yield (TFY) mode at approximately 90° from the incident X-ray beam and normalized by the incoming X-ray pulse intensity (I_0), measured by the scattering from a thin target placed on the beam path. The FEL was running at a repetition rate of 50 Hz, twice that of the pump laser, such that the transient data was obtained by subtracting consecutive laser-on from laser-off spectra. The experiments were carried out inside the Alvra prime experimental chamber which was set to 800 mbar He atmosphere to maximize X-ray transmission and minimize X-ray scattering noise. An overview over all the experimental parameters used for the time-resolved XAS measurements at Alvra, SwissFEL is given inTable 4-3.

Table 4-3: Overview of the experimental parameters at Alvra, SwissFEL, Switzerland.

Description	**Parameters**
Sample	4 mM MbNO in physiological medium
Sample delivery	100 µm jet in chamber (He atmosphere)
XFEL	
X-ray photon energy	7.1-7.2 keV
X-ray pulse energy	~600 µJ
Pulse duration	<50 fs (estimated)
Beam size at focus position	~8 µm
Repetition rate	50 Hz
Optical Laser (Ti:Sapph +OPA)	
Pump wavelength	530 nm (19 nm FWHM, ~30 fs at 800 nm)
Beam size at focus position	110x 110 µm
Pulse energy (Fluence) at sample position	1-29 uJ (10-300 mJ/cm^2)
Repetition rate	25 Hz

4.2 Sample Delivery Systems

Experiments involving air sensitive samples require measures to keep inert atmosphere at all time. The high peak power of X-ray free electron lasers and geometric constraints impose extra challenges for the design and implementation. Therefore, several sample delivery systems were developed fulfill the demands of keeping the sample under inert conditions and adapt to different X-ray free electron laser facilities and potential challenges during the experiments.

In detail an extra thin 3D printed diamond flow cell was developed based on the initial design of Lima F.[158] (see Figure 4-3). Starting from the initial design for the cell to be machined from alumina and being 8 mm thick, the goal was to enlarge the angle of the exit window on the back to a maximum to be able combine XES and X-ray diffuse scattering (XDS) in the forward direction. The idea is to use the cell in an 45° angle relative to the incoming X-ray beam and therefore obtain a high collection efficiency for XES and not to shadow the XDS detector. This was achieved by changing to 3D printing as production method, which made it possible to reduce the thickness of the cell to 3.5 mm and enlarging the exit angle to provide a large angle opening to combine ultrafast XES and XDS in one experiment. In addition, a novel way to mount the tubing to the cell was developed (Figure 4-4). The cell is used as a mount for two optical grade CVD diamond windows (10 mm and 15 mm in diameter and 50 µm thick) for minimal pump-laser and X-ray intensity losses. The diamond windows are placed on O-rings and separated by 100 µm thick Teflon spacers. In the updated design an additional Teflon spacer is placed between the 15 mm diamond window and the metal clamp to prevent mechanical stress on the diamond window. The empty hole below can be used to mount a pin hole, which is generally used to spatially overlap the optical pump laser with the X-ray probe laser.

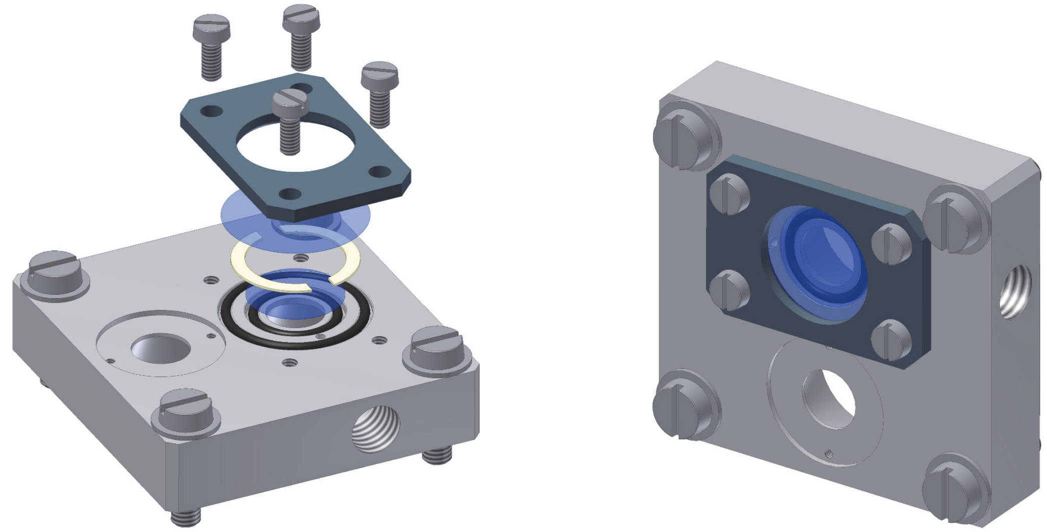

(a) Mounting diagram of the diamond flow cell

(b) Illustration of a completely mounted diamond-window flow cell.

Figure 4-3: Original flow cell design from Lima F.[158]

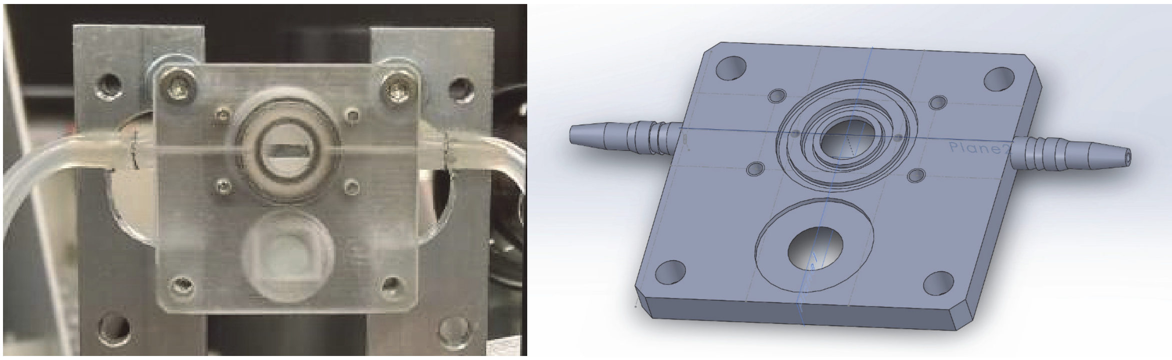

Figure 4-4: Novel 3D printed diamond flow cell. Left: mounted and in operation. Right: 3D drawing.

As a second sample delivery system a 3D printed mount for X-ray quartz capillaries (Figure 4-5). The top part can be removed to insert the capillary, which is afterwards glued to seal it. And on the top and bottom of the mount are connectors for variable tubing sizes. In addition, next to the capillary a pinhole can be mounted which is in the same plane as the capillary and can be used for spatial overlap between the optical pump laser beam and the X-ray probe laser.

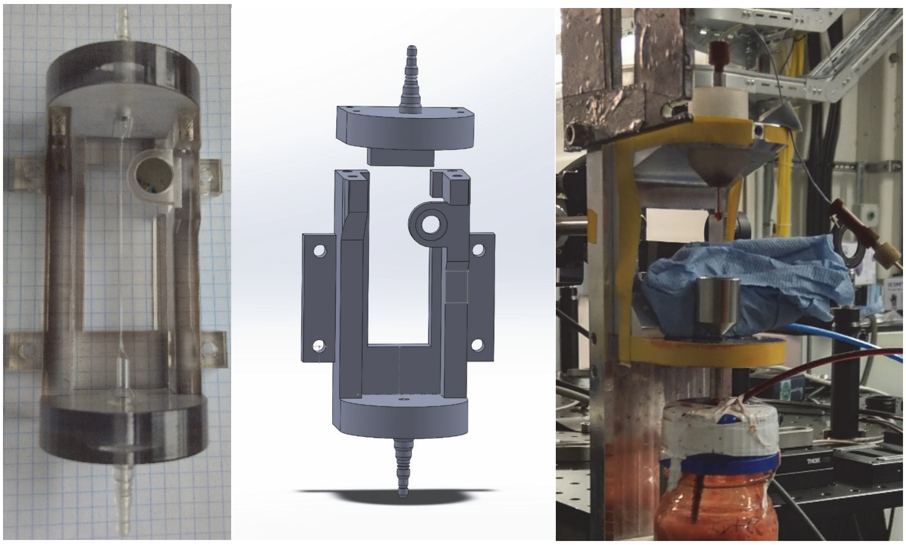

Figure 4-5: (a) Quartz capillary mount including pinhole. (b) 3D drawing showing the two parts separate. (c) Current design of the liquid jet at European XFEL, one can see the glass capillary the metal catcher with the sample reservoir right below. The yellow area is where the Kapton foil can be attached to seal the jet and work under inert atmosphere.

The design of the quartz capillary was then further developed into a liquid jet in a small chamber. This was achieved by closing it with Kapton foil and substituting the capillary through a glass nozzle connected to a HPLC tube (100 µm), a larger tube from the bottom serves as catcher and drilling a gas inlet through the bottom allows to create inert atmosphere. Several experiments have been carried out to test the newly developed sample delivery systems, namely UV-VIS measurements to ensure sample integrity and transient absorption measurements to test for laser damage and find optimal experimental parameters for the final experiments carried out at the European XFEL in Hamburg (Germany). An adapted version of the liquid jet in a small chamber design is currently being used at European XFEL for liquid phase experiments.

4.3 Sample Preparation and Handling

Lyophilized Myoglobin (equine skeletal muscle, 95-100%, Sigma Aldrich) was dissolved in the sodium phosphate buffer (100 mM, pH 7) to obtain a solution of metMb (4 mM). The Sodium phosphate buffer (100 mM, pH 7) was prepared with MiliQ water, sodium phosphate monobasic (BioXtra, 99.0%, Sigma Aldrich) and sodium phosphate dibasic (BioXtra, 99.0%, Sigma Aldrich). It was checked with pH paper and was degassed with N_2 for at least 24 h before use. The aim is to simulate physiological conditions, where the same phosphate system serves to buffer intracellular fluids and maintain a pH of 6.9 to 7.4. DeoxyMb was prepared by adding, under inert conditions, a five-fold molar excess of sodium hydrosulphite ($Na_2S_2O_4$, 85%, Sigma Aldrich) to a solution of metMb (4 mM). MbNO was prepared by adding, under inert conditions, a fivefold excess of sodium nitrite ($NaNO_2$, ReagentPlus, 99.0%, Sigma Aldrich). The sample was kept at all times in a glass bottle with an overpressure of N_2. The different samples were checked with UV-VIS spectrometry for full conversion and the spectra were compared to literature. At the EXFEL the liquid jet (100 µm) was kept in a small Kapton chamber with an N_2 overpressure, at SACLA the liquid jet (200 µm) was in a

He chamber (> 98% He) and at SwissFEL the liquid jet (100 µm) was placed in the Alvra experimental chamber in a 500 mbar He atmosphere.

For the preparation of $[Fe(bpy)_3]^{2+}$, used as a standard, $FeCl_2$ was dissolved in a minimum amount of water and heated up, then 3 equivalents of bipyridine with a slight stoichiometric excess were added and the solution was cooled down and dark red crystals were obtained. These were isolated by filtration and characterized by UV-VIS spectroscopy.

4.3.1 UV-VIS and Sample Monitoring

In Figure 4-6 the VIS spectra of deoxyMb, metMb, MbNO in the range of 450-700 nm are plotted, which is the so-called characteristic Q-bands. The UV-VIS spectra showing both the Soret and the Q-bands of the different species are plotted in Figure 2-15. Both bands originate from the porphyrin absorption and were used to monitor the sample integrity during all experiments using a portable spectrometer (AvaSpec-ULS2048) to detect oxidation of MbNO and formation of metMb. As soon as any small changes were detected the sample was either refreshed with adding sodium dithionite and sodium nitrite or replaced through a fresh sample. After a maximum of 12h of measurements, the sample was replaced by a new one.

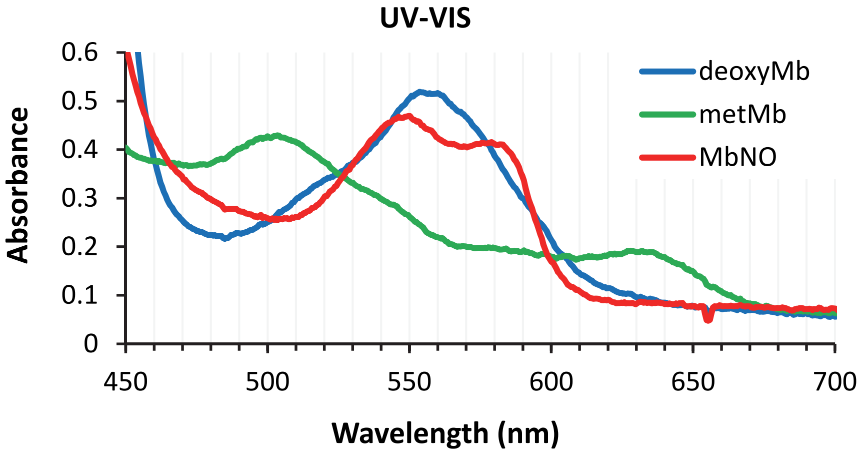

Figure 4-6: VIS spectra of deoxyMb, metMb and MbNO (4 mM physiological solution) recorded in a 100 µm flow cuvette under inert conditions. Shown are the Q-bands of the porphyrin ring.

Chapter 5 Femtosecond X-ray Emission Spectroscopy of Myoglobin

The content of this chapter is a publication with the title: "Femtosecond X-ray emission study of the spin cross-over dynamics in heme proteins", which is currently under review in Nature.

5.1 Introduction

Recently, the occurrence of prompt doming was questioned in a fs X-ray absorption study of photoexcited MbCO. Using a monochromatic probe at 7.123 keV (at the Fe K-edge), Levantino et al[56] observed a first event in <50–70 fs, which they attributed to CO photolysis from the LS (S=0) MbCO and partial SCO to a higher spin state, and a further 300-400 fs event, attributed to the passage to the HS (S=2) state of deoxyMb. This picture was supported by quantum wave packet dynamics simulations,[159] which accounted for coherent nuclear and electronic motion. While X-ray absorption spectroscopy (XAS) is an ideal element-selective probe of the electronic and geometric structure of metal-containing molecular complexes,[160] Levantino *et al*'s[56] use of a monochromatic probe could not spectroscopically identify the photoproducts, let alone their spin states. The latter is however possible using non-resonant X-ray emission spectroscopy (XES).[136] The $K_{\beta1,3}$ lines ($3p \rightarrow 1s$ emission, Figure 5-1a) are ideal markers of the spin state (number of unpaired 3*d* electrons) of transition metal complexes via the 3*p*-3*d* exchange interactions. As a matter of fact, fs transient K_β emission was recently used as a sensitive probe of the SCO dynamics in $[Fe(bpy)_3]^{2+}$,[161] as well as to identify the HS deoxy heme product of photoexcited ferrous cytochrome c after dissociation of its distal methionine ligand.[162] Similarly, the K_α lines ($2p \rightarrow 1s$ transitions, Figure 5-1a) can also be used as markers of the spin state, albeit slightly weaker because of the 2*p*-3*d* exchange interaction, giving rise to a linear dependence of the full-width at half-maximum (FWHM) of the $K_{\alpha1}$ line as a function of the number of unpaired metal 3*d* electrons.[136,163]

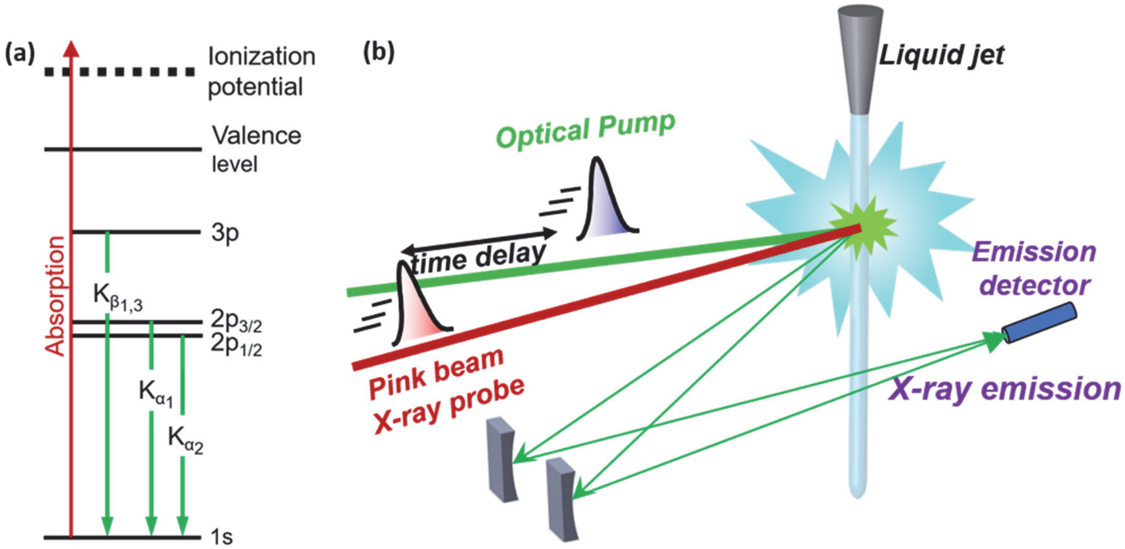

Figure 5-1: (a) Energy level diagram showing the origin of the K_α and K_β fluorescence after creation of a hole in the 1s (K) shell. The $K_{\alpha 1}$ and $K_{\alpha 2}$ lines originate from the splitting of the 2p orbital ($2p_{1/2}$ and $2p_{3/2}$), whereas for K_β these lines are degenerate, resulting in the line labelled $K_{\beta 1,3}$. (b) Experimental setup for the time-resolved X-ray emission spectroscopy measurements at the XFEL. A von Hamos geometry was used for these measurements.

Here, we focus on the case of Nitrosylmyoglobin (MbNO) that is characterised by a ligand dissociation-recombination cycle within ~250 ps,[88] i.e. much shorter than the commonly studied MbCO, so that both processes can be monitored in the same experiment. As for MbCO, NO photodissociation from the heme has been reported to be prompt (<100 fs) with a quantum yield of 55 %,[84] while recovery of the system occurs on typical timescales of 1-3 ps, 10-30 ps, 130-250 ps, and a weak (~10-20%) ns component.[54,73,75,78,88,164] The shortest time scale was attributed to vibrational relaxation in the pentacoordinated deoxyMb, while the next two were attributed to geminate recombination of, respectively, NO ligands from the distal pocket close to the heme and from the more distant Xe4 pocket. Finally, the nanosecond (ns) component is due to non-geminate recombination of a small fraction of NO ligands that escaped the protein. Contrary to other ligands (CO in particular), which can bind to a planar heme, the unpaired NO electron allows its binding to the domed HS deoxyMb,[73] and this was recently supported by a time-resolved Fe K-edge XAS study with 70 ps resolution.[88] The binding of NO to a domed deoxyMb (hereafter designated as deoxyMb-NO) was previously predicted by theoretical calculations on model hemes,[92] which argued that the return to the planar form is a reverse SCO from HS deoxyMb-NO to LS planar MbNO. Recent ultrafast resonance Raman studies[54] determined that the domed-to-planar transition in MbNO takes place in ~30 ps, but argued that the process is governed by a structural constraint exerted by the protein scaffold via the Fe-His bond (Figure 2-13).

5.2 Experimental Details

To identify the mechanism leading to HS deoxyMb formation in Mb's and its time scale, and the specific case of the deoxyMb to MbNO transition, here we use fs Fe K_α and K_β non-resonant X-ray emission spectroscopy (XES) with a von Hamos spectrometer (Figure 5-1b) at the SPring-8 Angstrom Compact Free Electron Laser (SACLA).[9,154] We recorded laser-on and laser-off XES spectra (whose difference is the transient spectrum) as a function of time delay with respect to the pump pulse. Details of the sample preparation can be found in Chapter 4.3.

5.2.1 Methods Summary

Femtosecond hard X-ray emission spectroscopy (XES) measurements were carried out on 4 mM solutions of MbNO in a physiological medium (pH = 7) under inert conditions (He or N_2 atmosphere) at BL3 at SACLA.[9,154] The sample solution was delivered through a 0.2 mm-thick round liquid jet and its integrity was continuously monitored by a mobile UV-VIS spectrometer. A laser pulse at 533 nm with a ~45 fs full width at half maximum (FWHM) was used to excite the Q-bands of MbNO in a near colinear geometry with the X-ray beam. An energy dispersive X-ray emission spectrometer (von Hamos geometry) and a 2D MPCCD detector are used to record the iron 2p-1s (K_α) and 3p-1s (K_β) fluorescence spectra. A timing tool was used to measure the X-ray/optical relative arrival time fluctuations on a pulse to pulse basis and sort each shot by its relative arrival time ($\sigma = 150 \pm 40$). For the analysis of the K_β transients, we have used reference spectra of Fe-containing compounds from ref.[161]. For the K_α emission, reference spectra are lacking, and we relied on Density Functional Theory (DFT) simulated XES spectra for the ground state of MbNO and states of different spins for deoxyMb.

5.2.2 Time-resolved X-ray Emission Spectroscopy (SACLA)

Details about the experimental setup and conditions at SACLA can be found in Chapter 4.1.1.

5.2.3 Determination of the Instrument Response Function

The determination of the instrument response function (IRF) is explained in detail in Chapter 4.1.1.

5.2.4 Fit of the Kinetic Traces

We are assuming a sequential kinetic scheme, for which the temporal evolution of the sample follows a sequence of events (rise or decays). These events can be described by specific first-order decay rates k_i and the corresponding lifetimes τ_i for which the kinetic response can be modelled by a sum of N model functions[165]:

$$\Delta A(t) = e^{-k_i t} \oplus IRF(t) =$$

$$= \frac{1}{2}\sum_{i=1}^{N} a_i * e^{\frac{1}{\tau_i}*(\mu-t)+\frac{(\sigma*\frac{1}{\tau_i})^2}{2}} *$$

$$* \left[1 + \mathrm{erf}\left(\frac{t-\left(\mu+\frac{1}{\tau_i}*\sigma^2\right)}{\sqrt{2}*\sigma}\right)\right]$$

Equation 5-1

Where a_i is the amplitude of the i^th^ decay, $\oplus$ indicates convolution, τ_i describes the decay time, which corresponds to $\frac{1}{k_i}$, μ the time origin of the IRF (time-zero) and σ its width.[165] Combinations of N=1 to N=4 were fitted and the best fit was chosen according to least correlated lifetimes and amplitudes larger 0.01, as well as quality of the fits.

Each time-point of the XES time-traces is an average of three to six individual scans, one scan corresponds to accumulation over 10,000 XFEL shots. For the K_β XES, the emission line of the averaged laser-on (pumped) spectra (Figure 5-9 and Figure 5-10) was fitted with a Gaussian function for each time delay and its peak maximum (b in Equation 5-2) was used to determine the shift in eV (Figure 5-2):

$$y = a * e^{\left[-\left(\frac{x-b}{\sigma}\right)^2\right]}$$

Equation 5-2

Where a is the amplitude, b is the centroid and σ is related to the peak width.

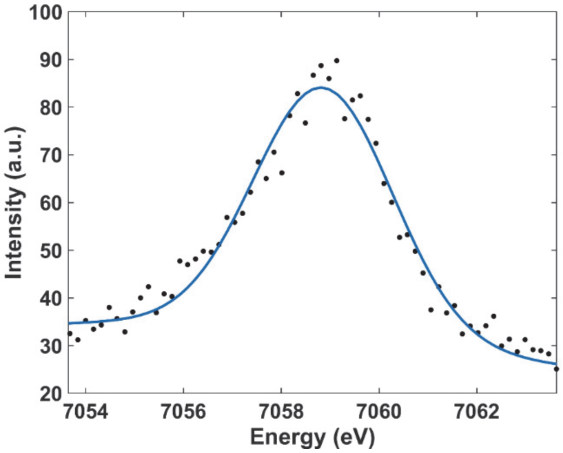

Figure 5-2: XES K_β laser-on spectra at 10 ps delay measured at SACLA (black dots). In blue, the Gaussian fitting used to obtain the peak maximum.

The obtained time trace was normalized to the maximum shift (~0.45 eV). For the K_α XES, the line was fitted with a Gaussian function (Equation 5-2) to obtain σ, which was also normalized.

We are assuming a sequential kinetic scheme, for which the temporal evolution of the sample follows a sequence of events (rise or decays). These events can be described by specific first-order decay rates k_i and the corresponding lifetimes τ_i for which the kinetic response can be modelled by a sum of N model functions. [165]

5.2.5 Steady-state X-ray Emission Spectroscopy (EXFEL)

Steady-state XES K_α and K_β reference spectra of $[Fe(bpy)_3]^{2+}$, deoxyMb and MbNO were recorded at the EXFEL (see Figure 5-8, Figure 5-3 and Figure 5-14), using the high-intensity X-ray pulses (pulse energy ~500 μJ) from the European XFEL. The ∼100 fs pulses are delivered at a repetition rate of 30 pulses per train (at 10 Hz) and 1.1 MHz intra-bunch train repetition rate.[11,12,149,150] The intrinsically broad X-ray photon energy distribution ($\Delta E/E \simeq 10^{-3}$) was centered at 9.3 keV. The non-resonant steady-state X-ray emission spectra were recorded in the von Hamos geometry using seven Ge(220) crystals at a Bragg angle of θ_B=75.45° for Fe K_α, eight Si(531) crystals at θ_B=73.09° for Fe K_β and a GreatEyes CCD(10 Hz) for detection. The X-ray (pink beam) was focused on the sample solution to a diameter of 40-50 μm by beryllium refraction lenses. The sample-jet was placed in a small chamber filled with Nitrogen gas to prevent oxidation and a Helium bag was placed between the sample chamber, the crystals and the detector to reduce X-ray light attenuation in air.

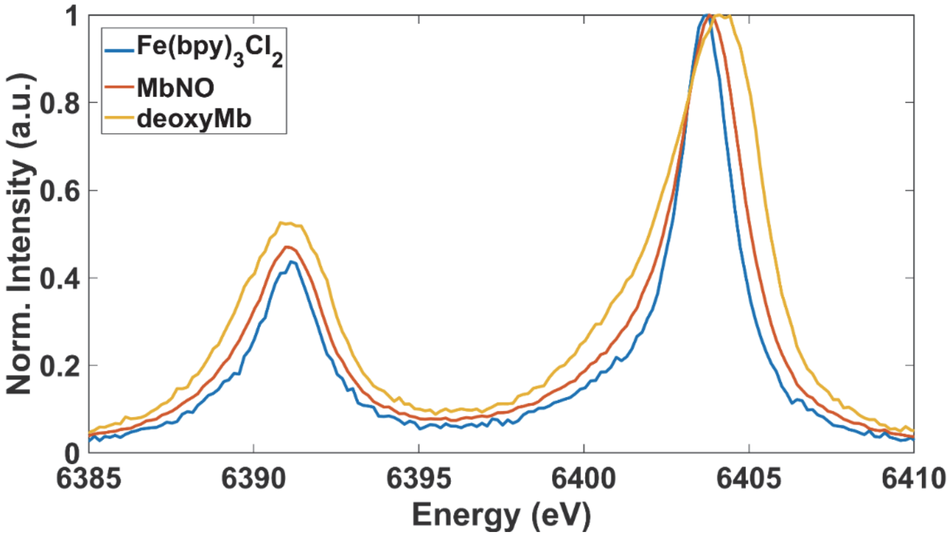

Figure 5-3: XES K_α spectra normalized to the maximum peak intensity for singlet ($Fe(bpy)_3Cl_2$), doublet (MbNO) and quintet (deoxyMb) compounds.

5.2.6 Theoretical Modelling (DFT)

Because K_α reference spectra of intermediate spin compounds are missing, Density functional theory (DFT) calculations were performed to simulate them. We benchmarked these calculations against the available MbNO and deoxyMb spectra (Figure 5-14 and Figure 5-5). The calculations use the CAM-B3LYP exchange-correlation functional.[166] Scalar relativistic effects were included using the second-order Douglas-Kroll-Hess Hamiltonian (DKH2)[167], including picture change and finite-nuclear effects. The def2-TZVP basis set, reparametrized for use with DKH (DKH-def2-TZVP) was applied[168–170]. Density fitting of the Coulomb and exchange integrals was employed using the resolution-of-the-identity chain-of-spheres approach (RIJCOSX), with the appropriate def2/JK auxiliary basis set. To approximate the effects of screening by the protein environment, a polarizable continuum model was applied using the conductor-like screening model (COSMO), using the same parameters as for toluene, in accordance with the low average dielectric constant within the interior of proteins.[171–173] Spin-orbit coupling was included using the one-electron mean-field/effective potential approach. To ensure proper description of the core electrons, the accuracy of the radial integral grid in the vicinity of the Fe-atom was increased to Orca's grid 7. All calculations were performed using Orca, version 3.0.3.[174] The geometry employed in the calculations was based on the PDB entry 2FRJ for MbNO and dissociated, but not domed Mb calculations, for which the NO was removed, and PDB entry 2V1K for deoxyMb calculations. Figure 5-4 overlays the structure of MbNO (red, PDB entry 2FRJ) and deoxyMb (green, PDB entry 2V1K) used in the present work. This highlights the main (as expected) structural differences that are probed in the ultrafast XES study.

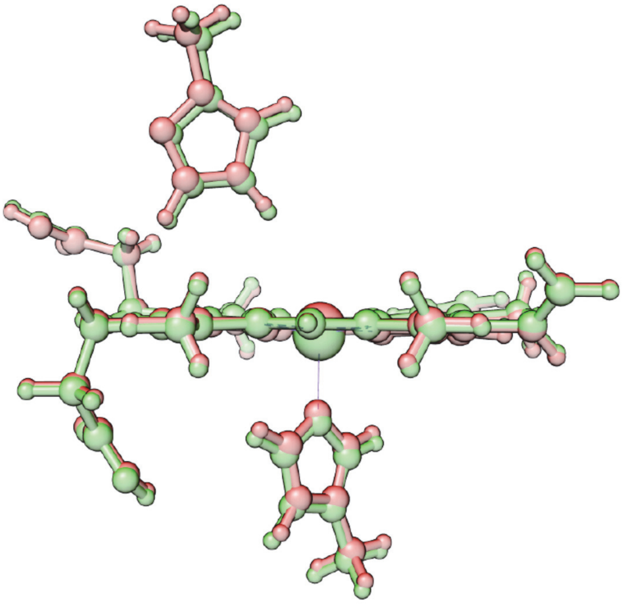

Figure 5-4: Overlaid structure of MbNO without NO (red, PDB: 2FRJ) and of deoxyMb (green, PDB: 2V1K).

Figure 5-14b shows the DFT simulated static Kα XES for MbNO (doublet), deoxyMb (quintet) and deoxyMb (triplet) and compares them to experimental laser-on spectra in Figure 5-14a. It is stressed that the DFT calculations do not reproduce absolute energies and the presented spectra are shifted for comparison to the experimental data. Furthermore, we do not reproduce the asymmetry on the red side of the spectral lines. This is due to the fact the DFT functional used here does not fully account for multi-electron correlations, which are responsible for the sidebands, as shown in multiplet calculations.[175] Therefore, while full line shapes do show deviations between theory and experiment, the relative changes reproduce the experimental trends, as seen in Figure 5-5 where changes in peak intensity and shifts between the deoxyMb and MbNO experimental spectra are compared with the calculated ones.

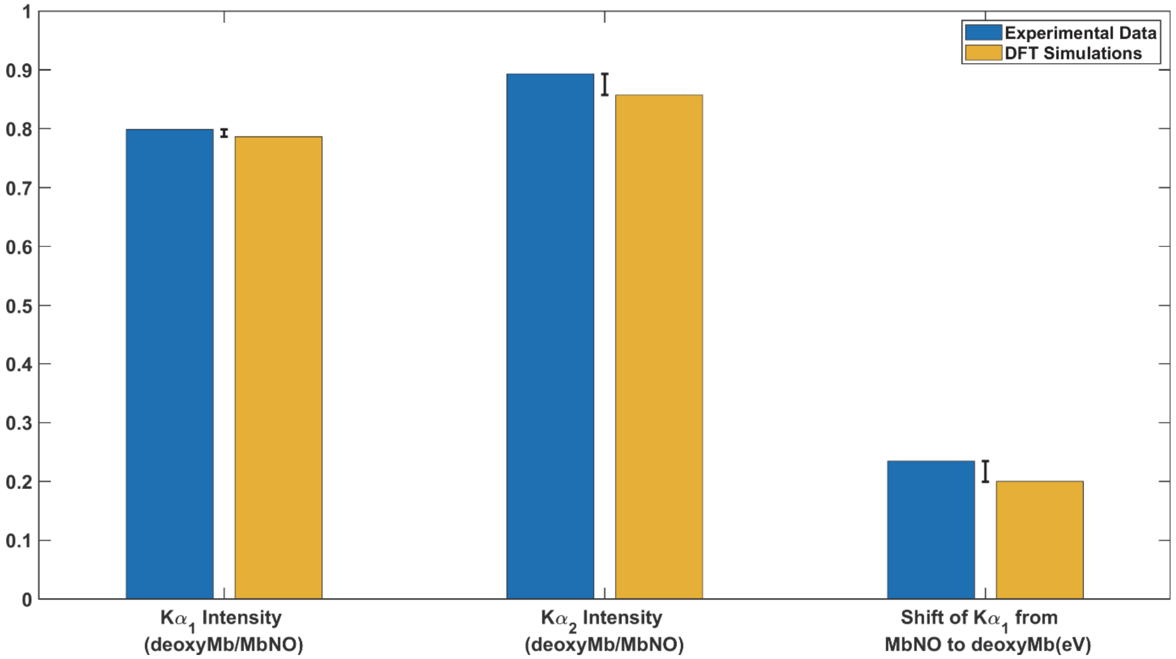

Figure 5-5: Comparison of relative ratios between deoxyMb and MbNO of the $K_{\alpha 1}$ intensity (left), the $K_{\alpha 2}$ intensity (middle) and the shift of $K_{\alpha 1}$ from deoxyMb to MbNO for experimental (blue) and DFT (orange) XES Kα spectra and the standard-deviation (STD) between the experimental results and DFT simulations are shown in between. This serves as benchmark of the DFT simulations, showing that relative changes in the spectra reproduce well the experimental trends.

5.2.7 Estimation of the Photodissociation Quantum Yield

To obtain meaningful difference spectra for K_β XES, we first estimate the photodissociation quantum yield and use it in the section below to calculate the difference spectra for comparison with our results. Considering the absorbance of MbNO in physiological solution at 533 nm (Figure 4-6), we obtain a ratio of photons per molecule of 2-3 and therefore assume that each MbNO absorbs at least one photon. Therefore we refer to the photodissociation quantum yield as the probability of ligand dissociation at time zero.From the K_β reference spectra of different spin states from Zhang et al,[161] one can obtain a shift of 1.6 eV for $K_{\beta_{1,3}}$ for a spin change from doublet to quintet state. For the case of MbNO this would mean that in the case of a photodissociation quantum yield of 100% we would expect the same energy shift. Taking the laser-on spectrum of MbNO at 1.36 ps delay, we observe a shift of ~0.45 eV for the $K_{\beta 1,3}$ line. Trying different ratios of doublet:quintet for the reference spectra from Zhang et al,[161] we obtain a shift of 0.45 eV from the doublet to doublet/quintet spectra with a ratio of 45:55 (doublet/quintet), which corresponds to a photodissociation quantum yield of 55%. This is in good agreement with the 50 ± 5% reported in the literature[84] and is therefore used in the next section to calculate the XES K_α and K_β difference spectra to be compared to our transient spectra for MbNO.

5.2.8 Derivation of the K_α and K_β Difference Spectra

The triplet and quintet difference spectra in Figure 5-11b are derived using data from ref.[161]. For the triplet state the XES K_β spectrum of Iron(ii)-phthalocyanine was used ($I_{triplet}$). The [Fe(phenanthroline)$_2$(NCS)$_2$] XES K_β spectrum represents the quintet state spectrum ($I_{quintet}$) and for the doublet ground state, the XES K_β spectrum of [Fe(2,2'-bipyridine)$_3$]$^{3+}$ was used. First the excited state spectra are calculated using a photodissociation quantum yield of 55%:

$$ES_{quintet} = 0.45 * I_{doublet} + 0.55 * I_{quintet}$$

Equation 5-3

$ES_{quintet}$ corresponds to the expected excited state spectrum for MbNO (deoxyMb) (quintet excited state), $I_{doublet}$ are the intensity values of the spectrum of ([Fe(bpy)$_3$]$^{3+}$) representing 100% doublet state and $I_{quintet}$ are the intensity values of the spectrum of ([Fe(Phen)$_2$(NCS)$_2$]) representing 100% quintet state. Afterwards the difference spectra are calculated:

$$quintet_{difference} = ES_{quintet} - I_{doublet}$$

Equation 5-4

to obtain the quintet difference spectrum ($quintet_{difference}$). For the triplet state pump-probe spectrum the same was done using the triplet state XES K_β spectrum of (iron(ii) phthalocyanine) from ref.[161]. The same procedure was used to obtain the triplet and quintet K_α transient spectra in Figure 4 using DFT simulated spectra (see 5.2.6) since experimental reference spectra are lacking for the K_α emission.

5.2.9 Error Analysis

The uncertainties on all time constants represent the 1-sigma uncertainty. The error bars in the time traces represent the 1-sigma uncertainty of the Gaussian fit.

All XES K_β data, the XES K_α transients at 0.26 ps and the data presented in Figure 5-15. Figure 5-16 and Figure 5-18 are smoothed using a 5-point moving average filter to make trends more visible. The first and last few elements of yy follow:

yy(1) = y(1)
yy(2) = (y(1) + y(2) + y(3))/3
yy(3) = (y(1) + y(2) + y(3) + y(4) + y(5))/5
yy(4) = (y(2) + y(3) + y(4) + y(5) + y(6))/5
...

Figure 5-6 and Figure 5-7 show the XES K_β and K_α spectra, respectively, with their error bars, calculated from the standard deviation of the scans acquired. This clearly shows that the observed trends are larger than the noise of the experiment.

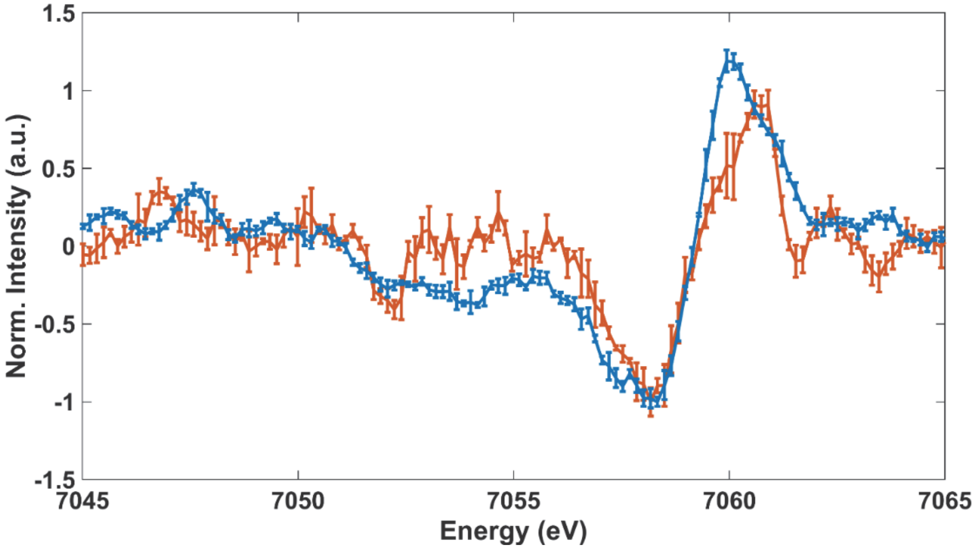

Figure 5-6: Transient K_β XES spectra of MbNO at 0.26 (red) and 1.36 ps (blue). The 0.26 ps spectrum represents predominantly triplet state species and the 1.36 ps spectrum the quintet state. Both are normalized to the maximum of the negative signal. The error bars are the standard deviation between the runs.

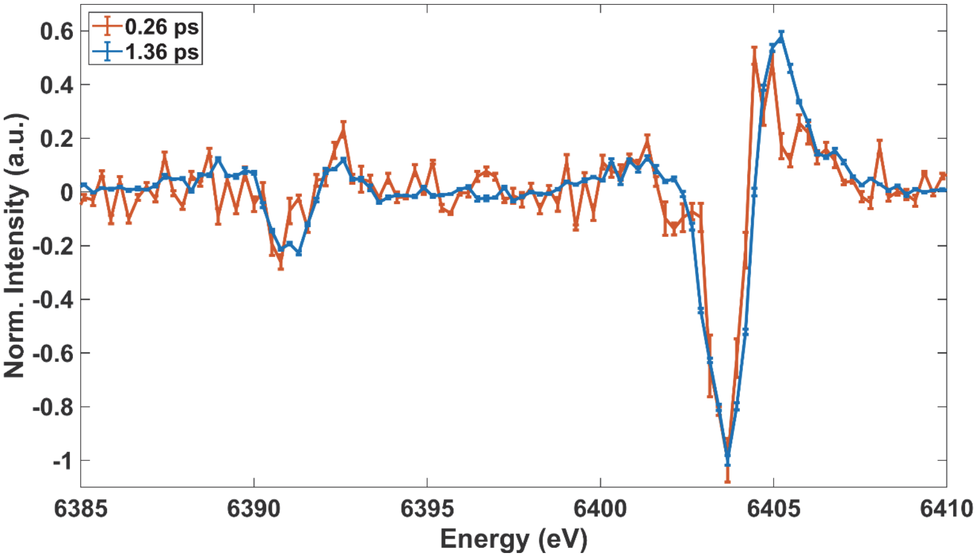

Figure 5-7: Transient K_α XES spectra of MbNO at 0.26 (red) and 1.36 ps (blue). The 0.26 ps spectrum represents predominantly triplet state species and the 1.36 ps spectrum the quintet state. Both are normalized to the maximum of the negative signal. The error bars are the standard deviation between the runs.

5.3 Results and Discussion

We find that upon 533 nm photoexcitation of MbNO into the Q-band (Figure 4-6), the transition from the ground state LS (S=1/2) MbNO[49] to the HS (S=2) deoxyMb involves an SCO in 500-800 fs via an intermediate spin state, while the return from the deoxyMb-NO to the MbNO takes place in ~30 ps and is a reverse SCO. Along with density functional theory (DFT) calculations, we establish for the first time the details of domed HS deoxyMb formation, which we argue is of general validity to all Mb's, and we identify the return to the initial MbNO ground state also as a HS-LS relaxation.

Just as in previous ultrafast[161,162] or quasi-static[176] XES studies, the assignment of spin states relies on the comparison with model compounds. Figure 5-8 shows the steady state K_β emission spectra of MbNO and deoxyMb and those of ferric $[Fe(bpy)_3]^{3+}$ (S=1/2) and of $[Fe(phen)_2(NCS)_2]$ (S=2).[161]

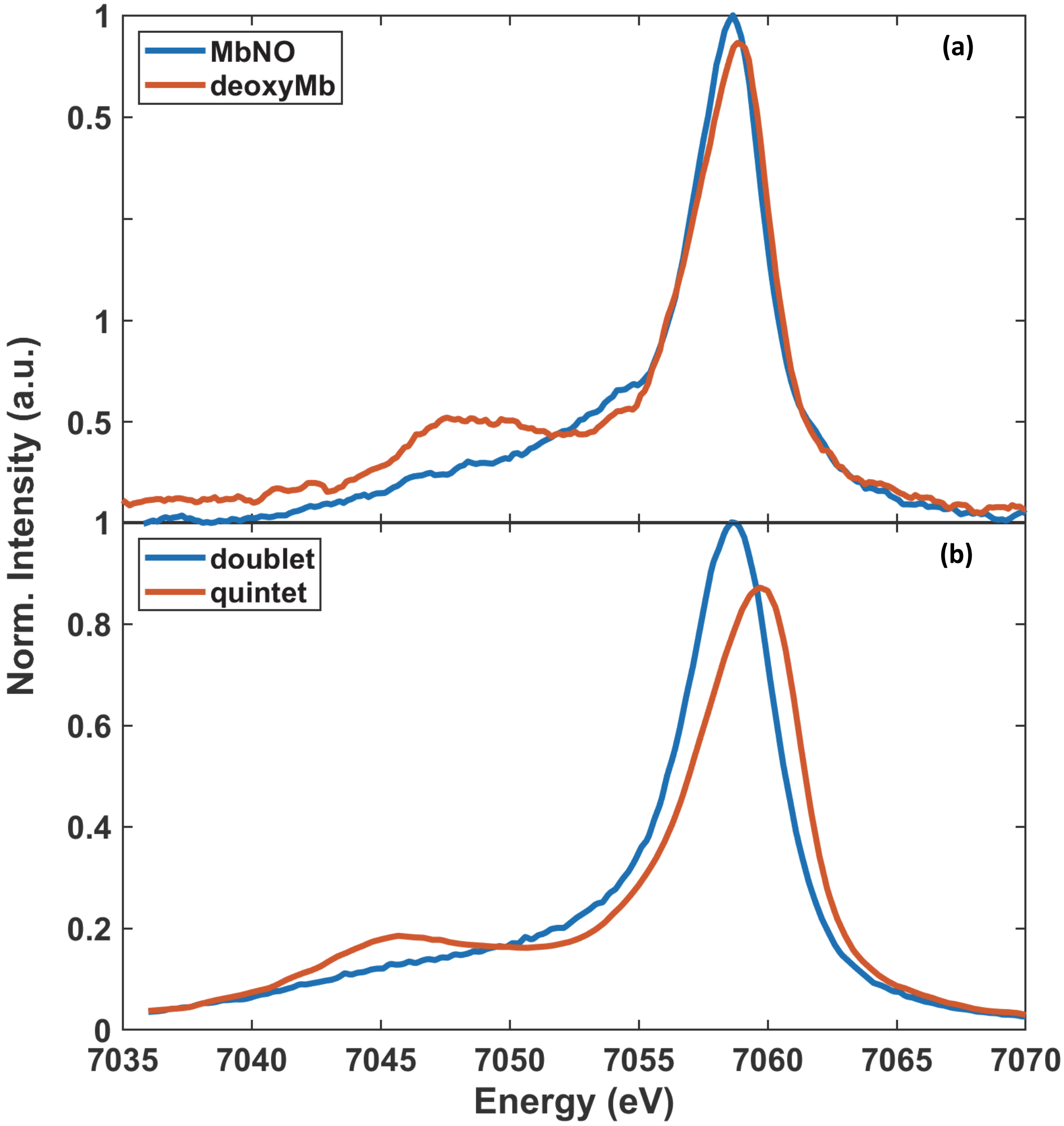

Figure 5-8: a) Steady-state XES K_β spectra of deoxyMb (S=2) and MbNO (S=1/2) measured at Eu-XFEL and SACLA, relative to the peak maximum of MbNO normalized to 1. b) Reference XES K_β spectra of ground state $[Fe(2,2'\text{-bipyridine})_3]^{3+}$ (S=1/2) and $[Fe(phenanthroline)_2(NCS)_2]$ (S=2) reproduced from ref.[161]

The two sets show identical trends with the HS spectrum of deoxyMb showing a more prominent and broader, so-called, $K_{\beta'}$ line around 7045 – 7050 eV and a weak blue shift of the $K_{\beta1,3}$ line near 7058 eV. We recorded the laser-off and laser-on K_{β} spectra at different time delays, see Figure 5-9, while Figure 5-10b zooms into the region of the $K_{\beta1,3}$ peak, which shows a clear blue shift within the first ps. Figure 5-10a zooms into the region of $K_{\beta'}$ and shows an intensity decrease in the region of 7051 – 7056 eV within the first ps and a positive dip at 7047 – 7048 eV at 1.36 ps.

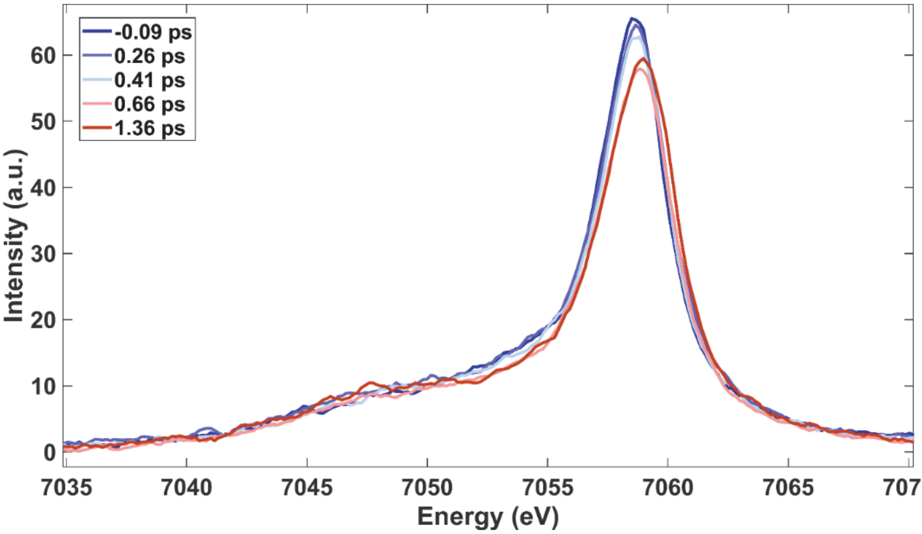

Figure 5-9: Laser-on (pumped) K_{β} XES spectra of MbNO at different time delays between -0.09 and 1.36 ps (from blue to red) showing a blue shift of the $K_{\beta1,3}$ line and an intensity decrease. The peak shifts, smaller than the energy resolution (~0.5 eV), are visible (see also Figure 5-10).

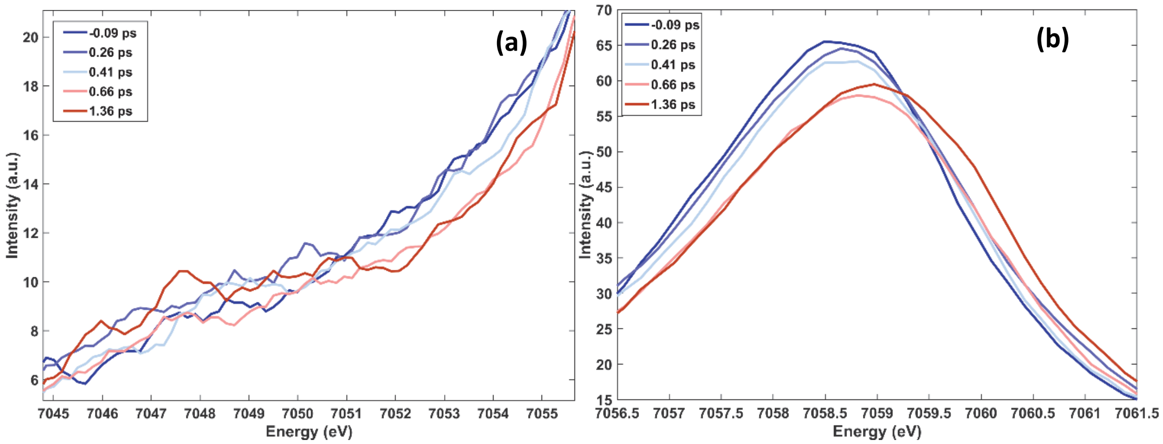

Figure 5-10: Zoom into the laser-on (pumped) $K_{\beta_{1,3}}$XES spectra of MbNO at different time delays between -0.09 and 1.36 ps (from blue to red) showing peak shifts smaller than the energy resolution of our experiment.

Figure 5-11a shows the transient K_{β} XES spectra (excited minus ground state signal) of MbNO 0.26 ps and 1.36 ps after excitation, and Figure 5-12 shows additional transients at early times, and up to 100 ps.

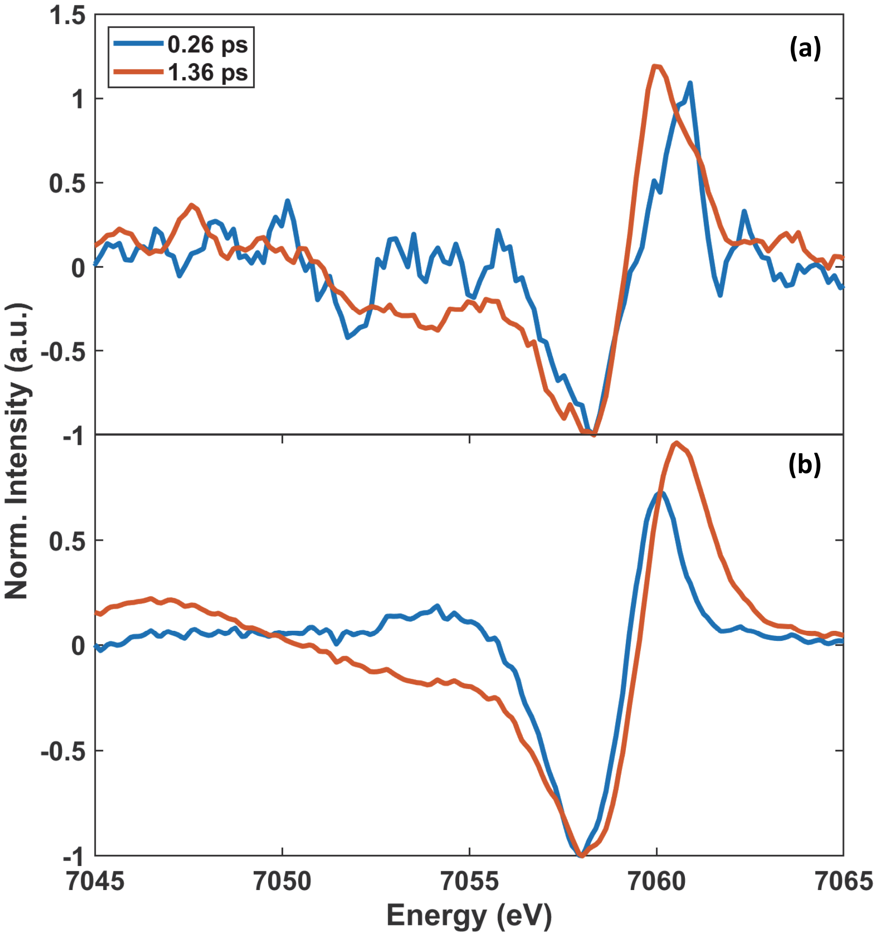

Figure 5-11: (a) Transient XES K_β spectra of MbNO in a physiological solution at pump-probe time delays of 0.26 and 1.36 ps. (b) Difference of steady-state XES K_β spectra from ref.[161]: triplet minus doublet (blue), quintet minus doublet (red), using the reference spectra of Fe(II)phthalocyanine (triplet state), $[Fe(2,2'\text{-bipyridine})_3]^{3+}$ (doublet state) and $[Fe(\text{phenanthroline})_2(NCS)_2]$ (quintet state), and taking into account NO dissociation quantum yield (Details can be found in § 5.2.8).

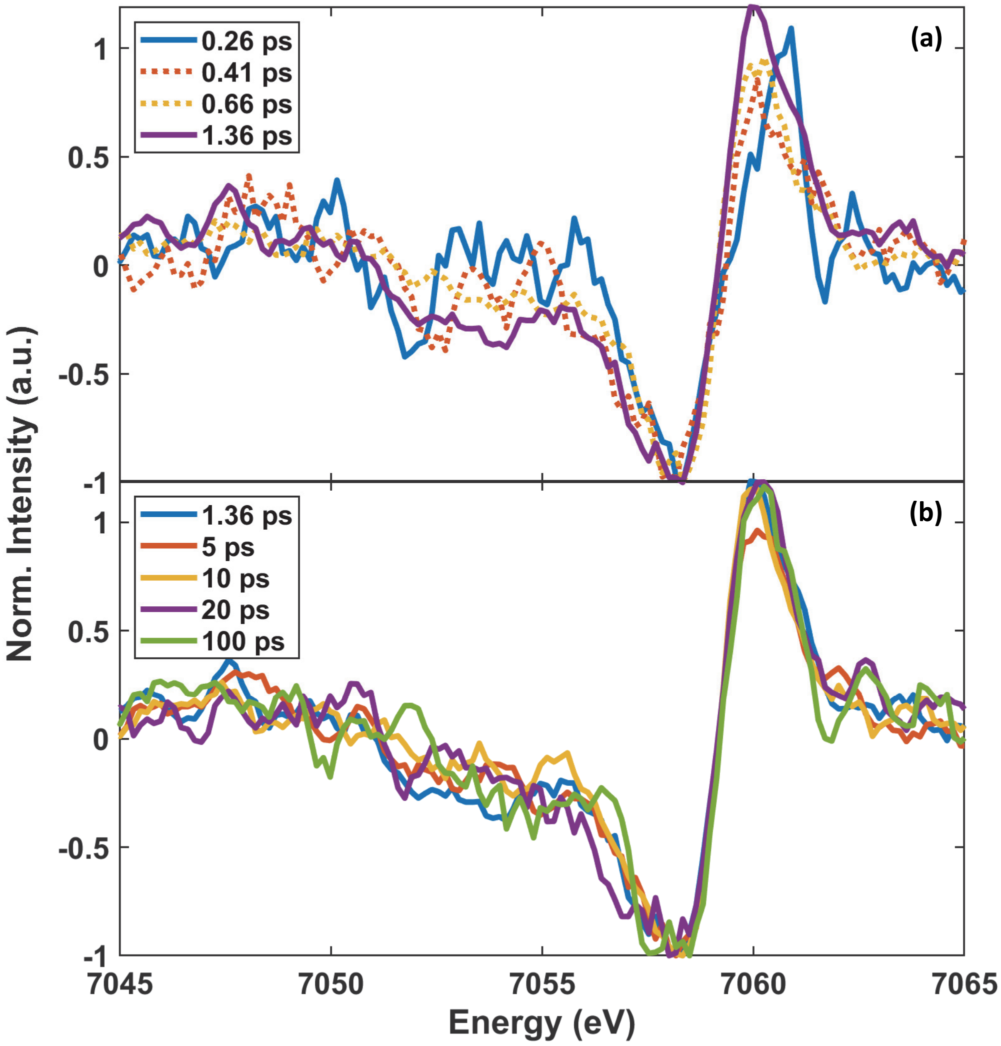

Figure 5-12: (a) Transient K_β XES spectra of photoexcited MbNO between 0.26 and 1.36 ps (normalized to the maximum of the negative signal). (b) same for transients between 1.36 and 100 ps.

These exhibit a derivative-like shape near 7058 keV, a negative signal that extends down to 7050 eV and a positive one below. The 7050-7057 eV region shows a gradual increase of negative amplitude from 0.26 to 1.36 ps (Figure 5-11a and Figure 5-12a), which stabilizes at times >1 ps (Figure 5-12b). These trends are in agreement with the static difference spectra of Fe-complexes of different spins (reproduced in Figure 5-11b),[161] that were used to demonstrate that the photoinduced SCO in $[Fe(bpy)_3]^{2+}$ proceeds via a triplet state. [161] From the comparison of our results with those of ref.[161], we conclude that here, a predominantly triplet excited state is transiently populated in ~0.3-0.5 ps. The 7057.5-7062.5 eV region (Figure 5-11a and Figure 5-12a) shows the positive feature around 7060 eV gradually shifting red by ~1 eV and stabilizing for t ≥ 1 ps. This shift is opposite to the case of Figure 5-11b, even though the laser-on spectra are shifting blue (Figure 5-9 and Figure 5-10). We attribute this difference to the ligand dependence of the K_β emission line both in peak position and shape (Figure 5-13).[136]

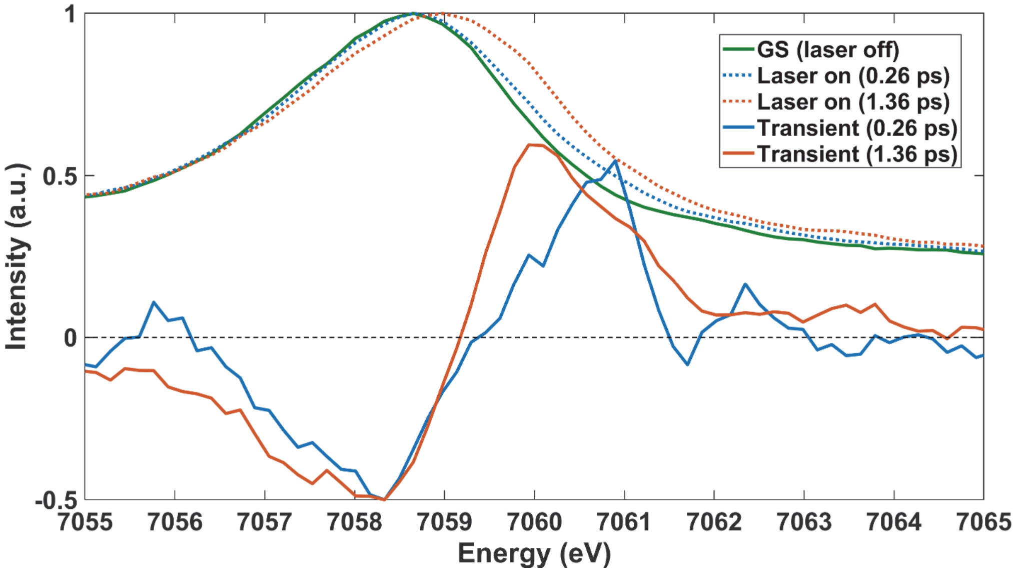

Figure 5-13: Normalized Laser-off and Laser-on (pumped) $K_{\beta_{1,3}}$XES spectra of MbNO at 0.26 ps and 1.36 ps time delays, highlighting the overall blue shift of the maximum. However, the transients exhibit a red shift of the maximum from 0.26 to 1.36 ps. This is due to different line shapes of the 1.36 ps and the 0.26 ps laser-on spectra (see region 7059 to 7062 eV).

The important point here is that the evolution of the 7057.5-7062.5 eV region in Figure 5-11a and Figure 5-12 shows that the final spin state requires ~1 ps to be formed after ligand detachment.

Further support in favour of an intermediate spin state comes from the K_α XES transients. The steady-state K_α lines of MbNO and deoxyMb are shown in Figure 5-14a.

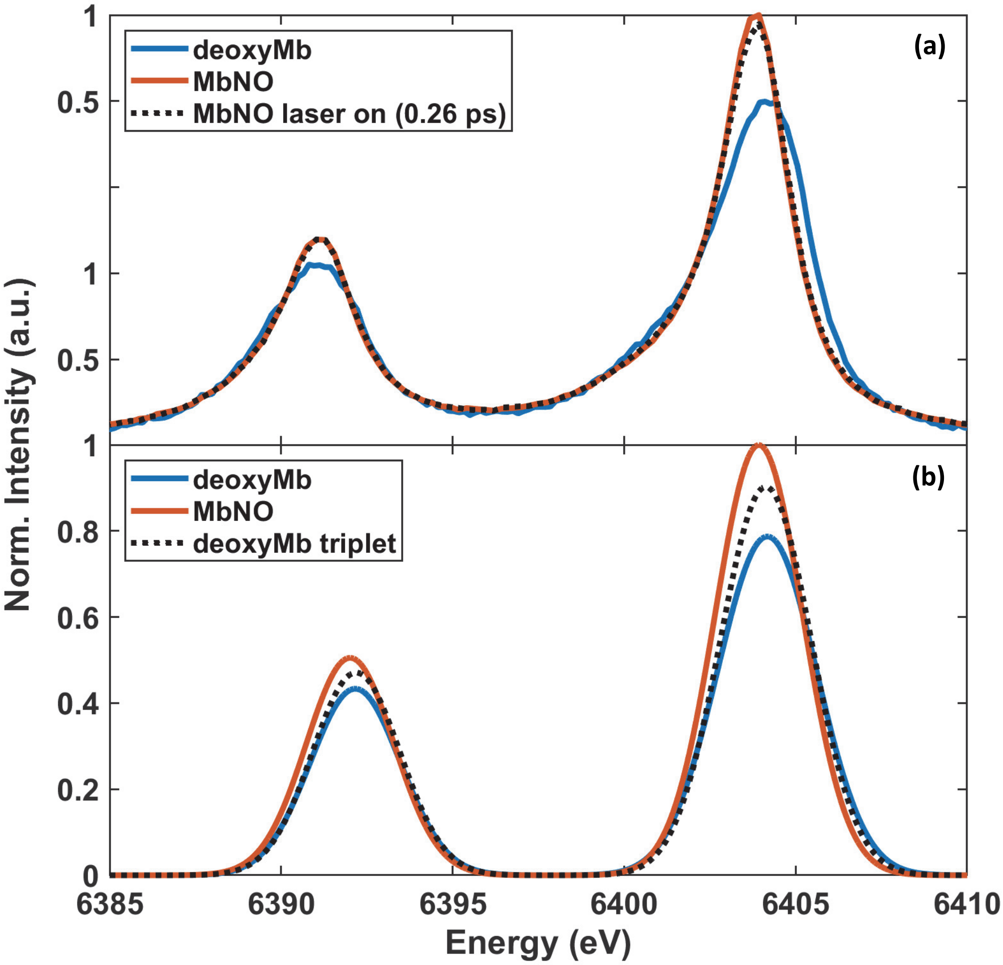

Figure 5-14: (a) Experimental Fe Kα spectra of ground state deoxyMb (S=2) and MbNO (S=1/2) and of the laser-on MbNO spectrum at 0.26 ps after excitation, all normalized relative to the peak maximum of the ground state MbNO spectrum. The Kα1 line is near 6404 eV and the Kα2 line is near 6391 eV. (b) DFT simulated XES Kα spectra of deoxyMb, MbNO and deoxyMb triplet state, all shifted by +86.3 eV and normalized relative to the peak maximum of the MbNO spectrum. In (a), the 0.26 ps contains both the XES of the ground state MbNO and of the triplet deoxyMb.

Note the intensity decrease and slight blue shift and broadening of the $K_{\alpha 1}$ line with increasing spin, as reported for other compounds,[136,163] while the $K_{\alpha 2}$ line undergoes an intensity weakening and a slight broadening. Because K_{α} reference spectra are lacking, we resorted to *density functional theory* (DFT) to simulate them (see § 5.2.6).

We first simulated the S=1/2 MbNO and S=2 deoxyMb spectra, which show similar trends to the experimental ones (Figure 5-14b and Figure 5-5). We also simulated the K_{α} spectrum of the triplet state of deoxyMb, which is intermediate to the LS and HS cases (Figure 5-14b). Laser-on K_{α} spectra at different time delays are shown in Figure 5-14 and Figure 5-15, while Figure 5-16 zooms into the region of their maxima.

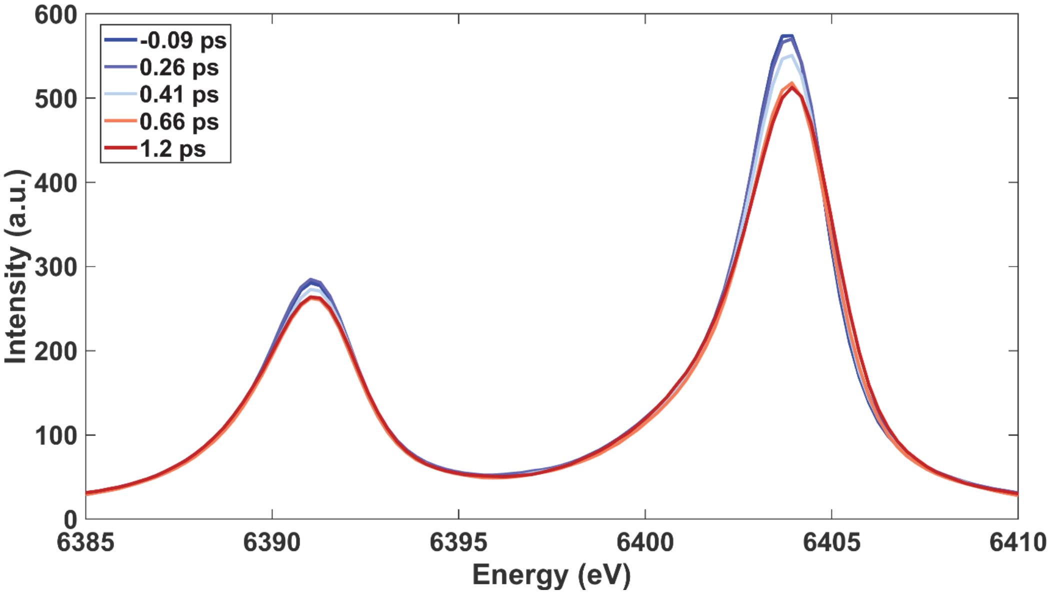

Figure 5-15: Laser-on (pumped) K_{α} XES spectra of MbNO at different time delays between -0.09 and 1.36 ps (from blue to red) showing an intensity decrease for $K_{\alpha2}$ over the first 1.2 ps after excitation and an intensity decrease and change in peak width for $K_{\alpha1}$. Also, the visibility of changes in peak width (σ) smaller than the energy resolution (~0.6 eV) can be well observed.

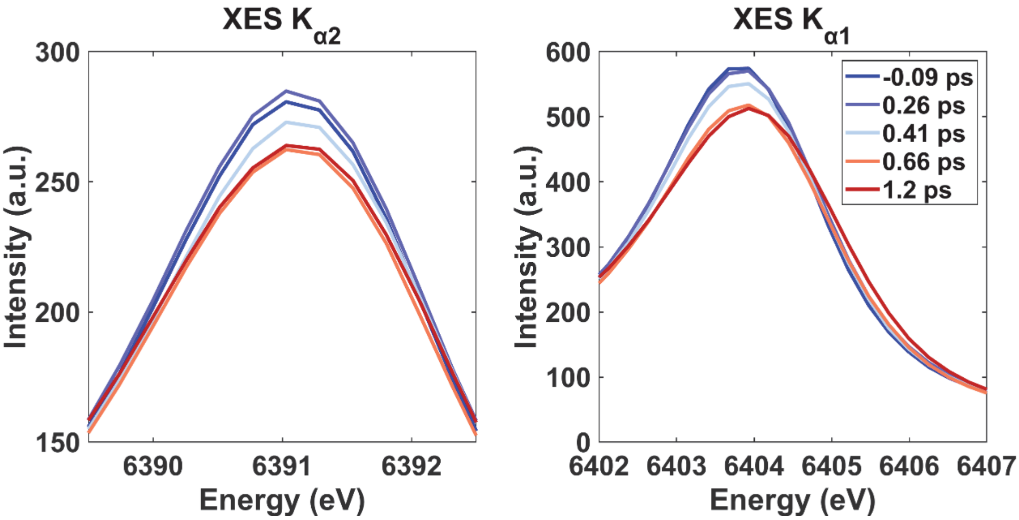

Figure 5-16: Zoom into the $K_{\alpha2}$ and $K_{\alpha1}$ laser-on (pumped) XES spectra of MbNO at different time delays between -0.09 and 1.36 ps (from blue to red) showing an intensity decrease for $K_{\alpha2}$ over the first 1.2 ps after excitation and an intensity decrease and change in peak width for $K_{\alpha1}$. Also, the visibility of changes in peak width (σ) smaller than the energy resolution (~0.6 eV) can be well observed.

One notices a clear gradual weakening and a slight broadening of the bands within the first ps, after which the spectra no longer evolve. The experimental K_{α} XES transients at 0.26 and 1.36 ps time delay are shown in Figure 5-17 and Figure 5-18, while those at intermediate times and at later ones are shown in Figure 5-19.

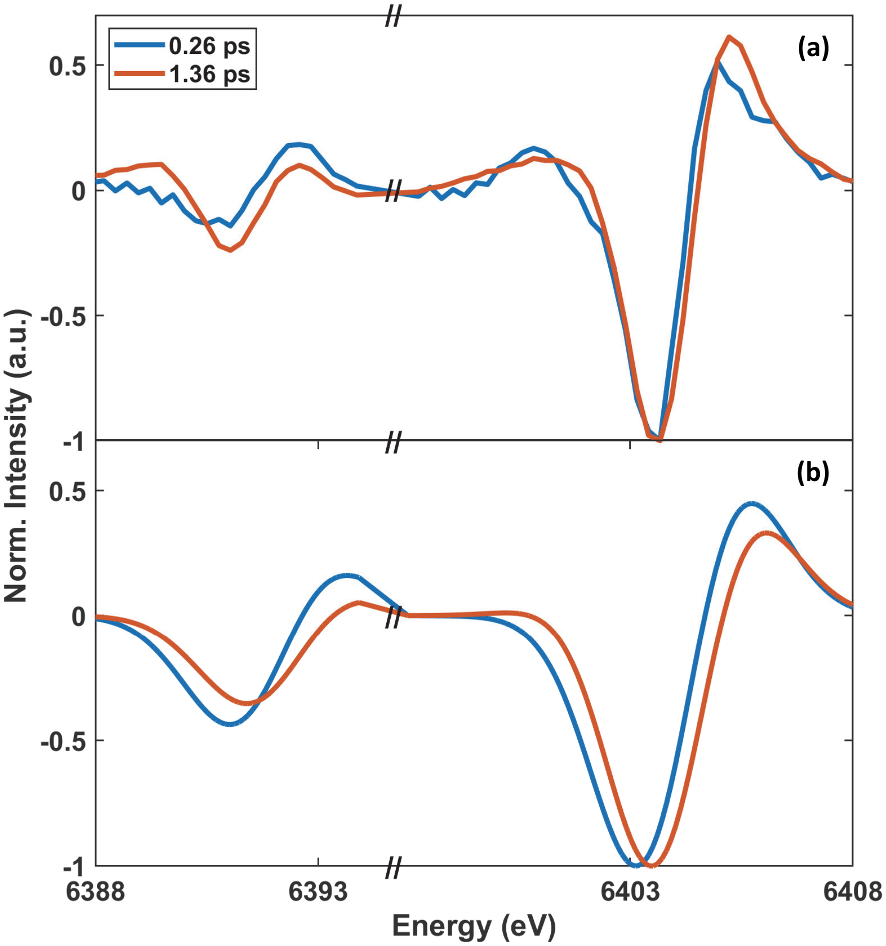

Figure 5-17: (a) Transient XES K_{α} spectra at 0.26 and 1.36 ps showing a blue shift of the positive $K_{\alpha1}$ transient feature (6405 eV) from 0.26 ps to 1.36 ps, and the presence of a positive dip at 6393 eV at 0.26 ps, which vanishes for later times (1.36 ps). (b) XES K_{α} difference spectra derived from DFT simulated XES K_{α} spectra: triplet minus doublet (blue), quintet minus doublet (red). Details can be found in § 5.2.8.

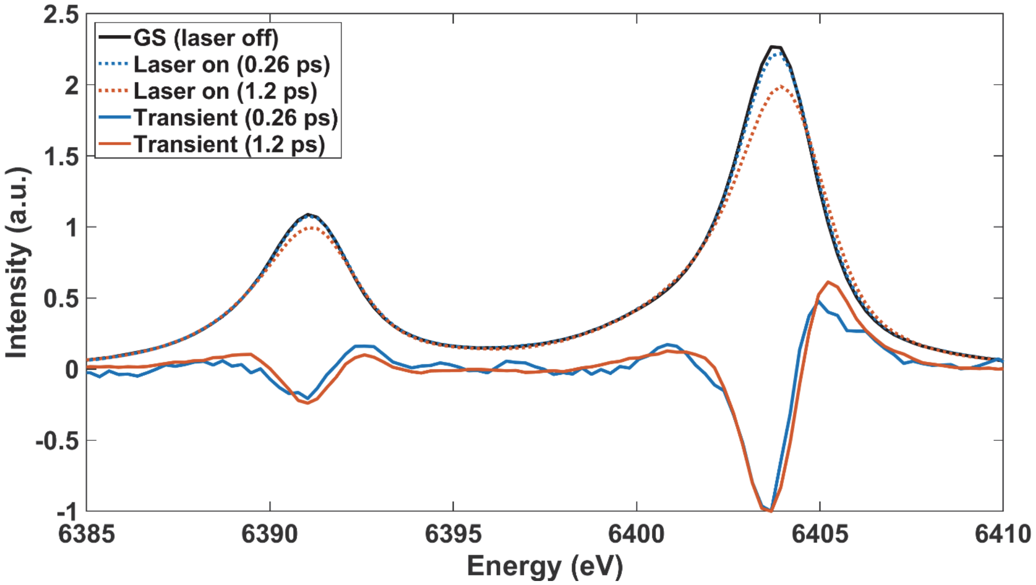

Figure 5-18: Laser-on (pumped) K_α spectra of MbNO at 0.26 ps (blue), representing mainly triplet state population and at 1.36 ps (red), representing mainly quintet state population and the corresponding transient spectra. In black is the ground-state spectrum of MbNO shown.

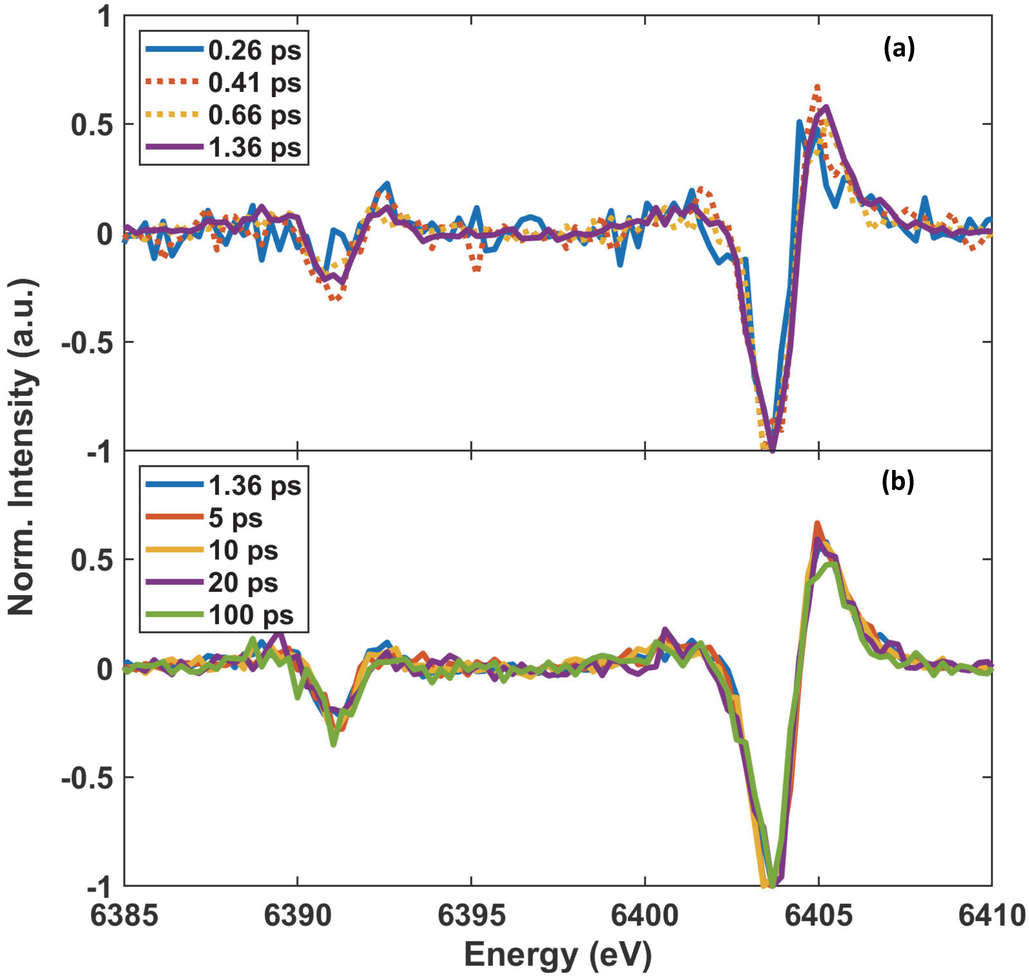

Figure 5-19: (a) Transient K$_\alpha$ XES spectra of MbNO between 0.26 and 1.36 ps (normalized to the maximum of the negative signal). (b) same for transients between 1.36 and 100 ps.

The transient line shapes reflect the broadening and intensity changes of the asymmetric emission lines, which do not change beyond ~1 ps, at which time the system is in the HS state, as confirmed by the difference of experimental steady state spectra deoxyMb minus MbNO (Figure 5-20).

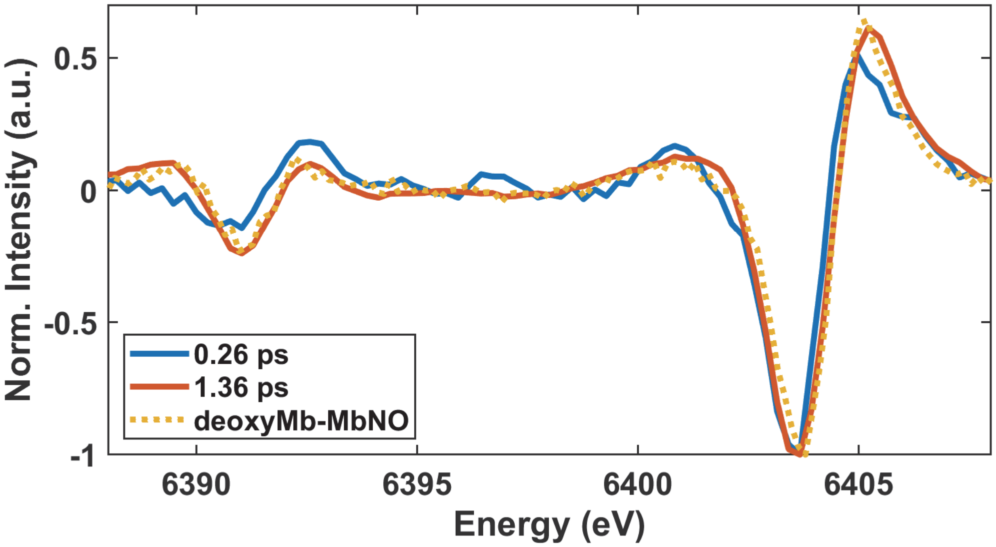

Figure 5-20: Transient XES K_α spectra at 0.26 and 1.36 ps showing a blue shift of the positive $K_{\alpha1}$ transient feature (6405 eV) from 0.26 ps to 1.36 ps, and the presence of a positive dip at 6393 eV at 0.26 ps, which vanishes for later times (1.36 ps). In yellow (dotted) the static difference signal of deoxyMb-MbNO is plotted, which resembles the spectrum at 1.36 ps. This indicates structural and electronic similarity of the excited state after ~1 ps and the deoxyMb.

The difference of simulated triplet minus doublet and quintet minus doublet spectra, show a similar trend (Figure 5-17b) as the experimental transients, further supporting the above conclusion of a transiently populated triplet state. In summary, both the K_α and K_β XES transients point to an intermediate triplet state being populated within <500 fs time delay, while the HS deoxyMb state is fully formed by ~1 ps.

The signal around 7053 eV in the transient XES K_β spectra of MbNO at short and long times (Figure 5-11 and Figure 5-12) best differentiate the triplet from the quintet state. By plotting its amplitude as a function of time for the transients available up to 3.6 ps, we can roughly estimate the triplet state lifetime, using a 3-level kinetic model (§8.3.1 and Figure 5-21), assuming 100% Q-state population at t=0, decaying to the triplet state in ~100 fs[59]. This yields a triplet lifetime of 500 ± 250 fs (Figure 5-22 and Figure 5-23).

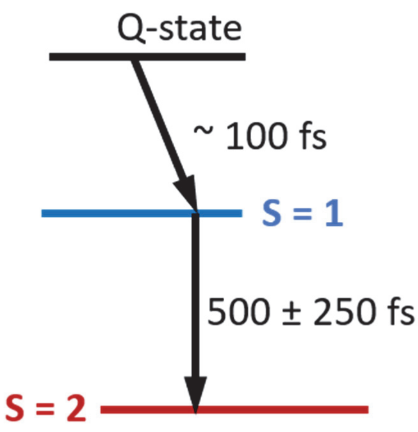

Figure 5-21: Energy level diagram showing the S=1/2, 1 and 2 states and the Q-state of the porphyrin with arrows indicating the relaxation pathways and their corresponding rates. The ~100 fs decay of the Q-state is taken from fluorescence up-conversion measurements and fixed for the kinetic model[59], the 500 ± 250 fs is derived from the kinetic model (see § 8.3.1).

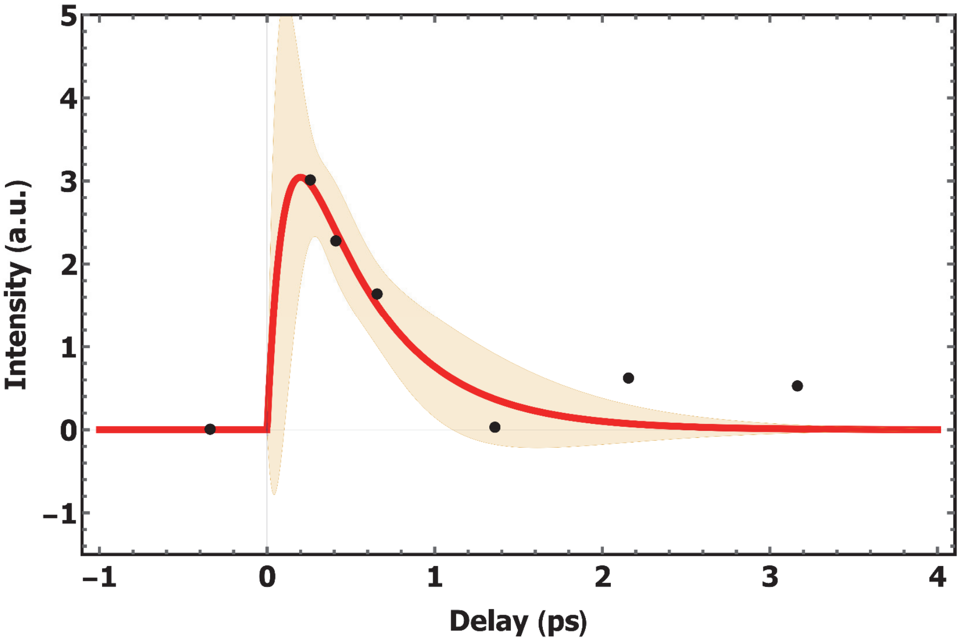

Figure 5-22: Plotted are the mean of seven points (7053.0 to 7054.0 eV) of the K_β XES pump-probe spectra (Figure S6) in the time range of 0.26 to 3.16 ps (black dots) and the fit (red) together with the 90% confidence bands (orange shade). See § 8.3.1 for details about the kinetic model.

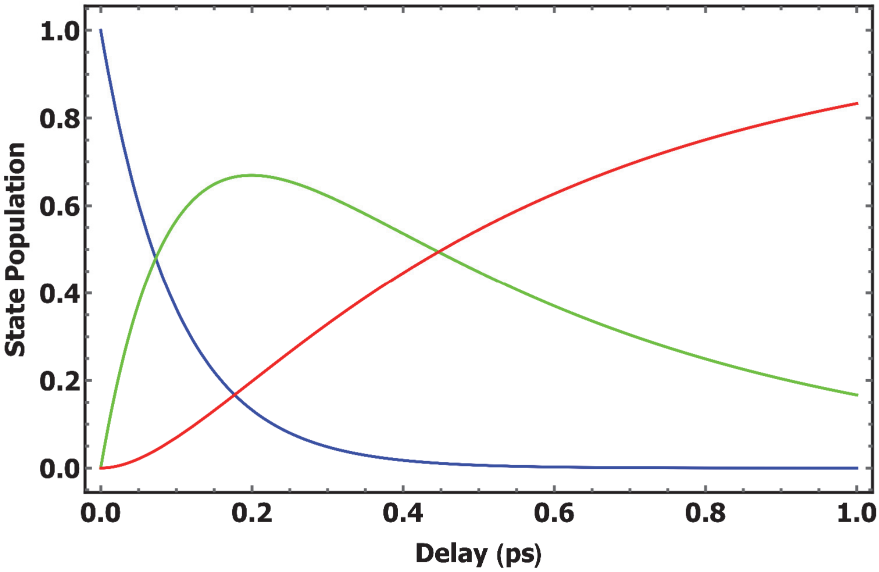

Figure 5-23: Displays the population dynamics obtained from the kinetic model (see § 8.3.1) after t_0 of $\rho_{Q\text{-state}}[t]$ (blue), $\rho_{Triplet}[t]$ (green) and $\rho_{Quintet}[t]$ (red).

Further details into the ultrafast kinetics comes from the peak position of the XES $K_{\beta 1,3}$ line, which is directly sensitive to the spin state of the system.[136,161] In Figure 5-12, its shift over the first ps is affected by the mixture of doublet, triplet and quintet states and is plotted in Figure 5-24a for times up to 750 ps, while Figure 5-24b zooms into the early times, which shows a rise of 800 ± 150 fs (see § 5.2.4), significantly longer than our cross-correlation (~150 fs). The long-time trace is fitted using this rise component and two decay ones having time constants (pre-exponential factors) of τ_1 = 30 ± 9 ps (A_1=0.6) and τ_2= 1.5 ± 0.9 ns (A_2=0.4). The FWHM of the $K_{\alpha 1}$ line shows the same evolution as the shift of the K_β line (Figure 5-25 and Figure 5-26).

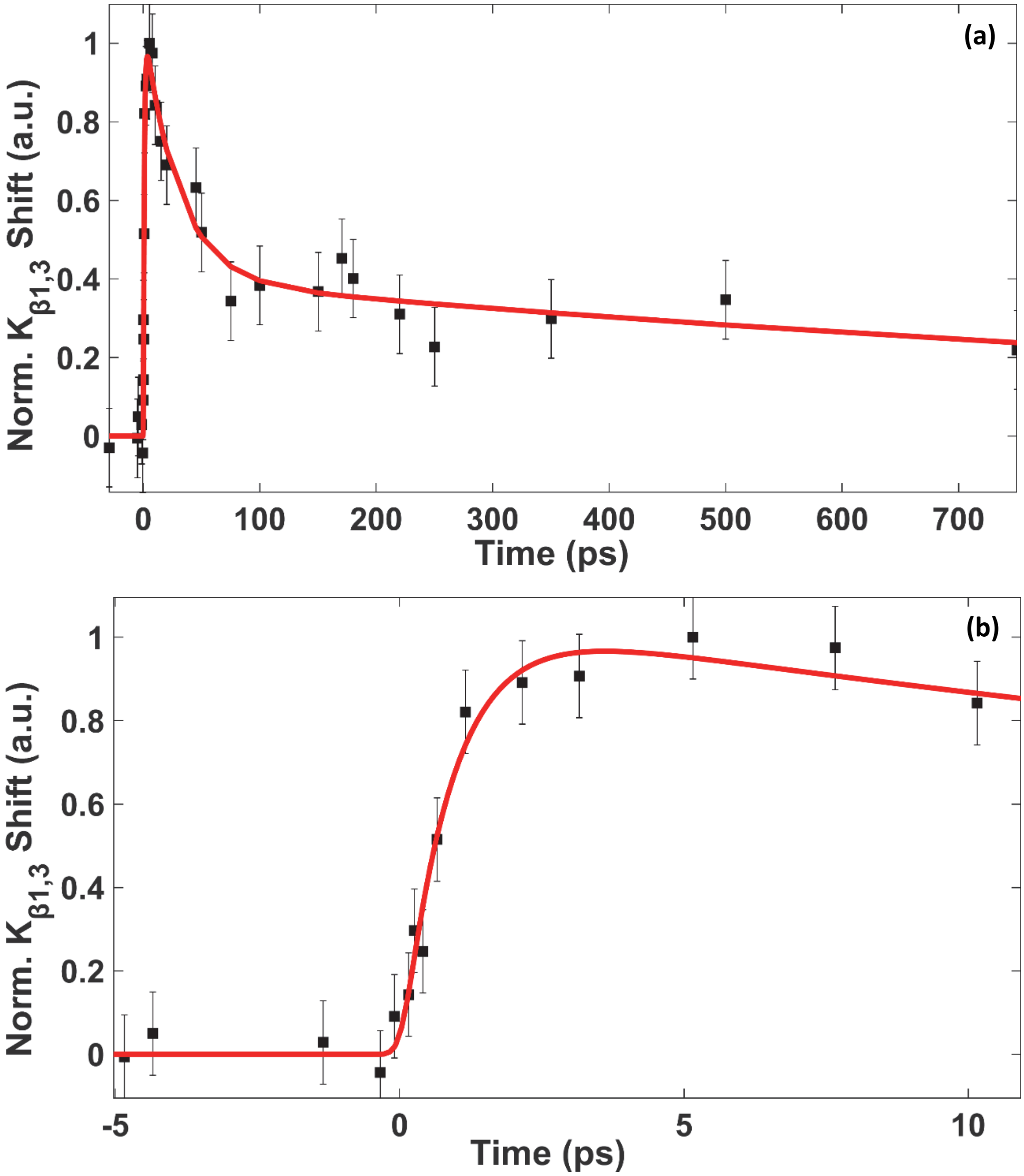

Figure 5-24: (a) Evolution of the normalized relative peak shift (of ~0.45 eV) of the XES $K_{\beta1,3}$ peak (points), fit using a biexponential function with an error function for the rise yielding decay times of 30 ± 9 ps and 1.5 ± 0.9 ns (red trace). (b) Zoom into the early times showing a rise of 800 ± 150 fs.

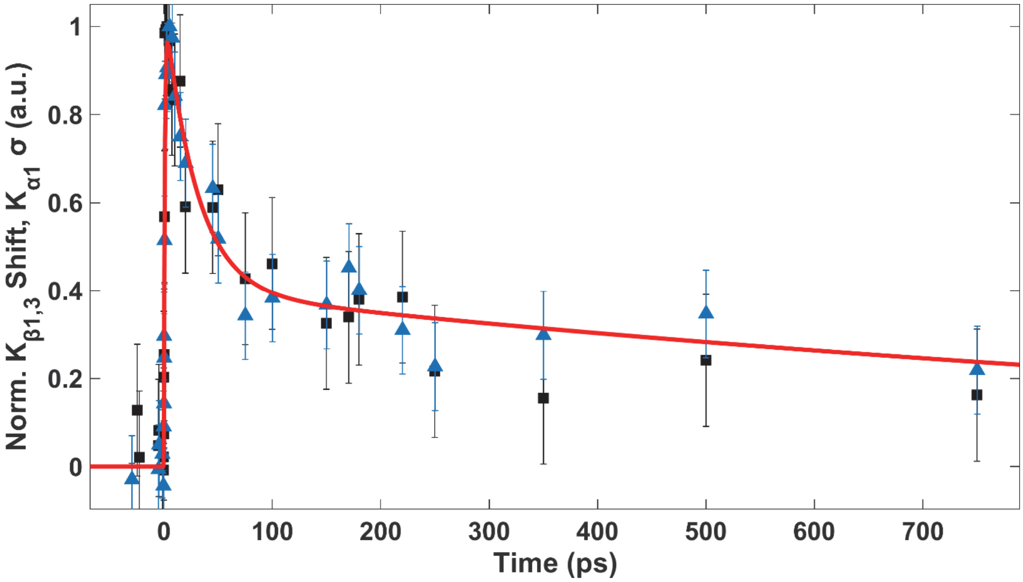

Figure 5-25: Temporal evolution of the relative $\mathrm{K}_{\beta_{1,3}}$ shift for MbNO (blue triangles, centroid obtained from Gaussian fit, max shift is ~0.45 eV, see § S6) and of the K_{α_1} peak width change for MbNO (black squares, normalized σ obtained from a Gaussian fit, maximum change in σ is ~0.3). Details are explained in § 5.2.4.

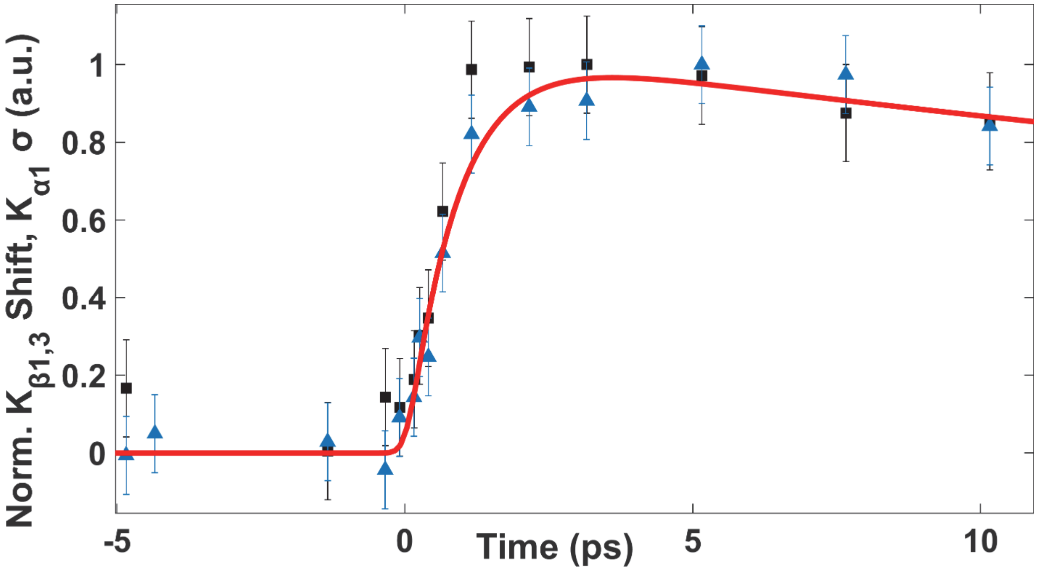

Figure 5-26: Temporal evolution at the rise of the relative $\mathrm{K}_{\beta_{1,3}}$shift for MbNO (blue triangles, centroid obtained from Gaussian fit, max shift is ~0.45 eV, see § S6) and of the K_{α_1} peak width change for MbNO (black squares, normalized σ obtained from a Gaussian fit, maximum change in σ is ~0.3). Details are explained in § 5.2.4.

Since the XES K_β line shift is sensitive to the spin state of the Fe atom, it does not distinguish between the HS deoxyMb and deoxyMb-NO species. The latter is formed by NO recombination on time scales of 10-20 ps, 130-250 ps and a weak ns (10-20%) component.[54,73,75,78,88,164] The first should appear as a rise, while the latter two as a decay because they are rate-determining to the 30 ps decay process. We refrained from extracting such times from the fits of Figure 5-24, Figure 5-25 and Figure 5-26 because the scatter of points is too large. We prefer the above phenomenological biexponential fit, which captures the important features. Namely, the decay of HS deoxyMb-NO species to LS planar MbNO in ~30 ps, directly confirming the conclusion of time-resolved resonance Raman studies.[54] However, and contrary to the latter, our results show that the process is a genuine HS to LS relaxation, as theoretically predicted by Franzen,[92] although a structural contraint[54] due to the F-helix (Figure 2-13) cannot be fully excluded. The long (ns) decay has a relatively large pre-exponential factor as it includes both geminate and non-geminate recombination of NO ligands (see ref.[88] and references therein). In summary, the entire cycle of ligand detachment and rebinding of NO to deoxyMb is accounted for by a SCO followed by a reverse SCO, as schematically depicted in Figure 5-27.

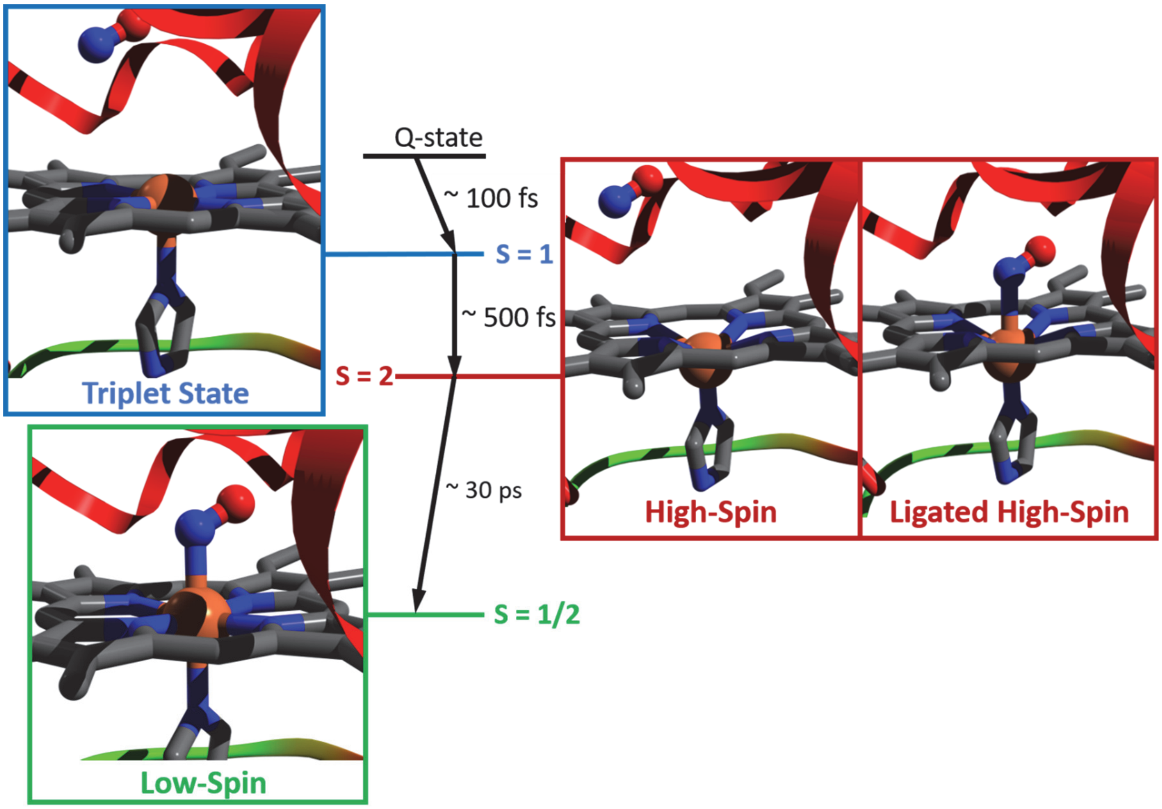

Figure 5-27: Schematic representation of the spin cross-over and reverse spin cross-over characterizing the photocycle of MbNO. The low-spin ground state MbNO (S = ½) heme undergoes prompt dissociation of NO upon π-π* excitation. The porphyrin Q-state decays to a triplet state (S = 1) of the pentacoordinated deoxyMb heme in < 100 fs. Further relaxation to the quintet state occurs in ~500±250 fs. The entire process occurs in ~800 fs. Upon recombination of NO to deoxyMb leading to a hexacoordinated HS domed heme, relaxation back to the LS planar ground state occurs in ~30 ps. The LS structure is PDB entry 2FRJ, the sizes of the Fe atom, the NO molecule and the doming are exaggerated to highlight the key changes in the photocycle. The actual structural differences between MbNO and deoxyMb are shown in Figure S1. Fe = orange, N = blue, O = red and C = grey.

5.4 Conclusion & Outlook

The above results have several implications on the description of the initial events of the respiratory function: a) upon ligand detachment, the formation of the fully domed deoxyMb requires ~800 fs, as it proceeds via an intermediate triplet state, which decays in 500 ± 250 fs; b) The ligand detachment is here mimicked by a photodissociation, which is prompt (<50 fs), implying that the ensuing dynamics are taking place in the pentacoordinated heme and should therefore be the same for all ferrous hemes involved in ligand release. In support of this conclusion, Table 2-5 compiles the time scales reported for various ligated heme proteins as well as for deoxyMb. Of note is the similarity of the two shortest time scales, which reflect formation of the HS deoxyMb.; b) Doming has been suggested to trigger large scale conformational changes of the protein, the so-called "protein quake", that opens a channel for the ligand to escape from the protein.[157,177] Our results show this is unlikely to be a very fast process, contrary to earlier claims that assumed it to occur on the time scale of the Fe out-of-plane oscillation half-period (200-300 fs);[178,179] c) In the electronic cascade via spin states,[82] the energy between them is given off in the form of heat to the environment. However, a direct electronic relaxation from the porphyrin Q-state to the ground state followed by thermal relaxation[81] is excluded.

The present works identifies the transition from the planar ligated heme involved in ligand release to the domed deoxy form as a spin cross-over, which we conclude to be identical in all ferrous heme proteins (Table 2-5). However, the ensuing events following ligand recombination are specific to the NO ligand and are characterized by a reverse SCO. This work also shows the power of ultrafast X-ray emission spectroscopy at unravelling exquisite details of the heme transformations upon ligand release and uptake in heme proteins.

Chapter 6 Femtosecond X-ray Absorption Spectroscopy of Myoglobin

In this chapter a study of the local electronic and geometric structure of MbNO in physiological medium utilizing femtosecond time-resolved XAS is presented. The data was recorded at BL3 at SACLA, Japan and Alvra at SwissFEL, Switzerland.

6.1 Introduction

The picosecond (ps) XAS study at the synchrotron Swiss Light Source (SLS) by Silatani et al.[88] revealed a transient XAS signature that was attributed to the hexacoordinated domed MbNO* (excited) transition state (Figure 6-1). Namely a small difference between the static difference (deoxyMb-MbNO) and the transients at 70 and 300 ps (shown in Figure 6-1) in the region of 7135 - 7145 eV was attributed to the presence of NO in domed state of the heme in myoglobin.[88] The weak signal difference, which is expected because NO is a weak scatterer, the low energy resolution and the insufficient time resolution of 70 ps calls for an XFEL experiment addressing those points. From the time resolved non-resonant XES study presented in Chapter 5, we concluded that doming in ligated ferrous myoglobins is a cascade among spin states and the XES time-scans revealed a ~500 fs triplet spin state lifetime and a ~30 ps long return from the quintet MbNO* spin state to the MbNO ground state (doublet, planar heme). But the investigated shifts of K_β XES and the full width half maximum (FWHM) of the K_α XES are not sensitive to the presence of the NO, but to the spin state of the metal.

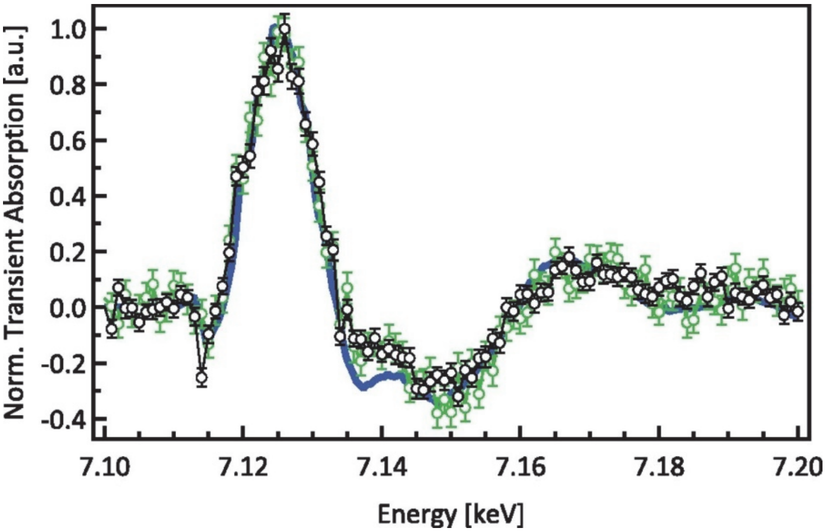

Figure 6-1: Transient XAS spectra of 3 mmol MbNO in physiological media, upon excitation at 530 nm. The normalized transient spectra recorded at 70 (black) and 300 ps (green) time delay are identical and differ from the static difference spectra (blue) of deoxyMb minus MbNO. (time resolution: 70 ps) From ref.[88]

Therefore, the following open questions remain: a) What is the timescale of NO dissociation? b) Can we observe structural signatures of any of the transition states, namely deoxyMb or hexacoordinated domed MbNO? The latter one has so far only been suggested by TR Raman studies[54] and TR-XAS with 70 ps time resolution[88]. c) Are there other sub-100 ps GR recombination or VR timescales channels which are currently unknown?

With the aim of a better insight with a better S/N and time resolution, we carried out a time-resolved femtosecond (fs) XAS study at the iron K-edge of MbNO in physiological solution (pH = 7). The structural information about the deoxyMb and hexacoordinated domed MbNO transition states can be obtained from the transient (TR) XANES, the local electronic structure from the iron XAS pre-edge[97,99] and the femtosecond to picosecond dynamics of electronic and structural changes in MbNO from XAS time-scans at different energies.

6.2 Static Reference Spectra

For comparison and to help in interpreting the transients, static XANES spectra of 4 mM physiological solutions of ferric high spin (HS) metMb (Fe^{3+}, slightly domed), ferrous HS deoxyMb (Fe^{2+}, domed) and ferrous LS MbNO (Fe^{2+}, planar) were recorded (Figure 6-2a). The XANES spectra from Lima and coworkers[94] of the same species are shown in Figure 6-2b and an overlap of the spectrum of each species with its corresponding spectrum from ref. [94] can be found in the Appendix (8.4.1) and shows good agreement. The reason why the deoxyMb spectrum in Figure 6-2a is cut off is because of liquid jet instabilities.

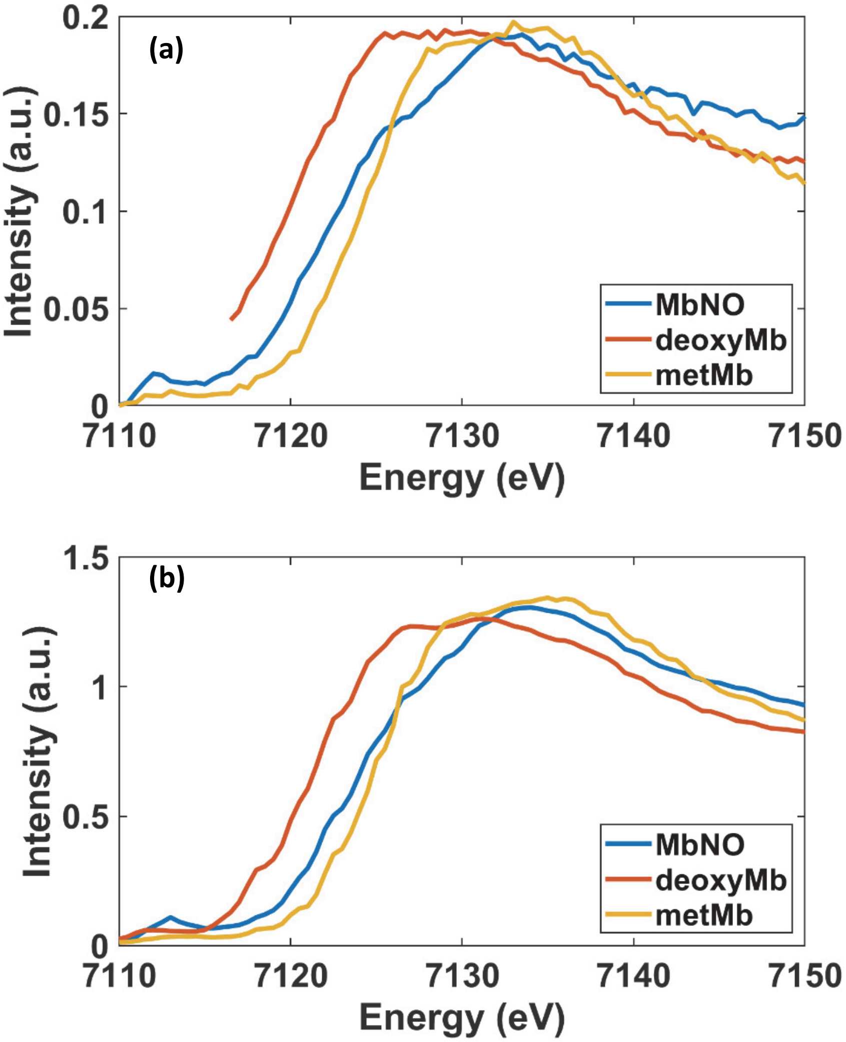

Figure 6-2: (a) Static XAS spectra measured at SACLA of MbNO, deoxyMb and metMb. The reason why the deoxy spectrum is cut off at 7117 eV is that the jet jumped at this point and the signal was lost. (b) Static XAS spectra of 4 mM physiological solution of MbNO, deoxyMb and metMb, data from Lima et al.[94]

The iron absorption edge reflects the oxidation state of the element, the ligation (both number and type of ligands) and the spin state.[176,180,181] The local structure of the heme in all three species is shown in Figure 6-3a together with the molecular orbitals of MbNO in (c) and the iron electronic structure in other myoglobins in (b). [180] The rising edge region of the XAS spectra of ferrous MbNO (S=1/2) which has a planar heme, domed deoxyMb (S=2), and ferric metMb (S=5/2), which is slightly domed are magnified in Figure 6-4a. We can see distinct shifts for all three species of myoglobin. Two of them (MbNO, deoxyMb) have formally the same oxidation state of iron (Fe^{2+}), but are different in coordination number and spin and therefore show different edge positions and shape. MetMb is different in both oxidation state (Fe^{3+})and spin state and shows the highest edge energy. This is explained by the fact that the higher the oxidation state of an atom, the stronger the

1s electrons are bound to the core, the higher K-edge energy of the (1s to unoccupied p-states).[124] Taking a closer look on the rising edge in Figure 6-4b, MbNO and deoxyMb are plotted together with the MbNO laser-on spectrum at 1 ps pump-probe delay. We can see that the MbNO laser-on (1 ps) spectrum is shifted by 1.5 eV to lower energy compared to the static MbNO spectrum. The photodissociation quantum yield for MbNO (the probability of the protein to dissociate NO at t=0 following the absorption of a single photon), was found to be 55%, from time-resolved non-resonant XES measurements (Chapter 4) and 50 ± 5 % from previous TA measurements[84]. This means that only ca. 55% of MbNO proteins will form to deoxyMb and a free NO upon laser excitation. The rest of laser excited MbNO will undergo non-radiative internal vibrational relaxation. The incomplete dissociation can be a first approximation of why the MbNO laser-on (1 ps) spectrum in Figure 6-4b lies between the deoxyMb and MbNO spectrum: at 1 ps we expect about 50% of deoxyMb (i.e. MbNO which dissociated NO) species and 50% MbNO, which decayed non-radiatively.

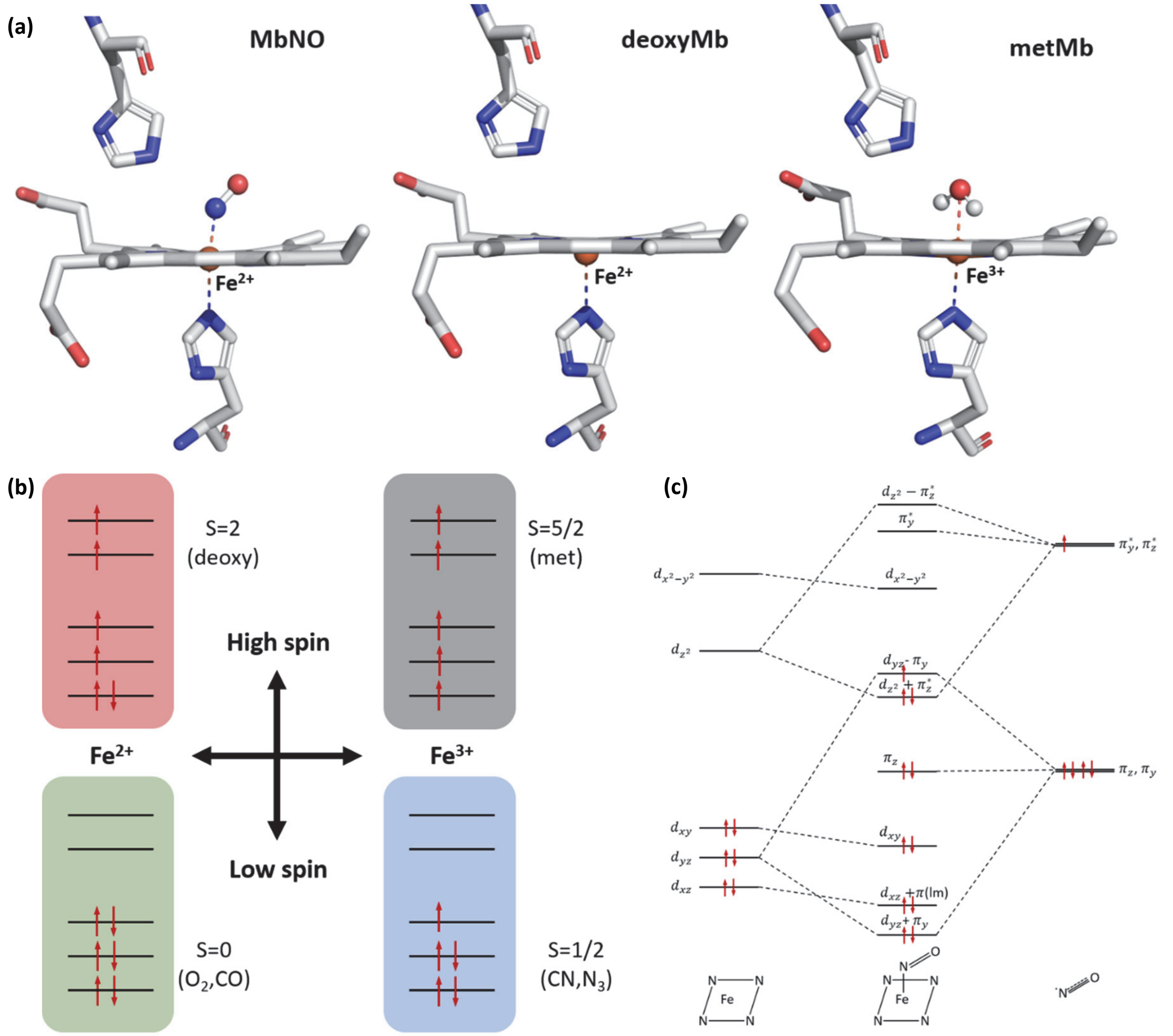
(a)
MbNO
deoxyMb
metMb
Fe2+
Fe2+
Fe3+
(b)
S=2
(deoxy)
S=5/2
(met)
High spin
Fe2+
Fe3+
Low spin
S=0
(O2,CO)
S=1/2
(CN,N3)
(c)
dz2 − π*z
π*y
π*y, π*z
dx2−y2
dx2−y2
dz2
dyz- πy
dz2 + π*z
πz
πz, πy
dxy
dyz
dxz
dxy
dxz +π(Im)
dyz+ πy
N
Fe
N
N
N
O
N
O

Figure 6-3: (a) Overview over the heme structure in different forms of myoglobin: MbNO (PDB: 2FRJ), deoxyMb (PDB: 2V1K) and metMb (PDB: 2MBW).Shown is the heme plane from the side with the His64 and His93 side chains. Grey (C),

blue (N), red (O), orange (Fe). (b) Schematic diagram of the electronic states of Iron (Fe) in different forms of Myoglobin, their multiplicity (S) and in brackets the ligands. (c) Molecular orbital diagram of MbNO, which is a special case as it is ferrous (Fe^{2+}) and low spin (S=1/2). Adapted from Morse R. H. et al.[49].

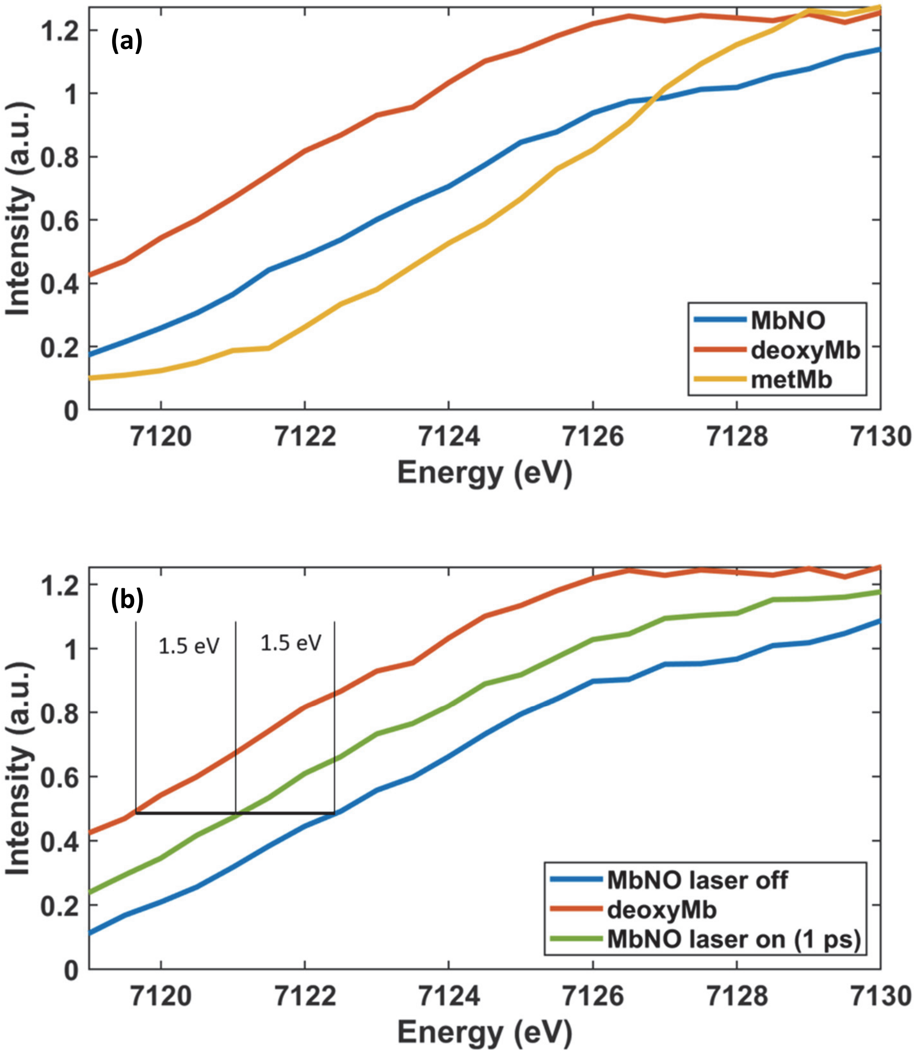

Figure 6-4: Magnification of the iron absorption edge of the static XAS spectra measured at SACLA of (a) MbNO, deoxyMb and metMb. (b) MbNO, deoxyMb and MbNO* laser-on at 1 ps.

Figure 6-5b shows the pre-edge region (7110 - 7116 eV) of deoxyMb, metMb and MbNO from ref.[94] and in (a) the MbNO, metMb and MbNO* laser-on (1 ps) spectra are plotted. The pre-edge for all forms of myoglobin is predominantly due to 1s -> d_σ and 1s -> $d_{\pi-\pi^*_{ligand}}$ transitions and due to the low symmetry of the heme 3d-4p orbital mixing is allowed and contributes weakly.[94] Summarizing, the pre-edge is most sensitive to the electronic structure of the d-shell.[88,94] The pre-edge XAS spectra of various forms of myoglobin have been analyzed by Lima et al.[94]. With the help of MXAN simulations[95] they correlate the intensity of the pre-edge to the Fe-ligand bond length. MbNO and MbCO which have and Fe-ligand bond length 1.8 Å show more intense pre-edge features than MbO_2 and MbCN with a 1.9 Å long Fe-ligand bond.

MbNO has clearly a more intense pre-edge feature (7113 eV) than metMb, whereas deoxyMb has its pre-edge peak at lower energy (7111.5 eV) and an intensity in between metMb and MbNO. The iron atoms in MbNO, deoxyMb and metMb have a different electronic structure, coordination sphere and oxidation state. MbNO having a planar heme (Fe^{2+}, hexacoordinated) with a nitric oxide ligand bound to the iron, deoxyMb (Fe^{2+}) has no ligand (pentacoordinated) and a domed heme and metMb (Fe^{3+}, hexacoordinated) has H_2O as a ligand and a slightly domed heme structure. The coordination and electronic structure of iron are presented in Figure 6-3.

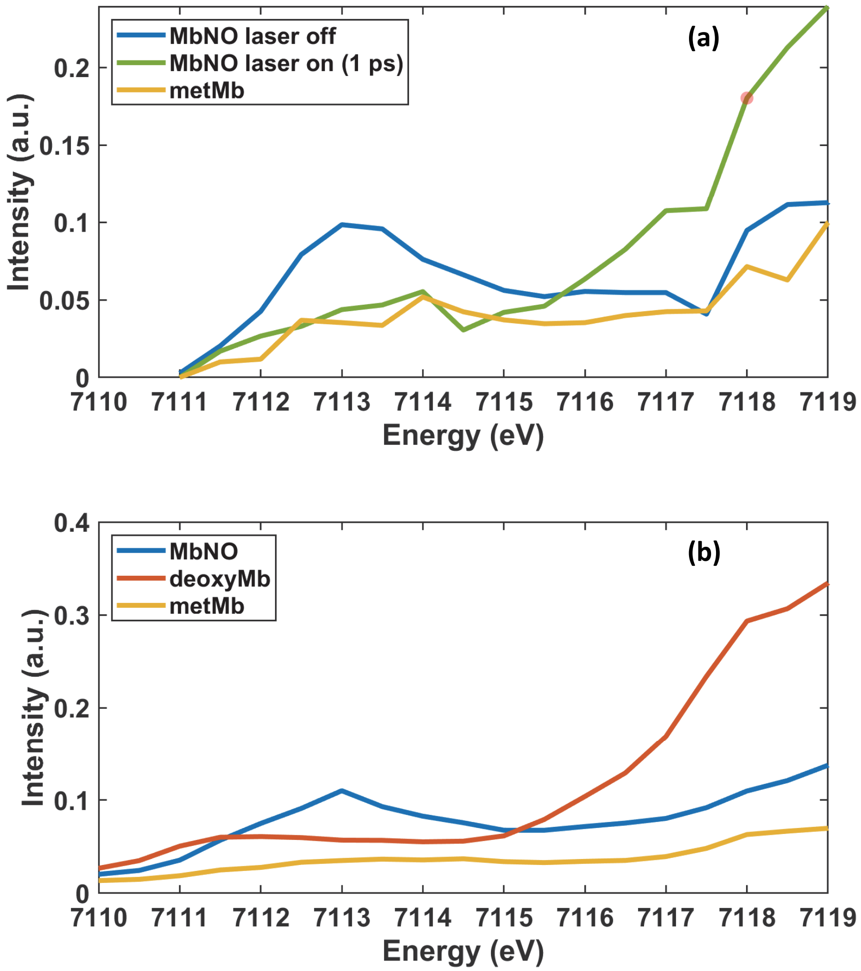

Figure 6-5: Zoom into the pre-edge of the static XAS spectra measured at SACLA of (a) MbNO, deoxyMb and MbNO* laser-on at 1 ps (data from SACLA) and (b) MbNO, deoxyMb and metMb, data from Lima et al.[94]

Looking at the region above the edge (>7133 eV) one can see a similarity between the MbNO laser-on spectrum at 1 ps delay (green) and the deoxyMb spectrum (red) which suggests a similar geometric structure of the two species (Figure 6-6). The region of 7130 - 7140 eV shows a similarity between metMb and MbNO, both hexacoordinated, and a larger difference to deoxyMb which is only pentacoordinated. The above the edge region is sensitive to all coordinating atoms and local structural changes start to dominate.

As we go higher in energy above the edge, we move from 1s -> 4p transitions to the multiple scattering regime and around 30 eV above the edge the so-called extended x-ray absorption fine structure (EXAFS) region starts which represents single scattering events and is not captured by the measurements in this work.[124] The region above the edge is more sensitive to the local structure around the iron[124] and as Silatani and co-workers found the region of 7135 - 7145 eV seems to be sensitive to the ligand in myoglobin (see Figure 6-1). In Figure 6-6 the region above the absorption-edge is plotted for MbNO, deoxyMb, metMb and MbNO* laser-on at 1 ps. Looking at the MbNO* laser-on at 1 ps spectrum, we can spot a high resemblance with the deoxyMb spectrum in the region above 7135 eV. This could possibly indicate the similarity in the structure.

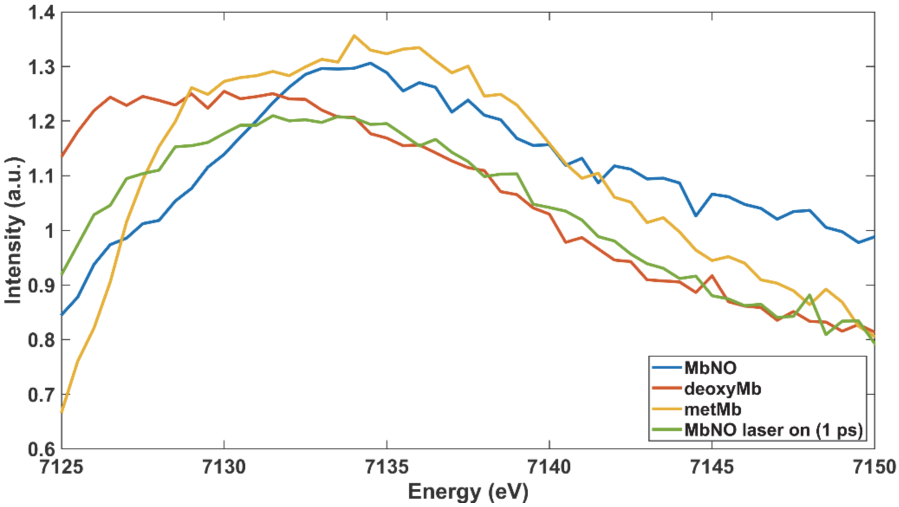

Figure 6-6: Zoom into the XAS region above the absorption edge (7130-7150 eV) of MbNO, deoxyMb, metMb and MbNO* laser-on at 1 ps pump-probe delay.

6.3 Static Difference Spectra

From previous studies[88] it is known that upon photoexcitation in the Q-bands of the porphyrin ring (Figure 4-6) nitric oxide (NO) is detached from MbNO and the iron atom moves out of plane into the domed heme structure. The resulting structure is expected to be similar to the molecular structure of deoxyMb. Therefore, the static difference spectrum (deoxyMb-MbNO) can be of help for the interpretation of any transient spectrum of photoexcited MbNO (MbNO*). A static XANES spectrum of deoxyMb can be either obtained using DFT simulations based on the crystal structure (PDB: 2V1K) of deoxyMb (Appendix Figure 8-11) or by measuring chemically prepared deoxyMb as shown in the Figure 6-2. Now we can use this deoxyMb XAS spectrum and subtract the

MbNO spectrum from it (excited state minus ground state), to obtain a model transient spectrum, plotted in Figure 6-7. The static difference (deoxyMb-MbNO) from Silatani M. et al.[88] (red) and the static difference measured at SACLA are plotted in Figure 6-7. The spectra agree within the signal-to-noise (S/N). This serves as a benchmark and allows us to conclude that the data acquisition, energy calibration and sample preparation of both species was performed well, and no artifacts are present in the static spectra.

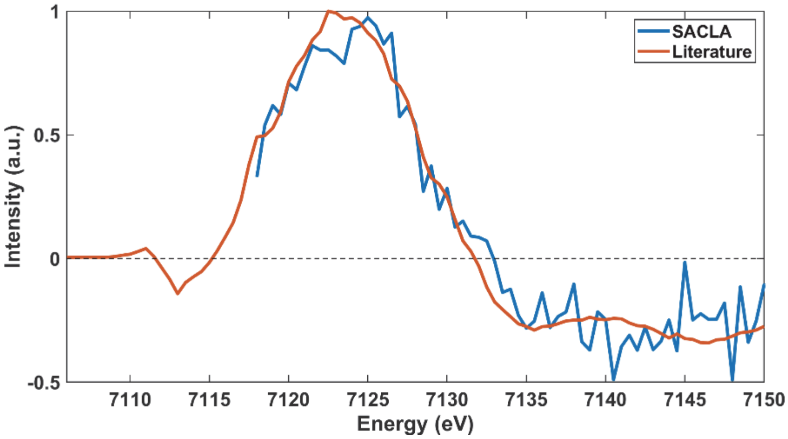

Figure 6-7: XAS deoxyMb minus MbNO static difference. In blue derived from steady state MbNO and deoxyMb spectra recorded at SACLA, in red from ref.[88] The SACLA difference spectrum is cut off due to difficulties recording the deoxyMb XAS spectrum (details explained above).

6.4 Fluence Dependence

To find the optimal pump laser fluence to obtain a high difference signal (pumped-unpumped) and at the same time avoid multi-photon absorption and non-linear effects a fluence scan on MbNO in physiological solution (pump-probe signal intensity at a fixed X-ray energy as a function of pump laser fluence) was performed at SACLA at the iron absorption edge (7122.5 eV) and 1.2 ps pump-probe delay and is shown in Figure 6-8. Due to the poor signal to noise and an offset (linear fit does not go through zero) of the fluence scan measured at SACLA it was repeated in a separate experiment at Alvra, SwissFEL. An explanation for the offset could not be found but might be because the low fluence range was not sampled well enough.

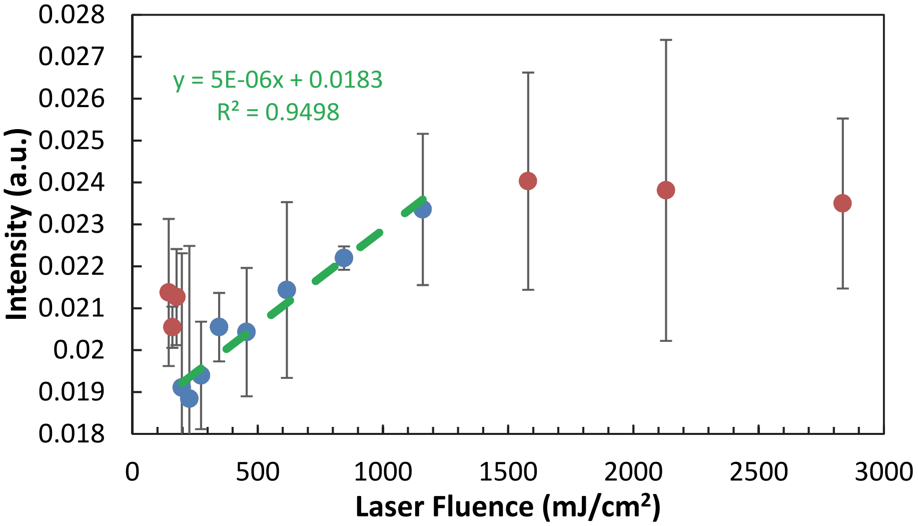

Figure 6-8: Fluence scan of the transient signal at the main X-ray absorption edge (7122.5 eV) at a time delay of about 1.2 ps. Plotted is the difference signal (pumped-unpumped) against the laser pulse energy in mJ/cm^2. The green dashed line represents a linear fit for which only the blue dots are used. Plotted is the mean of two runs, recorded at SACLA, and the error bars represent 2σ.

The fluence dependence of the XAS transient signal at 7122.5 eV (K-edge) and 1 ps time delay after excitation at 530 nm measured at SwissFEL, is shown in Figure 6-9. The dependence is linear up to at least 220 mJ/cm^2, indicating that although the fluence used for the SACLA measurements (195 mJ/cm^2, 13 photons per molecule) is rather high, it still lies in the linear regime. Silatani et al.[88] used a fluence of 26 mJ/cm^2, Levantino et al.[56] used 41 mJ/cm^2, Kim et al.[182] used 40 mJ/cm^2 and Barends et al.[183] used 80 mJ/cm^2. None of these reports a fluence scan.

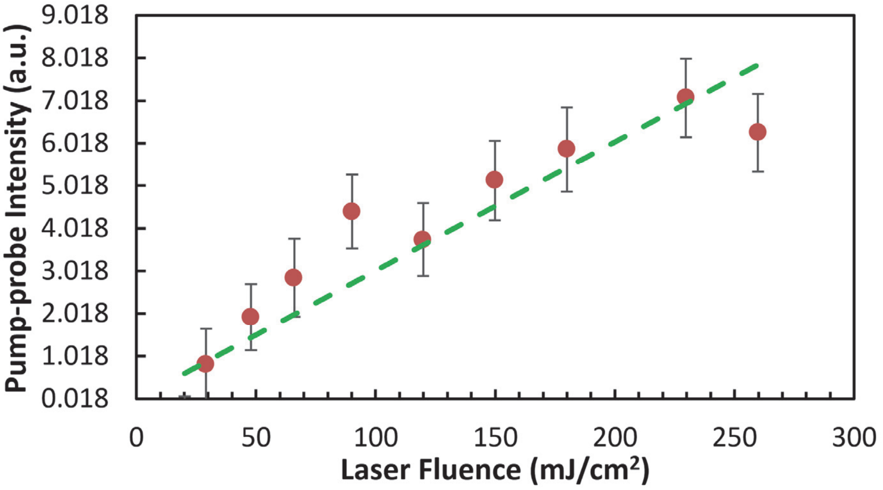

Figure 6-9: Laser fluence dependence scan of the XAS transient signal at 7122.5 eV, which is the main edge, at 1 ps time-delay. Plotted is the mean of 3 runs with the standard deviation as error bars, measured at SwissFEL. The dashed green line is the trendline using all data points.

In addition, transient X-ray absorption spectra were recorded at 1 ps time-delay and at the different pump-laser fluences to see if the spectrum changes with increasing laser fluence. Figure 6-10 shows how the transient spectrum changes with laser fluence. We can see that the pre-edge (7112 eV) and main-edge (7115 - 7131 eV) do not change within the signal-to-noise, but the post-edge region (7130 - 7145 eV) changes with increasing pump-laser fluence. This change occurs above about 150 mJ/cm^2 and is most pronounced for 810 mJ/cm^2. The XAS spectrum measured with a fluence of 160 mJ/cm^2 might be an outlier as the next higher fluence (320 mJ/cm^2) appears similar to the XAS spectra measured at low fluences (90 and 150 mJ/cm^2).

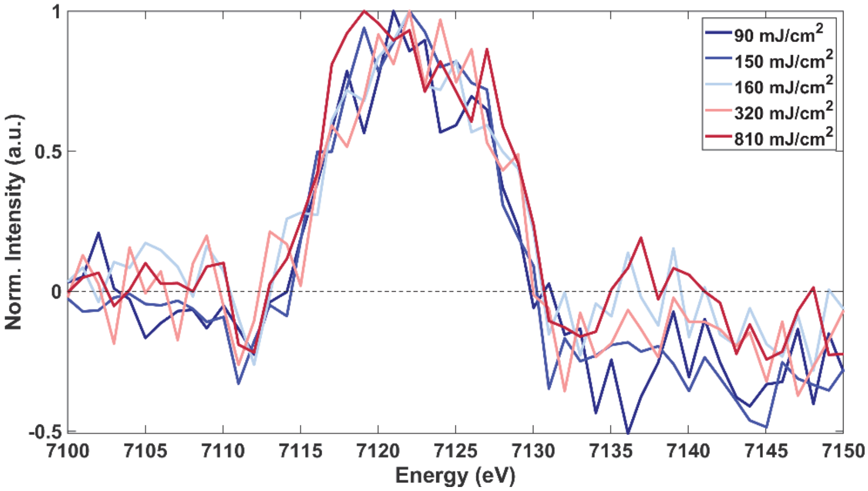

Figure 6-10: XAS energy scans at different pump laser fluences at 1 ps pump-probe delay measured at Alvra, SwissFEL.

Based on the fluence scan performed at SACLA (Figure 6-8) a value of 195 mJ/cm^2 (corresponds to ~45 µJ pulse energy) at the sample position was chosen for the experiment at SACLA to obtain a high signal to noise while remaining in the linear regime. It is important to note, that for most of the XAS measurements a 100 µm thick round jet was chosen, whereas for a few XAS and all the XES measurements a 200 µm thick round jet was used. This influences the effective number of photons per molecule, yielding ~13 photons/molecule for the XAS measurements and ~3 photons/molecule (absorption cross section considered) for all the XES measurements. The latter are comparable to previous experiments on myoglobin[56,58,184], whereas the former are a factor of 4-5 higher. The potential fluence effects are discussed below.

6.5 Potential Fluence Effects

In order to check for fluence effects the data from SACLA is compared to published spectra from ref.[88] (Figure 6-11 & Figure 6-12) and the measurements from Alvra, SwissFEL (Figure 6-13): The difference between the XAS transient spectrum of MbNO in physiological solution measured at SACLA at 100 ps delay is compared to the literature spectrum from ref.[88] and the comparison is plotted in Figure 6-11. The difference at the edge (7115 - 7131 eV) can be explained by the difference in energy resolution of the two experiments. Figure 6-12 shows that smoothing of the XAS transient measured at SACLA yields the same spectrum at the edge as the literature spectrum[88]. The difference in the pre-edge might be due to an outlier of the SLS experiment as only one point is different. But most evident is the mismatch in the region of 7135 to 7145 eV. This might be due to a higher laser fluence used at SACLA, as the XAS energy scans at different fluences measured at SwissFEL indicate changes in this region for very high fluences (Figure 6-10).

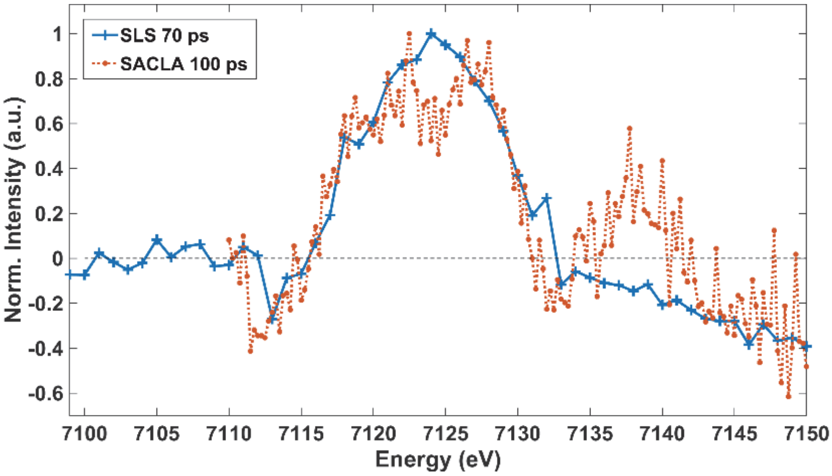

Figure 6-11: Comparison of transient XAS spectra of MbNO from SLS[88] and SACLA. In blue the 70 ps spectrum from SLS (pulse width of X-ray pulse at SLS is around 70 ps). In dotted red the transient MbNO XAS spectrum at 100 ps delay measured at SACLA.

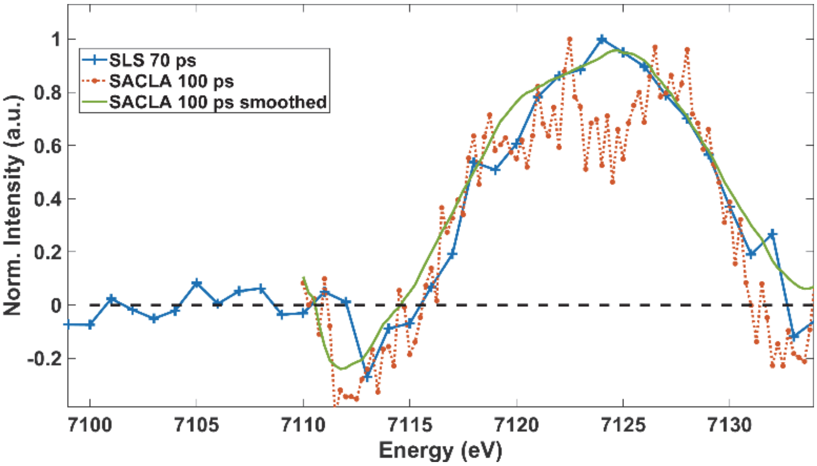

Figure 6-12: XAS transient spectrum at 100 ps delay from SACLA (red), compared to XAS transient spectrum at 70 ps measured at SLS (blue) from ref.[88]. The green curve is the SACLA transient smoothed with a span of 31 and shows that the double peak disappears and matches better the spectrum measured at SLS (blue).

Figure 6-13 shows the normalized static difference spectrum (deoxyMb-MbNO) and the XAS transient of MbNO measured at the Swiss Light Source (ref.[88]). The transient XAS spectrum of MbNO at 1 ps pump-probe delay at a fluence of 90 mJ/cm^2 (yellow) plotted, is comparable to the spectrum recorded at 65 mJ/cm^2 fluence by Silatani et al.[88]. The transient measured at SwissFEL (yellow) shows a good agreement of the static difference (deoxyMb-MbNO) which is expected from the photocycle for MbNO. Namely, that upon photoexcitation NO is dissociated from MbNO and an excited state species similar to deoxyMb is formed.

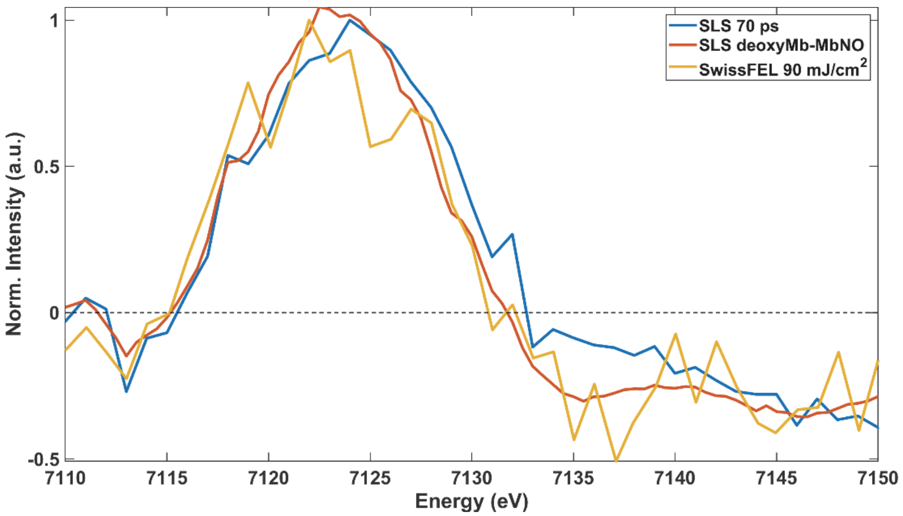

Figure 6-13: XAS transient spectra of MbNO. In blue the transient MbNO spectrum at 70 ps delay and in red the static difference spectrum (deoxyMb-MbNO) from ref.[88] In yellow that XAS transient measured at 1 ps delay and a fluence of 90 mJ/cm^2 at Alvra, SwissFEL is plotted. The transient measured at SwissFEL was shifted by +1 eV to match the published spectrum from SLS.

The comparison of the SwissFEL high fluence XAS spectrum to the data from SACLA is shown in Figure 6-14. Plotted are the XAS spectrum of MbNO at 1 ps pump-probe delay at a fluence of 810 mJ/cm^2, the same from SACLA, but at a fluence of 195 mJ/cm^2. And in red the static difference (deoxyMb-MbNO) from ref.[88] is shown. This indicates a fluence effect affecting mainly the region of 7135 to 7145 eV.

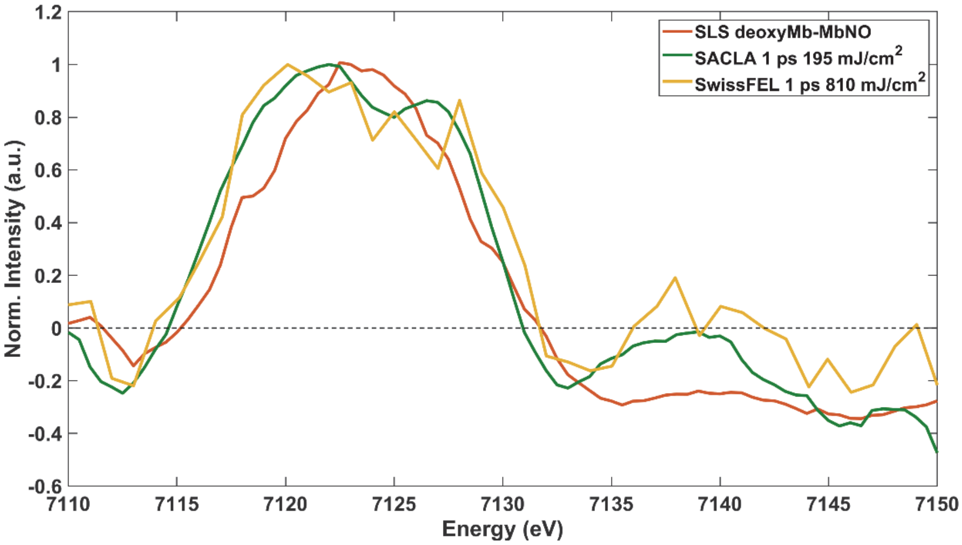

Figure 6-14: XAS transient spectra of MbNO. In red the static difference spectrum (deoxyMb-MbNO) from ref.[88] In yellow that XAS transient measured at 1 ps delay and a fluence of 810 mJ/cm^2 at Alvra, SwissFEL is plotted. In green the XAS transient at 1 ps delay measured at SACLA (fluence: 195 mJ/cm^2) is shown. The transient measured at SwissFEL was shifted by +1 eV to match the published spectrum from SLS.

One possible consequence of the high fluence could be the creation of the photo-excited deoxyMb species. Looking at the timescales of the deoxyMb photocycle in Table 2-3, these species life time is below 25 ps. However, in Figure 6-15b we observe the spectral changes in the region possibly affected by the high fluence (7135 to 7145 eV) lasting at least up to 100 ps . The thermal effects caused by the high laser fluence seem also unlikely to occur as they would not persist up to 100 ps[185]. Considering photooxidation caused by multi-photon excitation, this would cause a shift of the laser-on XAS spectra to higher energy, which is not the case, as we can see in Figure 6-15. Summarizing, multi-photon absorption with its different outcomes is the only reasonable possibility, but the fluence dependence at the absorption edge (7122.5 eV, shown in Figure 6-9) clearly shows a linear behavior. Nevertheless, it could be quadratic elsewhere. The exact consequences of multi-photon absorption in MbNO remains an open question, as none of the considered consequences seems reasonable. But the spectral region affected most (7133 – 7145 eV) is sensitive to the ligand (NO). The SACLA XAS data differs from previous published data by Silatani et al.[88], which may be due to high fluence.

6.6 Time-resolved X-ray Absorption Spectra (SACLA)

Several pumped (laser-on) XAS spectra at various time-delays and unpumped (laser-off) XAS spectra in the range of 7110 to 7150 eV were recorded. Figure 6-15a shows the laser-on spectra at a pump-probe delay of 1 ps (green) together with the steady state spectra of deoxyMb and MbNO. The transient XAS spectra at 1, 2, 10, 17, 27 and 100 ps time delay are plotted in Figure 6-15b showing the evolution of the whole spectrum with time. The magnitude of the maximum transient signal at 1 ps, corresponds to about 7% of the static maximum MbNO signal. for the MbNO laser-on 1 ps spectrum (Figure 6-15a) we observe an edge shift which lies exactly between deoxyMb (Δ = 1.5 eV) and MbNO (Δ = 1.5 eV).

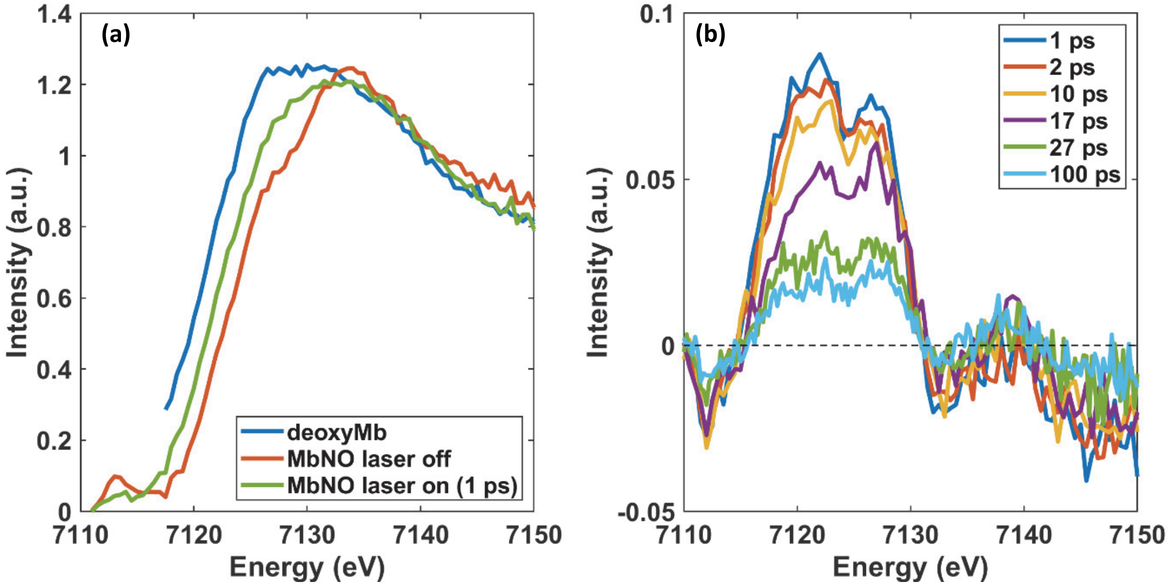

Figure 6-15: (a) Static XAS spectra (SACLA) of MbNO and deoxyMb and the MbNO* laser-on spectra at 1 ps pump-probe delay. Spectra are scaled. (b) Transient XAS spectra (pumped-unpumped) at 1, 2, 10, 17, 27 and 100 ps time delay. The magnitude of the maximum transient signal at 1 ps, corresponds to about 7% of the static maximum MbNO signal.

In panel (b) in Figure 6-15 the transient XAS spectra at six different time delays are plotted. We see a negative feature in the pre-edge which is enlarged in Figure 6-16. This feature appears to be stable for the first 10 ps and to decay later. A clear double peak with an additional low energy shoulder at the edge (7115 - 7131 eV) is observed especially for the range of 1 to 17 ps. For the two late time delays (27 and 100 ps) the shoulder becomes better visible and it the peak appears to be a triplet. For a better visibility of these trends, a zoom of the edge region is shown in Figure 6-17 (data is smoothed, details in 8.2.3). The following three peaks: A1 at 7118.5 eV, A2 at 7122 eV and A3 at 7126.5 eV are identified. All three of them seem to have different kinetics at early times, namely A1 and A2 seem to decay faster at early times, whereas at later times all three peaks seem to decay with similar rates. This will be discussed in more detail the next subchapter.

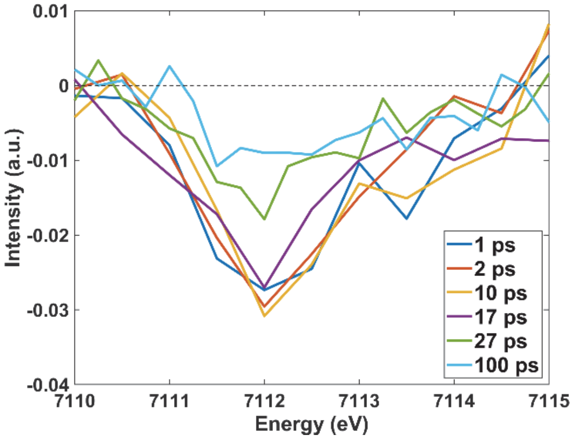

Figure 6-16: Zoom in the pre-edge region (7110-15) of transient XAS spectra (pumped-unpumped) at 1, 2, 10, 17, 27 and 100 ps time delay.

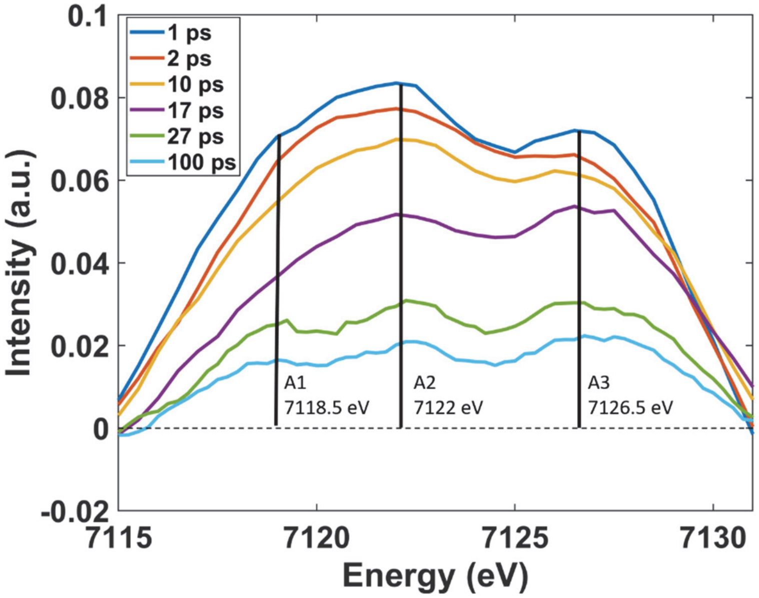

Figure 6-17: Zoom in the edge region (7115-41) of transient XAS spectra (pumped-unpumped) at 1, 2, 10, 17, 27 and 100 ps time delay. The transient spectra are smoothed (details in Appendix 8.2.3). Three peaks are identified: A1 at 7118.5 eV, A2 at 7122 eV and A3 at 7126.5 eV.

6.7 X-ray Absorption Time-Traces (SACLA)

As the previous chapter outlined, the XAS region of iron in MbNO is feature rich and different features seem to have different kinetics. The pre-edge reflects the valence electronic state and local symmetry, due to transitions into bound d shells. The edge corresponds to 1s -> 3p transitions and is sensitive to the oxidation state, the ligation and the spin state of the system.[94,176] Above the edge multiple scattering starts to contribute largely to the signal which makes it also sensitive to the ligation. As was found by Silatani et al.[88] (Figure 6-1) this region (7131 - 7145 eV) is sensitive to the presence of the NO ligand.

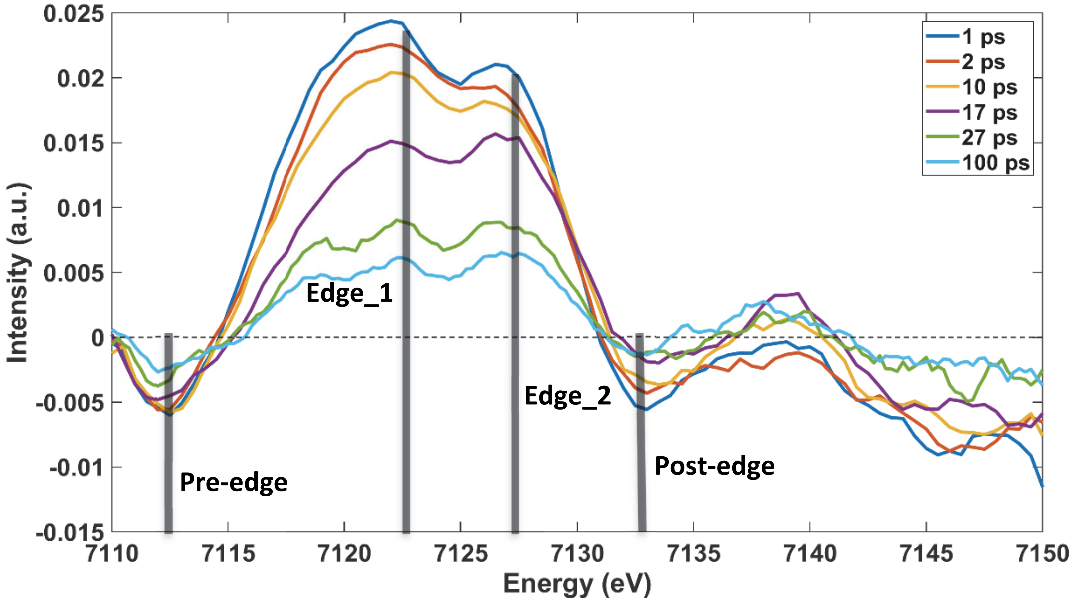

Figure 6-18: Shown are six XAS transient spectra of MbNO at different time delays and grey lines mark the energies at which time traces were recorded: Pre-edge at 7112 eV, Edge_1 at 7122.5 eV, Edge_2 at 7127 eV, Post-edge at 7133 eV.

6.7.1 Overview of All XAS Time-Traces

To get an overview over all XAS time-traces of MbNO recorded at SACLA, they are plotted in Figure 6-19. The time-traces represent an average of at least 2 runs each and the two negative ones (pre-edge, post-edge) were magnified (x4) for a better visibility. The first obvious difference is between Edge_1 and Edge_2. The signal at Edge_1 decays faster at early times (up to about 20-30 ps) after which they decay together with the same kinetics. The two time-traces are plotted in Figure 6-19, and their biexponential fits in Figure 6-25a and b. Another difference we can spot from the overview is between the pre-edge and post-edge, namely the post-edge seems to have a very short decay component not present in all other time-traces. A zoom into the first 40 ps, which is shown in Figure 6-20 highlights once more the difference between Edge_1 and Edge_2 at early times. In addition, it shows, it shows a difference between the pre-edge and post-edge in the region of 5 to 30 ps, but due to the small signal intensity for the latter two the signal-to-noise does not allow to obtain clear differences. Those findings are discussed in more detail in the following subchapters. SACLA XFEL provides X-ray pulses which are about ~10 fs in width, but due to short time jitters caused by the SASE operation, the actual time resolution is estimated to be 100-150 fs. Using arrival time diagnostics (spatial decoding technique)[156,186] for post-processing the data it was demonstrated to reach an accuracy of less than 17 fs rms[187]. Utilizing the arrival time diagnostics and post processing the data allows to resolve the rise-times at different X-ray probe energies. All time traces showing the decay of the pump-probe signal in the following chapters are not post-processed with the timing diagnostics, because for long time delays (>2 ps) it only introduces additional noise. Whereas for all the rise-times shown the data was post-processed with the timing diagnostics and sorted into 30 fs bins.

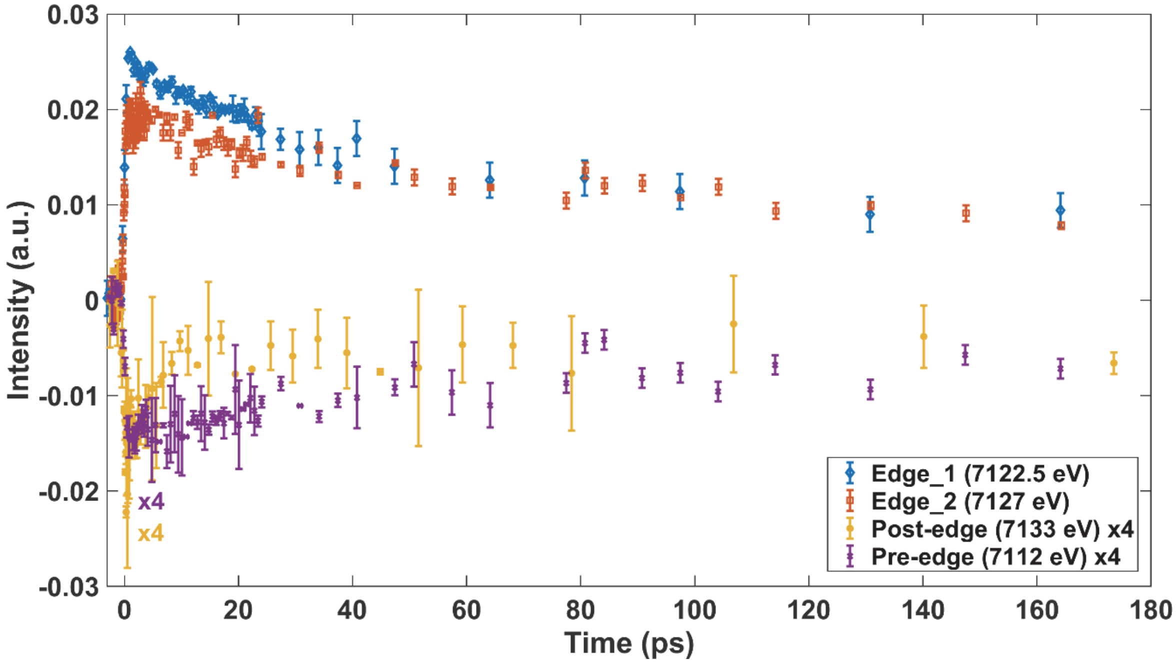

Figure 6-19: XAS time-traces at 7112 eV (Pre-edge) (*4), 7122.5 eV (Edge_1), 7127 eV (Edge_2) and 7133 eV (Post-edge) (*4). Edge_1 and Edge_2 show a clear difference in the early times < 30 ps and an agreement at longer times (>30 ps). Plotted are the average of 2 runs for Edge_1, Pre-edge, Post-edge and the average of 3 runs for Edge_2. The error bars represent the standard deviation between the runs.

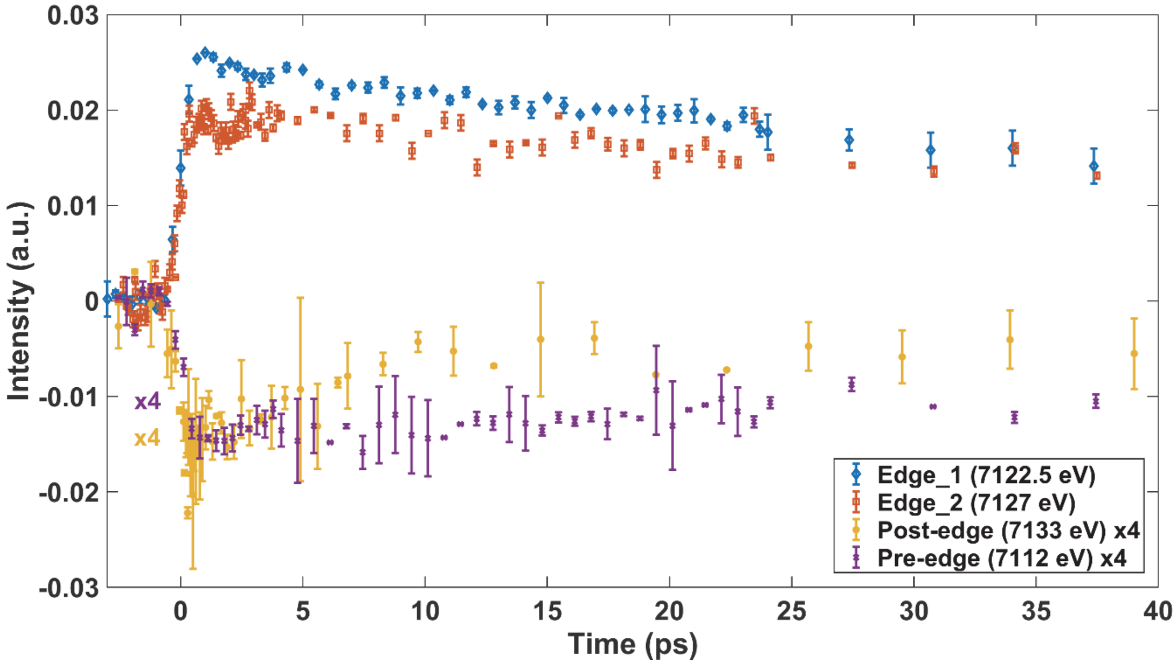

Figure 6-20: Zoom into the first 40 ps of the XAS time-traces at 7112 eV (Pre-edge) (*4), 7122.5 eV (Edge_1), 7127 eV (Edge_2) and 7133 eV (Post-edge) (*4). Plotted are the average of 2 runs for Edge_1, Pre-edge, Post-edge and the average of 3 runs for Edge_2. The error bars represent the standard deviation between the runs.

6.7.2 XAS Rise-Times

In this section the rise-times (-500 to 1500 fs) at the iron K-edge of MbNO measured at SACLA with a 100 µm liquid jet are presented. Utilizing the timing tool diagnostics at SACLA to post-process the XAS time-scans at: Pre-edge (7112 eV), Edge_1 (7122.5 eV), Edge_2 (7127 eV) and Post-edge (7133 eV) and applying a 30 fs binning we obtain clearly resolved rise-times, the arrival time of each X-ray pulse gets measured and the corresponding data corrected for the timing jitter caused by the SASE operation. We are assuming a sequential kinetic scheme, for which the temporal evolution of MbNO follows a sequence of events (rise or decays). All time-traces were modelled by a sum of N model functions (Equation 8-2) were N=1 to N=3 exponential decays were fitted (Appendix 8.2.2). The best fit was selected based on the least correlated lifetimes and amplitudes larger 0.01 as well as the quality of the fits.

Rise-times for MbNO and other heme proteins previously reported from other techniques like TA, resonance Raman, TR-XAS etc. are presented in Table 2-3 and can be summarized into a rise-time of 50-100 fs and a second component of several hundreds of femtoseconds (200-1000 fs).

First it is of importance to estimate the instrument response function (IRF) of the experiment. In Figure 6-22, the rise time at Edge_2 is plotted, which was found to be IRF limited. From fitting using the fit function described in Appendix 8.2.4 (Equation 8-2), we obtain a τ_{rise} = 75 ± 35 fs. Figure 6-21 shows the normalized rise time at Edge_1 with a τ_{rise} = 110 ± 15 fs and an interesting short-lived component with τ_f = 160 ± 70 fs. Also Figure 6-24a indicates this very fast decay, but the S/N is poor, so this can be doubted and a fit without the τ_f component is shown in Figure 6-24b. The rise times at 7112 eV (Pre-edge, Figure 6-23) and 7133 eV (Post-edge, Figure 6-24) and 7122.5 eV (Edge_1, Figure 6-21) show similar rise times in the range of around 110 fs.

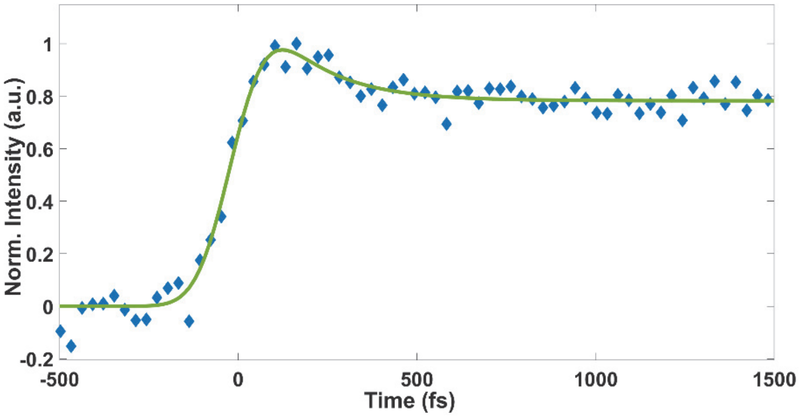

Figure 6-21: XAS rise at 7122.5 eV (Edge_1) with a biexponential fit (green). The obtained time constants are: τ_{rise} = 110 ± 15 fs and τ_f = 160 ± 70 fs. The errors on the time constants are 1σ.

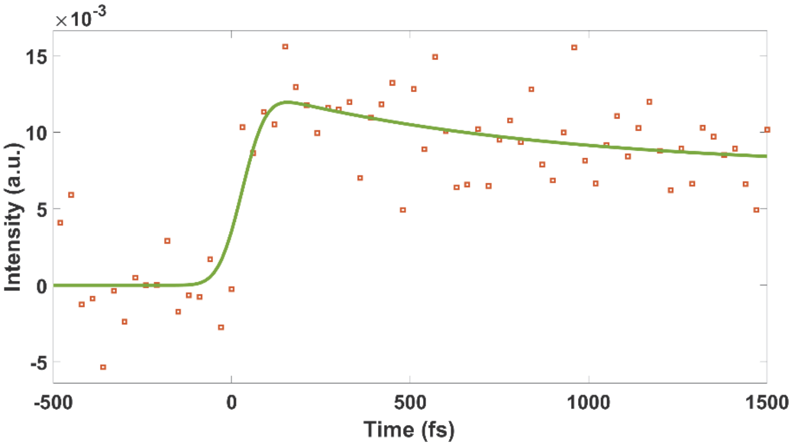

Figure 6-22: XAS rise at 7127 eV (Edge_2) with a biexponential fit (green). The obtained time constants are: τ_{rise} = 75 ± 35 fs and τ_f = 800 ± 1150 fs. The errors on the time constants are 1σ.

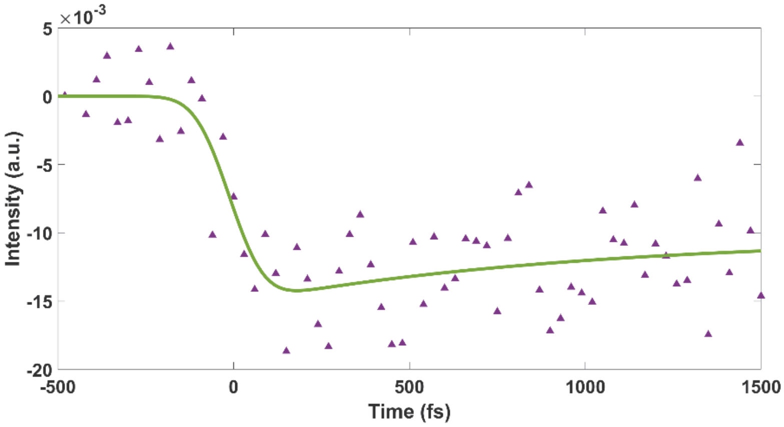

Figure 6-23: XAS rise at 7112 eV (Pre-edge) with a single exponential fit (green). The obtained time constant is: τ_{rise} = 110 ± 15 fs. The errors on the time constants are 1σ.

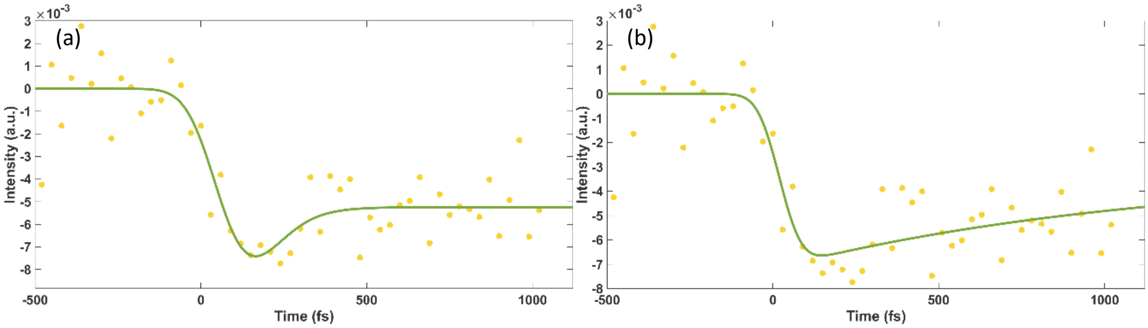

Figure 6-24: (a) XAS rise at 7133 eV (Post-edge) with a biexponential fit (green). The obtained time constants are: τ_{rise} = 110 ± 90 fs and τ_f = 70 ± 450 fs. (b) XAS rise at 7133 eV (Post-edge) with a single exponential fit (green). The obtained time constant is: τ_{rise} = 75 ± 58 fs. The errors on the time constants are 1σ.

6.7.3 Kinetic Time-Traces at the Iron K-edge of MbNO

In this chapter the time-traces at the iron K-edge of MbNO measured at SACLA are presented and discussed. Figure 6-25 shows all four time-traces: Pre-edge (7112 eV), Edge_1

(7122.5 eV), Edge_2 (7127 eV) and Post-edge (7133 eV) together with the best fit (green) and Figure 6-26a shows the zoom into the first 40 ps. We are assuming a sequential kinetic scheme, for which the temporal evolution of MbNO follows a sequence of events (rise or decays). All time-traces were modeled by a sum of N model functions (Equation 8-2) were N=1 to N=4 exponential decays were fitted (Appendix 8.2.4). The best fit was selected based on the least correlated lifetimes and amplitudes larger 0.01 as well as the quality of the fits.

Time-scales for MbNO previously reported form other techniques like TA, resonance Raman, TR-XAS etc. are presented in Table 2-4 and can be summarized into three groups of time-constants. The first two represent geminate recombination and are reported to be 10-30 ps and 170-250 ps. The last one was found to be due to NO leaving the protein and recombining on a >1 ns time-scale. For the time-traces at Edge_1 (Figure 6-25a, Figure 6-26a)and Edge_2 (Figure 6-25b, Figure 6-26b)both, a biexponential fit and a single exponential fit with an offset gave the best fit. This is because τ_2 is in the range of 300-500 ps and therefore out of the range we measured (up to 160 ps). This long component (τ_2) is likely to compensate for the two long recombination time-scales (170-250 ps, > 1 ns) for NO to myoglobin, which are out of the range of this experiment. Looking at decays in the range of tenths of ps, which can be safely obtained by fitting the measured time-traces, Edge_1 decays with τ_1 = 30 ± 9 ps (0.46) and Edge_2 with τ_1 = 30 ± 29 ps (0.22). In brackets are the normalized pre-exponential factors, which in the case of Edge_1 and 2 show a clear difference.

The signal-to-noise for the time-trace recorded at the Pre-edge (Figure 6-25c, Figure 6-26c) is not enough to obtain trustworthy time-constants. Nevertheless, a fit was attempted and a single exponential decay with an offset gives the best result. Any long (hundreds of ps to nanosecond) component is represented by the offset, as data was only recorded up to 160 ps. The short component, τ_1 = 43 ± 40 ps (0.5), is within the S/N similar to what we observe at Edge_1.

From previous X-ray experiments by Silatani M. et al.[88] and DFT simulations (Figure 6-27) we know that the Post-edge region (Figure 6-25d, Figure 6-26d)should be sensitive to ligation, namely the presence or absence of NO. Although the S/N is poor due to the weak signal, we observe very different kinetics at this energy. From a single exponential fit with an offset we obtain τ_v = 3.8 ± 2.5 ps. Any long (hundreds of ps to nanosecond) component is represented by the offset, as data was only recorded up to 160 ps.

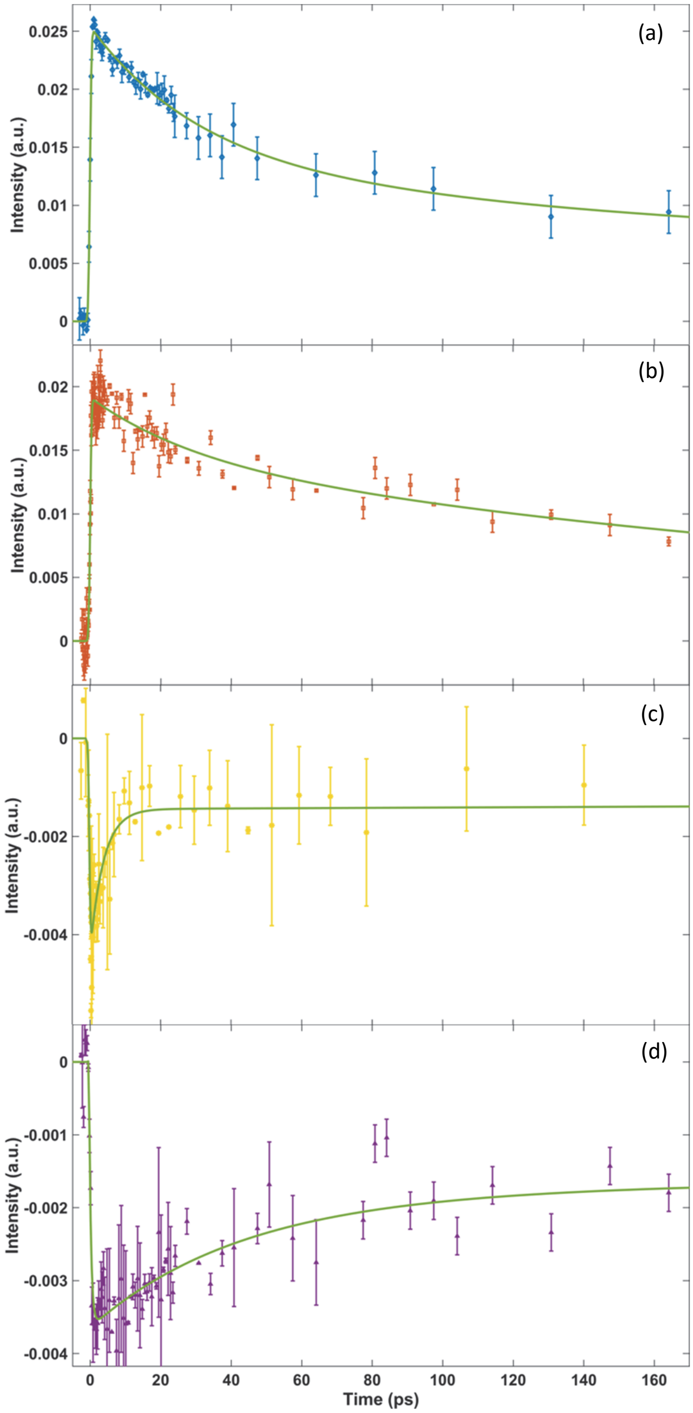

Figure 6-25: (a) XAS time-trace at 7122.5 eV (Edge_1) with a biexponential fit (green). The time constants with their normalized pre-exponential factors in brackets are: τ_1 = 30 ± 9 ps (0.46) and τ_2 = 450 ± 360 ps (0.54). (b) XAS time-trace at 7127 eV (Edge_2) with a biexponential fit (green). The time constants with their normalized pre-exponential factors in brackets are: τ_1 = 30 ± 29 ps (0.22) and τ_2 = 330 ± 272 ps (0.78). (c) XAS time-trace at 7133 eV (Post-edge) with a single exponential fit and an offset (green). The time constant is: τ_v = 3.8 ± 2.5 ps (0.6). (d) XAS time-trace at 7112 eV (Pre-edge) with a single exponential fit and an offset (green). The time constant is: τ_1 = 43 ± 40 ps (0.5). The error bars for all plots represent the standard deviation between the runs and the errors on the time constants are 1σ.

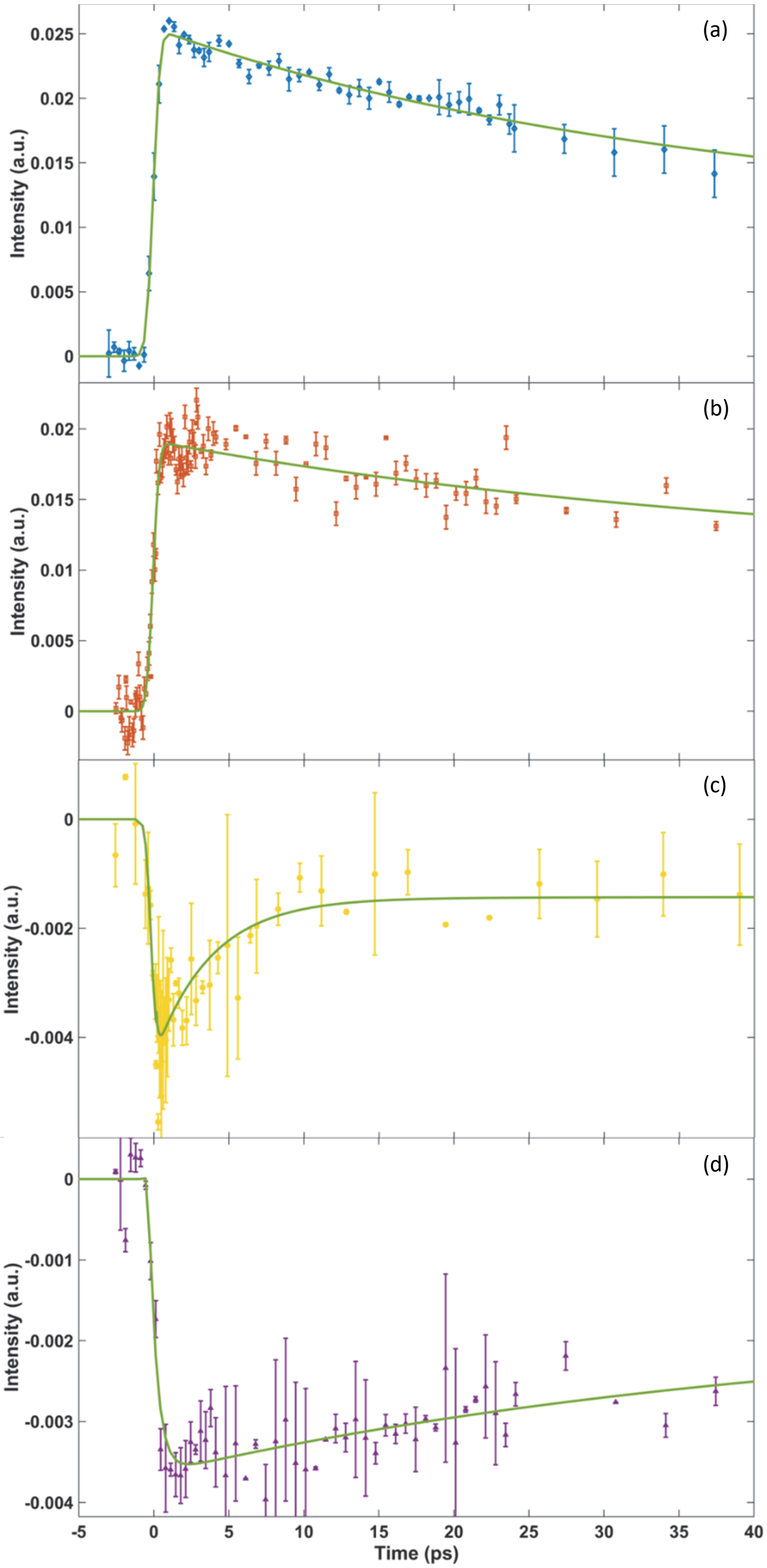

Figure 6-26: Zoom into the first 40 ps of the XAS time-traces of MbNO measured at SACLA, presented in Figure 6-25.

Table 6-1: Summary of all the XAS time-constants obtained in this study. In brackets are the pre-exponential factors. **These time-scales likely represent a convolution of the longer components (~200 ps and 1 ns) as they are out of the range to be determined by the measured data.

Feature (Energy)	τ_{rise}	τ_f	τ_v	τ_1	τ_2	**Offset**
Pre-edge (7112 eV)	110 ± 15 fs			43 ± 40 ps (0.5)		∞ (0.5)
Edge_1 (7122.5 eV)	110 ± 15 fs	160 ± 70 fs		30 ± 9 ps (0.46)	450 ± 360 ps (0.54) **	
Edge_2 (7127 eV)	75 ± 35 fs	800 ± 1150 fs		30 ± 29 ps (0.22)	330 ± 272 ps (0.78) **	
Post-edge (7133 eV)	75 ± 58 fs 110 ± 90 fs	70 ± 450 fs	3.8 ± 2.5 ps (0.6)			∞ (0.4)

6.8 Discussion

6.8.1 Assignments of Transitions for each Spectral Region

From the static XAS spectra of different forms of myoglobin (Figure 6-2) we can identify regions which are dominated by different effects (transitions, multiple scattering, etc.) and therefore show different sensitivity.

The **edge** region (7116-30 eV) shows the largest difference between hexacoordinated slightly domed metMb (Fe^{3+}, HS), pentacoordinated domed deoxyMb (Fe^{2+}, high spin) and hexacoordinated planar MbNO (Fe^{2+}, low spin) (Figure 6-3). Namely, shift, slope and shape are different. The iron K-edge corresponds to the dipole allowed 1s -> 4p transition which makes it sensitive to the oxidation state, the number of coordination numbers, the types of ligands as well as the spin state of the iron. [94,124,176,180] The edge position of deoxyMb is shifted to lower energies compared to MbNO (Figure 6-4), which is typical for HS and LS systems and different coordination numbers (deoxyMb: 5 and MbNO: 6) and caused by the elongation of the Fe-N in deoxyMb (Figure 6-3).[132,188]

The **pre-edge** features due to the dipole forbidden 1s -> d_σ and 1s -> $d_{\pi-\pi^*_{ligand}}$ transitions. However, 3d-4p orbital mixing as a result of the low symmetry give rise to the also dipole allowed transitions to 4p levels. This results in the MbNO showing the most intense pre-edge feature of the three species investigated and metMb the weakest (Figure 6-5). Looking at the XAS spectrum of MbNO* at 1 ps pump-probe delay (Figure 6-15) we can see in all regions (pre-edge, edge, post-edge) a shift towards deoxyMb. Due to the quantum photodissociation yield of around 55% (determined by TR-XES in this work) we observe a XAS spectrum of MbNO* at 1 ps in-between deoxyMb and ground state MbNO, which can hint to a similarity of the initial excited state at 1 ps to the deoxyMb electronic and geometric structure. This forms the basis for understanding the kinetics of different features in the XAS spectrum of MbNO.

Finally, the **post-edge** (7131-50 eV) represents the beginning of the multiple scattering regime and is therefore sensitive to the local structure around the iron. Silatani M. et al.[88] found the region of 7135-45 eV to be sensitive to the presence of the distal NO ligand. This is also supported by DFT simulations (Figure 6-27), which show a significant difference in the calculated difference spectra of deoxyMb-MbNO and MbNO*(domed)-MbNO in the region of 7130-40 eV.

6.8.1 Possible Fluence Effects

The fluence scans at the edge (7112.5 eV) of MbNO performed at SACLA and SwissFEL show both a linear dependence up to around 200-230 mJ/cm^2. Therefore, the fluence of 195 mJ/cm^2 used for the measurements at SACLA is in the linear regime. In addition, transient XAS spectra were recorded at SwissFEL at 1 ps time-delay and at different fluences to see if any features of the spectrum change with increasing laser fluence. Figure 6-10 shows how the transient spectrum changes with laser fluence. We can see that the pre-edge (7112 eV) and main-edge (7115 - 7130 eV) do not change within the S/N, but the post-edge region (7130 - 7145 eV) might indicate a change with increasing pump-laser fluence. Due to the limited S/N an unambiguous conclusion cannot be made. Nevertheless, comparing the XAS transients measured at SwissFEL at different fluences with the spectra measured at SLS by Silatani et al.[88] (Figure 6-13)and the 1 ps transient XAS measured at SACLA (Figure 6-14) we can observe a) the transient at 1 ps from SACLA matches the static difference (deoxyMb-MbNO, Figure 6-14) and b) The transient signal at 1 ps from SACLA and at high fluence from SwissFEL seem to show the same trend, namely, the region of 7135 - 7145 eV shows a transient signal close to zero. Potential effects of a high fluence are a) photoexcited deoxyMb species b) thermal effects and c) multi-photon absorption which can cause photooxidation. The timescales of (a), shown Table 2-3 are in the order of < 30 ps and are therefore too short to sustain up to 100 ps, where see a clear difference between the SACLA (100 ps) and SLS (70 ps) transients (Figure 6-11). Heating (b) is expected to on the order of ps[185] so it seems unlikely to sustain up to 100 ps. Multiphoton absorption (c) could be possible, but the fluence dependence at the edge (7122.5 eV) clearly shows a linear behavior (Figure 6-9), however it could be quadratic behavior elsewhere could be possible. Photooxidation due to multi-photon absorption would cause a shift of the absorption edge of the laser-on XAS spectra to higher energy (towards metMb, Fe^{3+}) which seems not be the case (Figure 6-15). Also, the pre-edge, being sensitive to the d-orbitals would show an indication of oxidation, although it would be small, concluding from the difference between deoxyMb (Fe^{2+}) and metMb (Fe^{3+}). The effects (a), (c) and (d) would create additional species probed by the X-rays, which seems unlikely due to the presence of two isosbestic points at 7115 and 7131 eV (Figure 6-15b).

6.8.1 Overall Model

In panel (b) in Figure 6-15 the transient XAS spectra at six different time delays are plotted. A characteristic double peak (A2 at 7122 eV, A3 at 7126.5 eV) at the main edge, especially for the range of 1 to 17 ps is observed and for the late time delays (27 and 100 ps) it seems there are three peaks (A1-A3) and not just two. The third peak (A1 at 7118.5 eV) shows up as a shoulder at early times. Interestingly all three identified peaks (A1-A3) seem to have different kinetics at early times, namely A1 and A2 seem to decay faster at early times, whereas at late times all three peaks seem to decay with similar rates. This is observed for the first time for MbNO, as previous experiments were limited in time-resolution (> 70 ps) and energy resolution (1 eV)[88] compared to femtosecond time-resolution and 0.25 eV (0.5 eV) energy sampling at SACLA. At the edge (7116 - 7131 eV) the dominating transition is the 1s -> 4p, so one possible explanation could be that we are observing a splitting of the p_x, p_y, p_z orbitals. As reported by Lima A.F. et al.[94], who performed a careful structural analysis of different forms of myoglobin, the local heme geometry is distorted and therefore it is likely that the iron p_x, p_y, p_z orbitals are not degenerate. This is also supported by DFT simulations of the deoxyMb-MbNO and MbNO*(domed)-MbNO transient XAS spectra (Figure 6-27a, (b) local structure around the iron atom of the species used for simulation of the DFT spectra), which also show a characteristic doublet, with a shoulder on the low energy side. This is similar to what we observe in the XAS transients from SACLA at early times (Figure 6-15) and suggests that at 1 ps predominantly deoxyMb species is present, whereas at later times NO recombined to deoxyMb forming a hexacoordinated domed transition state which then decays back to the planar MbNO ground state. The largest differences between the two difference spectra in Figure 6-27a are a decrease of the peak at 7120 eV and an increase (to less negative) of the feature at 7132 eV. For the experimental spectra (Figure 6-15b) we observe the same trends. Another support for the observation of an p-orbital splitting of the p_x, p_y, p_z orbitals comes from the DFT simulated density of states (DOS) for the p_x, p_y, p_z orbitals of iron in MbNO which show a difference for all three orbitals and can be found in the Appendix 8.5.2 (Figure 8-12).

Looking at the pre-edge feature evolution in the XAS spectra with time(Figure 6-16), we see a negative feature in the pre-edge which seems to stay stable for the first ~10 ps and then decays. Due to its sensitivity to the d-orbitals and therefore the electronic configuration of them we can compare the XAS transients with the changes observed for deoxyMb and MbNO (Figure 6-5) and observe the change from ground state MbNO to an MbNO* species similar to deoxyMb which then decays back to the ground state.

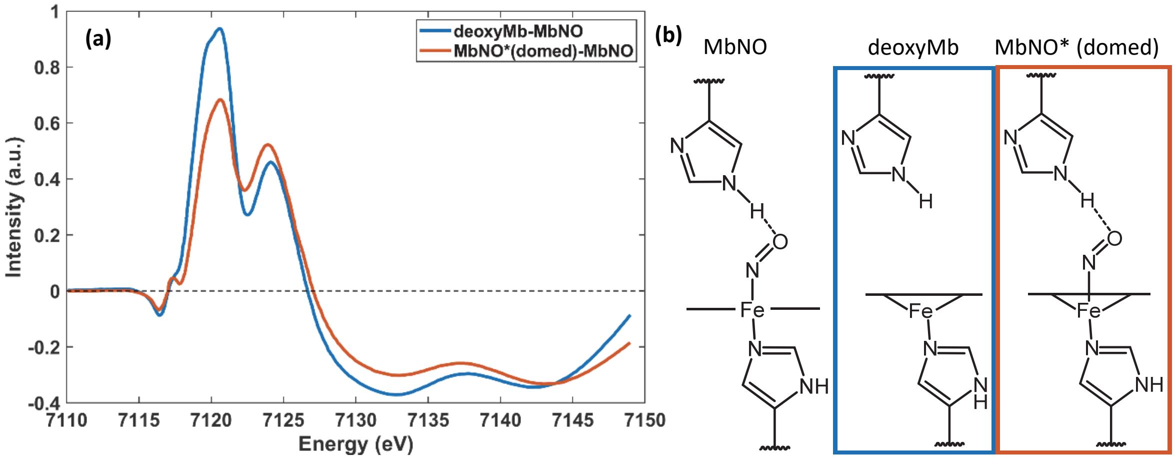

Figure 6-27: (a) Static difference spectra calculated with DFT ground state spectra of deoxyMb, MbNO, domed MbNO. (b) The chemical structures of the active center of different Myoglobin-NO, deoxyMb and the proposed transition state: domed MbNO. The color of the boxes correspond to which structure is used for the calculation of the difference spectrum from DFT simulated XAS spectra.

After having established which region in the XAS spectra is sensitive to what, we obtain their kinetics from the measured XAS time-traces at different energies (Figure 6-19 & Figure 6-20). The rise-times are shown in Table 6-1) and show a rise of ~110 fs for three features (Pre-edge at 7112 eV, Edge_1 at 7122.5 eV and Post-edge at 7133 eV). Only Edge_2 (at 7127 eV) seems to be IRF limited with a rise of ~75 fs. From previous studies[54,55,68,69,72,73,75,77,78] (summarized in Table 2-3) we know, the fastest process which occurs after photoexcitation is the NO ligand dissociation and the first step of the doming (π-π^* to triplet state decay, ~100 fs). This Fe-NO bond is formed by the d-orbitals of the iron and the π orbitals of the NO. From Lima A.F. et al.[94] it is established, that the local symmetry around the iron is distorted for the case of MbNO and that there is a 3d/4p orbital mixing. Thinking of the three different p-orbitals (p_x, p_y, p_z), the p_z should be the one which contributes most from the three p orbitals to the Fe-NO bond via 3d/4p_z orbital mixing. Therefore, we would expect if we selectively probe the p_z orbital in MbNO to observe a rise which corresponds to the NO dissociation from iron in MbNO. Comparing now the rise-times at four different energies (Pre-edge at 7112 eV, Edge_1 at 7122.5 eV and Post-edge at 7133 eV), we observe the fastest, IRF limited rise of ~75 fs for the signal at Edge_2 which can indicate that feature A3 (Figure 6-17) corresponds to the 1s -> 4p_z transition. Studying the rise-times of these four time-traces we observe an interesting difference at 7122.5 eV (Edge_1), which shows the most intense transient signal. We observe immediately after the rise a very short decay (Figure 6-21) of τ_f = 160 ± 70 fs. A possible origin of this very short decay could be the stretching of the Fe-His bond which is reported to be 140-166 fs (200–240 cm^{-1})[54,189], but if this is the case it should also show up at Edge_2 which it does not. Instead we can maybe observe similar kinetics of the post-edge (7133 eV, Figure 6-24a), but the S/N does not allow a clear assignment and yields a large error τ_f = 70 ± 450 fs. For comparison the same rise-time, fitted without τ_f is plotted in Figure 6-24b. Therefore, the question of origin of this feature remains open.

Looking at the decays of the time-traces in Figure 6-19, we notice that the Edge_1 (7122.5 eV) and Edge_2 (7127 eV) features overlap for times after ~30 ps. Fitting them with a biexponential fit (details about the fit can be found in the Appendix 8.2.4) gave the best result for both energies and reveals that τ_1 = ~30 ps is observed both at Edge_1 and Edge_2. Interestingly with very different pre-exponential factors (0.46 and 0.22, respectively). It is important to note that this ~30 ps is different from the ~30 ps component observed by XES due to the very different sensitives. Whereas the XES K_β peak position and the XES K_α peak width (σ) selectively look at the spin state of the system, the XAS Edge_1 and Edge_2 are sensitive to the ligation, both in number and type and therefore can be used as an indicator for the geminate recombination in MbNO. The longer component (~330-450 ps) compensates for the long components previously reported and summarized inTable 2-4, namely a ~200 ps and a >1 ns component, which cannot be determined by this work as only short time-delays up to ~160 ps were measured. Silatani M. et al.[88] assigned the signal at 7125 eV, which lies in-between Edge_1 and Edge_2 to being sensitive to geminate recombination and they observed a rate of 200 ps and 1.3 ns. Therefore, we assume that also Edge_1 and Edge_2, which are less than 3 eV away, are sensitive to geminate recombination of NO to the iron. Coming back to the difference in pre-exponential factors and equal decay rates for Edge_1 and Edge_2, it could indicate a different sensitivity to the geminate recombination of nitric oxide to deoxyMb. It seems that the Edge_1 peak is more sensitive to the recombination process compared to Edge_2. This could potentially indicate that Edge_2 is due to orbital mixing of 3d/4p_z more sensitive to changes in the distal (and proximal) position of the heme.

The post-edge time trace (7133 eV) was fitted with a single exponential and an offset. Due to the poor S/N, because of the small transient signal the fitted parameters should be viewed with care. The offset represents any long time scales which are not captured within 160 ps and the single exponential yields a time constant of τ_v = 3.8 ± 2.5 ps, which we assign to vibrational relaxation based on previous experiments in the optical regime[82,190,191] Because this ~4 ps component is lacking in the pre-edge or edge which is more sensitive to electronic changes an electronic excited-state decay can be excluded. This is contrary to what is reported for the MbCO from IR-TA[86], but in agreement with TA studies of MbNO[75].

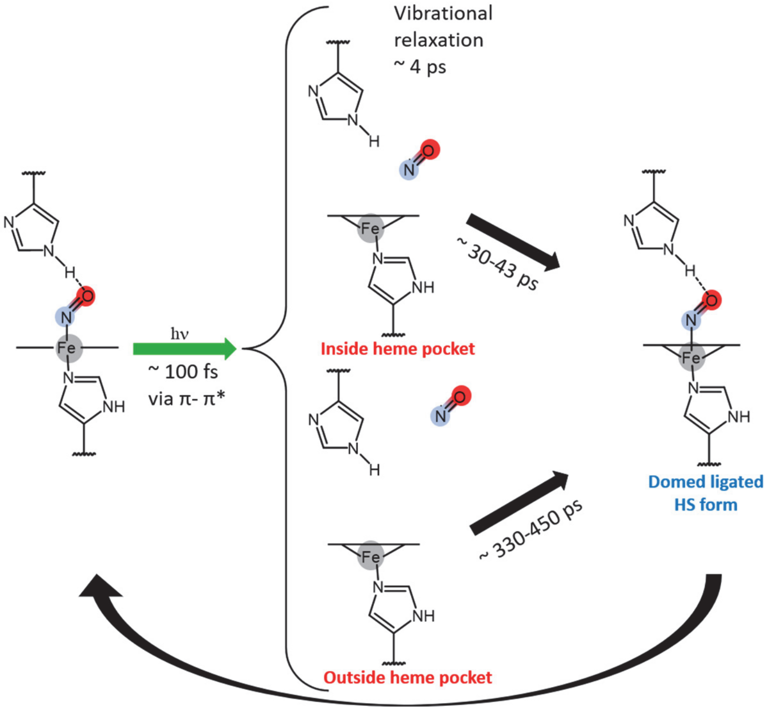

Figure 6-28: Schematic summary of the recombination kinetics in MbNO obtained from time-resolved XAS

6.9 Conclusion & Outlook

Summarizing, time-resolved X-ray absorption spectroscopy proves to be an excellent tool to investigate ultrafast structural and electronic dynamics of metalloproteins in physiological solution. With the help of previous optical, X-Ray spectroscopic studies together with density functional theory simulations, transition states can be identified, and the interpretation of the kinetics can be guided.

For the case of myoglobin-NO we could learn from the static XAS spectra and Lima et al.[94] which regions (pre-edge, edge, post-edge) are sensitive to what. The pre-edge arises from the dipole forbidden 1s -> d_σ and 1s -> $d_{\pi-\pi^*_{ligand}}$ transitions and due to the low symmetry around the heme also gains intensity due to 3d/4p orbital mixing, being sensitive to the d-electronic configuration. The edge region which has a high intensity due to dipole allowed 1s -> 4p transitions and due to orbital mixing (3d/4p) is sensitive to mainly the 4p orbitals with some 3d contribution[88,94] which means electronic structure like oxidation state, number and type of ligands and spin state.[94,124,176,180] Above the absorption edge starts the multiple scattering regime, which we call post-edge in this work (7131 - 7150 eV). The post-edge is sensitive to local structural changes around the iron and Silatani M. et al.[88] found the region of 7135 - 7145 eV to be sensitive to the presence of the distal NO ligand. This is also supported by DFT simulations (Figure 6-27).

Due to the rather high fluence used for the measurements at SACLA (195 mJ/cm^2) a careful investigation of the fluence dependence was performed at SACLA and in a separate experiment at SwissFEL. The fluence scans at the iron absorption edge (7122.5 eV) measured at both facilities show a linear dependence up to 200-230 mJ/cm^2 (Figure 6-8 & Figure 6-9), whereas XAS scans at different fluences measured at SwissFEL (Figure 6-10) indicate a potential fluence effect in the region of 7131 - 7145 eV (post-edge). Several potential effects of a high fluence, namely a) photoexcited deoxyMb species b) thermal effects c) and multi-photon absorption which can cause photooxidation are discussed and can all be excluded, so the question of what the high fluence is causing in MbNO remains open. But it seems that within the S/N for the fluence scans measured at SwissFEL (Figure 6-9 & Figure 6-10), only the post-edge region (7131 – 7145), which is sensitive to the ligand, is affected, but not the pre-edge and rising-edge region. Therefore, at the latter two we seem to be measuring mainly normally excited MbNO which reflect the MbNO kinetics.

The XAS transients of MbNO measured at SACLA at different time delays show an interesting three peak feature (A1-3) at the edge (7116 - 7131 eV). With consideration of the expected processes after photoexcitation (dissociation and first step of doming) and the help of DFT simulations we could assign it to a splitting of the p_x, p_y, p_z orbitals. Comparing the XAS transients measured at SACLA (Figure 6-15b) to the DFT simulated deoxyMb-MbNO spectrum and with the MbNO(domed)-MbNO(planar) spectrum (Figure 6-27) we observe similar trends. Namely, at 1 ps the peak at 7122 eV is higher in intensity compared to the peak at 7126 eV, which is the case for both, the 1 ps experimental spectrum (Figure 6-15b) as well as the DFT simulated deoxyMb spectrum (Figure 6-27). This, and overlap of the 1 ps transient XAS measured at SwissFEL and the deoxyMb-MbNO spectrum measured at SLS (Figure 6-13) suggest that at 1 ps predominantly deoxyMb species is present, whereas at later times NO recombined to deoxyMb forming a hexacoordinated domed transition state which then decays back to the planar MbNO ground state. This pathway is in agreement with previous studies[54,55,68,69,72,73,75,77,78].

Utilizing the timing-tool at SACLA sub 100 fs time resolution is achieved and the observation of the rise-times at all four energies (7112, 7122.5, 7127,7133 eV) show a rise-time of around ~110 fs indicating the first step of doming, triggered by the dissociation of NO and the π-π* to triplet state decay. The second, slower phase of reaching full doming, which we observed with time-resolved non-resonant XES (Chapter 4) is not found in the XAS time traces, likely due to its minimal structural change (<0.1 Å). The fastest and IRF limited rise of ~75 fs being at 7127 eV (Edge_2) could indicate that Edge_2 correspond to p_z, which due to 3d/4p orbital mixing, is sensitive to the dissociation of NO from the iron center. And therefore, A1 and A2 correspond to p_x and p_y with a definite assignment being still an open. A potential assignment could be achieved by performing a polarization dependent time-resolved XAS experiment, which can be used to determine orbital occupancy or the direction of covalent bonds.[192,193]

The decay times found by the XAS experiments presented in this work can be summarized into two main groups, ~4 ps and 30-40 ps. With a third group of 150-250 ps suggested by Silatani et al.[88] and optical TR experiments[54,75]. The first one corresponding to vibrational relaxation showing up in the post-edge region which represents multiple scattering and therefore is sensitive to structural changes. And the 30-40 ps one being geminate recombination (NO recombines to iron).

This is different from the ~30 ps observed with XES, for which we looked at metal spin-state markers (peak shift of Kβ and width of K. Both main groups of time-scales confirm the results of previous resonance Raman[75] and transient absorption measurements[67,75,78,164].

Summarizing, a schematic overview of the dissociation and recombination processes in MbNO is given in Figure 6-28 and a compilation of the obtained time constants is given in Table 6-1. Starting from ground-state (low spin) MbNO upon photo-excitation a π- π* state is reached immediately and dissociates the nitric oxide ligand and decays within <75 fs (rise-time at edge_2). Within ~110 fs (rise-time at pre-edge, edge_1, post-edge) an excited triplet state with antibonding character is reached. The transient XAS spectrum at 1 ps recorded at SwissFEL (Figure 6-13) is similar to the static difference spectrum (deoxyMb-MbNO), therefore indicating that at 1 ps we have mainly deoxyMb species present. From this excited state transition state similar to deoxyMb we can separate three different recombination pathways, depending on how far away the nitric oxide gets from the iron center. In pathway 1, the nitric oxide ligand stays in a close by heme pocket and recombines on a timescale of ~30 ps (time-decay at pre-edge, edge_1 and edge_2). For the case of nitric oxide reaching a distant heme pocket it takes around ~150-200 ps to recombine with the iron in the domed heme.[88] And in pathway 3 (not depicted in Figure 6-28) the nitric oxide ligand leaves the protein and recombines on a timescale of a few nanoseconds. [88] The hexacoordinated domed transition state formed by all three pathways relaxes back to the ground state (planar heme) in ~30 ps (obtained from TR-XES, Chapter 4) and its existence is proven by transient XAS spectra combined with DFT simulations.

Chapter 7 Conclusion & Outlook

This work demonstrates the potential of femtosecond time-resolved XAS and XES in investigating the local electronic changes like spin, oxidation state, coordination number and ligand structural changes in metalloproteins, under dilute physiological conditions. With time-resolved non-resonant X-ray emission spectroscopy we identify the transition from planar MbNO after immediate ligand release to the domed deoxyMb form as a spin cross-over via an intermediate triplet state, which takes ~800 fs. The lifetime of the triplet state, obtained from a simple kinetic model, is ~500 fs. We conclude this to be valid for all ferrous heme proteins, which is supported by a compilation of time-scales for other systems (Table 2-5). Of note are the two shorter time scales reported for various ligated heme proteins, which reflect the formation of the high spin (S=2) deoxyMb. The events of ligand recombination are instead specific to the NO ligand and are characterized by a reverse spin-cross-over (SCO) of the high spin (S=2) back to the ground state (S=1/2). When iron moves out of the heme plane into the domed form it has been suggested that it pushes on the His93 residue, which consequently triggers large scale conformational changes of the protein. This is called a "protein quake", which is proposed to open a channel for ligand-escape from the protein.[157,177] Our time-resolved non-resonant XES results show this is unlikely to be a very fast process, contrary to earlier studies which assumed it to occur on the time scale of the iron out-of-plane oscillation half period which is about 200-300 fs[178,179]. We propose this process is likely to happen on the time-scale of the spin-cross-over of approximately 800 fs.

For the time-resolved XAS study performed at SACLA, we established based on the work of Lima et al.[94], Silatani and coworkers[88] and DFT simulations (Figure 6-27) the sensitivity of different spectral regions (Figure 6-18). Namely: a) the pre-edge region (7110 - 7115 eV) which arises from dipole forbidden 1s → d_σ and 1s → $d_{\pi-\pi^*_{ligand}}$ transitions, which due to the low symmetry around the heme the pre-edge also gains intensity due to 3d/4p orbital mixing. Therefore, the pre-edge is mainly sensitive to the d-electronic configuration. b) The rising edge (7115 – 7131 eV), arising from the dipole allowed 1s → 4p transition, which grants its high intensity and due to orbital mixing of the 4p with 3d orbitals[88,94] it is sensitive to valence electronic structure, meaning oxidation state, ligation, both in number and type and spin state. [94,124,176,180] c) The post-edge (7131 – 7150 eV), which is sensitive to the local structure, in particular to the NO ligand presence (supported by DFT, Figure 6-27). Additionally, fluence scans measured at Alvra, SwissFEL, show that that in the post-edge region might have a potential fluence effect, whereas the pre-edge and main-edge region seem to be not affected and are therefore considered to only show one-photon excitation. Several potential effects of the high fluence causing changes only in the post-edge region which persist up to 100 ps are discussed: a) photoexcited deoxyMb species, b) thermal effects, c) photooxidation caused by multi-photon absorption. But the question for the effects of high pump-laser fluence remains open as all ideas (a-c) can be excluded.

The combination of the XES and XAS results gives us a comprehensive schematic overview of the dissociation and recombination processes in MbNO in Figure 6-28. A compilation of the obtained time constants is given in Table 6-1. Starting from ground-state (low spin, S=1/2) MbNO photo-excitation leads to the population of a π- π* state immediately and drives the dissociation of the nitric oxide ligand within <75 fs (rise-time at XAS edge_2) for about 55% of the molecules. The undissociated species undergo internal vibrational relaxation (IVR). Following the dissociated fraction, it reaches within ~110 fs (rise-time at XAS pre-edge, edge_1, post-edge) an excited triplet state. From here we can differentiate three distinct pathways for recombination of the NO to the heme. In pathway 1, the nitric oxide ligand stays in a close by heme pocket and recombines on a timescale of ~30 ps (time-decay at XAS pre-edge, edge_1 and edge_2). For pathway 2, the nitric oxide reaches a distant heme pocket and it takes around ~150-200 ps to recombine with the iron in the domed heme state.[88] And in pathway 3 the nitric oxide ligand leaves the protein and recombines on a much longer timescale of a few nanoseconds. [88] The hexacoordinated domed transition state formed by all three pathways relaxes back to the ground state (planar heme) in ~30 ps (obtained from TR-XES, Chapter 4) and its existence is supported by transient XAS spectra combined with DFT simulations.

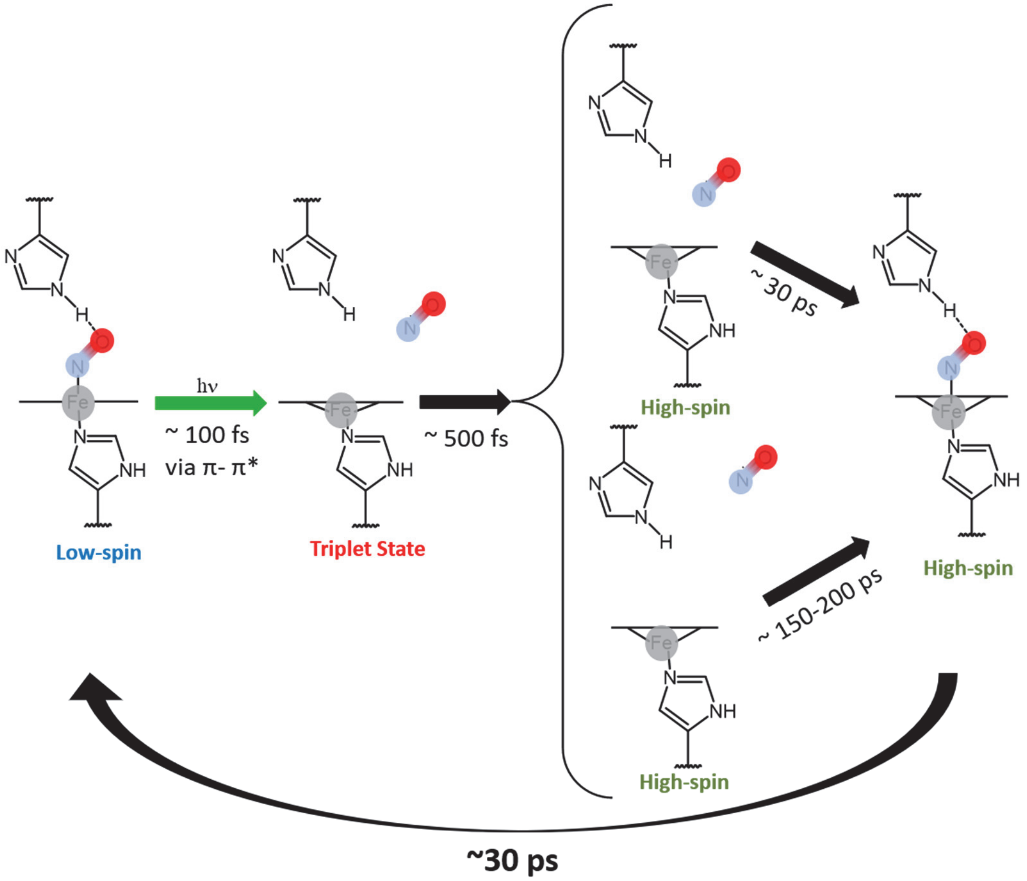

Figure 7-1: Schematic overview over the recombination kinetics in MbNO

Finally, it is important to highlight the unique capabilities of time-resolved X-ray spectroscopic techniques over the currently trending serial femtosecond x-ray scattering (SFX) [183,194], which works with crystalline samples while claiming to be close to physiological conditions[195]. The benefit of SFX lies in obtaining the structure of the whole protein at once, but it is limited in spatial resolution to a few Å (e.g. 1.8 Å for an experiment on MbCO[183] and 2.9 Å in the case of Bacillus thuringiensis[196]). For the case of myoglobin, Barends et al. performed SFX on MbCO and report structural changes throughout the protein within 500 fs after excitation, namely the C, F and H helices move away from the heme, whereas the E and A helices move towards the heme.[183] Often in nature very small effects have large impact on the function and properties of the protein, such as the doming of the iron in heme proteins which displaces the iron by about 0.4 Å, as shown in this work. Therefore, the combination of element selectivity, sub-Angström resolution and additional electronic information makes X-ray spectroscopy a unique and powerful tool for studying biological systems in physiological conditions. Nevertheless, SFX provides global structural information on the sample of interest which is currently not accessible by X-ray spectroscopic techniques. A combination of time-resolved XES and X-ray diffuse scattering (XDS) in a single experiment can be envisioned, where one could obtain both local electronic information from XES and structural information about the whole protein from XDS[197,198] could be obtained, but the data processing and analysis remains challenging up to now. Another option could be a separate X-ray spectroscopy and a separate SFX experiment, which would allow better understanding of both the local electronic structure of for example the metal active center and its surrounding from XAS and XES as well as detailed global structural information from SFX.

7.1 Future developments

Building up on the results and insights demonstrated in this thesis, a potential outlook of the project would be to perform a combined simultaneous XES and X-ray diffuse scattering (XDS) experiment to correlate the local electronic and spin changes from local (XES) to larger structural changes (XRD) and obtain information about solvation in heme proteins from the scattering experiment. Haldrup and coworkers have shown the feasibility of such an experiment on an iron complex[199], but it has not yet been applied to dilute biological systems with a larger structural complexity. The potential role of water in the oxygen binding kinetics in heme proteins was investigated by Collman et al.[200] with visible transient absorption (TA) and resonance Raman spectroscopy but it remains an open question if water may inhibit oxygen binding in heme proteins.

Another pathway would be to move towards more complex sample systems, repeating the same experiment performed in MbNO but with hemoglobin to get a deeper insight into cooperative effects like allostery[17,201]. This approach would require development on the experimental side to control oxygen partial pressure, while the measurement of time-resolved XAS and XES would yield detailed information cooperative oxygen binding in hemoglobin. Fundamental questions remain answered, such as postulated by Eaton et al.[202], for example, a quantitative structural explanation for the low oxygen affinity of the T-state in hemoglobin.

On technique development perspective, an important step would be the push towards time-resolved valence-to-core X-ray emission spectroscopy. March and coworkers performed a promising feasibility study[138]. Thanks to the advent of XFELs with very high pulse intensities and the availability of more crystals for the von Hamos spectrometers which greatly increase the emission collection efficiency (European XFEL provides up to 8 crystals, SACLA up to 6 crystals) we will potentially be able to measure even weaker signals like valence-to-core transitions (3% of the signal of K_β) . Those exhibit an even higher sensitivity to the chemical environment compared to core-to-core K_β emission. This might not seem relevant at first, but looking at the XES K_β study of Zhang et al.[161] we can see that for singlet, doublet and triplet spin state the observed changes in $K_{\beta1,3}$ emission are sufficient to differentiate them even in a time-resolved study as shown in this thesis. But if we look at the changes quartet to quintet the are minor and in cases where this is relevant it could be beneficial to have time-resolved valence-to-core XES as an available spectroscopic tool. It would potentially also allow for the mapping on weaker electronic density changes on top of spin transitions, that dominate the core-to-core emission spectra.

Chapter 8 Appendix

8.1 Fluence calculations (SACLA)

8.1.1 Calculations for the XAS measurements (SACLA)

Laser parameters:

Repetition rate = 15 Hz

Spot size x = 192 µm

Spot size y = 153 µm

Surface Area of the beam spot = 0.000230719 cm^2

Energy per pulse: 45 µJ

Fluence at focus (at sample position) = $= \frac{Energy\ per\ pulse}{Surface\ are\ of\ the\ beam} = \frac{0.045\ mJ}{0.000230719\ cm^2} = 195.04\ mJ/cm^2$

Energy of a single photon:

$$E = \frac{h * c}{\lambda}$$

Equation 8-1: Photon Energy

h = $6.63*10^{-34}$ J*s

c = $3*10^{8}$ m/s

$\lambda = 532\ nm = 5.32 * 10^{-7} m$

E = $3.73*10^{-19}$ J

Energy per pulse = 45 µJ

Only 66% of the beam hits the jet -> corrected Energy per pulse = $2.98*10^{-5}$ J

This equals $\underline{\underline{8.01*10^{13}\ \text{photons/pulse}}}$

Sample volume

V = (jet thickness) * (width of jet) * (height of beam)

V = 0.0001m*0.0001m*0.000153m = $1.53*10^{-12}$ m^3 = $1.53*10^{-9}$ dm^3

Avogadro constant = $6.02214*10^{23}$

Number of molecules (4mM) in probed volume = $3.68555*10^{12}$

Ratio of photons per molecule (without including absorption cross section): 21.7

Ratio of photons per molecule (including absorption cross section): **13**

8.1.2 Calculations for the XES measurements (SACLA)

This includes also three XAS measurements which were performed with the 200 µm thick round jet.

Laser parameters:

Repetition rate = 15 Hz

Spot size x = 192 µm

Spot size y = 153 µm

Surface Area of the beam spot = 0.000230719 cm^2

Energy per pulse: 45 µJ

Fluence at focus (at sample position) = $= \frac{Energy\ per\ pulse}{Surface\ are\ of\ the\ beam} = \frac{0.045\ mJ}{0.000230719\ cm^2} = 195.04\ mJ/cm^2$

Energy of a single photon:

Above is explained how the photon energy is calculated. And the same calculation as in Section 8.1.1 was performed to obtain the photons per pulse:

$8.01*10^{13}$ photons/pulse

Sample volume

V = jet thickness*width of jet*height of beam

V = 0.0002m*0.0001m*0.000153m = $1.53*10^{-12}$ m^3 = $6.12*10^{-9}$ dm^3

Avogadro constant = $6.02214*10^{23}$

Nr of molecules (4mM) in probed volume = $1.47422*10^{13}$

Ratio of photons per molecule (without including absorption cross section): 5.4

Ratio of photons per molecule (including absorption cross section): **3.2**

8.2 Data Processing and Treatment

8.2.1 XES Raw Data Processing

The XES data is recorded as 2D images on a position sensitive detector and an example image recorded at EXFEL is shown in Figure 8-1. At y=20 and x=90 we can see a bright spot corresponding to $K_{\alpha1}$ and on the right side of it at x=180 we find the weaker $K_{\alpha2}$ line.

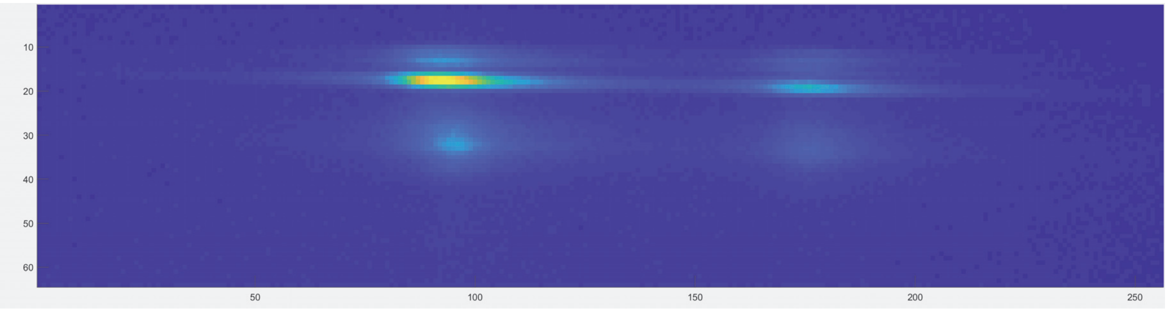

Figure 8-1: Raw XES K_α image recorded at EXFEL for illustration. Clearly visible is the yellow $K_{\alpha1}$ peak and next to it on the right side the weaker $K_{\alpha2}$ peak. The units of the x and y axis are pixels and the sample is $Fe(bpy)_3$. Detector: GreatEyes.

The first step of data processing is to select the region for summing up the signal. For optimal signal-to-noise a small region (in y) is selected, covering only the region of maximum signal. An example is shown in Figure 8-2 marked with a red rectangle. To remove any potential scattering background, electronic noise and other noise sources a region away from the signal, for simplicity with the same number of pixels, is chosen as a background (marked in green in Figure 8-2).

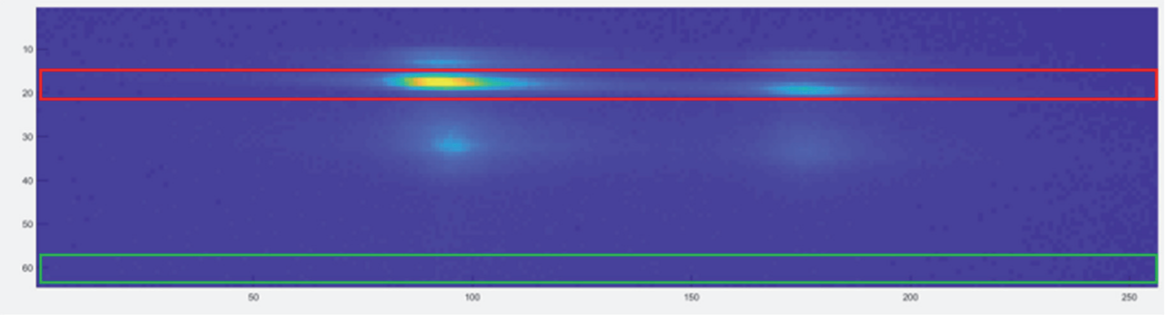

Figure 8-2: Raw XES K_α image recorded at EXFEL with the integration regions indicated in red and green. Red is the signal region, green the region for the background. The units of the x and y axis are pixels and the sample is MbNO. Detector: GreatEyes.

After the red and green regions in Figure 8-2 are summed up along their y-axis and the background (green) is subtracted from the signal (red), we obtain the spectra shown in Figure 8-3.

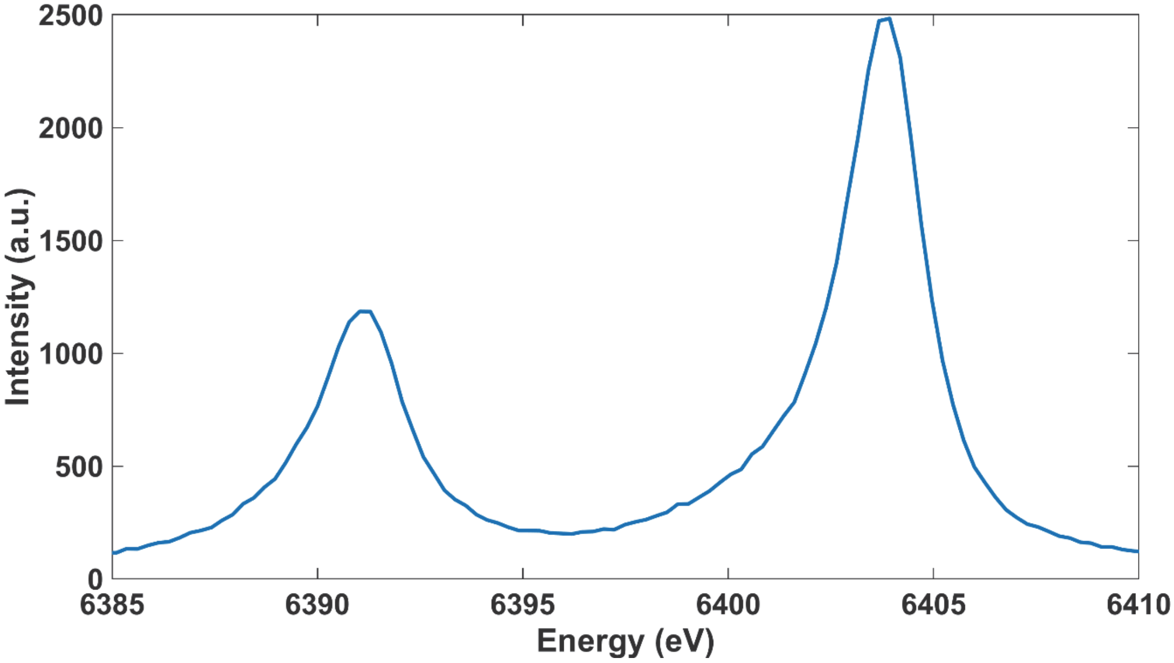

Figure 8-3: XES K_α spectrum of MbNO in physiological solution for illustration of the data processing.

8.2.2 Energy Calibration XES

The XES spectra we obtained from summing up and subtracting the background are then energy calibrated using reference spectra from Zhang et al.[161] for XES K_β and from Vankó et al.[203] for XES K_α. For the case of XES K_α the difference between the $K_{\alpha 1}$ and $K_{\alpha 2}$ peak of $Fe(bpy)_3$ was used to reference the pixels to energy. For XES K_β the FWHM of the $K_{\beta 1,3}$ line of $Fe(bpy)_3$ was compared to literature[161] to obtain the pixel to energy conversion factor and the absolute X-ray energies. Once the calibration was obtained it was applied to all other measured spectra.

8.2.3 Smoothing

All plots which are specified as smoothed, are smoothed using a 5-point moving average filter to make trends more visible. The first few elements of yy follow:

yy(1) = y(1)
yy(2) = (y(1) + y(2) + y(3))/3
yy(3) = (y(1) + y(2) + y(3) + y(4) + y(5))/5
yy(4) = (y(2) + y(3) + y(4) + y(5) + y(6))/5
...

8.2.4 XAS Raw Data Processing

The XAS data presented in this work is normalized with I_0, the incoming X-ray probe pulse intensity on a shot-to-shot bases to correct for intensity fluctuations. As indicated in the plots the data is then presented either in its original way or scaled for comparison with other data.

8.2.5 Fitting of the Time-Traces

We are assuming a sequential kinetic scheme, for which the temporal evolution of the sample is follows a sequence of events (rise or decays). Those events can be described by specific first-order decay rates k_i and the corresponding lifetimes τ_i for which the kinetic response can be modelled by a sum of N model functions:[165]

$$\Delta A(t) = e^{-k_i t} \oplus IRF(t) =$$

$$= \frac{1}{2}\sum\nolimits_{i=1}^{N} a_i * e^{\frac{1}{\tau_i}*(\mu-t)+\frac{(\sigma*\frac{1}{\tau_i})^2}{2}} *$$

$$* \left[1+\operatorname{erf}\left(\frac{t-\left(\mu+\frac{1}{\tau_i}*\sigma^2\right)}{\sqrt{2}*\sigma}\right)\right]$$

Equation 8-2

Where a_i is the amplitude of the ith decay, $\oplus$ indicates convolution, τ_i describes the decay time, which corresponds to $\frac{1}{k_i}$, μ the time origin of the IRF (time-zero) and σ its width.[165] Combinations of N=1 to N=4 were fitted and the best fit was chosen according to least correlated lifetimes and amplitudes larger 0.01, as well as quality of the fits.

Every time-point of the XAS time-traces corresponds to 1,000 XFEL shots (half pumped, half unpumped) per run, and for each time-trace presented 1-3 runs were acquired. Each time-point of the XES time-traces is an average of three to six individual scans, one scan corresponds to accumulation over 10,000 XFEL shots. For the K_β XES, the line of the averaged laser-on (pumped) spectra (Figure 5-9 & Figure 5-10) was fitted with a Gaussian function (Equation 8-3, Figure 5-2) for each time delay and its peak maximum (b in Equation 8-3) was used to determine the shift in eV.

$$y = a * e^{\left[-\left(\frac{x-b}{\sigma}\right)^2\right]}$$

Equation 8-3

Where a is the amplitude, b is the centroid and σ is related to the peak width.

The obtained time trace was normalized to the maximum shift (~0.45 eV). For the K_α XES, the line was fitted with a Gaussian function (Equation 8-3) to obtain σ, which was also normalized.

We are assuming a sequential kinetic scheme, for which the temporal evolution of the sample follows a sequence of events (rise or decays). Those events can be described by specific first-order decay rates k_i and the corresponding lifetimes τ_i for which the kinetic response can be modelled by a sum of N model functions.[165]

8.3 Additional Information -XES

The contributions to Chapter 5 (XES of MbNO) are the following:

M. Chergui conceived the project. D. Kinschel, M. Chergui, C. Bacellar and O. Cannelli designed the experiment. D. Kinschel, C. Bacellar, O. Cannelli, B. Sorokin prepared and planned the experiment at BL3, SACLA, Japan. D. Kinschel, C. Bacellar, O. Cannelli, B. Sorokin, T. Katayama, Y. Obara, H. Ito, T. Ito, J. Nishitani, C. Higashimura, S. Kudo, M. Yabashi and N. Kurahashi carried out the measurements at BL3, SACLA; Japan. D. Kinschel and F. Lima prepared and planned the experiment at European XFEL, Hamburg, Germany. D. Kinschel, C. Bacellar, O. Cannelli, B. Sorokin, G.F. Mancini, J. Budarz, F.A. Lima, W. Gawelda, P. Zalden, S. Schulz and D. Khakhulin performed the experiments at European XFEL, Hamburg, Germany. T. Penfold and T. Keane performed the DFT simulations. D. Kinschel processed and analysed the data with the help of C. Bacellar, J. Rouxel and M. Chergui. J. Rouxel calculated the kinetic model. D. Kinschel and M. Chergui wrote the manuscript. All authors discussed the results and contributed to the manuscript.

8.3.1 Kinetic Model

To estimate the decay rate from the excited triplet state to the quintet state using the K_β transient spectra in the time range of 0.26 to 3.16 ps (Figure 5-11 and Figure 5-12), we use a simple 3-level kinetic model (Figure 5-21), with decay rates of $\Gamma_{LUMO\rightarrow triplet}$ and $\Gamma_{triplet\rightarrow quintet}$, for the Q-state (LUMO) of the porphyrin and triplet levels, respectively. The master equation of the model is

$$\frac{d}{dt}\begin{pmatrix} \rho_{Q-state(t)} \\ \rho_{Triplet(t)} \\ \rho_{Quintet(t)} \end{pmatrix} = \Gamma * \begin{pmatrix} \rho_{Q-state(t)} \\ \rho_{Triplet(t)} \\ \rho_{Quintet(t)} \end{pmatrix}$$

Equation 8-4: Master equation.

Where Γ is defined by

$$\Gamma = \begin{pmatrix} -\Gamma_{Q-state\rightarrow Triplet} & 0 & 0 \\ \Gamma_{Q-state\rightarrow Triplet} & -\Gamma_{Triplet\rightarrow Quintet} & 0 \\ 0 & \Gamma_{Triplet\rightarrow Quintet} & 0 \end{pmatrix}$$

Equation 8-5

From fluorescence up-conversion measurements[59] $\left(\Gamma_{Q-state\rightarrow Triplet}\right)^{-1} = 100\ fs.$

The boundary conditions are: 100% Q-state population, 0% population of the Triplet and Quintet state population at t=0. Solving the system of differential equations provides the time evolution of $\rho_{Triplet}(t)$.

$$\rho_{Triplet}(t) = \frac{\Gamma_L}{\Gamma_L - \Gamma_T} * \left(e^{-t*\Gamma_T} - e^{-t*\Gamma_L}\right)$$

Equation 8-6

$$\rho_{Quintet}(t) = \frac{\Gamma_L}{\Gamma_L - \Gamma_T} * \left(1 - e^{-t*\Gamma_T}\right) - \frac{\Gamma_T}{\Gamma_L - \Gamma_T} * \left(1 - e^{-t*\Gamma_L}\right)$$

Equation 8-7

with $\Gamma_L = \Gamma_{Q-state\rightarrow Triplet}$ and $\Gamma_T = \Gamma_{Triplet\rightarrow Quintet}$.

The data points are the mean of seven points (7053.0 to 7054.0 eV) in Figure 5-12. The means are plotted in Figure 5-22 and fitted assuming that the relaxation after t_0 is proportional to the population of the triplet state. The derived triplet to quintet relaxation time is $\tau_{triplet\rightarrow quintet}$ = 500± 250 fs. Figure 5-22 shows the fit together with the 90% confidence bands. Figure 5-23 shows the evolution of Q-state, triplet and quintet populations derived from the kinetic model. It can be seen, that the quintet state rises in approximately 700 fs.

8.3.2 Further insight into the XES K_α DFT simulations

In Chapter 5 the DFT simulated triplet state structure is calculated using the deoxyMb crystal structure, but the real structure at 300 fs is not exactly known and as the reference spectra used to interpret the K_β results are all from hexacoordinate iron complexes they don't allow further insight. Therefore, we simulated a DFT XES K_α spectrum of the MbNO crystal structure without NO. Figure 8-4 shows the XES K_α spectra of three different species, the deoxyMb form in the quintet (red) and triplet state (blue) compared to the MbNO without NO in the triplet state (planar heme) in yellow. Comparing the triplet state (planar heme) spectrum to the experimental spectrum at 0.26 ps in Figure 5-17 it seems the heme is not in a planar configuration as the spectra look very different.

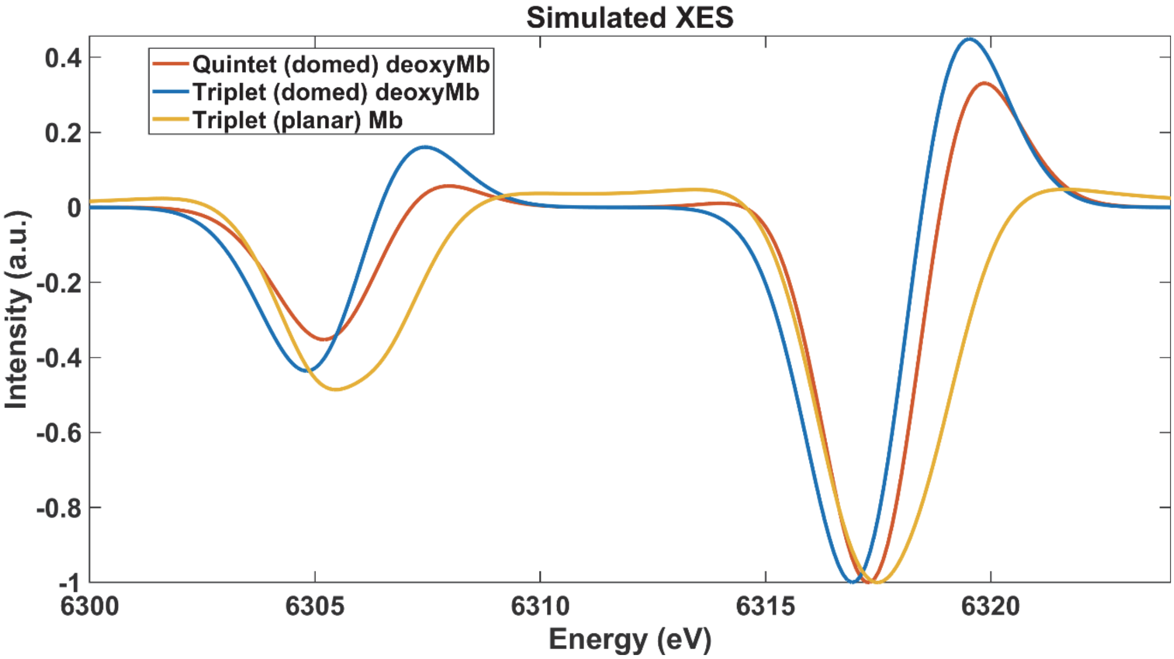

Figure 8-4: DFT simulated K_α XES transient spectra of different Mb species. The spectra are scaled to the negative transient feature at 6317 eV and were derived as described in § 5.2.8. In red the transient spectrum of deoxyMb in the quintet spin state is plotted (domed heme), in blue the transient spectrum of deoxyMb in the triplet spin state (domed heme) is

plotted and in yellow the transient spectrum of MbNO, where NO was removed in the triplet spin state (planar heme) is plotted.

For further analysis linear combinations of the transient DFT XES K_α spectrum of MbNO without NO (Mb) in the triplet state with a planar heme and the transient spectrum of deoxyMb in the triplet state with a domed heme were calculated and plotted in Figure 8-5. In addition, the corresponding local structure around the Fe is shown for the planar and domed configuration on the left in Figure 8-5 and with red boxes the regions of highest sensitivity to domed vs. planar structure are highlighted (A, B, C).

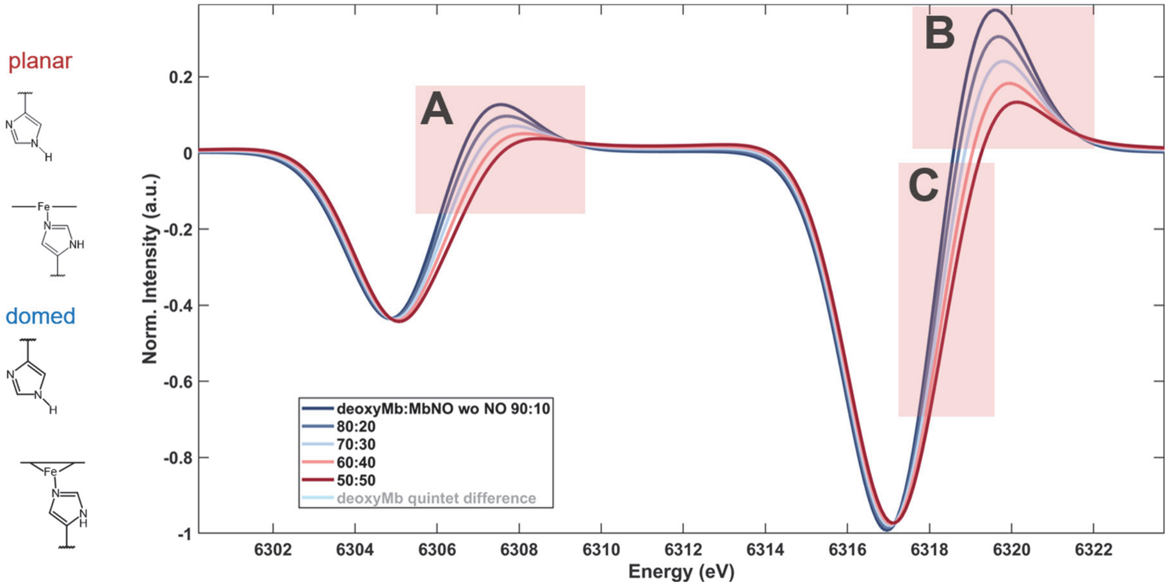

Figure 8-5: DFT simulated K_α XES transient spectra of different linear combinations of deoxyMb (triplet) and MbNO without NO (triplet) transient spectra. The spectra were derived as described in § 5.2.8 before the linear combinations were calculated. In blue the transient spectrum of 90% deoxyMb in the triplet spin state (domed heme) and 10% Mb in triplet state (planar heme) is plotted and in red the transient spectrum of a mixture of 50% deoxyMb in the triplet spin state (domed heme) and 50% Mb in the triplet state (planar heme) is plotted. In addition, the ratios of 80:20, 70:30 and 60:40 domed:planar are shown. And on the left the corresponding structures around the iron atom are illustrated. The marked regions (A, B, C) highlight the areas showing the largest changes between domed and planar heme.

From comparison of the spectra shown in Figure 8-5 to the experimental K_α XES transient spectra (Figure 5-17) the best agreement was found between the 80:20 domed:planar triplet state spectrum of Figure 8-5 and the 0.26 ps spectrum of Figure 5-17. The result is shown in

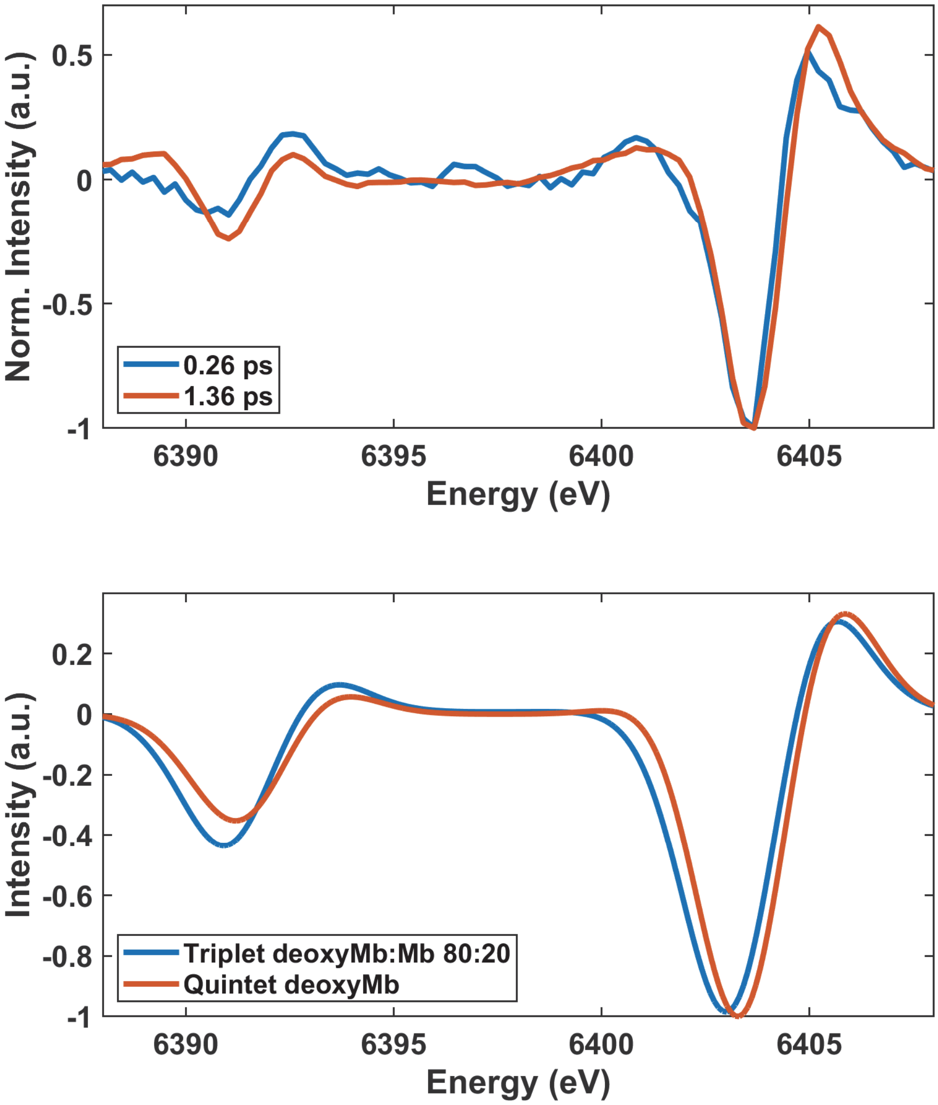

Figure 8-6: (a) Transient XES K_α spectra at 0.26 and 1.36 ps showing a blue shift of the positive $K_{\alpha1}$ transient feature (6405 eV) from 0.26 ps to 1.36 ps, and the presence of a positive dip at 6393 eV at 0.26 ps, which vanishes for later times (1.36 ps). (b) XES K_α difference spectra derived from DFT simulated XES K_α spectra: triplet (80% domed and 20% planar) minus doublet (blue), quintet minus doublet (red). Details can be found in § 5.2.8.

8.3.3 Additional Plots

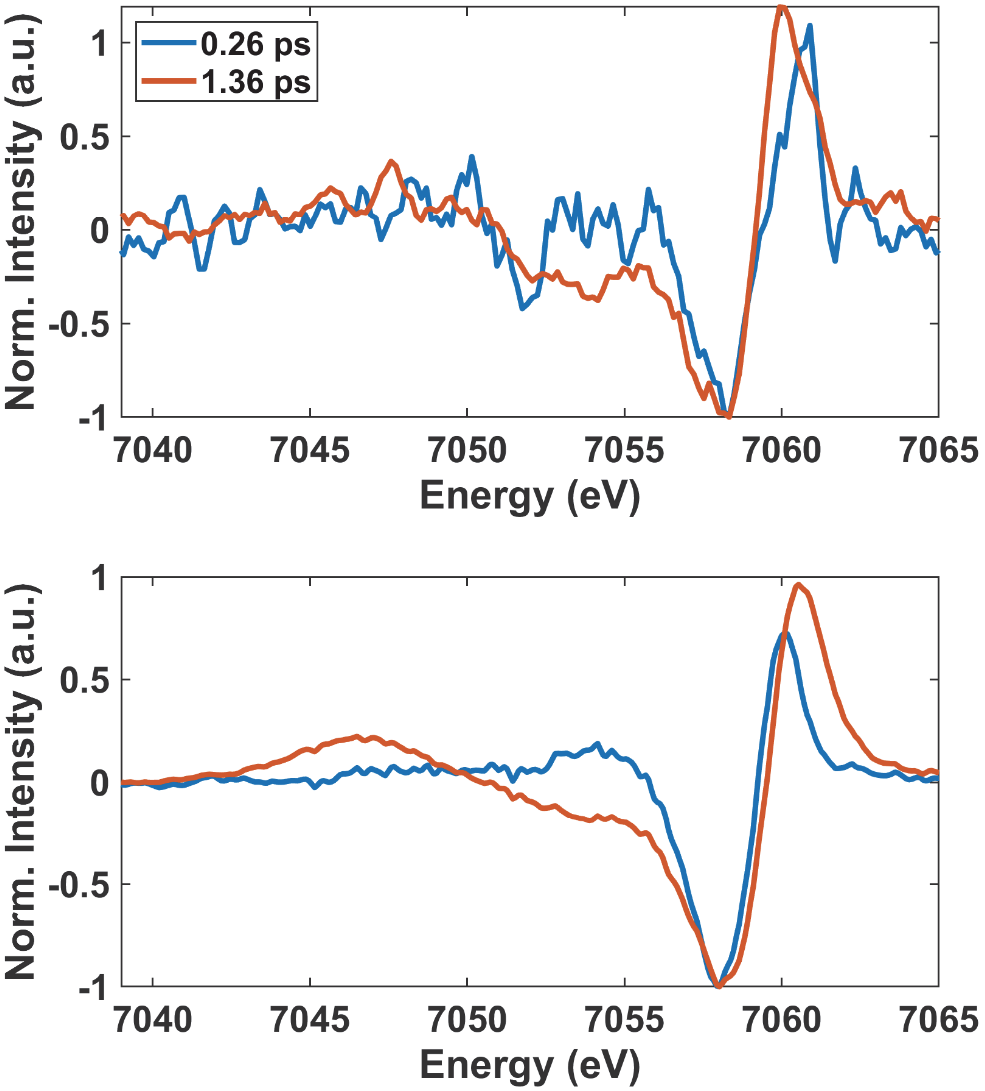

Figure 8-7: Same as Figure 5-11 but with an extended energy range. (a) Transient XES K_β spectra of MbNO in a physiological solution at pump-probe time delays of 0.26 and 1.36 ps. (b) Difference of steady-state XES K_β spectra from ref.[161]: triplet minus doublet (blue), quintet minus doublet (red), using the reference spectra of Fe(II)phthalocyanine (triplet state), $[Fe(2,2'\text{-bipyridine})_3]^{3+}$ (doublet state) and $[Fe(phenanthroline)_2(NCS)_2]$ (quintet state), and taking into account NO dissociation quantum yield (Details can be found in § 5.2.8).

8.4 Additional XAS Plots (SACLA)

8.4.1 Comparison of Static XAS (SACLA) to Literature

The static XAS spectra measured at SACLA are compared to literature[94] in Figure 8-8. Experimental conditions for these measurements are listed in section 4.1.1. The overlap of these spectra was used to determine the energy calibration of all XAS data, as the reference measurement at SACLA was done only with a Ni foil long before our measurement.

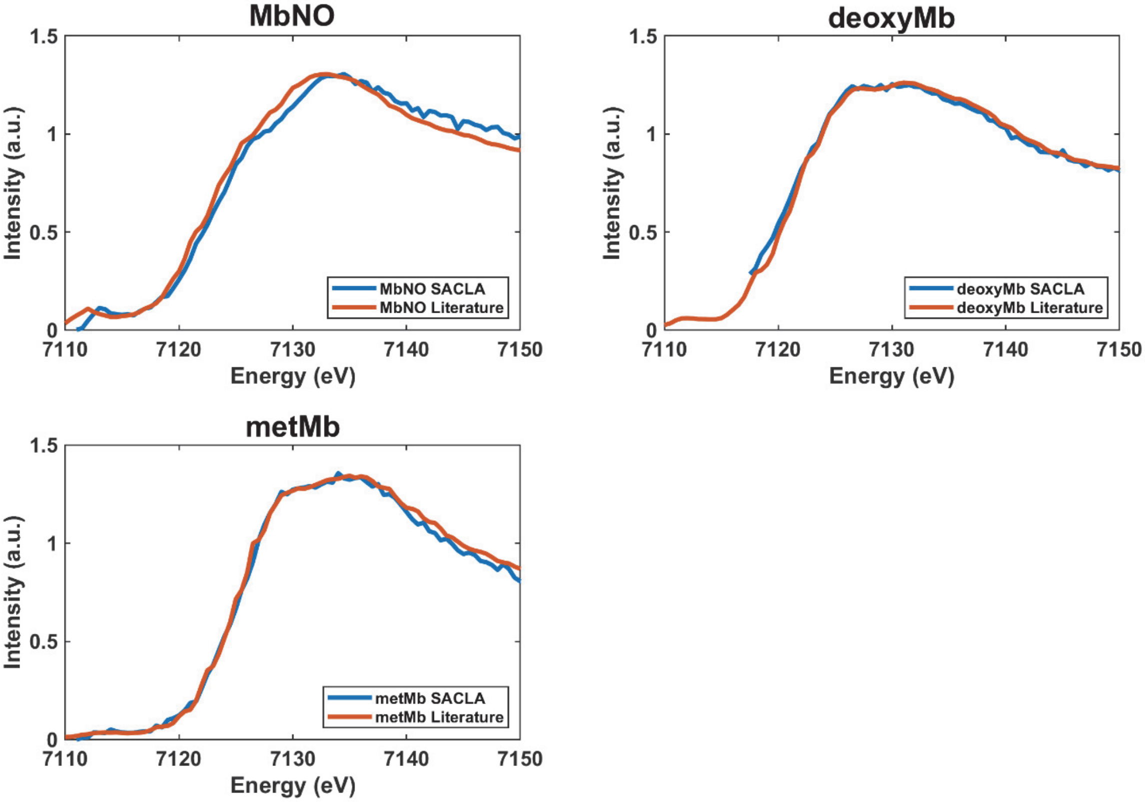

Figure 8-8: Comparison of static XAS measurements (blue) to published spectra (red) from Lima et al.[94] The spectra are in good agreement within their signal to noise. At SACLA no measurement over a larger energy range was performed, therefore the SACLA data is I_0 normalized and offset corrected, but not background corrected. This can be the reason for small deviations in the case of MbNO. The SACLA spectra are shifted by +1 eV in energy to match with literature.

8.4.2 GVM Calculation for Different Jet Thicknesses

To estimate the expected temporal resolution of the experiments carried out at SACLA we consider the group-velocity mismatch (G_{VM}) between the X-rays and the laser in the liquid jet. The G_{VM} was calculated using the following equation:

$$G_{VM} = \frac{d_{jet}}{c} * (n_L - n_X)$$

Equation 8-8: Group-velocity-mismatch

Where d_{jet} is the thickness of the jet, c is the speed of light, n_L is the refractive index for the 533nm laser light and n_X is the refractive index for the X-rays. Using d_{jet} = 100 and 200 µm, n_X = 1 and n_L = 1.33 from ref.[204] we obtain a G_{VM} of 133 fs for the 100 µm thick jet and 267 fs for the 200 µm thick jet.

8.4.1 Absorbance at Different Jet Thicknesses

The Absorbance (sometimes also referred to as optical density) of a 4 mM solution of MbNO at 532 nm in a 100 µm cuvette was found to be 0.4. From this, using Beer-Lamberts law () we can calculate the molar attenuation coefficient:

$$A = \varepsilon \times c \times d$$

Equation 8-9: Beer-Lambert law

Where A is the Absorbance, ε is the molar attenuation coefficient, c is the concentration and d is the thickness of the sample. Using d = 100 µm, c = 4 mM and A = 0.4 we get a molar attenuation coefficient for MbNO at 532 nm of ε = 10,000. From this we can calculate the Absorbance for d = 200 µm, which is A = 0.8. The transmission of 532 nm light for the 100 µm jet is 39.8 % and for the 200 µm jet it is 15.8 %.

8.4.2 IRF of Different Jet Thicknesses

The rise of the XAS signal at 7127 eV (Edge_2) was recorded with two different liquid jet thicknesses, 100 µm and 200 µm. In addition, the rise at this energy with the 100 µm jet appears IRF limited, as there are no points on the signal rise shown in Figure 8-9. Therefore the influence of the jet thickness on the rise time of the signal and the IRF can be seen in Figure 8-10, which shows the time-scan under the same conditions, but with a 200 µm liquid jet. The comparison of the two time traces (Figure 8-9 and Figure 8-10) shows that the IRF increases from ~75 fs for a 100 µm thick liquid jet to ~150 fs for a 200 µm thick liquid jet.

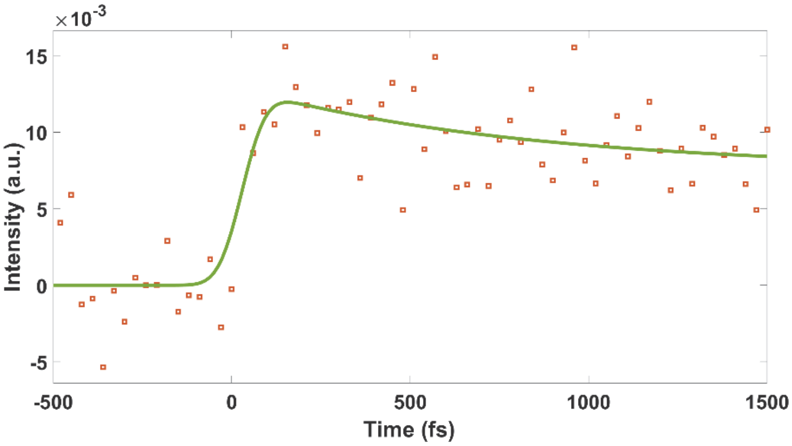

Figure 8-9: XAS rise of MbNO using a 100 µm jet at 7127 eV (Edge_2) with a biexponential fit (green). The obtained time constants are: τ_{rise} = 75 ± 35 fs and τ_f = 800 ± 1150 fs. The errors on the time constants are 1σ. 30 fs binning applied.

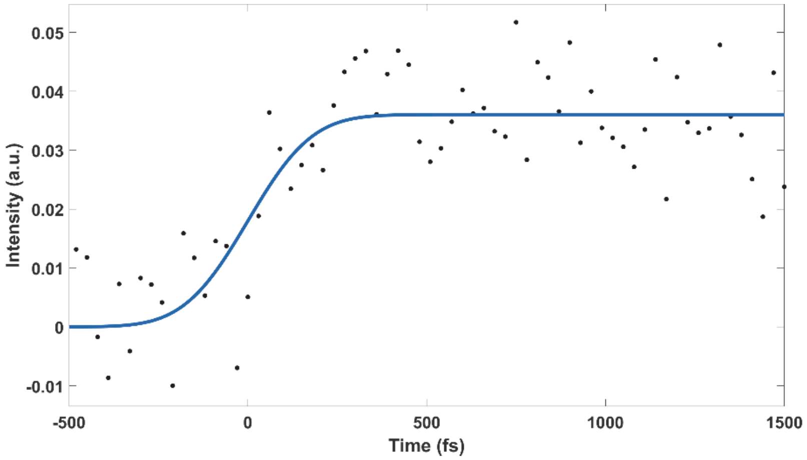

Figure 8-10: XAS rise of MbNO using a 200 µm jet at 7127 eV (Edge_2) with a single-exponential fit (blue). The obtained time constant is: τ_{rise} = 150 ± 39 fs. The error on the time constant is 1σ. 30 fs binning applied.

8.5 DFT Simulations

All DFT XES and XAS spectra have been simulated by Thomas Penfold and Theo Keane (Chemistry-School of Natural and Environmental Science, Newcastle University, Newcastle upon Tyne, NE1 7RU, England). Further analysis using the DFT simulated spectra was performed by D. Kinschel.

8.5.1 Experimental Details (DFT)

The calculations use the CAM-B3LYP exchange-correlation functional. Scalar relativistic effects were included using the second-order Douglas-Kroll-Hess Hamiltonian (DKH2), including picture change and finite-nuclear effects. The def2-TZVP basis set, reparametrized for use with DKH (DKH-def2-TZVP) was applied. Density fitting of the Coulomb and exchange integrals was employed using the resolution-of-the-identity chain-of-spheres approach (RIJCOSX), with the appropriate def2/JK auxiliary basis set. To approximate the effects of screening by the protein environment, a polarizable continuum model was applied using the conductor-like screening model (COSMO), using the same parameters as for toluene, in accordance with the low average dielectric constant within the interior of proteins.[171–173] Spin-orbit coupling was included using the one-electron mean-field/effective potential approach. To ensure proper description of the core electrons, the accuracy of the radial integral grid in the vicinity of the Fe-atom was increased to Orca's grid 7. All calculations were performed using Orca, version 3.0.3.[174,205] The geometry employed in the calculations was based on the PDB entry 2FRJ for MbNO and dissociated, but not domed Mb calculations, for which the NO was removed, and PDB entry 2V1K for deoxyMb calculations. Figure 5-4 overlays the structure of MbNO (red, PDB entry 2FRJ) and deoxyMb (green, PDB entry 2V1K) used in the present work. This highlights the main (as expected) structural differences that are probed in the ultrafast XES study.

It is stressed that the DFT calculations do not reproduce absolute energies and the presented spectra are shifted for comparison to the experimental data. Furthermore, we do not reproduce the asymmetry of the spectral lines. This is due to the fact the DFT functional used here does not fully account for electron-electron correlations, which are responsible for the sidebands, as shown in atomic multiplet calculations.[175] Therefore, while full line shapes do show deviations between theory and experiment, the relative changes reproduce the experimental trends, as seen in Figure 5-5 where changes in peak intensity and shifts between deoxyMb and MbNO are compared with those of the calculations .

8.5.2 DFT Spectra

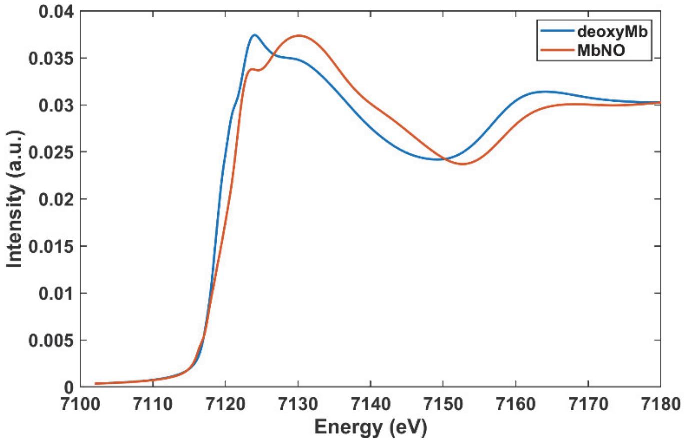

Figure 8-11: DFT simulated XAS spectra of deoxyMb (blue) and MbNO.

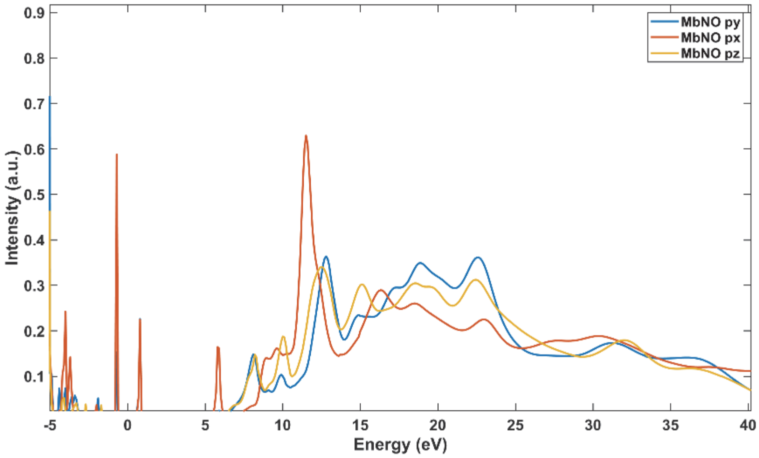

Figure 8-12: Density-of-States of the p orbitals in MbNO, obtained from DFT simulations.

Table of Figures

Figure 2-1: (a) Myoglobin with the heme as active center as stick structure, a globular protein (PDB: 2FRJ); (b) Potassium channel with potassium ions (purple) moving through the pore in the center, a membrane protein (PDB: 1BL8); (c) Keratin, a fibrous structural protein (PDB: 3TNU). 21

Figure 2-2: (a) General structure of an α-amino acid. The atoms are labelled, and R stands for side chain. (b) Histidine structure with its imidazole side chain......... 22

Figure 2-3: (a) Full chemical structure of the first ten amino acids of myoglobin connected by peptide bond (highlighted in blue) (b) One letter code corresponding to each of the ten amino acids (H indicates the beginning of the chain).. 23

Figure 2-4: (a) “Shorthand” α-Helix; (b) α-Helix with the structure of the amino acids shown as sticks, C (grey), N (blue), O (red), Hydrogen bonds (magenta). Shown are the first 16 amino acids of Myoglobin (PDB: 2FRJ); (c) “Shorthand” β-Strand; (d) β-Strand with the structure of the amino acids shown as sticks, C (cyan), N (blue), O (red). β-Strand is taken from Inward-rectifier potassium channel (PDB: 1N9P) and represents an eight amino acid sequence (Q_{310}-E_{317}). (e) β-Sheet consisting of 5 β-Strands from human C (cyan), N (blue), O (red), H (white), Hydrogen bonds (magenta). PCNA (PDB: 1AXC). 23

Figure 2-5: (a) Myoglobin-NO tertiary structure (dark blue), heme is highlighted as stick structure, C (green), N (blue), O (red), PDB: 2FRJ; (b) Trypsin ribbon showing the three-dimensional arrangement of α-Helices and β-Strands, PDB: 1FXY; (c) Myoglobin-NO surface representation, with its open pocket containing the heme; (d) Myoglobin-NO space filling model, the different colors mark the different α-Helices (Figure 2-1a). PDB: 2FRJ. 24

Figure 2-6: Ribbon structure of Hemoglobin, which is a tetramer of four polypeptide chains (two so called α chains and two β chains). The hemes are presented as stick structures. PDB: 1GZX 25

Figure 2-7: (a) Shorthand line structure of heme B with atomic numbering for the ring carbon atoms. Important are the functional groups in positions 3, 8 and 18. (b), (c), (d) Different views on the heme stick structure in Myoglobin-NO, carbon (grey), nitrogen (blue), oxygen (red), iron (orange). PDB: 1HJT. In (c) the plane of the porphyrin ring is clearly visible as well as the distal histidine residue under the iron and the nitric oxide (NO) in the proximal position. 26

Figure 2-8: Chemical structure of α-farnesene 27

Figure 2-9: Structure of Myoglobin-NO, the heme b, the proximal His93, the distal His64 and the NO ligand are highlighted as stick structure. PDB: 2FRJ 28

Figure 2-10: Ribbon structures of the α- and β-chain of horse methemoglobin (PDB: 1NS9) and Human myoglobin (PDB: 3RGK) and in the bottom right the overlap of all of them. The α- and β-chain of horse methemoglobin share 64 residues of their approximately 140 amino acids. Myoglobin and the α-chain of hemoglobin have 38 amino acid sequence identities. This strong degree of homology is also reflected in the tertiary structure which is shown in the bottom right. 29

Figure 2-11: Overview over the heme structure in different forms of myoglobin: MbNO (PDB: 2FRJ), deoxyMb (PDB: 2V1K), metMb (PDB: 2MBW), MbO_2 (PDB: 1MNO). Shown is the heme plane from the side with the His64 and His93 side chains. Grey (C), blue (N), red (O), orange (Fe). 29

Figure 2-12: Schematic diagram of the electron configuration of the d-orbitals of Iron (Fe) in different forms of Myoglobin, their multiplicity (S) and in brackets the ligands (deoxyMb[37], metMb[38], MbO_2[39], MbCO[40], MbCN[41], MbN_3[42]). On the right side the schematic structure is shown of the domed deoxyMb (top) and the planar Mb geometry (bottom). 30

Figure 2-13: Crystal structure of the Nitrosyl-Myoglobin (MbNO). The heme is highlighted as sticks (Fe [orange], C [grey], N [blue], O [red]). PDB: 1HJT. The zoom (left) shows the distal NO ligand and proximal histidine 93 (His93), which links the Fe atom of the heme porphyrin to the F helix. 31

Figure 2-14: Molecular Orbital diagram of MbNO. Adapted from Morse R. H. et al.[43] 32

Figure 2-15: UV-VIS spectra of solutions of deoxyMb, metMb and MbNO measured in a quartz cuvette. The region of 500-650 nm contains the Q-bands and the region of 3700-460 nm the soret-band. 35

Figure 2-16: Overview of photocycle for the dissociation and recombination of MbNO suggested by previous experiments. 37

Figure 2-17: XAS transient spectra of MbNO at 70 ps time-delay. Presented are two series of measurements (series I: red, series II: black) and the static difference spectrum in blue (deoxyMb minus MbNO). Norm. Trans. Abs., normalized transient absorption. From Silatani et al.[85] 38

Figure 3-1: (a) Scheme of pump-probe spectroscopy showing the pump pulse (green) and the probe pulse (black) and the time delay (Δt) between the two. After interaction at the sample cell (cuvette) the probe pulse can be detected in transmission (I_F) or fluorescence from the sample (I_F). (b) Reaction coordinate diagram showing a reaction starting from the reactant (A), which reacts via two transition states and one intermediate state to the product (B) along the reaction coordinate. 41

Figure 3-2: Overview of dynamic events happening at femto to micro second time-scales. An electron orbital jump refers to an electron absorbing energy and "jumping" to a higher orbital. Information from Turro et al.[109] 42

Figure 3-3: Transitions contributing to XAS absorption edges. (By Atenderholt at English Wikipedia, CC BY-SA 3.0, https://commons.wikimedia.org/w/index.php?curid=38941860). 44

Figure 3-4: : XAS spectrum of the K-edge of Fe(II) in MbNO in solution illustrating the two regions: the low-energy XANES region up to ∼50 eV above the ionization potential and the high-energy EXAFS region >7170 eV. 45

Figure 3-5: Simplified representation of XAS and XES. Static spectra in the top right are MbNO in physiological solution measured at SACLA. 46

Figure 3-6: Energy level diagram showing the origin of the K_α and K_β fluorescence after creation of a hole in the 1s (K) shell. The $K_{\alpha1}$ and $K_{\alpha2}$ lines (green) originate from the splitting of the 2p orbital ($2p_{1/2}$ and $2p_{3/2}$), whereas for K_β these lines are degenerate, resulting in the line labelled $K_{\beta1,3}$ (red). The valence-to-core transition is responsible for the $K_{\beta2,5}$ line (purple). The resulting spectra for all these transitions for the case of MbNO are shown in Figure 3-7. 47

Figure 3-7: Static XES spectra of iron in MbNO in physiological medium to illustrate the different emission lines and their intensities. The corresponding transitions are shown in the energy level diagram in Figure 3-6 and are colour coded. 48

Figure 3-8: (a) von Hamos geometry (top view, along the dispersive plane) for iron Kα and Kβ emission measurements. Θ is the Bragg angle. (b) Schematic of the von Hamos geometry (side view), illustrating the dispersion and focusing directions of the crystal and the energy range (ΔE) covered by the crystal. (c) Projection along the focusing plane, R is the radius of the curvature. The grey area illustrates the solid angle which defines the collection efficiency. Figure adapted from ref.[143] 49

Figure 3-9: Scheme of an X-ray Free Electron Laser (XFEL). After acceleration of an electron bunch to relativistic velocities, it travels through the undulator section, where it is forced to wiggle by electromagnetic fields and emits X-ray radiation. After the undulator section the electrons are dumped into an electron dump and the tunable X-rays can be used for experiments. 50

Figure 3-10: Illustration of self-amplification of spontaneous emission (SASE) in an undulator. SASE results from the interaction of the electrons with the X-ray radiation they emit. In the bottom left and middle part of the figure, the micro-bunching (longitudinal density modulation) of the electron bunch is shown.

Micro-bunching results in an exponential growth of the X-ray radiation power during the travel through the undulators. It is important to note that in reality the number of micro-bunches is much larger (>10^5). From ref.[8] 51

Figure 4-1: (a) Experimental Setup at BL3, SACLA, Japan. XAS was recorded in total fluorescence yield (TFY). XES Kα and Kβ were recorded with two crystals each in Von Hamos geometry and the laser pump and X-ray probe beam were close to colinear. (b) Photograph of the inside of the experimental chamber illustrating the beam path of X-rays and pump-laser, the liquid jet, catcher and the XAS (TFY) diode. The XES crystals were placed outside of the chamber and are not visible in the photograph.. 53

Figure 4-2: Rise time of the X-ray absorption transient signal of MbNO at 7127 eV (dots). The red trace is a fit to obtain the IRF of the experiment (see § S6), which is σ = 150 fs. 53

Figure 4-3: Original flow cell design from Lima F.[156] 58

Figure 4-4: Novel 3D printed diamond flow cell. Left: mounted and in operation. Right: 3D drawing. 58

Figure 4-5: (a) Quartz capillary mount including pinhole. (b) 3D drawing showing the two parts separate. (c) Current design of the liquid jet at European XFEL, one can see the glass capillary the metal catcher with the sample reservoir right below. The yellow area is where the Kapton foil can be attached to seal the jet and work under inert atmosphere. 59

Figure 4-6: VIS spectra of deoxyMb, metMb and MbNO (4 mM physiological solution) recorded in a 100 µm flow cuvette under inert conditions. Shown are the Q-bands of the porphyrin ring. 60

Figure 5-1: (a) Energy level diagram showing the origin of the K_α and K_β fluorescence after creation of a hole in the 1s (K) shell. The $K_{\alpha1}$ and $K_{\alpha2}$ lines originate from the splitting of the 2p orbital ($2p_{1/2}$ and $2p_{3/2}$), whereas for K_β these lines are degenerate, resulting in the line labelled $K_{\beta1,3}$. (b) Experimental setup for the time-resolved X-ray emission spectroscopy measurements at the XFEL. A von Hamos geometry was used for these measurements. 62

Figure 5-2: XES K_β laser-on spectra at 10 ps delay measured at SACLA (black dots). In blue, the Gaussian fitting used to obtain the peak maximum. 64

Figure 5-3: XES K_α spectra normalized to the maximum peak intensity for singlet ($Fe(bpy)_3Cl_2$), doublet (MbNO) and quintet (deoxyMb) compounds..................... 65

Figure 5-4: Overlaid structure of MbNO without NO (red, PDB: 2FRJ) and of deoxyMb (green, PDB: 2V1K). 66

Figure 5-5: Comparison of relative ratios between deoxyMb and MbNO of the $K_{\alpha1}$ intensity (left), the $K_{\alpha2}$ intensity (middle) and the shift of $K_{\alpha1}$ from deoxyMb to MbNO for experimental (blue) and DFT (orange) XES Kα spectra and the standard-deviation (STD) between the experimental results and DFT simulations are shown in between. This serves as benchmark of the DFT simulations, showing that relative changes in the spectra reproduce well the experimental trends. 67

Figure 5-6: Transient K_β XES spectra of MbNO at 0.26 (red) and 1.36 ps (blue). The 0.26 ps spectrum represents predominantly triplet state species and the 1.36 ps spectrum the quintet state. Both are normalized to the maximum of the negative signal. The error bars are the standard deviation between the runs. 69

Figure 5-7: Transient K_α XES spectra of MbNO at 0.26 (red) and 1.36 ps (blue). The 0.26 ps spectrum represents predominantly triplet state species and the 1.36 ps spectrum the quintet state. Both are normalized to the maximum of the negative signal. The error bars are the standard deviation between the runs. 69

Figure 5-8: a) Steady-state XES K_β spectra of deoxyMb (S=2) and MbNO (S=1/2) measured at Eu-XFEL and SACLA, relative to the peak maximum of MbNO normalized to 1. b) Reference XES K_β spectra of ground state $[Fe(2,2'\text{-bipyridine})_3]^{3+}$ (S=1/2) and $[Fe(phenanthroline)_2(NCS)_2]$ (S=2) reproduced from ref.[165] 70

Figure 5-9: Laser-on (pumped) K_β XES spectra of MbNO at different time delays between -0.09 and 1.36 ps (from blue to red) showing a blue shift of the $K_{\beta1,3}$ line and an intensity decrease. The peak shifts, smaller than the energy resolution (~0.5 eV), are visible (see also Figure 5-10). 71

Figure 5-10: Zoom into the laser-on (pumped) $K\beta1,3XES$ spectra of MbNO at different time delays between -0.09 and 1.36 ps (from blue to red) showing peak shifts smaller than the energy resolution of our experiment. 71

Figure 5-11: (a) Transient XES K_β spectra of MbNO in a physiological solution at pump-probe time delays of 0.26 and 1.36 ps. (b) Difference of steady-state XES K_β spectra from ref.[165]: triplet minus doublet (blue), quintet minus doublet (red), using the reference spectra of Fe(II)phthalocyanine (triplet state), $[Fe(2,2'\text{-bipyridine})_3]^{3+}$ (doublet state) and $[Fe(phenanthroline)_2(NCS)_2]$ (quintet state), and taking into account NO dissociation quantum yield (Details can be found in § 5.2.8). 72

Figure 5-12: (a) Transient K_β XES spectra of photoexcited MbNO between 0.26 and 1.36 ps (normalized to the maximum of the negative signal). (b) same for transients between 1.36 and 100 ps. 73

Figure 5-13: Normalized Laser-off and Laser-on (pumped) $K\beta 1,3 XES$ spectra of MbNO at 0.26 ps and 1.36 ps time delays, highlighting the overall blue shift of the maximum. However, the transients exhibit a red shift of the maximum from 0.26 to 1.36 ps. This is due to different line shapes of the 1.36 ps and the 0.26 ps laser-on spectra (see region 7059 to 7062 eV). 74

Figure 5-14: (a) Experimental Fe Kα spectra of ground state deoxyMb (S=2) and MbNO (S=1/2) and of the laser-on MbNO spectrum at 0.26 ps after excitation, all normalized relative to the peak maximum of the ground state MbNO spectrum. The Kα1 line is near 6404 eV and the Kα2 line is near 6391 eV. (b) DFT simulated XES Kα spectra of deoxyMb, MbNO and deoxyMb triplet state, all shifted by +86.3 eV and normalized relative to the peak maximum of the MbNO spectrum. In (a), the 0.26 ps contains both the XES of the ground state MbNO and of the triplet deoxyMb. 75

Figure 5-15: Laser-on (pumped) $K\alpha$ XES spectra of MbNO at different time delays between -0.09 and 1.36 ps (from blue to red) showing an intensity decrease for $K_{\alpha 2}$ over the first 1.2 ps after excitation and an intensity decrease and change in peak width for $K_{\alpha 1}$. Also, the visibility of changes in peak width (σ) smaller than the energy resolution (~0.6 eV) can be well observed. 76

Figure 5-16: Zoom into the $K_{\alpha 2}$ and $K_{\alpha 1}$ laser-on (pumped) XES spectra of MbNO at different time delays between -0.09 and 1.36 ps (from blue to red) showing an intensity decrease for $K_{\alpha 2}$ over the first 1.2 ps after excitation and an intensity decrease and change in peak width for $K_{\alpha 1}$. Also, the visibility of changes in peak width (σ) smaller than the energy resolution (~0.6 eV) can be well observed. 76

Figure 5-17: (a) Transient XES K_{α} spectra at 0.26 and 1.36 ps showing a blue shift of the positive $K_{\alpha 1}$ transient feature (6405 eV) from 0.26 ps to 1.36 ps, and the presence of a positive dip at 6393 eV at 0.26 ps, which vanishes for later times (1.36 ps). (b) XES K_{α} difference spectra derived from DFT simulated XES K_{α} spectra: triplet minus doublet (blue), quintet minus doublet (red). Details can be found in § 5.2.8. 77

Figure 5-18: Laser-on (pumped) K_{α} spectra of MbNO at 0.26 ps (blue), representing mainly triplet state population and at 1.36 ps (red), representing mainly quintet state population and the corresponding transient spectra. In black is the ground-state spectrum of MbNO shown. 78

Figure 5-19: (a) Transient K_{α} XES spectra of MbNO between 0.26 and 1.36 ps (normalized to the maximum of the negative signal). (b) same for transients between 1.36 and 100 ps. 79

Figure 5-20: Transient XES K_{α} spectra at 0.26 and 1.36 ps showing a blue shift of the positive $K_{\alpha 1}$ transient feature (6405 eV) from 0.26 ps to 1.36 ps, and the presence of a positive dip at 6393 eV at 0.26 ps, which vanishes for later times (1.36 ps). In yellow (dotted) the static difference signal of deoxyMb-MbNO is plotted, which resembles the spectrum at 1.36 ps. This indicates structural and electronic similarity of the excited state after ~1 ps and the deoxyMb. 80

Figure 5-21: Energy level diagram showing the S=1/2, 1 and 2 states and the Q-state of the porphyrin with arrows indicating the relaxation pathways and their corresponding rates. The ∼100 fs decay of the Q-state is taken from fluorescence up-conversion measurements and fixed for the kinetic model[53], the 500 ± 250 fs is derived from the kinetic model (see § 8.3.1). 81

Figure 5-22: Plotted are the mean of seven points (7053.0 to 7054.0 eV) of the K_β XES pump-probe spectra (Figure S6) in the time range of 0.26 to 3.16 ps (black dots) and the fit (red) together with the 90% confidence bands (orange shade). See § 8.3.1 for details about the kinetic model. 81

Figure 5-23: Displays the population dynamics obtained from the kinetic model (see § 8.3.1) after t_0 of $\rho_{\text{Q-state}}[t]$ (blue), $\rho_{\text{Triplet}}[t]$ (green) and $\rho_{\text{Quintet}}[t]$ (red). 82

Figure 5-24: (a) Evolution of the normalized relative peak shift (of ~0.45 eV) of the XES $K_{\beta1,3}$ peak (points), fit using a biexponential function with an error function for the rise yielding decay times of 30 ± 9 ps and 1.5 ± 0.9 ns (red trace). (b) Zoom into the early times showing a rise of 800 ± 150 fs. 83

Figure 5-25: Temporal evolution of the relative $K\beta1,3$ shift for MbNO (blue triangles, centroid obtained from Gaussian fit, max shift is ~0.45 eV, see § S6) and of the $K\alpha1$ peak width change for MbNO (black squares, normalized σ obtained from a Gaussian fit, maximum change in σ is ~0.3). Details are explained in § 5.2.4. 84

Figure 5-26: Temporal evolution at the rise of the relative $K\beta1,3$shift for MbNO (blue triangles, centroid obtained from Gaussian fit, max shift is ∼0.45 eV, see § S6) and of the $K\alpha1$ peak width change for MbNO (black squares, normalized σ obtained from a Gaussian fit, maximum change in σ is ∼0.3). Details are explained in § 5.2.4. 84

Figure 5-27: Schematic representation of the spin cross-over and reverse spin cross-over characterizing the photocycle of MbNO. The low-spin ground state MbNO (S = ½) heme undergoes prompt dissociation of NO upon π-π* excitation. The porphyrin Q-state decays to a triplet state (S = 1) of the pentacoordinated deoxyMb heme in < 100 fs. Further relaxation to the quintet state occurs in ~500±250 fs. The entire process occurs in ~800 fs. Upon recombination of NO to deoxyMb leading to a hexacoordinated HS domed heme, relaxation back to the LS planar ground state occurs in ~30 ps. The LS structure is PDB entry 2FRJ, the sizes of the Fe atom, the NO molecule and the doming are exaggerated to highlight the key changes in the photocycle. The actual structural differences between MbNO and deoxyMb are shown in Figure S1. Fe = orange, N = blue, O = red and C = grey. 85

Figure 6-1: Transient XAS spectra of 3 mmol MbNO in physiological media, upon excitation at 530 nm. The normalized transient spectra recorded at 70 (black) and 300 ps (green) time delay are identical and differ from the static difference spectra (blue) of deoxyMb minus MbNO. (time resolution: 70 ps) From ref.[85] 88

Figure 6-2: (a) Static XAS spectra measured at SACLA of MbNO, deoxyMb and metMb. The reason why the deoxy spectrum is cut off at 7117 eV is that the jet jumped at this point and the signal was lost. (b) Static XAS spectra of 4 mM physiological solution of MbNO, deoxyMb and metMb, data from Lima et al.[91] ... 89

Figure 6-3: (a) Overview over the heme structure in different forms of myoglobin: MbNO (PDB: 2FRJ), deoxyMb (PDB: 2V1K) and metMb (PDB: 2MBW).Shown is the heme plane from the side with the His64 and His93 side chains. Grey (C), blue (N), red (O), orange (Fe). (b) Schematic diagram of the electronic states of Iron (Fe) in different forms of Myoglobin, their multiplicity (S) and in brackets the ligands. (c) Molecular orbital diagram of MbNO, which is a special case as it is ferrous (Fe^{2+}) and low spin (S=1/2). Adapted from Morse R. H. et al.[43] 90

Figure 6-4: Magnification of the iron absorption edge of the static XAS spectra measured at SACLA of (a) MbNO, deoxyMb and metMb. (b) MbNO, deoxyMb and MbNO* laser-on at 1 ps. 91

Figure 6-5: Zoom into the pre-edge of the static XAS spectra measured at SACLA of (a) MbNO, deoxyMb and MbNO* laser-on at 1 ps (data from SACLA) and (b) MbNO, deoxyMb and metMb, data from Lima et al.[91] 92

Figure 6-6: Zoom into the XAS region above the absorption edge (7130-7150 eV) of MbNO, deoxyMb, metMb and MbNO* laser-on at 1 ps pump-probe delay. 93

Figure 6-7: XAS deoxyMb minus MbNO static difference. In blue derived from steady state MbNO and deoxyMb spectra recorded at SACLA, in red from ref.[85] The SACLA difference spectrum is cut off due to difficulties recording the deoxyMb XAS spectrum (details explained above). 94

Figure 6-8: Fluence scan of the transient signal at the main X-ray absorption edge (7122.5 eV) at a time delay of about 1.2 ps. Plotted is the difference signal (pumped-unpumped) against the laser pulse energy in mJ/cm^2. The green dashed line represents a linear fit for which only the blue dots are used. Plotted is the mean of two runs, recorded at SACLA, and the error bars represent 2σ. 95

Figure 6-9: Laser fluence dependence scan of the XAS transient signal at 7122.5 eV, which is the main edge, at 1 ps time-delay. Plotted is the mean of 3 runs with the standard deviation as error bars, measured at SwissFEL. The dashed green line is the trendline using all data points. 95

Figure 6-10: XAS energy scans at different pump laser fluences at 1 ps pump-probe delay measured at Alvra, SwissFEL. 96

Figure 6-11: Comparison of transient XAS spectra of MbNO from SLS[85] and SACLA. In blue the 70 ps spectrum from SLS (pulse width of X-ray pulse at SLS is around 70 ps). In dotted red the transient MbNO XAS spectrum at 100 ps delay measured at SACLA. 97

Figure 6-12: XAS transient spectrum at 100 ps delay from SACLA (red), compared to XAS transient spectrum at 70 ps measured at SLS (blue) from ref.[85]. The green curve is the SACLA transient smoothed with a span of 31 and shows that the double peak disappears and matches better the spectrum measured at SLS (blue). 97

Figure 6-13: XAS transient spectra of MbNO. In blue the transient MbNO spectrum at 70 ps delay and in red the static difference spectrum (deoxyMb-MbNO) from ref.[85] In yellow that XAS transient measured at 1 ps delay and a fluence of 90 mJ/cm^2 at Alvra, SwissFEL is plotted. The transient measured at SwissFEL was shifted by +1 eV to match the published spectrum from SLS. 98

Figure 6-14: XAS transient spectra of MbNO. In red the static difference spectrum (deoxyMb-MbNO) from ref.[85] In yellow that XAS transient measured at 1 ps delay and a fluence of 810 mJ/cm^2 at Alvra, SwissFEL is plotted. In green the XAS transient at 1 ps delay measured at SACLA (fluence: 195 mJ/cm^2) is shown. The transient measured at SwissFEL was shifted by +1 eV to match the published spectrum from SLS. 98

Figure 6-15: (a) Static XAS spectra (SACLA) of MbNO and deoxyMb and the MbNO* laser-on spectra at 1 ps pump-probe delay. Spectra are scaled. (b) Transient XAS spectra (pumped-unpumped) at 1, 2, 10, 17, 27 and 100 ps time delay. The magnitude of the maximum transient signal at 1 ps, corresponds to about 7% of the static maximum MbNO signal. 99

Figure 6-16: Zoom in the pre-edge region (7110-15) of transient XAS spectra (pumped-unpumped) at 1, 2, 10, 17, 27 and 100 ps time delay. 100

Figure 6-17: Zoom in the edge region (7115-41) of transient XAS spectra (pumped-unpumped) at 1, 2, 10, 17, 27 and 100 ps time delay. The transient spectra are smoothed (details in Appendix 8.2.3). Three peaks are identified: A1 at 7118.5 eV, A2 at 7122 eV and A3 at 7126.5 eV. 101

Figure 6-18: Shown are six XAS transient spectra of MbNO at different time delays and grey lines mark the energies at which time traces were recorded: Pre-edge at 7112 eV, Edge_1 at 7122.5 eV, Edge_2 at 7127 eV, Post-edge at 7133 eV. 102

Figure 6-19: XAS time-traces at 7112 eV (Pre-edge) (*4), 7122.5 eV (Edge_1), 7127 eV (Edge_2) and 7133 eV (Post-edge) (*4). Edge_1 and Edge_2 show a clear difference in the early times < 30 ps and an agreement at longer times (>30 ps). Plotted are the average of 2 runs for Edge_1, Pre-edge, Post-edge and the average of 3 runs for Edge_2. The error bars represent the standard deviation between the runs. 103

Figure 6-20: Zoom into the first 40 ps of the XAS time-traces at 7112 eV (Pre-edge) (*4), 7122.5 eV (Edge_1), 7127 eV (Edge_2) and 7133 eV (Post-edge) (*4). Plotted are the average of 2 runs for Edge_1, Pre-edge, Post-edge and the average of 3 runs for Edge_2. The error bars represent the standard deviation between the runs. 103

Figure 6-21: XAS rise at 7122.5 eV (Edge_1) with a biexponential fit (green). The obtained time constants are: τ_{rise} = 110 ± 15 fs and τ_f = 160 ± 70 fs. The errors on the time constants are 1σ. 104

Figure 6-22: XAS rise at 7127 eV (Edge_2) with a biexponential fit (green). The obtained time constants are: τ_{rise} = 75 ± 35 fs and τ_f = 800 ± 1150 fs. The errors on the time constants are 1σ. 105

Figure 6-23: XAS rise at 7112 eV (Pre-edge) with a single exponential fit (green). The obtained time constant is: τ_{rise} = 110 ± 15 fs. The errors on the time constants are 1σ. 105

Figure 6-24: (a) XAS rise at 7133 eV (Post-edge) with a biexponential fit (green). The obtained time constants are: τ_{rise} = 110 ± 90 fs and τ_f = 70 ± 450 fs. (b) XAS rise at 7133 eV (Post-edge) with a single exponential fit (green). The obtained time constant is: τ_{rise} = 75 ± 58 fs. The errors on the time constants are 1σ. 105

Figure 6-25: (a) XAS time-trace at 7122.5 eV (Edge_1) with a biexponential fit (green). The time constants with their normalized pre-exponential factors in brackets are: τ_1 = 30 ± 9 ps (0.46) and τ_2 = 450 ± 360 ps (0.54). (b) XAS time-trace at 7127 eV (Edge_2) with a biexponential fit (green). The time constants with their normalized pre-exponential factors in brackets are: τ_1 = 30 ± 29 ps (0.22) and τ_2 = 330 ± 272 ps (0.78). (c) XAS time-trace at 7133 eV (Post-edge) with a single exponential fit and an offset (green). The time constant is: τ_v = 3.8 ± 2.5 ps (0.6). (d) XAS time-trace at 7112 eV (Pre-edge) with a single exponential fit and an offset (green). The time constant is: τ_1 = 43 ± 40 ps (0.5). The error bars for all plots represent the standard deviation between the runs and the errors on the time constants are 1σ. 107

Figure 6-26: Zoom into the first 40 ps of the XAS time-traces of MbNO measured at SACLA, presented in Figure 6-25. 108

Figure 6-27: (a) Static difference spectra calculated with DFT ground state spectra of deoxyMb, MbNO, domed MbNO. (b) The chemical structures of the active center of different Myoglobin-NO, deoxyMb and the proposed transition state: domed MbNO. The color of the boxes correspond to which structure is used for the calculation of the difference spectrum from DFT simulated XAS spectra. 112

Figure 6-28: Schematic summary of the recombination kinetics in MbNO obtained from time-resolved XAS 114

Figure 7-1: Schematic overview over the recombination kinetics in MbNO 119

Figure 8-1: Raw XES K_α image recorded at EXFEL for illustration. Clearly visible is the yellow $K_{\alpha1}$ peak and next to it on the right side the weaker $K_{\alpha2}$ peak. The units of the x and y axis are pixels and the sample is Fe(bpy)$_3$. Detector: GreatEyes. 125

Figure 8-2: Raw XES K_α image recorded at EXFEL with the integration regions indicated in red and green. Red is the signal region, green the region for the background. The units of the x and y axis are pixels and the sample is MbNO. Detector: GreatEyes. 125

Figure 8-3: XES K_α spectrum of MbNO in physiological solution for illustration of the data processing. 126

Figure 8-4: DFT simulated K_α XES transient spectra of different Mb species. The spectra are scaled to the negative transient feature at 6317 eV and were derived as described in § 5.2.8. In red the transient spectrum of deoxyMb in the quintet spin state is plotted (domed heme), in blue the transient spectrum of deoxyMb in the triplet spin state (domed heme) is plotted and in yellow the transient spectrum of MbNO, where NO was removed in the triplet spin state (planar heme) is plotted. 129

Figure 8-5: DFT simulated K_α XES transient spectra of different linear combinations of deoxyMb (triplet) and MbNO without NO (triplet) transient spectra. The spectra were derived as described in § 5.2.8 before the linear combinations were calculated. In blue the transient spectrum of 90% deoxyMb in the triplet spin state (domed heme) and 10% Mb in triplet state (planar heme) is plotted and in red the transient spectrum of a mixture of 50% deoxyMb in the triplet spin state (domed heme) and 50% Mb in the triplet state (planar heme) is plotted. In addition, the ratios of 80:20, 70:30 and 60:40 domed:planar are shown. And on the left the corresponding structures around the iron atom are illustrated. The marked regions (A, B, C) highlight the areas showing the largest changes between domed and planar heme. 130

Figure 8-6: (a) Transient XES K_α spectra at 0.26 and 1.36 ps showing a blue shift of the positive $K_{\alpha1}$ transient feature (6405 eV) from 0.26 ps to 1.36 ps, and the presence of a positive dip at 6393 eV at 0.26 ps, which vanishes for later times (1.36 ps). (b) XES K_α difference spectra derived from DFT simulated XES K_α spectra: triplet (80% domed and 20% planar) minus doublet (blue), quintet minus doublet (red). Details can be found in § 5.2.8. 131

Figure 8-7: Same as Figure 5-11 but with an extended energy range. (a) Transient XES K_β spectra of MbNO in a physiological solution at pump-probe time delays of 0.26 and 1.36 ps. (b) Difference of steady-state XES K_β spectra from ref.[165]: triplet minus doublet (blue), quintet minus doublet (red), using the reference spectra of Fe(II)phthalocyanine (triplet state), $[Fe(2,2'\text{-bipyridine})_3]^{3+}$ (doublet state) and $[Fe(\text{phenanthroline})_2(NCS)_2]$ (quintet state), and taking into account NO dissociation quantum yield (Details can be found in § 5.2.8). 132

Figure 8-8: Comparison of static XAS measurements (blue) to published spectra (red) from Lima et al.[91] The spectra are in good agreement within their signal to noise. At SACLA no measurement over a larger energy range was performed, therefore the SACLA data is I_0 normalized and offset corrected, but not background corrected. This can be the reason for small deviations in the case of MbNO. The SACLA spectra are shifted by +1 eV in energy to match with literature. 133

Figure 8-9: XAS rise of MbNO using a 100 µm jet at 7127 eV (Edge_2) with a biexponential fit (green). The obtained time constants are: $\tau_{rise} = 75 \pm 35$ fs and $\tau_f = 800 \pm 1150$ fs. The errors on the time constants are 1σ. 30 fs binning applied. 134

Figure 8-10: XAS rise of MbNO using a 200 µm jet at 7127 eV (Edge_2) with a single-exponential fit (blue). The obtained time constant is: $\tau_{rise} = 150 \pm 39$ fs. The error on the time constant is 1σ. 30 fs binning applied. 135

Figure 8-11: DFT simulated XAS spectra of deoxyMb (blue) and MbNO. 136

Figure 8-12: Density-of-States of the p orbitals in MbNO, obtained from DFT simulations. 136

References

(1) Kendrew, J. C.; Bodo, G.; Dintzis, H. M.; ParrishARRISH, R. G.; Wyckoff, H.; Phillips, D. C. A Three-Dimensional Model of the Myoglobin Molecule Obtained by X-Ray Analysis. *Nature* **1958**, *181* (4610), 662–666. https://doi.org/10.1038/181662a0.

(2) Kendrew, J. C.; Dickerson, R. E.; Strandberg, B. E.; Hart, R. G.; Davies, D. R.; Phillips, D. C.; Shore, V. C. Structure of Myoglobin: A Three-Dimensional Fourier Synthesis at 2 Å. Resolution. *Nature* **1960**, *185* (4711), 422–427. https://doi.org/10.1038/185422a0.

(3) *CRC Handbook of Chemistry and Physics: A Readyreference Book of Chemical and Physical Data*, 65. ed.; CRC press: Florida, Fla., 1985.

(4) Ballou, D. P. [7] Freeze-Quench and Chemical-Quench Techniques. In *Methods in Enzymology*; Elsevier, 1978; Vol. 54, pp 85–93. https://doi.org/10.1016/S0076-6879(78)54010-X.

(5) de Vries, S. Freeze-Quench Kinetics. In *Encyclopedia of Inorganic and Bioinorganic Chemistry*; Scott, R. A., Ed.; John Wiley & Sons, Ltd: Chichester, UK, 2011; p eibc0314. https://doi.org/10.1002/9781119951438.eibc0314.

(6) Norrish, R. G. W.; Porter, G. Chemical Reactions Produced by Very High Light Intensities. *Nature* **1949**, *164* (4172), 658–658. https://doi.org/10.1038/164658a0.

(7) Jung, I. D.; Kärtner, F. X.; Matuschek, N.; Sutter, D. H.; Morier-Genoud, F.; Zhang, G.; Keller, U.; Scheuer, V.; Tilsch, M.; Tschudi, T. Self-Starting 6.5-Fs Pulses from a Ti:Sapphire Laser. *Opt. Lett., OL* **1997**, *22* (13), 1009–1011. https://doi.org/10.1364/OL.22.001009.

(8) Hentschel, M.; Kienberger, R.; Spielmann, Ch.; Reider, G. A.; Milosevic, N.; Brabec, T.; Corkum, P.; Heinzmann, U.; Drescher, M.; Krausz, F. Attosecond Metrology. *Nature* **2001**, *414* (6863), 509–513. https://doi.org/10.1038/35107000.

(9) Tono, K.; Togashi, T.; Inubushi, Y.; Sato, T.; Katayama, T.; Ogawa, K.; Ohashi, H.; Kimura, H.; Takahashi, S.; Takeshita, K.; et al. Beamline, Experimental Stations and Photon Beam Diagnostics for the Hard x-Ray Free Electron Laser of SACLA. *New Journal of Physics* **2013**, *15* (8), 083035. https://doi.org/10.1088/1367-2630/15/8/083035.

(10) Katayama, T.; Hirano, T.; Morioka, Y.; Sano, Y.; Osaka, T.; Owada, S.; Togashi, T.; Yabashi, M. X-Ray Optics for Advanced Ultrafast Pump–Probe X-Ray Experiments at SACLA. *J Synchrotron Rad* **2019**, *26* (2), 333–338. https://doi.org/10.1107/S1600577518018362.

(11) Palmer, G.; Kellert, M.; Wang, J.; Emons, M.; Wegner, U.; Kane, D.; Pallas, F.; Jezynski, T.; Venkatesan, S.; Rompotis, D.; et al. Pump–Probe Laser System at the FXE and SPB/SFX Instruments of the European X-Ray Free-Electron Laser Facility. *J Synchrotron Rad* **2019**, *26* (2), 328–332. https://doi.org/10.1107/S160057751900095X.

(12) Galler, A.; Gawelda, W.; Biednov, M.; Bomer, C.; Britz, A.; Brockhauser, S.; Choi, T.-K.; Diez, M.; Frankenberger, P.; French, M.; et al. Scientific Instrument Femtosecond X-Ray Experiments (FXE): Instrumentation and Baseline Experimental Capabilities. *J Synchrotron Rad* **2019**, *26* (5), 1432–1447. https://doi.org/10.1107/S1600577519006647.

(13) Milne, C.; Schietinger, T.; Aiba, M.; Alarcon, A.; Alex, J.; Anghel, A.; Arsov, V.; Beard, C.; Beaud, P.; Bettoni, S.; et al. SwissFEL: The Swiss X-Ray Free Electron Laser. *Applied Sciences* **2017**, *7* (7), 720. https://doi.org/10.3390/app7070720.

(14) Berg, J. M.; Stryer, L.; Tymoczko, J. L.; Gatto, G. J. *Biochemistry*, Eighth edition.; Macmillan Education: New York, 2015.

(15) Garrett, R.; Grisham, C. M. *Biochemistry*, 5th ed.; Brooks/Cole, Cengage Learning: Belmont, CA, 2013.

(16) Scheiner, S.; Kar, T.; Pattanayak, J. Comparison of Various Types of Hydrogen Bonds Involving Aromatic Amino Acids. *J. Am. Chem. Soc.* **2002**, *124* (44), 13257–13264. https://doi.org/10.1021/ja027200q.

(17) Négrerie, M. Iron Transitions during Activation of Allosteric Heme Proteins in Cell Signaling. *Metallomics* **2019**, *11* (5), 868–893. https://doi.org/10.1039/C8MT00337H.

(18) Lippard, S. J.; Berg, J. M. *Principles of Bioinorganic Chemistry*; University Science Books: Mill Valley, Calif, 1994.

(19) Hüttemann, M.; Pecina, P.; Rainbolt, M.; Sanderson, T. H.; Kagan, V. E.; Samavati, L.; Doan, J. W.; Lee, I. The Multiple Functions of Cytochrome c and Their Regulation in Life and Death Decisions of the Mammalian Cell: From Respiration to Apoptosis. *Mitochondrion* **2011**, *11* (3), 369–381. https://doi.org/10.1016/j.mito.2011.01.010.

(20) Bachmann, K. Drug Metabolism. In *Pharmacology*; Elsevier, 2009; pp 131–173. https://doi.org/10.1016/B978-0-12-369521-5.00008-7.

(21) Cederbaum, A. I. Cytochrome P450 and Oxidative Stress in the Liver. In *Liver Pathophysiology*; Elsevier, 2017; pp 401–419. https://doi.org/10.1016/B978-0-12-804274-8.00031-X.

(22) Chapman, S. K.; Davies, D. M.; Watson, A. D.; Sykes, A. G. Metalloproteins and Electron Transfer. In *Inorganic Chemistry: Toward the 21st Century*; Chisholm, M. H., Ed.; AMERICAN CHEMICAL SOCIETY: WASHINGTON, D.C., 1983; Vol. 211, pp 177–197. https://doi.org/10.1021/bk-1983-0211.ch009.

(23) Garcia-Ruiz, E.; Mate, D. M.; Gonzalez-Perez, D.; Molina-Espeja, P.; Camarero, S.; Martínez, A. T.; Ballesteros, A. O.; Alcalde, M. Directed Evolution of Ligninolytic Oxidoreductases: From Functional Expression to Stabilization and Beyond. In *Cascade Biocatalysis*; Riva, S., Fessner, W.-D., Eds.; Wiley-VCH Verlag GmbH & Co. KGaA: Weinheim, Germany, 2014; pp 1–22. https://doi.org/10.1002/9783527682492.ch1.

(24) Calderón, F.; Wilson, D. M.; Gamo, F.-J. Antimalarial Drug Discovery. In *Progress in Medicinal Chemistry*; Elsevier, 2013; Vol. 52, pp 97–151. https://doi.org/10.1016/B978-0-444-62652-3.00003-X.

(25) Bhagavan, N. V.; Ha, C.-E. Electron Transport Chain, Oxidative Phosphorylation, and Other Oxygen-Consuming Systems. In *Essentials of Medical Biochemistry*; Elsevier, 2015; pp 187–204. https://doi.org/10.1016/B978-0-12-416687-5.00013-0.

(26) Shiro, Y.; Nakamura, H. Heme-Based Oxygen Sensor Protein FixL: Its Structure and Function. *International Congress Series* **2002**, *1233*, 251–257. https://doi.org/10.1016/S0531-5131(02)00236-4.

(27) Aono, S.; Nakajima, H. Structure and Function of CooA, a Novel Transcriptional Regulator Containing a b-Type Heme as a CO Sensor. *Coordination Chemistry Reviews* **1999**, *190–192*, 267–282. https://doi.org/10.1016/S0010-8545(99)00070-3.

(28) Childers, K. C.; Garcin, E. D. Structure/Function of the Soluble Guanylyl Cyclase Catalytic Domain. *Nitric Oxide* **2018**, *77*, 53–64. https://doi.org/10.1016/j.niox.2018.04.008.

(29) Wittenberg, J. B. Myoglobin Function Reassessed. *Journal of Experimental Biology* **2003**, *206* (12), 2011–2020. https://doi.org/10.1242/jeb.00243.

(30) Garrett, R. H.; Grisham, C. M. *Biochemistry*; Thomson [u.a.: South Melbourne [u.a., 2002.

(31) Griffith, O. W.; Stuehr, D. J. Nitric Oxide Synthases: Properties and Catalytic Mechanism. *Annual Review of Physiology* **1995**, *57* (1), 707–734. https://doi.org/10.1146/annurev.ph.57.030195.003423.

(32) Ignarro, L. J.; Barry, B. K.; Gruetter, D. Y.; Ohlstein, E. H.; Gruetter, C. A.; Kadowitz, P. J.; Baricos, W. H. Selective Alterations in Responsiveness of Guanylate Cyclase to Activation by Nitroso Compounds during Enzyme Purification. *Biochimica et Biophysica Acta (BBA) - General Subjects* **1981**, *673*, 394–407. https://doi.org/10.1016/0304-4165(81)90471-2.

(33) White, K. A.; Marletta, M. A. Nitric Oxide Synthase Is a Cytochrome P-450 Type Hemoprotein. *Biochemistry* **1992**, *31* (29), 6627–6631. https://doi.org/10.1021/bi00144a001.

(34) Ribeiro, J.; Hazzard, J.; Nussenzveig, R.; Champagne, D.; Walker, F. Reversible Binding of Nitric Oxide by a Salivary Heme Protein from a Bloodsucking Insect. *Science* **1993**, *260* (5107), 539–541. https://doi.org/10.1126/science.8386393.

(35) Ding, X. D.; Weichsel, A.; Andersen, J. F.; Shokhireva, T. Kh.; Balfour, C.; Pierik, A. J.; Averill, B. A.; Montfort, W. R.; Walker, F. A. Nitric Oxide Binding to the Ferri- and Ferroheme States of Nitrophorin 1, a Reversible NO-Binding Heme Protein from the Saliva of the Blood-Sucking Insect, *Rhodnius Prolixus*. *Journal of the American Chemical Society* **1999**, *121* (1), 128–138. https://doi.org/10.1021/ja982979i.

(36) Bourassa, J. L.; Ives, E. P.; Marqueling, A. L.; Shimanovich, R.; Groves, J. T. Myoglobin Catalyzes Its Own Nitration. *Journal of the American Chemical Society* **2001**, *123* (21), 5142–5143. https://doi.org/10.1021/ja015621m.

(37) Wakasugi, K.; Nakano, T.; Morishima, I. Oxidized Human Neuroglobin Acts as a Heterotrimeric G Protein Guanine Nucleotide Dissociation Inhibitor. *Journal of Biological Chemistry* **2003**, *278* (38), 36505–36512. https://doi.org/10.1074/jbc.M305519200.

(38) Sun, Y.; Jin, K.; Mao, X. O.; Zhu, Y.; Greenberg, D. A. Neuroglobin Is Up-Regulated by and Protects Neurons from Hypoxic-Ischemic Injury. *Proceedings of the National Academy of Sciences* **2001**, *98* (26), 15306–15311. https://doi.org/10.1073/pnas.251466698.

(39) Brunori, M. Myoglobin Strikes Back. *Protein Science* **2010**, *19* (2), 195–201. https://doi.org/10.1002/pro.300.

(40) Coyle, C. M.; Vogel, K. M.; Rush, T. S.; Kozlowski, P. M.; Williams, R.; Spiro, T. G.; Dou, Y.; Ikeda-Saito, M.; Olson, J. S.; Zgierski, M. Z. FeNO Structure in Distal Pocket Mutants of Myoglobin Based on Resonance Raman Spectroscopy. *Biochemistry* **2003**, *42* (34), 10342–10342. https://doi.org/10.1021/bi033009x.

(41) Wiberg, N.; Wiberg, E.; Holleman, A. F. *Lehrbuch der Anorganischen Chemie*, 102.; Gruyter: Berlin, 2007.

(42) *Femtochemistry: Ultrafast Chemical and Physical Processes in Molecular Systems: Lausanne, Switzerland, September 4-8, 1995*; Chergui, M., Ed.; World Scientific: Singapore ; River Edge, NJ, 1996.

(43) Consani, C.; Auböck, G.; Bräm, O.; van Mourik, F.; Chergui, M. A Cascade through Spin States in the Ultrafast Haem Relaxation of Met-Myoglobin. *The Journal of Chemical Physics* **2014**, *140* (2), 025103. https://doi.org/10.1063/1.4861467.

(44) Wilson, S. A.; Green, E.; Mathews, I. I.; Benfatto, M.; Hodgson, K. O.; Hedman, B.; Sarangi, R. X-Ray Absorption Spectroscopic Investigation of the Electronic Structure Differences in Solution and Crystalline Oxyhemoglobin. *Proceedings of the National Academy of Sciences* **2013**, *110* (41), 16333–16338. https://doi.org/10.1073/pnas.1315734110.

(45) Eisert, W. G.; Degenkolb, E. O.; Noe, L. J.; Rentzepis, P. M. Kinetics of Carboxymyoglobin and Oxymyoglobin Studied by Picosecond Spectroscopy. *Biophysical Journal* **1979**, *25* (3), 455–464. https://doi.org/10.1016/S0006-3495(79)85315-1.

(46) Bertini, I.; Luchinat, C.; Parigi, G.; Ravera, E. *NMR of Paramagnetic Molecules: Applications to Metallobiomolecules and Models*, Second edition.; Elsevier: Amsterdam, 2017.

(47) Helbing, J. Spin State Transitions upon Visible and Infrared Excitation of Ferric MbN3. *Chemical Physics* **2012**, *396*, 17–22. https://doi.org/10.1016/j.chemphys.2011.04.001.

(48) Perutz, M. F.; Wilkinson, A. J.; Paoli, M.; Dodson, G. G. The Stereochemical Mechanism of the Cooperative Effects in Hemoglobin Revisited. *Annu. Rev. Biophys. Biomol. Struct.* **1998**, *27* (1), 1–34. https://doi.org/10.1146/annurev.biophys.27.1.1.

(49) Morse, R. H.; Chan, S. I. Electron Paramagnetic Resonance Studies of Nitrosyl Ferrous Heme Complexes. Determination of an Equilibrium between Two Conformations. *Journal of Biological Chemistry* **1980**, *255* (16), 7876–7882.

(50) Decatur, S. M.; Franzen, S.; DePillis, G. D.; Dyer, R. B.; Woodruff, W. H.; Boxer, S. G. *Trans* Effects in Nitric Oxide Binding to Myoglobin Cavity Mutant H93G †. *Biochemistry* **1996**, *35* (15), 4939–4944. https://doi.org/10.1021/bi951661p.

(51) Galindo, M. I.; Pueyo, J. I.; Fouix, S.; Bishop, S. A.; Couso, J. P. Peptides Encoded by Short ORFs Control Development and Define a New Eukaryotic Gene Family. *PLoS Biol* **2007**, *5* (5), e106. https://doi.org/10.1371/journal.pbio.0050106.

(52) Fulton, A. B.; Isaacs, W. B. Titin, a Huge, Elastic Sarcomeric Protein with a Probable Role in Morphogenesis. *Bioessays* **1991**, *13* (4), 157–161. https://doi.org/10.1002/bies.950130403.

(53) Vilhjálmsdóttir, J.; Gennis, R. B.; Brzezinski, P. The Electron Distribution in the “Activated” State of Cytochrome c Oxidase. *Sci Rep* **2018**, *8* (1), 7502. https://doi.org/10.1038/s41598-018-25779-w.

(54) Kruglik, S. G.; Yoo, B.-K.; Franzen, S.; Vos, M. H.; Martin, J.-L.; Negrerie, M. Picosecond Primary Structural Transition of the Heme Is Retarded after Nitric Oxide Binding to Heme Proteins. *Proceedings of the National Academy of Sciences* **2010**, *107* (31), 13678–13683. https://doi.org/10.1073/pnas.0912938107.

(55) Kholodenko, Y.; Gooding, E. A.; Dou, Y.; Ikeda-Saito, M.; Hochstrasser, R. M. Heme Protein Dynamics Revealed by Geminate Nitric Oxide Recombination in Mutants of Iron and Cobalt Myoglobin †. *Biochemistry* **1999**, *38* (18), 5918–5924. https://doi.org/10.1021/bi983022v.

(56) Levantino, M.; Lemke, H. T.; Schirò, G.; Glownia, M.; Cupane, A.; Cammarata, M. Observing Heme Doming in Myoglobin with Femtosecond X-Ray Absorption Spectroscopya). *Structural Dynamics* **2015**, *2* (4), 041713. https://doi.org/10.1063/1.4921907.

(57) Henry, E. R.; Sommer, J. H.; Hofrichter, J.; Eaton, W. A.; Gellert, M. Geminate Recombination of Carbon Monoxide to Myoglobin. *Journal of Molecular Biology* **1983**, *166* (3), 443–451. https://doi.org/10.1016/S0022-2836(83)80094-1.

(58) Ishizaka, S.; Wada, T.; Kitamura, N. Femtosecond Transient Absorption Study on Relaxation Intermediates in Oxymyoglobin. *Photochem. Photobiol. Sci.* **2009**, *8* (4), 562. https://doi.org/10.1039/b814170c.

(59) Bräm, O.; Cannizzo, A.; Chergui, M. Ultrafast Broadband Fluorescence Up-Conversion Study of the Electronic Relaxation of Metalloporphyrins. *J. Phys. Chem. A* **2019**, *123* (7), 1461–1468. https://doi.org/10.1021/acs.jpca.9b00007.

(60) Consani, C.; Bräm, O.; van Mourik, F.; Cannizzo, A.; Chergui, M. Energy Transfer and Relaxation Mechanisms in Cytochrome c. *Chemical Physics* **2012**, *396*, 108–115. https://doi.org/10.1016/j.chemphys.2011.09.002.

(61) Yabushita, A.; Kobayashi, T. Ultrafast Spectroscopy of Oxyhemoglobin during Photodissociation. *J. Phys. Chem. B* **2010**, *114* (35), 11654–11658. https://doi.org/10.1021/jp103593q.

(62) Kholodenko, Y.; Volk, M.; Gooding, E.; Hochstrasser, R. M. Energy Dissipation and Relaxation Processes in Deoxy Myoglobin after Photoexcitation in the Soret Region. *Chemical Physics* **2000**, *259* (1), 71–87. https://doi.org/10.1016/S0301-0104(00)00182-8.

(63) Heftmann, E. *Chromatography: Fundamentals and Applications of Chromatography and Related Differential Migration Methods. Part B, Part B,*; Elsevier: Amsterdam; New York, 1992.

(64) Dayer, M.; Moosavi-Movahedi, A.; Dayer, M. Band Assignment in Hemoglobin Porphyrin Ring Spectrum: Using Four-Orbital Model of Gouterman. *PPL* **2010**, *17* (4), 473–479. https://doi.org/10.2174/092986610790963645.

(65) Gouterman, M.; Wagnière, G. H.; Snyder, L. C. Spectra of Porphyrins. *Journal of Molecular Spectroscopy* **1963**, *11* (1–6), 108–127. https://doi.org/10.1016/0022-2852(63)90011-0.

(66) Haldane, J.; Smith, J. L. The Oxygen Tension of Arterial Blood. *J. Physiol. (Lond.)* **1896**, *20* (6), 497–520. https://doi.org/10.1113/jphysiol.1896.sp000634.

(67) Cornelius, P. A.; Hochstrasser, R. M.; Steele, A. W. Ultrafast Relaxation in Picosecond Photolysis of Nitrosylhemoglobin. *Journal of Molecular Biology* **1983**, *163* (1), 119–128. https://doi.org/10.1016/0022-2836(83)90032-3.

(68) Petrich, J. W.; Lambry, J. C.; Kuczera, K.; Karplus, M.; Poyart, C.; Martin, J. L. Ligand Binding and Protein Relaxation in Heme Proteins: A Room Temperature Analysis of Nitric Oxide Geminate Recombination. *Biochemistry* **1991**, *30* (16), 3975–3987. https://doi.org/10.1021/bi00230a025.

(69) Petrich, J. W.; Lambry, J.-C.; Balasubramanian, S.; Lambright, D. G.; Boxer, S. G.; Martin, J. L. Ultrafast Measurements of Geminate Recombination of NO with Site-Specific Mutants of Human Myoglobin. *Journal of Molecular Biology* **1994**, *238* (3), 437–444. https://doi.org/10.1006/jmbi.1994.1302.

(70) Shreve, A. P.; Franzen, S.; Simpson, M. C.; Dyer, R. B. Dependence of NO Recombination Dynamics in Horse Myoglobin on Solution Glycerol Content. *The Journal of Physical Chemistry B* **1999**, *103* (37), 7969–7975. https://doi.org/10.1021/jp991163g.

(71) Rosca, F.; Kumar, A. T. N.; Ionascu, D.; Sjodin, T.; Demidov, A. A.; Champion, P. M. Wavelength Selective Modulation in Femtosecond Pump–Probe Spectroscopy and Its Application to Heme Proteins. *The Journal of Chemical Physics* **2001**, *114* (24), 10884. https://doi.org/10.1063/1.1363673.

(72) Ye, X.; Demidov, A.; Champion, P. M. Measurements of the Photodissociation Quantum Yields of MbNO and MbO $_2$ and the Vibrational Relaxation of the Six-Coordinate Heme Species. *Journal of the American Chemical Society* **2002**, *124* (20), 5914–5924. https://doi.org/10.1021/ja017359n.

(73) Ionascu, D.; Gruia, F.; Ye, X.; Yu, A.; Rosca, F.; Beck, C.; Demidov, A.; Olson, J. S.; Champion, P. M. Temperature-Dependent Studies of NO Recombination to Heme and Heme Proteins. *Journal of the American Chemical Society* **2005**, *127* (48), 16921–16934. https://doi.org/10.1021/ja054249y.

(74) Negrerie, M.; Kruglik, S. G.; Lambry, J.-C.; Vos, M. H.; Martin, J.-L.; Franzen, S. Role of Heme Iron Coordination and Protein Structure in the Dynamics and Geminate Rebinding of Nitric Oxide to the H93G Myoglobin Mutant IMPLICATIONS FOR NITRIC OXIDE SENSORS. *J. Biol. Chem.* **2006**, *281* (15), 10389–10398. https://doi.org/10.1074/jbc.M513375200.

(75) Yoo, B.-K.; Kruglik, S. G.; Lamarre, I.; Martin, J.-L.; Negrerie, M. Absorption Band III Kinetics Probe the Picosecond Heme Iron Motion Triggered by Nitric Oxide Binding to Hemoglobin and Myoglobin. *The Journal of Physical Chemistry B* **2012**, *116* (13), 4106–4114. https://doi.org/10.1021/jp300849y.

(76) Kim, J.; Park, J.; Lee, T.; Lim, M. Dynamics of Geminate Rebinding of NO with Cytochrome c in Aqueous Solution Using Femtosecond Vibrational Spectroscopy. *The Journal of Physical Chemistry B* **2012**, *116* (46), 13663–13671. https://doi.org/10.1021/jp308468j.

(77) Kim, S.; Lim, M. Protein Conformation-Controlled Rebinding Barrier of NO and Its Binding Trajectories in Myoglobin and Hemoglobin at Room Temperature. *The Journal of Physical Chemistry B* **2012**, *116* (20), 5819–5830. https://doi.org/10.1021/jp300176q.

(78) Zemojtel, T.; Rini, M.; Heyne, K.; Dandekar, T.; Nibbering, E. T. J.; Kozlowski, P. M. NO-Bound Myoglobin: Structural Diversity and Dynamics of the NO Ligand. *Journal of the American Chemical Society* **2004**, *126* (7), 1930–1931. https://doi.org/10.1021/ja039086x.

(79) Kim, S.; Jin, G.; Lim, M. Dynamics of Geminate Recombination of NO with Myoglobin in Aqueous Solution Probed by Femtosecond Mid-IR Spectroscopy. *The Journal of Physical Chemistry B* **2004**, *108* (52), 20366–20375. https://doi.org/10.1021/jp0489020.

(80) Kitagawa, T.; Haruta, N.; Mizutani, Y. Time-Resolved Resonance Raman Study on Ultrafast Structural Relaxation and Vibrational Cooling of Photodissociated Carbonmonoxy Myoglobin. *Biopolymers* **2002**, *67* (4–5), 207–213. https://doi.org/10.1002/bip.10096.

(81) Ye, X.; Demidov, A.; Rosca, F.; Wang, W.; Kumar, A.; Ionascu, D.; Zhu, L.; Barrick, D.; Wharton, D.; Champion, P. M. Investigations of Heme Protein Absorption Line Shapes, Vibrational Relaxation, and Resonance Raman Scattering on Ultrafast Time Scales †. *J. Phys. Chem. A* **2003**, *107* (40), 8156–8165. https://doi.org/10.1021/jp0276799.

(82) Petrich, J. W.; Poyart, C.; Martin, J. L. Photophysics and Reactivity of Heme Proteins: A Femtosecond Absorption Study of Hemoglobin, Myoglobin, and Protoheme. *Biochemistry* **1988**, *27* (11), 4049–4060. https://doi.org/10.1021/bi00411a022.

(83) Franzen, S.; Kiger, L.; Poyart, C.; Martin, J.-L. Heme Photolysis Occurs by Ultrafast Excited State Metal-to-Ring Charge Transfer. *Biophysical Journal* **2001**, *80* (5), 2372–2385. https://doi.org/10.1016/S0006-3495(01)76207-8.

(84) Ye, X.; Demidov, A.; Champion, P. M. Measurements of the Photodissociation Quantum Yields of MbNO and MbO $_2$ and the Vibrational Relaxation of the Six-Coordinate Heme Species. *Journal of the American Chemical Society* **2002**, *124* (20), 5914–5924. https://doi.org/10.1021/ja017359n.

(85) Sagnella, D. E.; Straub, J. E. Directed Energy “Funneling" Mechanism for Heme Cooling Following Ligand Photolysis or Direct Excitation in Solvated Carbonmonoxy Myoglobin. *J. Phys. Chem. B* **2001**, *105* (29), 7057–7063. https://doi.org/10.1021/jp0107917.

(86) Lim, M.; Jackson, T. A.; Anfinrud, P. A. Femtosecond Near-IR Absorbance Study of Photoexcited Myoglobin: Dynamics of Electronic and Thermal Relaxation. *J. Phys. Chem.* **1996**, *100* (29), 12043–12051. https://doi.org/10.1021/jp9536458.

(87) Henry, E. R.; Eaton, W. A.; Hochstrasser, R. M. Molecular Dynamics Simulations of Cooling in Laser-Excited Heme Proteins. *Proceedings of the National Academy of Sciences* **1986**, *83* (23), 8982–8986. https://doi.org/10.1073/pnas.83.23.8982.

(88) Silatani, M.; Lima, F. A.; Penfold, T. J.; Rittmann, J.; Reinhard, M. E.; Rittmann-Frank, H. M.; Borca, C.; Grolimund, D.; Milne, C. J.; Chergui, M. NO Binding Kinetics in Myoglobin Investigated by Picosecond Fe K-Edge Absorption Spectroscopy. *Proceedings of the National Academy of Sciences* **2015**, *112* (42), 12922–12927. https://doi.org/10.1073/pnas.1424446112.

(89) Tilton, R. F.; Kuntz, I. D.; Petsko, G. A. Cavities in Proteins: Structure of a Metmyoglobin Xenon Complex Solved to 1.9 .ANG. *Biochemistry* **1984**, *23* (13), 2849–2857. https://doi.org/10.1021/bi00308a002.

(90) Stavrov, S. S. The Effect of Iron Displacement out of the Porphyrin Plane on the Resonance Raman Spectra of Heme Proteins and Iron Porphyrins. *Biophysical Journal* **1993**, *65* (5), 1942–1950. https://doi.org/10.1016/S0006-3495(93)81265-7.

(91) Petrich, J. W.; Lambry, J. C.; Poyart, C.; Martin, J. L. Subpicosecond Resonance Raman Spectroscopy of Carbonmonoxy-Hemoglobin: Dynamics of Heme-Protein Interations and Vibrational Cooling. *Biophysical Journal* **1988**, *53* (2), 281. https://doi.org/10.1016/S0006-3495(88)83099-6.

(92) Franzen, S. Spin-Dependent Mechanism for Diatomic Ligand Binding to Heme. *Proceedings of the National Academy of Sciences* **2002**, *99* (26), 16754–16759. https://doi.org/10.1073/pnas.252590999.

(93) Strickland, N.; Harvey, J. N. Spin-Forbidden Ligand Binding to the Ferrous−Heme Group: Ab Initio and DFT Studies. *The Journal of Physical Chemistry B* **2007**, *111* (4), 841–852. https://doi.org/10.1021/jp064091j.

(94) Lima, F. A.; Penfold, T. J.; van der Veen, R. M.; Reinhard, M.; Abela, R.; Tavernelli, I.; Rothlisberger, U.; Benfatto, M.; Milne, C. J.; Chergui, M. Probing the Electronic and Geometric Structure of Ferric and Ferrous Myoglobins in Physiological Solutions by Fe K-Edge Absorption Spectroscopy. *Phys. Chem. Chem. Phys.* **2014**, *16* (4), 1617–1631. https://doi.org/10.1039/C3CP53683A.

(95) Benfatto, M.; Della Longa, S. Geometrical Fitting of Experimental XANES Spectra by a Full Multiple-Scattering Procedure. *J Synchrotron Rad* **2001**, *8* (4), 1087–1094. https://doi.org/10.1107/S0909049501006422.

(96) Benfatto, M.; Congiu-Castellano, A.; Daniele, A.; Della Longa, S. *MXAN* : A New Software Procedure to Perform Geometrical Fitting of Experimental XANES Spectra. *J Synchrotron Rad* **2001**, *8* (2), 267–269. https://doi.org/10.1107/S0909049500015338.

(97) Westre, T. E.; Kennepohl, P.; DeWitt, J. G.; Hedman, B.; Hodgson, K. O.; Solomon, E. I. A Multiplet Analysis of Fe K-Edge 1s → 3d Pre-Edge Features of Iron Complexes. *Journal of the American Chemical Society* **1997**, *119* (27), 6297–6314. https://doi.org/10.1021/ja964352a.

(98) Mills, D. M.; Lewis, A.; Harootunian, A.; Huang, J.; Smith, B. Time-Resolved X-Ray Absorption Spectroscopy of Carbon Monoxide-Myoglobin Recombination After Laser Photolysis. *Science* **1984**, *223* (4638), 811–813. https://doi.org/10.1126/science.223.4638.811.

(99) DeBeer George, S.; Petrenko, T.; Neese, F. Prediction of Iron K-Edge Absorption Spectra Using Time-Dependent Density Functional Theory [†]. *The Journal of Physical Chemistry A* **2008**, *112* (50), 12936–12943. https://doi.org/10.1021/jp803174m.

(100) Chergui, M. Empirical Rules of Molecular Photophysics in the Light of Ultrafast Spectroscopy. *Pure and Applied Chemistry* **2015**, *87* (6), 525–536. https://doi.org/10.1515/pac-2014-0939.

(101) Auböck, G.; Consani, C.; Monni, R.; Cannizzo, A.; Mourik, F. van; Chergui, M. Femtosecond Pump/Supercontinuum-Probe Setup with 20 KHz Repetition Rate. *Review of Scientific Instruments* **2012**, *83* (9), 093105. https://doi.org/10.1063/1.4750978.

(102) Henriksen, N. E.; Engel, V. Femtosecond Pump-Probe Spectroscopy: A Theoretical Analysis of Transient Signals and Their Relation to Nuclear Wave-Packet Motion. *International Reviews in Physical Chemistry* **2001**, *20* (2), 93–126. https://doi.org/10.1080/01442350010028523.

(103) Auböck, G.; Chergui, M. Sub-50-Fs Photoinduced Spin Crossover in [Fe(Bpy)3]2+. *Nature Chemistry* **2015**, *7* (8), 629–633. https://doi.org/10.1038/nchem.2305.

(104) Chergui, M. Time-Resolved X-Ray Spectroscopies of Chemical Systems: New Perspectives. *Struct. Dyn.* **2016**, *3* (3), 031001. https://doi.org/10.1063/1.4953104.

(105) Chergui, M. Ultrafast Photoinduced Energy and Charge Transfer. *Faraday Discuss.* **2019**, *216*, 9–37. https://doi.org/10.1039/C9FD00036D.

(106) Chergui, M. Ultrafast Photophysics and Photochemistry of Iron Hexacyanides in Solution: Infrared to X-Ray Spectroscopic Studies. *Coordination Chemistry Reviews* **2018**, *372*, 52–65. https://doi.org/10.1016/j.ccr.2018.05.021.

(107) Cavalieri, A. L.; Müller, N.; Uphues, Th.; Yakovlev, V. S.; Baltuška, A.; Horvath, B.; Schmidt, B.; Blümel, L.; Holzwarth, R.; Hendel, S.; et al. Attosecond Spectroscopy in Condensed Matter. *Nature* **2007**, *449* (7165), 1029–1032. https://doi.org/10.1038/nature06229.

(108) Frank, F.; Arrell, C.; Witting, T.; Okell, W. A.; McKenna, J.; Robinson, J. S.; Haworth, C. A.; Austin, D.; Teng, H.; Walmsley, I. A.; et al. Invited Review Article: Technology for Attosecond Science. *Review of Scientific Instruments* **2012**, *83* (7), 071101. https://doi.org/10.1063/1.4731658.

(109) Lara-Astiaso, M.; Galli, M.; Trabattoni, A.; Palacios, A.; Ayuso, D.; Frassetto, F.; Poletto, L.; De Camillis, S.; Greenwood, J.; Decleva, P.; et al. Attosecond Pump–Probe Spectroscopy of Charge Dynamics in Tryptophan. *J. Phys. Chem. Lett.* **2018**, *9* (16), 4570–4577. https://doi.org/10.1021/acs.jpclett.8b01786.

(110) Turro, N. J.; Ramamurthy, V.; Scaiano, J. C. *Principles of Molecular Photochemistry: An Introduction*; University Science Books: Sausalito, Calif, 2009.

(111) Jonas, D. M.; Bradforth, S. E.; Passino, S. A.; Fleming, G. R. Femtosecond Wavepacket Spectroscopy: Influence of Temperature, Wavelength, and Pulse Duration. *J. Phys. Chem.* **1995**, *99* (9), 2594–2608. https://doi.org/10.1021/j100009a018.

(112) Dhar, L.; Rogers, J. A.; Nelson, K. A. Time-Resolved Vibrational Spectroscopy in the Impulsive Limit. *Chemical Reviews* **1994**, *94* (1), 157–193. https://doi.org/10.1021/cr00025a006.

(113) Zewail, A. H. Chemistry at the Uncertainty Limit. *Angewandte Chemie International Edition* **2001**, *40* (23), 4371–4375. https://doi.org/10.1002/1521-3773(20011203)40:23<4371::AID-ANIE4371>3.0.CO;2-I.

(114) Zhu, L.; Sage, J.; Champion, P. Observation of Coherent Reaction Dynamics in Heme Proteins. *Science* **1994**, *266* (5185), 629–632. https://doi.org/10.1126/science.7939716.

(115) Capano, G.; Chergui, M.; Rothlisberger, U.; Tavernelli, I.; Penfold, T. J. A Quantum Dynamics Study of the Ultrafast Relaxation in a Prototypical Cu(I)–Phenanthroline. *The Journal of Physical Chemistry A* **2014**, *118* (42), 9861–9869. https://doi.org/10.1021/jp509728m.

(116) Penfold, T. J.; Karlsson, S.; Capano, G.; Lima, F. A.; Rittmann, J.; Reinhard, M.; Rittmann-Frank, M. H.; Braem, O.; Baranoff, E.; Abela, R.; et al. Solvent-Induced Luminescence Quenching: Static and Time-Resolved X-Ray Absorption Spectroscopy of a Copper(I) Phenanthroline Complex. *J. Phys. Chem. A* **2013**, *117* (22), 4591–4601. https://doi.org/10.1021/jp403751m.

(117) De Giovannini, U.; Brunetto, G.; Castro, A.; Walkenhorst, J.; Rubio, A. Simulating Pump–Probe Photoelectron and Absorption Spectroscopy on the Attosecond Timescale with Time-Dependent Density Functional Theory. *ChemPhysChem* **2013**, *14* (7), 1363–1376. https://doi.org/10.1002/cphc.201201007.

(118) Chergui, M. Picosecond and Femtosecond X-Ray Absorption Spectroscopy of Molecular Systems. *Acta Cryst A, Acta Cryst Sect A, Acta Crystallogr A, Acta Crystallogr Sect A, Acta Crystallogr A Found Crystallogr, Acta Crystallogr Sect A Found Crystallogr* **2010**, *66* (2), 229–239. https://doi.org/10.1107/S010876730904968X.

(119) Chergui, M.; Zewail, A. H. Electron and X-Ray Methods of Ultrafast Structural Dynamics: Advances and Applications. *ChemPhysChem* **2009**, *10* (1), 28–43. https://doi.org/10.1002/cphc.200800667.

(120) McNeil, B. W. J.; Thompson, N. R. X-Ray Free-Electron Lasers. *Nature Photonics* **2010**, *4*, 814.

(121) November 8, 1895: Roentgen's Discovery of X-Rays https://www.aps.org/publications/apsnews/200111/history.cfm (accessed Dec 23, 2019).

(122) Frequently asked questions (FAQ) on Synchrotron Light https://www.psi.ch/en/sls/synchrotron-light (accessed Dec 23, 2019).

(123) Trachanas, S.; Antonoyiannakis, M.; Tsetseris, L. *An Introduction to Quantum Physics: A First Course for Physicists, Chemists, Materials Scientists, and Engineers*; Wiley-VCH: Weinheim, 2018.

(124) *X-Ray Absorption and X-Ray Emission Spectroscopy: Theory and Applications*; Van Bokhoven, J. A., Lamberti, C., Eds.; John Wiley & Sons, Ltd: Chichester, UK, 2016.

(125) Yano, J.; Yachandra, V. K. X-Ray Absorption Spectroscopy. *Photosynth Res* **2009**, *102* (2–3), 241. https://doi.org/10.1007/s11120-009-9473-8.

(126) Chergui, M. Time-Resolved X-Ray Spectroscopies of Chemical Systems: New Perspectives. *Structural Dynamics* **2016**, *3* (3), 031001. https://doi.org/10.1063/1.4953104.

(127) Bair, R. A.; Goddard, W. A. *Ab Initio* Studies of the x-Ray Absorption Edge in Copper Complexes. I. Atomic Cu 2 + and Cu(Ii) Cl 2. *Physical Review B* **1980**, *22* (6), 2767–2776. https://doi.org/10.1103/PhysRevB.22.2767.

(128) Brouder, C. Angular Dependence of X-Ray Absorption Spectra. *Journal of Physics: Condensed Matter* **1990**, *2* (3), 701–738. https://doi.org/10.1088/0953-8984/2/3/018.

(129) Randall, C. R.; Shu, L.; Chiou, Y.-M.; Hagen, K. S.; Ito, M.; Kitajima, N.; Lachicotte, R. J.; Zang, Y.; Que, L. X-Ray Absorption Pre-Edge Studies of High-Spin Iron(II) Complexes. *Inorganic Chemistry* **1995**, *34* (5), 1036–1039. https://doi.org/10.1021/ic00109a007.

(130) Wilke, M.; Farges, F.; Petit, P.-E.; Brown, G. E.; Martin, F. Oxidation State and Coordination of Fe in Minerals: An Fe *K*- XANES Spectroscopic Study. *American Mineralogist* **2001**, *86* (5–6), 714–730. https://doi.org/10.2138/am-2001-5-612.

(131) Glatzel, P.; Smolentsev, G.; Bunker, G. The Electronic Structure in 3d Transition Metal Complexes: Can We Measure Oxidation States? *J. Phys.: Conf. Ser.* **2009**, *190* (1), 012046. https://doi.org/10.1088/1742-6596/190/1/012046.

(132) Briois, V.; dit Moulin, Ch. C.; Sainctavit, Ph.; Brouder, Ch.; Flank, A.-M. Full Multiple Scattering and Crystal Field Multiplet Calculations Performed on the Spin Transition FeII(Phen)2(NCS)2 Complex at the Iron K and L2,3 X-Ray Absorption Edges. *J. Am. Chem. Soc.* **1995**, *117* (3), 1019–1026. https://doi.org/10.1021/ja00108a018.

(133) Penner-Hahn, J. E. X-Ray Absorption Spectroscopy. In *Encyclopedia of Life Sciences*; John Wiley & Sons, Ltd, Ed.; John Wiley & Sons, Ltd: Chichester, UK, 2005; p a0002984. https://doi.org/10.1038/npg.els.0002984.

(134) Calvin, S.; Furst, K. E. *XAFS for Everyone*; CRC Press: Boca Raton, 2013.

(135) Dong, C.-L. Soft-x-Ray Spectroscopy Probes Nanomaterial-Based Devices. *SPIE Newsroom* **2007**. https://doi.org/10.1117/2.1200708.0812.

(136) Glatzel, P.; Bergmann, U. High Resolution 1s Core Hole X-Ray Spectroscopy in 3d Transition Metal Complexes—Electronic and Structural Information. *Coordination Chemistry Reviews* **2005**, *249* (1–2), 65–95. https://doi.org/10.1016/j.ccr.2004.04.011.

(137) Kuzmenko, D.; Vogelsang, U.; Hitz, S.; Müller, D.; Clark, A. H.; Kinschel, D.; Czapla-Masztafiak, J.; Milne, C.; Szlachetko, J.; Nachtegaal, M. A von Hamos Spectrometer for *in*

Situ Sulfur Speciation by Non-Resonant Sulfur Kα Emission Spectroscopy. *J. Anal. At. Spectrom.* **2019**, 10.1039.C9JA00195F. https://doi.org/10.1039/C9JA00195F.

(138) March, A. M.; Assefa, T. A.; Bressler, C.; Doumy, G.; Galler, A.; Gawelda, W.; Kanter, E. P.; Németh, Z.; Pápai, M.; Southworth, S. H.; et al. Feasibility of Valence-to-Core X-Ray Emission Spectroscopy for Tracking Transient Species. *J. Phys. Chem. C* **2015**, *119* (26), 14571–14578. https://doi.org/10.1021/jp511838q.

(139) Mathe, Z.; Pantazis, D. A.; Lee, H. B.; Gnewkow, R.; Van Kuiken, B. E.; Agapie, T.; DeBeer, S. Calcium Valence-to-Core X-Ray Emission Spectroscopy: A Sensitive Probe of Oxo Protonation in Structural Models of the Oxygen-Evolving Complex. *Inorg. Chem.* **2019**, *58* (23), 16292–16301. https://doi.org/10.1021/acs.inorgchem.9b02866.

(140) Willmott, P. *An Introduction to Synchrotron Radiation: Techniques and Applications*, 1st ed.; Wiley, 2011. https://doi.org/10.1002/9781119970958.

(141) Johann, H. H. Die Erzeugung lichtstarker Röntgenspektren mit Hilfe von Konkavkristallen. *Z. Physik* **1931**, *69* (3–4), 185–206. https://doi.org/10.1007/BF01798121.

(142) Johansson, T. Über ein neuartiges, genau fokussierendes Röntgenspektrometer: Erste Mitteilung. *Z. Physik* **1933**, *82* (7–8), 507–528. https://doi.org/10.1007/BF01342254.

(143) Hamos, L. v. Röntgenspektroskopie Und Abbildung Mittels Gekrümmter Kristallreflektoren. *Annalen der Physik* **1933**, *17* (5. Folge), 716.

(144) Szlachetko, J.; Nachtegaal, M.; de Boni, E.; Willimann, M.; Safonova, O.; Sa, J.; Smolentsev, G.; Szlachetko, M.; van Bokhoven, J. A.; Dousse, J.-Cl.; et al. A von Hamos X-Ray Spectrometer Based on a Segmented-Type Diffraction Crystal for Single-Shot x-Ray Emission Spectroscopy and Time-Resolved Resonant Inelastic x-Ray Scattering Studies. *Review of Scientific Instruments* **2012**, *83* (10), 103105. https://doi.org/10.1063/1.4756691.

(145) Marshall, T. C. *Free-Electron Lasers*; Macmillan Pub. Co. ; Collier Macmillan: New York : London, 1985.

(146) Freund, H. P.; Antonsen, T. M. *Principles of Free Electron Lasers*; 2018.

(147) Saldin, E. L.; Schneidmiller, E. A.; Yurkov, M. V. *The Physics of Free Electron Lasers*; Springer Berlin Heidelberg: Berlin, Heidelberg, 2000.

(148) Huang, Z.; Kim, K.-J. Review of X-Ray Free-Electron Laser Theory. *Phys. Rev. ST Accel. Beams* **2007**, *10* (3), 034801. https://doi.org/10.1103/PhysRevSTAB.10.034801.

(149) Sinn, H.; Dommach, M.; Dickert, B.; Di Felice, M.; Dong, X.; Eidam, J.; Finze, D.; Freijo-Martin, I.; Gerasimova, N.; Kohlstrunk, N.; et al. The SASE1 X-Ray Beam Transport System. *J Synchrotron Rad* **2019**, *26* (3), 692–699. https://doi.org/10.1107/S1600577519003461.

(150) Grünert, J.; Carbonell, M. P.; Dietrich, F.; Falk, T.; Freund, W.; Koch, A.; Kujala, N.; Laksman, J.; Liu, J.; Maltezopoulos, T.; et al. X-Ray Photon Diagnostics at the European XFEL. *J Synchrotron Rad* **2019**, *26* (5). https://doi.org/10.1107/S1600577519006611.

(151) European XFEL - Documents - Flyers http://www.xfel.eu/documents/flyers_and_brochures/ (accessed Dec 12, 2016).

(152) Emma, P.; Akre, R.; Arthur, J.; Bionta, R.; Bostedt, C.; Bozek, J.; Brachmann, A.; Bucksbaum, P.; Coffee, R.; Decker, F.-J.; et al. First Lasing and Operation of an Ångstrom-Wavelength Free-Electron Laser. *Nature Photonics* **2010**, *4* (9), 641–647. https://doi.org/10.1038/nphoton.2010.176.

(153) Kang, H.-S.; Yang, H.; Kim, G.; Heo, H.; Nam, I.; Min, C.-K.; Kim, C.; Baek, S. Y.; Choi, H.-J.; Mun, G.; et al. FEL Performance Achieved at PAL-XFEL Using a Three-Chicane Bunch Compression Scheme. *J Synchrotron Rad* **2019**, *26* (4), 1127–1138. https://doi.org/10.1107/S1600577519005861.

(154) Ishikawa, T.; Aoyagi, H.; Asaka, T.; Asano, Y.; Azumi, N.; Bizen, T.; Ego, H.; Fukami, K.; Fukui, T.; Furukawa, Y.; et al. A Compact X-Ray Free-Electron Laser Emitting in the Sub-Ångström Region. *Nature Photonics* **2012**, *6* (8), 540–544. https://doi.org/10.1038/nphoton.2012.141.

(155) Katayama, T.; Inubushi, Y.; Obara, Y.; Sato, T.; Togashi, T.; Tono, K.; Hatsui, T.; Kameshima, T.; Bhattacharya, A.; Ogi, Y.; et al. Femtosecond X-Ray Absorption Spectroscopy with Hard x-Ray Free Electron Laser. *Appl. Phys. Lett.* **2013**, *103* (13), 131105. https://doi.org/10.1063/1.4821108.

(156) Katayama, T.; Owada, S.; Togashi, T.; Ogawa, K.; Karvinen, P.; Vartiainen, I.; Eronen, A.; David, C.; Sato, T.; Nakajima, K.; et al. A Beam Branching Method for Timing and Spectral Characterization of Hard X-Ray Free-Electron Lasers. *Struct. Dyn.* **2016**, *3* (3), 034301. https://doi.org/10.1063/1.4939655.

(157) Levantino, M.; Schirò, G.; Lemke, H. T.; Cottone, G.; Glownia, J. M.; Zhu, D.; Chollet, M.; Ihee, H.; Cupane, A.; Cammarata, M. Ultrafast Myoglobin Structural Dynamics Observed with an X-Ray Free-Electron Laser. *Nature Communications* **2015**, *6*, 6772. https://doi.org/10.1038/ncomms7772.

(158) Alves Lima, F. Investigation of Physiological Solutions of Metalloproteins in a High-Repetition Rate Picosecond X-Ray Absorption Experiment. **2011**, 244. https://doi.org/10.5075/epfl-thesis-5249.

(159) Falahati, K.; Tamura, H.; Burghardt, I.; Huix-Rotllant, M. Ultrafast Carbon Monoxide Photolysis and Heme Spin-Crossover in Myoglobin via Nonadiabatic Quantum Dynamics. *Nature Communications* **2018**, *9* (1), 4502. https://doi.org/10.1038/s41467-018-06615-1.

(160) Milne, C. J.; Penfold, T. J.; Chergui, M. Recent Experimental and Theoretical Developments in Time-Resolved X-Ray Spectroscopies. *Coordination Chemistry Reviews* **2014**, *277–278*, 44–68. https://doi.org/10.1016/j.ccr.2014.02.013.

(161) Zhang, W.; Alonso-Mori, R.; Bergmann, U.; Bressler, C.; Chollet, M.; Galler, A.; Gawelda, W.; Hadt, R. G.; Hartsock, R. W.; Kroll, T.; et al. Tracking Excited-State Charge and Spin Dynamics in Iron Coordination Complexes. *Nature* **2014**, *509* (7500), 345–348. https://doi.org/10.1038/nature13252.

(162) Mara, M. W.; Hadt, R. G.; Reinhard, M. E.; Kroll, T.; Lim, H.; Hartsock, R. W.; Alonso-Mori, R.; Chollet, M.; Glownia, J. M.; Nelson, S.; et al. Metalloprotein Entatic Control of Ligand-Metal Bonds Quantified by Ultrafast x-Ray Spectroscopy. *Science* **2017**, *356* (6344), 1276–1280. https://doi.org/10.1126/science.aam6203.

(163) Kawai, J.; Suzuki, C.; Adachi, H.; Konishi, T.; Gohshi, Y. Charge-Transfer Effect on the Linewidth of Fe *K* α x-Ray Fluorescence Spectra. *Phys. Rev. B* **1994**, *50* (16), 11347–11354. https://doi.org/10.1103/PhysRevB.50.11347.

(164) Petrich, J. W.; Lambry, J. C.; Kuczera, K.; Karplus, M.; Poyart, C.; Martin, J. L. Ligand Binding and Protein Relaxation in Heme Proteins: A Room Temperature Analysis of Nitric Oxide Geminate Recombination. *Biochemistry* **1991**, *30* (16), 3975–3987. https://doi.org/10.1021/bi00230a025.

(165) van Stokkum, I. H. M.; Larsen, D. S.; van Grondelle, R. Global and Target Analysis of Time-Resolved Spectra. *Biochimica et Biophysica Acta (BBA) - Bioenergetics* **2004**, *1657* (2–3), 82–104. https://doi.org/10.1016/j.bbabio.2004.04.011.

(166) Yanai, T.; Tew, D. P.; Handy, N. C. A New Hybrid Exchange–Correlation Functional Using the Coulomb-Attenuating Method (CAM-B3LYP). *Chemical Physics Letters* **2004**, *393* (1–3), 51–57. https://doi.org/10.1016/j.cplett.2004.06.011.

(167) Hess, B. A. Relativistic Electronic-Structure Calculations Employing a Two-Component No-Pair Formalism with External-Field Projection Operators. *Phys. Rev. A* **1986**, *33* (6), 3742–3748. https://doi.org/10.1103/PhysRevA.33.3742.

(168) Weigend, F. Accurate Coulomb-Fitting Basis Sets for H to Rn. *Phys. Chem. Chem. Phys.* **2006**, *8* (9), 1057. https://doi.org/10.1039/b515623h.

(169) Pantazis, D. A.; Chen, X.-Y.; Landis, C. R.; Neese, F. All-Electron Scalar Relativistic Basis Sets for Third-Row Transition Metal Atoms. *J. Chem. Theory Comput.* **2008**, *4* (6), 908–919. https://doi.org/10.1021/ct800047t.

(170) Roy, L. E.; Jakubikova, E.; Batista, E. R. Accurate Calculation of Redox Potentials Using Density Functional Methods.

(171) Klamt, A. Conductor-like Screening Model for Real Solvents: A New Approach to the Quantitative Calculation of Solvation Phenomena. *J. Phys. Chem.* **1995**, *99* (7), 2224–2235. https://doi.org/10.1021/j100007a062.

(172) Klamt, A.; Schüürmann, G. COSMO: A New Approach to Dielectric Screening in Solvents with Explicit Expressions for the Screening Energy and Its Gradient. *J. Chem. Soc., Perkin Trans. 2* **1993**, No. 5, 799–805. https://doi.org/10.1039/P29930000799.

(173) Klamt, A.; Jonas, V. Treatment of the Outlying Charge in Continuum Solvation Models. *The Journal of Chemical Physics* **1996**, *105* (22), 9972–9981. https://doi.org/10.1063/1.472829.

(174) Neese, F. The ORCA Program System: The ORCA Program System. *WIREs Comput Mol Sci* **2012**, *2* (1), 73–78. https://doi.org/10.1002/wcms.81.

(175) Wang, X.; de Groot, F. M. F.; Cramer, S. P. Spin-Polarized x-Ray Emission of 3 d Transition-Metal Ions: A Comparison via K α and K β Detection. *Phys. Rev. B* **1997**, *56* (8), 4553–4564. https://doi.org/10.1103/PhysRevB.56.4553.

(176) Schuth, N.; Mebs, S.; Huwald, D.; Wrzolek, P.; Schwalbe, M.; Hemschemeier, A.; Haumann, M. Effective Intermediate-Spin Iron in O $_2$ -Transporting Heme Proteins. *Proceedings of the National Academy of Sciences* **2017**, *114* (32), 8556–8561. https://doi.org/10.1073/pnas.1706527114.

(177) Brinkmann, L. U. L.; Hub, J. S. Ultrafast Anisotropic Protein Quake Propagation after CO Photodissociation in Myoglobin. *Proc Natl Acad Sci USA* **2016**, *113* (38), 10565–10570. https://doi.org/10.1073/pnas.1603539113.

(178) Franzen, S.; Bohn, B.; Poyart, C.; Martin, J. L. Evidence for Sub-Picosecond Heme Doming in Hemoglobin and Myoglobin: A Time-Resolved Resonance Raman Comparison of Carbonmonoxy and Deoxy Species. *Biochemistry* **1995**, *34* (4), 1224–1237. https://doi.org/10.1021/bi00004a016.

(179) Franzen, S.; Bohn, B.; Poyart, C.; DePillis, G.; Boxer, S. G.; Martin, J.-L. Functional Aspects of Ultra-Rapid Heme Doming in Hemoglobin, Myoglobin, and the Myoglobin Mutant H93G. *J. Biol. Chem.* **1995**, *270* (4), 1718–1720. https://doi.org/10.1074/jbc.270.4.1718.

(180) Chandrasekaran, P.; Chiang, K. P.; Nordlund, D.; Bergmann, U.; Holland, P. L.; DeBeer, S. Sensitivity of X-Ray Core Spectroscopy to Changes in Metal Ligation: A Systematic Study of Low-Coordinate, High-Spin Ferrous Complexes. *Inorg. Chem.* **2013**, *52* (11), 6286–6298. https://doi.org/10.1021/ic3021723.

(181) Rudd, D. J.; Goldsmith, C. R.; Cole, A. P.; Stack, T. D. P.; Hodgson, K. O.; Hedman, B. X-Ray Absorption Spectroscopic Investigation of the Spin-Transition Character in a Series of Single-Site Perturbed Iron(II) Complexes. *Inorg. Chem.* **2005**, *44* (5), 1221–1229. https://doi.org/10.1021/ic048765l.

(182) Kim, K. H.; Oang, K. Y.; Kim, J.; Lee, J. H.; Kim, Y.; Ihee, H. Direct Observation of Myoglobin Structural Dynamics from 100 Picoseconds to 1 Microsecond with Picosecond X-Ray

Solution Scattering. *Chem. Commun.* **2011**, *47* (1), 289–291. https://doi.org/10.1039/C0CC01817A.

(183) Barends, T. R. M.; Foucar, L.; Ardevol, A.; Nass, K.; Aquila, A.; Botha, S.; Doak, R. B.; Falahati, K.; Hartmann, E.; Hilpert, M.; et al. Direct Observation of Ultrafast Collective Motions in CO Myoglobin upon Ligand Dissociation. *Science* **2015**, *350* (6259), 445–450. https://doi.org/10.1126/science.aac5492.

(184) Kholodenko, Y.; Gooding, E. A.; Dou, Y.; Ikeda-Saito, M.; Hochstrasser, R. M. Heme Protein Dynamics Revealed by Geminate Nitric Oxide Recombination in Mutants of Iron and Cobalt Myoglobin †. *Biochemistry* **1999**, *38* (18), 5918–5924. https://doi.org/10.1021/bi983022v.

(185) Schade, M.; Moretto, A.; Crisma, M.; Toniolo, C.; Hamm, P. Vibrational Energy Transport in Peptide Helices after Excitation of C−D Modes in Leu- d_{10}. *J. Phys. Chem. B* **2009**, *113* (40), 13393–13397. https://doi.org/10.1021/jp906363a.

(186) Sato, T.; Togashi, T.; Ogawa, K.; Katayama, T.; Inubushi, Y.; Tono, K.; Yabashi, M. Highly Efficient Arrival Timing Diagnostics for Femtosecond X-Ray and Optical Laser Pulses. *Appl. Phys. Express* **2015**, *8* (1), 012702. https://doi.org/10.7567/APEX.8.012702.

(187) Gorgisyan, I.; Ischebeck, R.; Erny, C.; Dax, A.; Patthey, L.; Pradervand, C.; Sala, L.; Milne, C.; Lemke, H. T.; Hauri, C. P.; et al. THz Streak Camera Method for Synchronous Arrival Time Measurement of Two-Color Hard X-Ray FEL Pulses. *Opt. Express* **2017**, *25* (3), 2080. https://doi.org/10.1364/OE.25.002080.

(188) Gawelda, W.; Pham, V.-T.; Benfatto, M.; Zaushitsyn, Y.; Kaiser, M.; Grolimund, D.; Johnson, S. L.; Abela, R.; Hauser, A.; Bressler, C.; et al. Structural Determination of a Short-Lived Excited Iron(II) Complex by Picosecond X-Ray Absorption Spectroscopy. *Phys. Rev. Lett.* **2007**, *98* (5), 057401. https://doi.org/10.1103/PhysRevLett.98.057401.

(189) Findsen, E.; Friedman, J.; Ondrias, M.; Simon. Picosecond Time-Resolved Resonance Raman Studies of Hemoglobin: Implications for Reactivity. *Science* **1985**, *229* (4714), 661–665. https://doi.org/10.1126/science.4023704.

(190) Negrerie, M.; Cianetti, S.; Vos, M. H.; Martin, J.-L.; Kruglik, S. G. Ultrafast Heme Dynamics in Ferrous versus Ferric Cytochrome *c* Studied by Time-Resolved Resonance Raman and Transient Absorption Spectroscopy. *J. Phys. Chem. B* **2006**, *110* (25), 12766–12781. https://doi.org/10.1021/jp0559377.

(191) Li, P.; Sage, J. T.; Champion, P. M. Probing Picosecond Processes with Nanosecond Lasers: Electronic and Vibrational Relaxation Dynamics of Heme Proteins. *The Journal of Chemical Physics* **1992**, *97* (5), 3214–3227. https://doi.org/10.1063/1.463008.

(192) Choy, J.-H.; Yoon, J.-B.; Jung, H. Polarization-Dependent X-Ray Absorption Spectroscopic Study of [Cu(Cyclam)]2+-Intercalated Saponite. *J. Phys. Chem. B* **2002**, *106* (43), 11120–11126. https://doi.org/10.1021/jp020374+.

(193) Yano, J.; Robblee, J.; Pushkar, Y.; Marcus, M. A.; Bendix, J.; Workman, J. M.; Collins, T. J.; Solomon, E. I.; DeBeer George, S.; Yachandra, V. K. Polarized X-Ray Absorption Spectroscopy of Single-Crystal Mn(V) Complexes Relevant to the Oxygen-Evolving Complex of Photosystem II. *J. Am. Chem. Soc.* **2007**, *129* (43), 12989–13000. https://doi.org/10.1021/ja071286b.

(194) Johansson, L. C.; Stauch, B.; Ishchenko, A.; Cherezov, V. A Bright Future for Serial Femtosecond Crystallography with XFELs. *Trends in Biochemical Sciences* **2017**, *42* (9), 749–762. https://doi.org/10.1016/j.tibs.2017.06.007.

(195) Panneels, V.; Wu, W.; Tsai, C.-J.; Nogly, P.; Rheinberger, J.; Jaeger, K.; Cicchetti, G.; Gati, C.; Kick, L. M.; Sala, L.; et al. Time-Resolved Structural Studies with Serial Crystallography: A

New Light on Retinal Proteins. *Struct. Dyn.* **2015**, *2* (4), 041718. https://doi.org/10.1063/1.4922774.

(196) Sawaya, M. R.; Cascio, D.; Gingery, M.; Rodriguez, J.; Goldschmidt, L.; Colletier, J.-P.; Messerschmidt, M. M.; Boutet, S.; Koglin, J. E.; Williams, G. J.; et al. Protein Crystal Structure Obtained at 2.9 A Resolution from Injecting Bacterial Cells into an X-Ray Free-Electron Laser Beam. *Proceedings of the National Academy of Sciences* **2014**, *111* (35), 12769–12774. https://doi.org/10.1073/pnas.1413456111.

(197) Cho, H. S.; Dashdorj, N.; Schotte, F.; Graber, T.; Henning, R.; Anfinrud, P. Protein Structural Dynamics in Solution Unveiled via 100-Ps Time-Resolved x-Ray Scattering. *Proceedings of the National Academy of Sciences* **2010**, *107* (16), 7281–7286. https://doi.org/10.1073/pnas.1002951107.

(198) Wall, M. E.; Wolff, A. M.; Fraser, J. S. Bringing Diffuse X-Ray Scattering into Focus. *Current Opinion in Structural Biology* **2018**, *50*, 109–116. https://doi.org/10.1016/j.sbi.2018.01.009.

(199) Haldrup, K.; Gawelda, W.; Abela, R.; Alonso-Mori, R.; Bergmann, U.; Bordage, A.; Cammarata, M.; Canton, S. E.; Dohn, A. O.; van Driel, T. B.; et al. Observing Solvation Dynamics with Simultaneous Femtosecond X-Ray Emission Spectroscopy and X-Ray Scattering. *J. Phys. Chem. B* **2016**, *120* (6), 1158–1168. https://doi.org/10.1021/acs.jpcb.5b12471.

(200) Collman, J. P.; Decreau, R. A.; Dey, A.; Yang, Y. Water May Inhibit Oxygen Binding in Hemoprotein Models. *Proceedings of the National Academy of Sciences* **2009**, *106* (11), 4101–4105. https://doi.org/10.1073/pnas.0900893106.

(201) Takayanagi, M.; Kurisaki, I.; Nagaoka, M. Non-Site-Specific Allosteric Effect of Oxygen on Human Hemoglobin under High Oxygen Partial Pressure. *Scientific Reports* **2014**, *4*, 4601.

(202) Eaton, W. A.; Henry, Eric. R.; Hofrichter, J.; Mozzarelli, A. Is Cooperative Oxygen Binding by Hemoglobin Really Understood? *Nat. Struct Biol.* **1999**, *6* (4), 351–358. https://doi.org/10.1038/7586.

(203) Vankó, G.; Neisius, T.; Molnár, G.; Renz, F.; Kárpáti, S.; Shukla, A.; de Groot, F. M. F. Probing the 3d Spin Momentum with X-Ray Emission Spectroscopy: The Case of Molecular-Spin Transitions. *The Journal of Physical Chemistry B* **2006**, *110* (24), 11647–11653. https://doi.org/10.1021/jp0615961.

(204) RefractiveIndex.INFO - Refractive index database https://refractiveindex.info/ (accessed Dec 12, 2019).

(205) Neese, F. Software Update: The ORCA Program System, Version 4.0: Software Update. *WIREs Comput Mol Sci* **2018**, *8* (1), e1327. https://doi.org/10.1002/wcms.1327.

Curriculum Vitae

Dominik Kinschel
kinscheldominik@gmail.com
www.linkedin.com/in/dominik-kinschel

EDUCATION

2016 – 2019 PhD in Chemical Science and Engineering

École polytechnique fédérale de Lausanne, Paul Scherrer Institute, Villigen, Switzerland

2013 – 2015 Master of Science in Molecular Science and Engineering

KTH – Royal Institute of Technology, Stockholm, Sweden
Master Thesis: Stable Redox Systems for Dye-Sensitized Solar Cells
Prof. Lars Kloo

2009 – 2013 Bachelor of Science in Chemistry

Technical University Graz / Karl-Franzens University Graz, Austria
Bachelor Thesis: Complexes of Group 4 Transition Metals with Tris(trimethylsilyl)silanyl Containing Cp-ligands
Prof. Christoph Marschner

EMPLOYMENT HISTORY

2015 Stanford University, SLAC National Accelerator Laboratory, California, USA

Research project
DFT simulations on heterogenous catalysis of hydrocarbons

2015 Dyenamo AB, Stockholm, Sweden

Master thesis in Dynamo AB on novel electrolytes for dye sensitized solar cells, completed 2 product developments.

AWARDS

Invited "Hot topic" talk at the Science@FELs conference, Stockholm 2018

SCNAT/SCS/SSFEC Chemistry Travel Award 2018

UXSS Travel Grant 2016

PUBLICATIONS

Bacellar, C., Kinschel, D., Mancini, G.F., Rouxel, J.R., Cirelli, C., Knopp, G., Szlachetko, J., Lima, F.A., Menzi, S., Pamfilidis, G., Arrell, C.A., Johnson, P.J.M., Milne, C., Chergui, M., 2019. Doming in Ferric Heme Proteins: Femtosecond X-ray Absorption and X-ray Emission Studies. *Manuscript in preparation*

Rouxel, J.R., Rosner, B., Karpov, D., Kinschel, D., Bacellar, C., Mancini, G.F., Cannelli, O., Lacour, J., David, C., Chergui, M., 2019. Probing molecular chirality with the orbital angular momentum of X-ray light. *Manuscript in preparation*

Rossi, T. C.; Grolimund, D.; Nachtegaal, M.; Cannelli, O.; Mancini, G. F.; Bacellar, C.; Kinschel, D.; Rouxel, J. R.; Ohannessian, N.; Pergolesi, D.; et al. X-Ray Absorption Linear Dichroism at the Ti K Edge of Anatase TiO 2 Single Crystals. Phys. Rev. B 2019, 100 (24), 245207. https://doi.org/10.1103/PhysRevB.100.245207

Cannelli, O.; Bacellar, C.; Ingle, R. A.; Bohinc, R.; Kinschel, D.; Bauer, B.; Ferreira, D. S.; Grolimund, D.; Mancini, G. F.; Chergui, M. Toward Time-Resolved Laser T-Jump/X-Ray Probe Spectroscopy in Aqueous Solutions. Structural Dynamics 2019, 6 (6), 064303. https://doi.org/10.1063/1.5129626

Kinschel, D., Bacellar, C., Cannelli, O., Sorokin, B., Lima, F.A., Mancini, G.F., Rouxel, J.R, Katayama, T., Keane, T., Gawelda, W., Zalden, P., Schulz, S., Budarz, J., Khakhulin, D., Obara, Y., Nishitani, J., Ito, H., Ito, T., Kurahashi, N., Higashimura, C., Kudo, S., Bressler, C., Milne, C.J., Penfold, T., Yabashi, M., Suzuki, T., Misawa, K., Chergui, M., 2019. Femtosecond X-ray emission study of the spin cross-over dynamics in heme proteins. *In review at Nature*

Kuzmenko, D., Vogelsang, U., Hitz, S., Müller, D., Clark, A.H., Kinschel, D., Czapla-Masztafiak, J., Milne, C., Szlachetko, J., Nachtegaal, M., 2019. A von Hamos spectrometer for *in situ* sulfur speciation by non-resonant sulfur Kα emission spectroscopy. J. Anal. At. Spectrom. 10.1039.C9JA00195F. https://doi.org/10.1039/C9JA00195F

Zitz, R., Hlina, J., Arp, H., Kinschel, D., Marschner, C., Baumgartner, J., 2019. Group 4 Metal and Lanthanide Complexes in the Oxidation State +3 with Tris(trimethylsilyl)silyl Ligands. Inorg. Chem. 58, 7107–7117. https://doi.org/10.1021/acs.inorgchem.9b00866

Budarz, J., Santomauro, F.G., Rittmann-Frank, M.H., Milne, C.J., Huthwelker, T., Grolimund, D., Rittmann, J., Kinschel, D., Rossi, T., Chergui, M., 2017. Time-resolved Element-selective Probing of Charge Carriers in Solar Materials. CHIMIA International Journal for Chemistry 71, 768–772. https://doi.org/10.2533/chimia.2017.768

Santomauro, F.G., Grilj, J., Mewes, L., Nedelcu, G., Yakunin, S., Rossi, T., Capano, G., Al Haddad, A., Budarz, J., Kinschel, D., Ferreira, D.S., Rossi, G., Gutierrez Tovar, M., Grolimund, D., Samson, V., Nachtegaal, M., Smolentsev, G., Kovalenko, M.V., Chergui, M., 2017. Localized holes and delocalized electrons in photoexcited inorganic perovskites: Watching each atomic actor by picosecond X-ray absorption spectroscopy. Structural Dynamics 4, 044002. https://doi.org/10.1063/1.4971999

Monni, R., Auböck, G., Kinschel, D., Aziz-Lange, K.M., Gray, H.B., Vlček, A., Chergui, M., 2017. Conservation of vibrational coherence in ultrafast electronic relaxation: The case of diplatinum complexes in solution. Chemical Physics Letters 683, 112–120. https://doi.org/10.1016/j.cplett.2017.02.071

Cong, J.*, Kinschel, D.*, Daniel, Q., Safdari, M., Gabrielsson, E., Chen, H., Svensson, P.H., Sun, L., Kloo, L., 2016. Bis(1,1-bis(2-pyridyl)ethane)copper(I / II) as an efficient redox couple for liquid dye-sensitized solar cells. Journal of Materials Chemistry A 4, 14550–14554. https://doi.org/10.1039/C6TA06782D
*Authors contributed equally

ORAL PRESENTATIONS (SELECTED)

09.10.2018 SLS Symposium, PSI, Villigen, Switzerland: “Time resolved X-ray spectroscopy of Nitrosyl-myoglobin in physiological solution”

25.09.2018 Alvra-SwissFEL Group Seminar, Villigen, Switzerland: “Updates on the Data Analysis of Nitrosyl-myoglobin in physiological media studied by ultrafast X-ray spectroscopy”

31.08.2018 Annual Meeting of the Swiss Physical Society, EPFL, Lausanne, Switzerland: “Time Resolved X-ray Spectroscopy and Scattering of Myoglobin in Solution”

26.06.2018 Science@FELs Conference, Stockholm, Sweden: “Ligand dissociation and recombination of Nitrosyl-myoglobin in physiological media studied by ultrafast X-ray spectroscopy and X-ray Diffuse Scattering”

23.02.2018 LSU Winter Seminar, Saas-Fee, Switzerland: “Time Resolved X-ray Spectroscopy and Scattering of Myoglobin in Solution at EXFEL and SACLA”

04.12.2017 Post-Experiment Meeting, SACLA, Japan: “First results of the study on Correlated spin and structural dynamics in the recombination of NO to deoxy-Myoglobin in physiological media”

30.11.2017 Pre-Experiment Meeting, SACLA, Japan: “Correlated spin and structural dynamics in the recombination of NO to deoxy-Myoglobin in physiological media”

07.11.2017 LSU Group Meeting, EPFL, Lausanne, Switzerland; “Time Resolved X-ray Spectroscopy and Scattering of Myoglobin in Solution”

POSTER PRESENTATIONS (SELECTED)

“Ligand dissociation and recombination of Nitrosyl-myoglobin in physiological media studied by ultrafast X-ray spectroscopy and X-ray Diffuse Scattering” for the Swiss Chemical Society Fall Meeting, EPFL, Lausanne, Switzerland, 07.09.2018

"Ligand dissociation and recombination of Nitrosyl-myoglobin in physiological media studied by ultrafast X-ray spectroscopy and X-ray Diffuse Scattering", for the X-ray Absorption Fine Structure Conference, Krakow, Poland, 23.07.2018

"Ligand dissociation and recombination of Nitrosyl-myoglobin in physiological media studied by ultrafast X-ray spectroscopy and X-ray Diffuse Scattering" for the Science@FELs Conference, Stockholm, Sweden, 26.06.2018

“Correlated spin and structural dynamics in the recombination of NO to deoxy-Myoglobin in physiological media” for the LACUS day, EPFL, Lausanne, Switzerland, 14.02.2018

“Correlated spin and structural dynamics in the recombination of NO to deoxy-Myoglobin in physiological media” for the 2018 European XFEL Users’ Meeting and Satellite Meetings, Hamburg, Germany, 24.01.-26.01.2018

TEACHING

Teaching assistant for:

- Experimental physical Chemistry
- Advanced General Chemistry

Supervisor for Semester Project in Molecular & Biological Chemistry

- Fluorescence up-conversion and UV-VIS investigation of Cobalt-polypyridine complexes, Tomislav Begusic, 2016